Supramolecular Biopolymeric Composite Materials: Green Synthesis, Characterization and Applications

Tamutsiwa Moven Mututuvari
Marquette University

SUPRAMOLECULAR BIOPOLYMERIC COMPOSITE MATERIALS: GREEN SYNTHESIS, CHARACTERIZATION AND APPLICATIONS

by

Tamutsiwa M. Mututuvari, B.Sc. (Honors, Chemistry)

A Dissertation submitted to the Faculty of the Graduate School,
Marquette University,
in Partial Fulfillment of the Requirements for
the Degree of Doctor of Philosophy

Milwaukee, Wisconsin

December 2014

ABSTRACT
SUPRAMOLECULAR BIOPOLYMERIC COMPOSITE MATERIALS: GREEN SYNTHESIS, CHARACTERIZATION AND APPLICATIONS

Tamutsiwa M. Mututuvari, B.Sc. (Honors, Chemistry)

Marquette University, 2014

Macrocycles, such as crown ethers (CRs) and resorcinarenes (RESs), exhibit selective complexation of heavy metal ions and organic pollutants respectively. Consequently, they have been investigated for their suitability in adsorbing these aqueous pollutants. However, they are difficult to handle and recycle for reuse because, by themselves, they can only be fabricated in powder form. To alleviate this challenge, we developed a method to encapsulate these macrocycles into film-forming polysaccharides—cellulose (CEL) and chitosan (CS). This was achieved by using a green and recyclable solvent, an ionic liquid, to dissolve both macrocycles and polysaccharides and regenerate corresponding composites in water. Resultant composites were characterized by FTIR, UV-Visible, X-ray powder diffraction and scanning electron microscopy. These polysaccharides are attractive because they are naturally abundant, biodegradable and biocompatible. The composites retained desirable properties of their individual constituents, namely superior mechanical strength (from CEL), excellent adsorption capability for cadmium and zinc ions (from CRs and CS) and organic solutes (from RESs and CS). Specifically, increasing the concentration of CEL from 50% to 90% in [CEL+CR] resulted in almost 2X increase in tensile strength. Adding 40% benzo 15-crown-5 ether (B15C5) to CS led to a 4X enhancement in the amount of cadmium ions adsorbed by [CS+B15C5]. Interestingly, RES-based composites exhibited selectivity amongst dinitrobenzene (DNB) isomers. For example, one g of [CEL+RES] adsorbed more *1,2*-DNB (5.37±0.05 mol L^{-1}) than *1,3*-DNB (4.52±0.03 mol L^{-1}) and *1,4*-DNB (2.74±0.04 mol L^{-1}). These results help to extend the potential applications of supramolecular composites in water remediation.

We also successfully synthesized hydroxyapatite (HAp) *in situ* by alternately soaking [CEL+CS] composite films in calcium and phosphate salt solutions. These composites will be expected to be osteoconductive (due to HAp), thereby necessitating their use in bone tissue engineering. In another related study, we developed a simple, one step process to encapsulate an antibiotic, ciprofloxacin (CPX) in composites containing various proportional concentrations of CEL, CS, and keratin (KER). KER was found to slow down the release of CPX from the composites. These results clearly indicate that the release of CPX can be controlled by judicious adjustment of the concentrations of KER in the composites.

ACKNOWLEDGMENTS

Tamutsiwa M. Mututuvari, B.Sc. (Honors, Chemistry)

This document summarizes half of a decade worth of effort, frustration and achievement all bundled together. With God on my side, I knew that I was destined for success. I, therefore give Glory to the Almighty for leading the way and for opening all the doors for success. As I transition back into the real world, I would like to acknowledge those individuals who have enriched my professional portfolio through our interactions at various stages of my research.

My advisor, Professor Chieu D. Tran (Pfletschinger-Haberman Professor) has changed my whole perspective of the research trade. His hands-on management approach has helped me to stay on track and finish tasks 'as soon as possible.' I believe science can only progress when you have individuals like him who are dedicated and who uphold integrity in research. I thank Prof. Tran for his patience with me during the course of my Ph.D. studies.

I was fortunate to have Profs. Fiedler and Timerghazin who set aside time out of their busy schedules to offer constructive criticism each time we met to discuss my research progress. Their suggestions have helped to shape my approach to finding scientific solutions to real world challenges. With their help, this journey turned out to be an awesome experience.

I would also want to thank Drs. S. Hardcastle (Advanced Analysis Facility, University of Wisconsin Milwaukee), H. Försterling (NMR Facility, University of Wisconsin Milwaukee), R. Fournelle (Department of Mechanical Engineering, Marquette

University), and Messrs. Mark Bartelt (Department of Chemistry, Marquette University), and Jack Holbus (Machine Shop, Physics Department, Marquette University). Dr. Hardcastle took SEM images and XPS spectra of our film samples. Dr. Försterling took solid state NMR spectra of our samples. Dr. Fournelle recorded SEM images of our hydroxyapatite composite films and also granted access for me to use his tensile tester machine. Mark Bartelt helped with setting up analytical instruments. Jack Holbus assembled the home-made drier chamber and prepared mould specimens upon which we casted our gel samples.

I would like to thank my lab seniors, Drs. Irena Mejac and Simon Duri for all their support during the initial days of my stay in the lab.

DEDICATION

Tamutsiwa M. Mututuvari, B.Sc. (Honors, Chemistry)

To my parents, Lovely Shava and Clever V. Mututuvari for your unconditional love, prayers, and encouragement throughout this journey. Most importantly, thank you for your sacrifices in educating and preparing me for my future. I am glad that you have lived to witness this wonderful achievement. I hope that I have made you prouder than you were before.

To my life partner, Joyline and little angel, Tadisaishe, for being my true and best cheerleaders. Whenever my cards were down due to making slower-than-expected progress in my research, having little to no personal or social life, imagining my life, had I chosen to continue my professional career in the "real world", you would assure me that pursuing a Ph.D. was the right thing to do and the pleasures of normal life could wait. After all, I just lost a mere 7% of 'normal' life, based on the life expectancy of 76 years and the Ph.D. program of 5.5 years. I know you dearly missed the time with me because I was 'always at work.' Thank you for your understanding.

To my siblings, Megina, Tawe, Tsvakai, Lily, Simbarashe, Memory, Ishe and your families for being wonderful and very patient when I was pursuing these studies. Who would have imagined two decades ago that this year of 2014, we would be celebrating the addition of a special title, Ph.D., to our lineage? It's all by the Grace of God, the Almighty.

To my parents-in-law, Mr. and Mrs. Muzondo, for all the prayers throughout my studies. May God continue to bless you two.

To my brothers-in-law and your families for being wonderful and patient throughout this endeavor. Special thanks go to the late Tapfumaneyi Muzondo who played a key role as my small family transitioned from Zimbabwe to USA. It's heartbreaking that you could not live to witness this achievement. May your dear soul rest in eternal peace.

To the vast extended family from both my side and my wife's side for inspiring me to attain this great qualification. Brighton, thank you muzaya for inspiring me because of the high value you have always placed in education. I hope this Ph.D. qualification will be a source of inspiration to the upcoming generation in our family.

TABLE OF CONTENTS

LIST OF TABLES

LIST OF FIGURES

LIST OF SCHEMES

CHAPTER 1
INTRODUCTION

1.1. Background

The interest in syntheses and applications of bio-based composites has grown tremendously over the years and this trend is expected to continue into the foreseeable future. This interest is mainly driven by the need for a sustainable alternative to the depleting petroleum reserves.[1-4] The depletion of petroleum reserves is caused by their increasing use as chemical feed stocks in industries without adequate replacement in a timely manner. For example, it takes 10^6 years to synthesize petroleum from biomass yet when consumed as plastics or fuel, it takes 1-10 years to convert it to CO_2.[5] Aside from the depletion problem, petroleum-based materials are usually non-biodegradable and therefore cause potential harm to the environment after their disposal. In addition, petroleum-based materials cause CO_2 emissions which, in turn cause undesirable greenhouse effects. Therefore, with increasing environmental awareness and demands of legislative authorities worldwide, green composites derived from plants and animals are being pursued in many different scientific fields.

Biopolymers, such as cellulose (CEL), chitosan (CS), keratin (KER) and other related biopolymers offer the best alternative to address the challenges posed by continued use of petroleum products. These natural biopolymers are replaced at the rate that is more than the rate of consumption. Therefore, using such materials whereby the rate of CO_2 sequestered is balanced with the rate of consumption contributes significantly to developing carbon neutral materials. Another advantage of using natural biopolymers

is that they are inherently biodegradable. This is a desirable property since it prevents the accumulation of solid waste. In addition to the above advantages, natural biopolymers are derived from cheaper sources. Therefore, their use is bound to be economically sustainable. In addition, natural biopolymers are generally non-toxic. This enables them to be used safely in biomedical applications without concern for health hazards and environmental damage throughout their lifecycle. Also, natural biopolymers are both biocompatible and bioactive that is they exist in harmony within a biological system (biocompatible) and elicit a beneficial response from the biological system (bioactive). As a result of them being biodegradable, natural biopolymers can be applied to make short life-span products such as packaging, toys and sporting equipment.[6]

Although these biopolymers appear to be the ideal alternative to the petroleum-based polymers, their use is accompanied by some processing challenges. These challenges arise from the nature of their structures. Their structures are stabilized by extensive intra- and inter-molecular hydrogen bonds (H-bonds) and van der Waals (VDW) forces formed between the bio-polymeric chains.[7,8] For example, these H-bonds enable CEL to adopt a crystalline structure which imparts tough texture to CEL. In KER, in addition to the H-bonds, there is an extensive network of intra- and inter-molecular disulfide bridges which impart the tough, fibrous structure to the keratinous materials such as hair and wool.[9,10] Now, before these biopolymers can be used in most applications, they have to be processed into usable form such as films and fibers, among many other forms. This processing involves dissolving the material and then regenerating it into the desired shape or structure. However, these biopolymers are recalcitrant to most conventional solvents due to the presence of this extensive network of H-bonds, VDW

forces (in CEL and CS) and disulfide bridges (in KER). As a result, a wide variety of solvent systems have been developed to dissolve and process these biopolymers. Whilst these solvents enabled the adoption of biopolymers in many applications, they had serious limitations. The solvent systems developed for dissolving these biopolymers may cause degradation of the biopolymers and also may generate undesirable by-products.[8] In addition, they generate harmful vapors. Therefore, as these solvent systems are not economically and environmentally sustainable, it is necessary to design environmentally friendly solvents to tap in the potential benefits of using these biopolymers.

These concerns prompted us to initiate this study. In this study, we used ionic liquids as better alternative solvents to dissolve and reconstitute biopolymers (CEL, CS, and KER) into their usable film form. The ionic liquid used was 1-butyl-3-methylimidazolium chloride, $BMIm^+Cl^-$. Ionic liquids are generating a lot of attention because they exhibit the following attractive properties; 1) they exhibit negligible vapor pressure which eliminates vapor emissions into the environment; 2) they can be recovered and reused thereby ensuring economic sustainability and 3) they are thermally stable thereby allowing the dissolution of biopolymers at moderate temperatures without concerns about their decomposition. In addition, $BMIm^+Cl^-$ is miscible with water thereby allowing its removal from gel films by just immersing the films in water; $BMIm^+Cl^-$ leaches into the water leaving an ionic liquid-free gel film. The ionic liquid is then recovered by distilling the aqueous washings.

Each biopolymer alone does not always satisfy the complex demands of industrial and biomedical applications. As a way to go around this problem, we blended these biopolymers in different proportions using $BMIm^+Cl^-$ as the common solvent. The

resultant composites were expected to possess desirable properties derived from their individual components. For example, composites of CEL and CS ([CEL+CS]) were expected to possess superior mechanical properties (from CEL) and good adsorption capability for organic pollutants (from CS). Even after this blending, these composites may still not possess all the properties required for certain applications. For example, these biopolymers cannot show selectivity towards the adsorption of either organic or inorganic pollutants. In our case, we used crown ethers (CRs) and resorcinarene (RES) to impart selectivity, to these biopolymers, towards their adsorption of heavy metal ions and organic pollutants respectively.

1.2. General Overview of Materials used in the Study

1.2.1. Cellulose

Cellulose (CEL), a naturally occurring polysaccharide, constitute the main structural component of cell walls of plants, algae, fungi and bacteria. Being a natural biopolymer, CEL presents numerous interesting properties such as being renewable, biodegradable, biocompatible and environmentally friendly. These unique properties have earned CEL the U.S. Generally Recognized as Safe (GRAS) status.[11] Most importantly, CEL is the most abundant natural biopolymer on Earth with an estimated 10^{11} tons of CEL being produced annually by plants through photosynthesis.[12] Plant CEL is found naturally embedded in polymer matrices that are composed of hemicelluloses, pectins and lignins. For example, CEL of naturally opened bolls of cotton constitute 85-97% of the dry weight of the cotton fibers with the remainder being hemicellulose, lignin

and pectin.[13] This CEL is often isolated from these non-cellulosic polymers through acid hydrolysis.

The structure of CEL is entirely composed of linear chains, of variable length, of D-glucose residues linked through β-(1-4)-glycosidic bonds (Figure 1-1). The presence of hydroxyl groups allow the formation of a wide network of intra- and inter-molecular hydrogen bonding (H-bonding) within and between its polymer chains. Intramolecular H-bonding between adjacent anhydroglucose residues maintains the linear integrity of the polymer chains. In addition, intra- and intermolecular H-bonding together with Van der Waals (VDW) forces enables CEL to adopt a fibrillar structure which imparts superior mechanical strength to CEL. This superior mechanical strength has enabled CEL to be used as a structural engineering material in a wide range of applications including paper, wood, textiles, cosmetics, biofuels and composite material strengthening among other applications. In addition, CEL has been used to fabricate paper-based application devices including field effect transistors, biosensors and chemical sensors.[14]

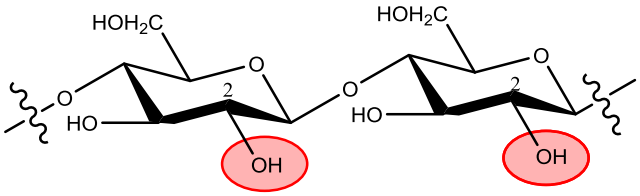

Cellulose (CEL)

Figure 1-1 Structure of cellulose (CEL).

Interestingly, CEL chains aggregate into portions of various degrees of lateral order ranging from crystalline to amorphous regions. The distribution of these regions

control the chemical reactivity of CEL. For instance, those hydroxyl groups residing in the amorphous regions are relatively more accessible to chemical reactants than those hydroxyl groups residing in crystalline regions. This topochemical property has a bearing on making it essentially impossible to dissolve CEL in the common organic solvents. This has limited the potential of CEL to be used in a wide range of applications in the scientific field.

Successful attempts to dissolve CEL date back to the year 1846 when Christian Friedrich Schoenbein discovered, by coincidence, that a mixture of HNO_3/H_2SO_4 could dissolve CEL by converting it to cellulose nitrate.[15] Since then, a variety of derivatizing and non-derivatizing solvents have been developed. Derivatizing solvent systems achieve dissolution by funtionalizing CEL into soluble derivatives. For examples CEL was converted to xanthate,[16] carbamate,[17] trifluoroacetate[18] and methylol[19] derivatives using mixtures of CS_2/NaOH, urea/NaOH, trifluoroacetic acid, and DMSO/paraformaldehyde respectively. The resultant derivatives could easily dissolve in common organic solvents. However, these derivatizing solvents suffer from a variety of drawbacks. For examples; the HNO_3/H_2SO_4 systems are too reactive for subsequent functionalization; carbon disulfide is flammable and toxic therefore it requires large investments in safety equipment;[20] sodium hydroxide is corrosive and trifluoroacetic acid is both expensive and corrosive. During dissolution in DMSO/paraformaldehyde, undesired side reactions, such as the growth of oligo (oxymethylene) chains and crosslinking may occur.[15]

Non-derivatizing solvents have merged as the most promising candidates for the dissolution of CEL. These solvents achieve dissolution through their physical interactions with hydroxyl groups on CEL thereby disrupting H-bonding with this polysaccharide

framework. Examples of such solvents include *N*-methylmorpholine-*N*-oxide (NMMO),[21] *N, N*-dimethylacetamide (DMAc)/LiCl,[22] and DMSO/tert (butyl) ammonium fluoride (TBAF).[23] These solvent systems can achieve dissolution of CEL with negligible depolymerization. However, these solvent systems are limited by a myriad of challenges. Specifically, NMMO is unstable, which may cause a safety risk due to its spontaneous decomposition.[24] In addition, side reactions may cause consumption of this expensive solvent leading to economic losses. *N, N*-dimethylacetamide (DMAc)/LiCl system suffers from incomplete recycling of this expensive solvent system.[15] As a result of these challenges, the search for better alternatives remains an ongoing area of research. Recently, a new and promising class of solvents, ionic liquids, has emerged. Ionic liquids (ILs) possess unusual physical and chemical properties which enable them to be used in a variety of applications including the dissolution of polysaccharides such as CEL.[25] Ionic liquids have negligible vapor pressure which help to cut down on harmful emissions.[25,26] In addition, they are both thermally stable[27] and non-flammable.[28] A detailed treatise on the subject of ionic liquids has been reserved for section 1.4.

1.2.2. Chitosan

Chitosan (CS) is a semi-synthetic biopolymer obtained by alkaline deacetylation of chitin, the second most abundant natural biopolymer after CEL.[29] Chitin is found widely distributed as a structural material in anthropods (crabs, lobsters, shrimps, crayfish, king crabs and insects) as well as mollusks (e.g., squids). Although chitin was the first polysaccharide to be identified by humans, 30 years preceding CEL, it has remained unused until just recently when interest in its use has increased.[30] To realize its potential, chitin is often converted to CS through alkaline deacetylation. Alongside CEL,

CS exhibits unique properties such as renewable, biodegradable, biocompatible and environmentally friendly.

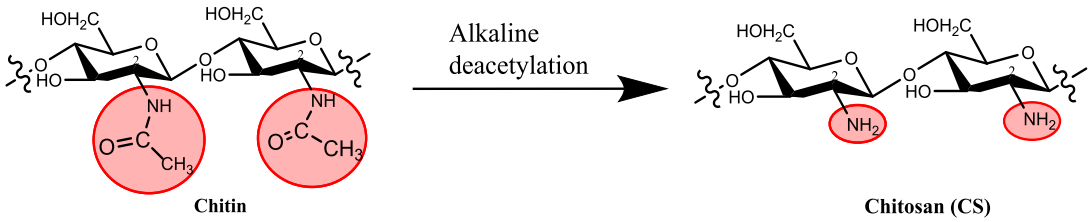

Figure 1-2 Deacetylation of chitin to form chitosan (CS).

Chitosan is composed of D-glucosamine and N-acetyl-D-glucosamine units linked through β-(1-4)-glycosidic bonds where the ratio of D-glucosamine to N-acetyl-D-glucosamine residues exceed 60% within the bio-polymeric chain (Figure 1-2).[30] The presence of the amine group at C-2 of the D-glucosamine residues imparts some interesting properties to CS. Notably, whereas all other naturally occurring polysaccharides are acidic, CS (and chitin) is basic and therefore it can be protonated easily in acidic solutions. This property has enabled CS to be used as an antibacterial agent in a variety of pharmaceutical formulations.[31] In its cationic state, CS is believed to interact with anionic groups on the bacterial cell surface resulting in membrane permeability which facilitates leakage of essential cellular proteins.[32] Alternatively, these amine groups can form chelates with essential nutrients resulting in the inhibition of important enzymes. Aside from its use as an antimicrobial agent, CS can be used to promote wound healing; stimulates favorable immune response; stop bleeding (hemostasis); and to manage exudate thereby keeping the wound surface relatively moist.[33,34]

Unarguably, the most important feature of CS and all natural biopolymers is that they can be processed into different usable forms such as films, sponges, gels, scaffolds, micro- and nano-particles and nanofibers for use in a variety of biomedical and environmental applications.[35] This enables CS to be used in a wide variety of applications in both biomedical and environmental applications. In addition to its use as an antimicrobial agent, CS can serve as a scaffold in tissue engineering such as bone tissue engineering, cartilage tissue engineering, liver tissue engineering, and nerve tissue engineering. In bone tissue engineering, CS is preferred because it promotes cell growth and mineral rich matrix deposition by osteoblasts cells in culture. Essentially, studies have focused on chitosan-calcium phosphate composites as scaffolds for bone tissue engineering.[36] In cartilage and liver tissue engineering, CS is often chosen due to its structural similarity with various glycosaminoglycans found in articular cartilage.[37] In addition to being biocompatible and biodegradable, CS can support the growth of neurons cultured on its surface thereby enhancing its potential to promote repair of peripheral nervous system.[38]

Apart from its use in the biomedical applications, CS has also been used in the adsorption of pollutants, both organic and inorganic pollutants, from water or wastewater. Essentially, CS use in adsorption dates back to the 1980s when it was used to adsorb a variety of toxic heavy metal ions including Cu, Zn, Cd, Cr, and Pb.[39] Such reports laid the foundation for the interesting field of adsorption using natural biopolymers. During the years that followed, CS-based composites have been widely applied to the adsorption and separation of heavy metal ions, dyes and other organic pollutants.[40-42]

An emerging application of CS is in the synthesis of gold and silver nanoparticles. In most of the documented studies, CS has been used as both a reducing- and a stabilizing agent. The presence of chemically active ammino- and hydroxyl groups enable CS to reduce Ag (1) and Au (III) to their corresponding zero valent states. The resultant CS-Ag/Au nanoparticle composites display interesting properties which can be exploited in a variety of novel applications. In one study, CS films with silver nanoparticles showed both fast and long lasting antibacterial effectiveness against *Eschericia coli*.[43] In all these composites, CS, in its polycationic state is believed to interact with the negatively charged surface of the metal nanoparticles through electrostatic interactions.[44]

In spite of all these potential applications of CS, there are still challenges encountered in its processing and use. The main processing solvent used to fabricate CS is chiefly acetic acid. However, prior to its use, this acid has to be neutralized in an alkali solution. Other solvents that have been investigated include trifluoroacetic acid, etc. These solvent systems are corrosive and therefore unattractive. An additional challenge encountered in using CS-based composites is that CS exhibits poor selectivity in adsorption of heavy metal ions. In addition, CS suffers from poor mechanical and rheological properties. These and other associated challenges require urgent attention. For example, the mechanical properties of CS may be improved through reinforcements using other structural strong materials such as CEL, KER and calcium phosphate. Selectivity may be improved by incorporating a selective agent such organic macrocycles. These have to be incorporated in such a way that the unique properties of CS, for example adsorption capacity, antibacterial, hemostatic and excellent wound healing, remain intact. Recent progress in developing solvent systems seem to suggest the use of a potentially

green solvent, ionic liquid. The properties and justification of using this novel solvent will be described in section 1.4.

1.2.3. Keratin

Keratins (KERs) are the most abundant structural proteins and form a protective layer of all epidermal tissues.[45] They are tough, fibrous proteins found in hair, wool, horns and nails of most vertebrates. KER can exist in one of two conformations; the α- and the β-conformations. In the α-conformation, two chains coil around each other through H-bonding and disulfide linkages to form helices which assemble to form protofilaments prior to the formation of intermediate filaments (IFs). In the β-conformation, the polypeptide chains can bind side-by-side through H-bonding and disulfide linkages to form pleated sheets (the β-pleated sheets).[46] The distribution of these and other polypeptide conformations vary significantly in different materials. For example, α-helix conformation is more prominent in hair, nails, hooves, quills, etc whereas the β-sheet conformation is more prominent in tougher structures such as claws, scales, feathers, beaks, etc. Most importantly, the distribution of these conformations has a significant influence on the mechanical properties of the keratinous material. Owing to the versatility in its structure, KER can have superior tensile (hair and wool) and superior compressional (hooves) strengths.[46]

The use of KER for therapeutic applications dates back to the 16th century. However, their widespread use was limited by the unavailability of suitable solvents that could be used to extract the KER from tissues. Thus, in early 20th century and the years that followed, KER research was focused mainly on designing solvent systems for extracting the KER. These solvent systems were based on both oxidative and reductive

chemistries.[47] One notable solvent system was based on the Shindai solvent system.[48] This solvent system was composed of urea, 2-mercaptoethanol, and sodium dodecyl sulfate all mixed together in an aqueous solution. These advances in KER extraction, purification and characterization led to the potential growth in KER-based material development. For example, the extracted KER could be fabricated into a variety of functional forms including powders, films, gels, coatings, and fibers.[47] These KER-based materials could be used in a wide range of potential applications in biomedical, biopharmaceutical and environmental applications. One of the main driving forces was that KER-based materials possess excellent biocompatibility in addition to being a renewable resource. As a result, the KER could be self-assembled into complex three-dimensional structures and then subsequently used to develop scaffolds in tissue engineering. Apart from these biomedical applications, KER can also be used to adsorb heavy metal ions from water.[47]

Although KER holds so much promise, its mechanical properties deteriorate considerably after processing. For example, pure KER films regenerated from wool were too fragile for any practical use.[49] However, it has been reported that adding glycerol resulted in a transparent, relatively strong, flexible and biodegradable film.[49] Such developments have charted a whole new platform for the expansion of the applications of KER. As a result, a lot of KER-based materials are now designed with some reinforcement from materials such as CS,[50] CEL,[51] and silk,[52] among other reinforcement materials. Interestingly, synergistic interactions between silk and KER resulted in composite films exhibiting superior mechanical properties.

Another active area for KER research is in designing more benign solvents in light of green chemistry. Among many solvent systems already developed, ionic liquids seem to hold the best option for reasons which would be discussed in the following sections.

1.3. Supramolecular Chemistry

The history of supramolecular chemistry can be traced back to late 19th century when Emil Fischer proposed the lock and key model.[53] In this model, an enzyme (lock) would selectively bind to a substrate (key) possessing a structure that is complementary to the active site of the enzyme. This lock and key concept laid the foundation for what is now called supramolecular chemistry.[54] Since its inception, the value of this field of supramolecular chemistry has grown exponentially. One of the major contributions of supramolecular chemistry has been the design and synthesis of macrocycles that can selectively bind to particular guests of complementary structure. Some of the selective macrocycles that have been synthesized include crown ethers (CRs), resorcinarenes (RES), calixarenes, podands, cryptands and spherands. In the studies presented here, only CRs and RES were investigated for their applicability in selective adsorption of heavy metal ions and organic pollutants respectively.

1.3.1. Crown Ethers

Crown ethers represent a group of macrocyclic compounds consisting of repeating –O-CH_2-CH_2- units (Figure 1-3). Their remarkable selectivity to coordinate with alkali and alkali earth metal ions was initially demonstrated by Pedersen in 1967.[55] Since then, this group of macrocycles has evolved to include a number of similar structures that make

use of other heteroatoms (nitrogen, sulfur and phosphorus) to join carbon bridges of different sizes in the macrocycle. Furthermore, different types of substituents have been incorporated into the CR structure to modify the electronic, solubility and other desirable properties of these CRs. The interaction of CRs with metal ions arises due to ion-dipole interactions between the metal ion and the electronegative heteroatoms of the crown ring. These complexes can be classified into three categories; 1) the "nesting" complex, 2) the "perching" complex and 3) the "sandwich" complex.[56] As illustrated in Figure 1-4, the nesting complex is formed when the metal ion fits within the crown ether cavity. However, when the size of the metal ion is slightly larger than the crown ether cavity, a "perching" complex can be formed. In this complex, the metal ion is raised slightly above the plane of the crown ether oxygen atoms. In the "sandwich" complex case, the cation is too large to fit into the crown ether cavity. Consequently, a stable complex can then be formed by having two crown ether moieties sandwiching the metal ion.

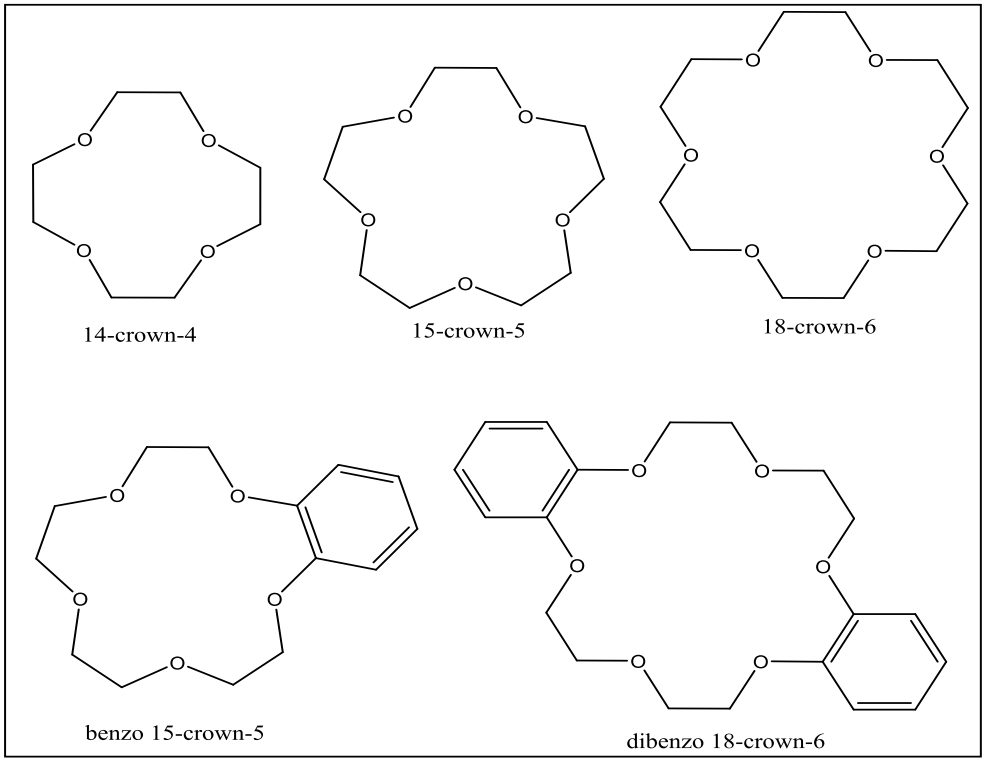

Figure 1-3 Chemical structures of some common crown ethers.

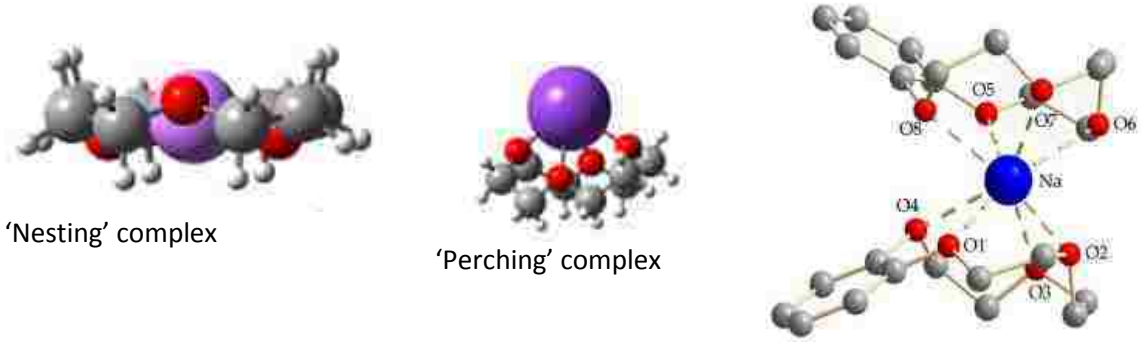

Figure 1-4 Molecular models of the three types of complexes formed by crown ethers and metal ions.[57]

Since their discovery, CRs have found a wide range of applications in diverse fields of science and industry. One of the most important applications of CRs is in selective extraction of toxic metal ions from wastewater.[58-61] In this application, CR is either chemically bonded to a biopolymer or encapsulated in a synthetic polymer resin. This is done to avert problems associated with using CR alone in powder form. In powder form, CR cannot be recycled easily after use. Therefore, incorporating it in a biopolymer framework either chemically or physically is more attractive. However, chemical attachment usually involves the use of potentially harmful solvents such as chloroform.[59] It may also alter properties of CR. In addition, it requires personnel with expertise in synthesis.

In our study, we developed a novel method to synthesize CR-based adsorbents and investigated them for their suitability in selective adsorption of heavy metal ions (Zn^{2+} and Cd^{2+}). We used benzo 15-crown-5 adsorbent partly because its cavity size (~1.7-1.9 Å)[62] is similar to the ionic size of Cd^{2+} (1.94 Å)[58] but it is very different from the ionic size of Zn^{2+} (1.48 Å).[62] Therefore, based on size-fit concept, we would expect B15C5 to adsorb Cd^{2+} more strongly than Zn^{2+}. An additional advantage of this method is that B15C5 is encapsulated into the polysaccharide matrices without forming any new covalent bonds. Consequently, the desirable properties of both B15C5 and polysaccharides (CEL and CS) are expected to be maintained. In addition, no organic solvents were used; the method is therefore expected to be *green*. Furthermore, using a solid sorbent eliminates the generation of secondary waste and is also time efficient. In addition, adsorbents are portable and therefore applicable for field sampling.

1.3.2. Resorcinarenes

Resorcinarenes, a subclass of calixarenes, are cyclic tetramers produced from polycondensation of resorcinol and a variety of aldehydes (Figure 1-5).[63-66] Their history stretches back to 1872 when Baeyer first reported reactions between resorcinol and aldehydes.[64] However, it took several years before the tetramer structure of these products was elucidated by single crystal X-ray analysis.[67] The structure of these resorcinarenes is held by hydrogen bonds formed between hydroxyl groups from adjacent resorcinol rings. The bowl-shaped aromatic cavity which is made up of four electron rich benzene rings serve as a π-base that interacts with guest molecules through mainly CH---π (dispersion) interactions.[68] In addition, analytes, especially poly aromatic hydrocarbons (PAHs) interact with the alkyl substituents (lining the lower rim of RES) through VDW forces. This enabled the separation of PAHs when RES was applied as a pseudo-stationary phase in electrokinetic chromatography (EKC).[69] Furthermore, polar organic analytes can form complexes with RES through hydrogen bonding or electrostatic interactions with the hydroxyl groups on the four resorcinol rings.[70-72]

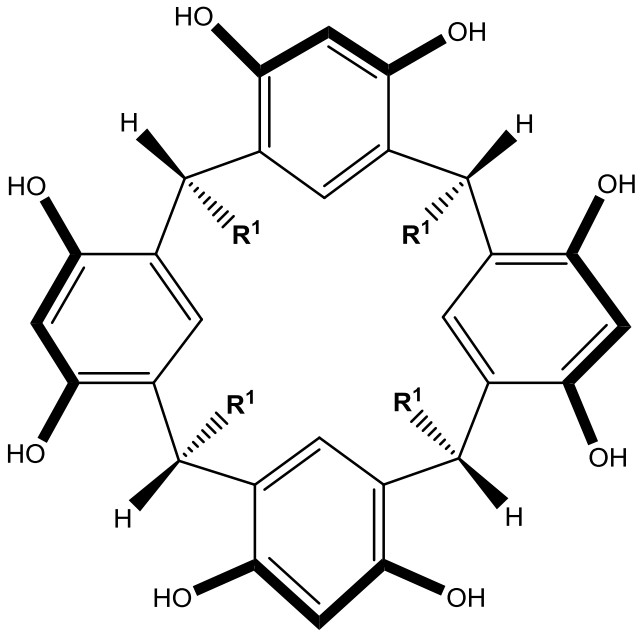

R^1= $-CH_2(CH_2)_9CH_3$ C-undecyl calix[4]resorcinarene
= $-CH_3$ C-methyl calix[4]resorcinarene

Figure 1-5 Chemical structures of tetra-(C-alkyl)-calix[4]resorcinarene.

Resorcinarenes are versatile compounds which can be modified with a variety of substituents on both the upper and the lower rims to impart specific properties. These modifications help to extend the applications of RES to include such applications as inter alia chromatographic separation (HPLC, GC, IC and electro kinetic chromatography), chiral NMR resolution, reaction catalysis, drug encapsulation, protection and delivery.[72-75]

Despite the considerable potential of RES in molecular recognition, it has barely been used to selectively remove organic pollutants from water. As described in the case of CRs, using RES in powder form would create challenges in recovery and recyclability

of this adsorbent. In addition, a powder is difficult to handle. We therefore, undertook this study to develop a method to encapsulate RES in biopolymer matrix and then investigate the suitability of this resultant composite in adsorbing a variety of phenyl-based pollutants. Polysaccharides, CEL and CS, were chosen for their film-forming capability. Other benefits of using these biopolymers have been discussed previously under relevant sections. We hypothesized that encapsulating RES in the biopolymer matrices without any chemical modifications would help to transfer selectivity of this RES to the composite. To ensure that there is no chemical modification, we used a novel solvent, an ionic liquid, to dissolve both polysaccharides and RES simultaneously and then regenerate the film composites from water.

1.4. Ionic Liquids

Ionic liquids (ILs) are materials that are composed entirely of organic cations and organic/inorganic counter anions that exist as liquids at relatively low temperatures (< 100 ^{0}C). Thus, they are termed Room-Temperature Ionic Liquids in order to differentiate them from traditional salts, which melt at much higher temperatures. The typical cations and anions of these ILs are presented in Scheme 1-1. It is possible to synthesize some ILs in one or two sequential steps, where necessary. The first step involves quaternization of a Lewis base (an amine, a phosphine or a sulfide) with a haloalkane (chloroalkanes, bromoalkanes and iodoalkanes) or protonation of the Lewis base with a free mineral acid (Scheme 1-2a). As illustrated in this Scheme, all reactants are incorporated in the product, thus this quaternization process is theoretically 100% atom efficient. The second step involves a simple metathesis reaction whereby an anion of the IL synthesized in the first step is exchanged with an anion of a group 1 metal or silver(1) salt, MY or a mineral acid

(Scheme 1-2b). It is therefore possible to synthesize a wide variety of ionic liquids using either of these two methods. In fact, there are at least a million ILs that can be synthesized by combining different organic cations and anions.[76] As a result, the physical and chemical properties of these ILs can be tuned to suit the intended application by simply varying either the cation or the anion. For example, whereas hydrophilic ILs can be synthesized using halides as anions, hydrophobic ILs can be synthesized using hydrophobic anions such as hexafluorophosphate, tetrafluoroborate, etc. For this reason, ILs are christened 'designer' solvents.

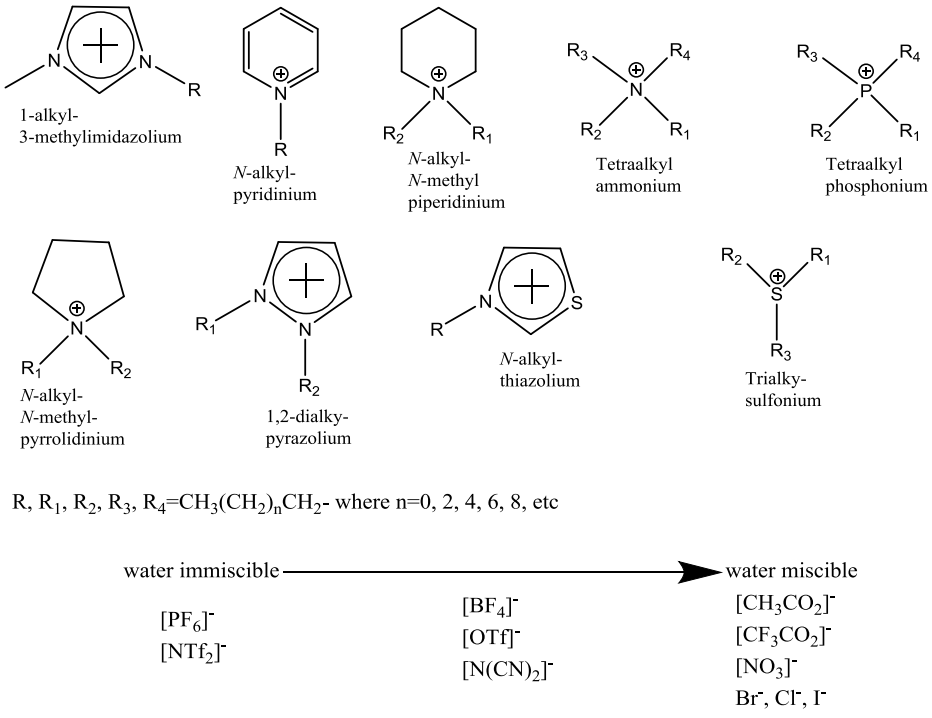

Scheme 1-1 Typical cations and anions of ionic liquids.

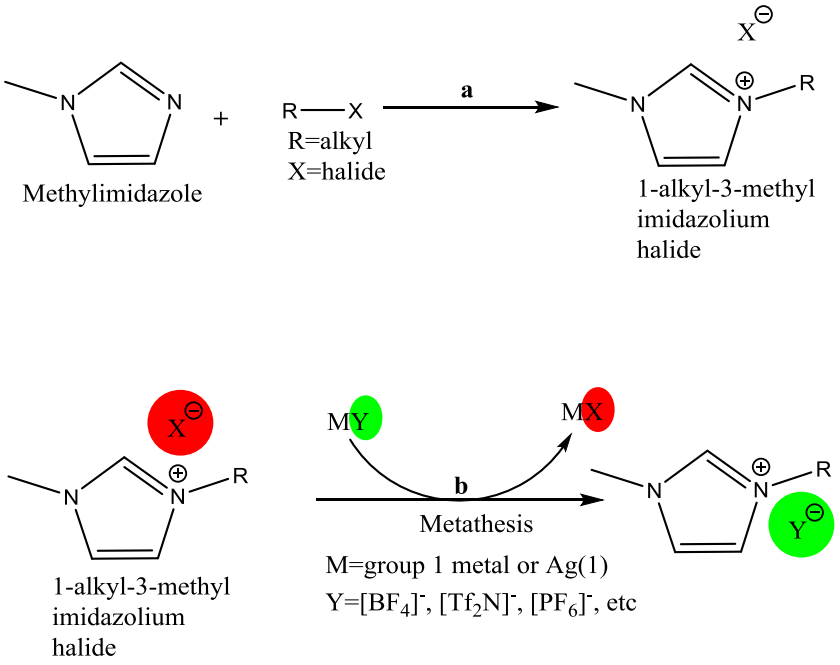

Scheme 1-2 Common pathways for synthesis of ILs. (a) An amine, methylimidazole is reacted with an alkyl halide to form a quaternized imidazolium halide IL. (b) The halide in imidazolium halide IL from (a) is exchanged with an anion from a group 1 metal or Ag(I) salt to form another IL.

The history of ILs can be traced back to the landmark report of the first ionic liquid, ethyl ammonium nitrate ($[EtNH_3][NO_3]$; mp 13-14 ^{0}C), in 1914.[77] Despite this landmark discovery, it took several years for this field of ILs to attract significant attention from the scientific community. This lack of attention was partly due to the lack of information about the physical and chemical properties of these ILs. In addition, early studies on ILs were mainly focused on their applications in electrochemistry[78] with the only exception being a patented method for dissolving cellulose in halide-based ionic liquids.[79] During the late 1990s, it was suggested that ILs could be used for both 'green'

and industrial chemistry. Since then, there has been an increasing interest in the field of applications of ILs.

Ionic liquids continue to gain increasing interest because of their unusual physical and chemical properties which enable them to be used in a wide range of scientific and industrial applications. One of the most interesting and important properties of ILs is negligible vapor pressure. Negligible vapor pressure helps to minimize the risk of atmospheric pollution thereby reducing associated health concerns. For this reason, ILs are often called 'green solvents.' As a result, ILs are continuously being explored to replace volatile organic solvents in a wide range of chemical processes. For example, dissolution of biopolymers (such as CEL, CS, KER) is often carried out at temperatures high enough to cause boiling of some of the classic organic solvents for these biopolymers thereby posing additional health and safety risks. However, with negligible vapor pressure, ILs can be safely used to dissolve these biopolymers.

Another important property of ILs in the dissolution of biopolymers is that ILs are both thermally stable and non-flammable. A classic example is $BMIm^+Cl^-$ which has an onset of thermal decomposition of 240 ^{0}C.[80] This is advantageous because this temperature is almost twice the temperatures required to dissolve CEL, CS (~90-105 ^{0}C)[81,82] or KER (~115 ^{0}C).[51,83] Therefore, the dissolution of these biopolymers can be carried out without concerns for decomposing the IL. At these high temperatures, typical solvent systems such as LiCl/DMAc degrade into species that are capable of cleaving CEL chains.[24]

The properties discussed above prompted us to use ILs, exclusively $BMIm^+Cl^-$, to dissolve biopolymers including CEL, CS, and wool KER. The dissolution of all these

three biopolymers in this common solvent enabled us to synthesize composites containing different proportions of each of these biopolymers. More importantly, the IL could be leached from the films using water and subsequently recovered for reuse by distillation.

1.5. Outline of the Dissertation

In chapter 2, the synthesis and characterization of polysaccharide-crown ether composites will be described. In addition, there application for the selective adsorption of heavy metal ions and organic pollutants will also be described in the same chapter. Chapter 3 involves the synthesis and application of polysaccharide-resorcinarene composites for the selective adsorption of several organic pollutants. In chapter 4, we will describe the synthesis and characterization of a potential bone tissue engineering material from chitosan, cellulose and hydroxyapatite. Chapter 5 encompasses a study on the controlled release of an antibiotic, ciprofloxacin, from composites containing various proportions of cellulose, chitosan and keratin. Chapter 6 will be about the synthesis of gold and silver nanoparticles in cellulose, chitosan and keratin composite films. Chapter 7 will be on conclusions and recommendations for future research.

1.6. References

1. Ray, S. S.; Bousmina, M., Biodegradable polymers and their layered silicate nanocomposites: In greening the 21st century materials world. *Prog. Mater. Sci.* **2005,** *50*, 962-1079.

2. Meyers, M. A.; Chen, P.-Y.; Lin, A. Y.-M.; Seki, Y., Biological materials: Structure and mechanical properties. *Prog. Mater. Sci.* **2007,** *53*, 1-206.

3. Faruk, O.; Bledzki, A. K.; Fink, H.-P.; Sain, M., Biocomposites reinforced with natural fibers: 2000-2010. *Prog. Polym. Sci.* **2012,** *37*, 1552-1596.

4. Flores-Hernandez, C. G.; Colin-Cruz, A.; Velasco-Santos, C.; Castano, V. M.; Rivera-Armenta, J. L.; Almendarez-Camarillo, A.; Garcia-Casillas, P. E.; Martinez-Hernandez, A. L., All green composites from fully renewable biopolymers: chitosan-starch reinforced with keratin from feathers. *Polymers* **2014,** *6*, 686-705, 20 pp.

5. Satyanarayana, K. G.; Arizaga, G. G. C.; Wypych, F., Biodegradable composites based on lignocellulosic fibers-An overview. *Prog. Polym. Sci.* **2009,** *34*, 982-1021.

6. Dicker, M. P. M.; Duckworth, P. F.; Baker, A. B.; Francois, G.; Hazzard, M. K.; Weaver, P. M., Green composites: A review of material attributes and complementary applications. *Composites, Part A* **2014,** *56*, 280-289.

7. Zhang, L.; Ruan, D.; Gao, S., Dissolution and regeneration of cellulose in NaOH/thiourea aqueous solution. *J. Polym. Sci., Part B Polym. Phys.* **2002,** *40*, 1521-1529.

8. Zhang, H.; Wu, J.; Zhang, J.; He, J., 1-Allyl-3-methylimidazolium chloride room temperature ionic liquid: A new and powerful nonderivatizing solvent for cellulose. *Macromolecules* **2005,** *38*, 8272-8277.

9. Xie, H.; Li, S.; Zhang, S., Ionic liquids as novel solvents for the dissolution and blending of wool keratin fibers. *Green Chem.* **2005,** *7*, 606-608.

10. Idris, A.; Vijayaraghavan, R.; Rana, U. A.; Patti, A. F.; MacFarlane, D. R., Dissolution and regeneration of wool keratin in ionic liquids. *Green Chem.* **2014,** *16*, 2857-2864.

11. Lawandy, N. M. Authenticatable coatings for pharmaceutical tablets and ingestible materials. US Patent 20130084249 A1, April 4, 2013.

12. Read, S. M.; Bacic, T., Prime time for cellulose. *Science* **2002,** *295*, 59-60.

13. Teixeira, E. M.; Correa, A. C.; Manzoli, A.; Leite, F. L.; Oliveira, C. R.; Mattoso, L. H. C., Cellulose nanofibers from white and naturally colored cotton fibers. *Cellulose* **2010,** *17* 595-606.

14. Poplin, J. H.; Swatloski, R. P.; Holbrey, J. D.; Spear, S. K.; Metlen, A.; Gratzel, M.; Nazeeruddin, M. K.; Rogers, R. D., Sensor technologies based on a cellulose supported platform. *Chem. Commun.* **2007,** (20), 2025-2027.

15. Liebert, T. F. Cellulose solvents-Remarkable history, bright future. http://pubs.acs.org/doi/pdf/10.1021/bk-2010-1033.ch001. (accessed Nov 30, 2014).

16. Cockroft, M. R.; Fisher, L. Process for processing cellulose films or shaped articles. European Patent 2710054 A1, March 26, 2014.
.

17. Song, J.; Ge, H.; Xu, M.; Chen, Q.; Zhang, L., Study on the interaction between urea and cellulose by combining solid-state 13C CP/MAS NMR and extended Huckel charges. *Cellulose* **2014,** *21* (6), 4019-4027.

18. Hasegawa, M.; Isogai, A.; Onabe, F.; Usuda, M., Dissolving states of cellulose and chitosan in trifluoroacetic acid. *J. Appl. Polym. Sci.* **1992,** *45*, 1857-63.

19. Hammer, R. B.; O'Shaughnessy, M. E.; Strauch, E. R.; Turbak, A. F., Process and fiber spinning studies for the cellulose/paraformaldehyde/dimethyl sulfoxide system. *J. Appl. Polym. Sci.* **1979,** *23*, 485-94.

20. Zabetakis, M. G.; Jones, G. W., Flammability of carbon disulfide in mixtures of air and water vapor. *Ind. Eng. Chem.* **1953,** *45*, 2079-80.

21. Rosenau, T.; Potthast, A.; Adorjan, I.; Hofinger, A.; Sixta, H.; Firgo, H.; Kosma, P., Cellulose solutions in N-methylmorpholine-N-oxide (NMMO) degradation processes and stabilizers. *Cellulose* **2002,** *9* (3/4), 283-291.

22. Potthast, A.; Rosenau, T.; Buchner, R.; Roeder, T.; Ebner, G.; Bruglachner, H.; Sixta, H.; Kosma, P., The cellulose solvent system N,N-dimethylacetamide/lithium chloride revisited: the effect of water on physicochemical properties and chemical stability. *Cellulose* **2002,** *9*, 41-53.

23. Ostlund, A.; Lundberg, D.; Nordstierna, L.; Holmberg, K.; Nyden, M., Dissolution and gelation of cellulose in TBAF/DMSO solutions: the roles of fluoride ions and water. *Biomacromolecules* **2009,** *10*, 2401-7.

24. Potthast, A.; Rosenau, T.; Sartori, J.; Sixta, H.; Kosma, P., Hydrolytic processes and condensation reactions in the cellulose solvent system N,N-dimethylacetamide/lithium chloride. Part 2: Degradation of cellulose. *Polymer* **2002,** *44*, 7-17.

25. Wang, H.; Gurau, G.; Rogers, R. D., Ionic liquid processing of cellulose. *Chem. Soc. Rev.* **2012,** *41*, 1519-1537.

26. Rebelo Luis, P. N.; Canongia Lopes Jose, N.; Esperanca Jose, M. S. S.; Filipe, E., On the critical temperature, normal boiling point, and vapor pressure of ionic liquids. *J Phys Chem B* **2005,** *109*, 6040-3.

27. Maton, C.; De Vos, N.; Stevens, C. V., Ionic liquid thermal stabilities: decomposition mechanisms and analysis tools. *Chem. Soc. Rev.* **2013,** *42*, 5963-5977.

28. Fox, D. M.; Gilman, J. W.; Morgan, A. B.; Shields, J. R.; Maupin, P. H.; Lyon, R. E.; De Long, H. C.; Trulove, P. C., Flammability and Thermal Analysis Characterization of Imidazolium-Based Ionic Liquids. *Ind. Eng. Chem. Res.* **2008,** *47*, 6327-6332.

29. Bailey, S. E.; Olin, T. J.; Bricka, R. M.; Adrian, D. D., A review of potentially low-cost sorbents for heavy metals. *Water Res.* **1999,** *33*, 2469-2479.

30. SeKwon, K.; Jae-Young, J. Continuous production of chitooligosaccharides by enzymatic hydrolysis. In *Chitin, chitosan, oligosaccharides and their derivatives: biological activities and applications*. Se-Kwon, K., Ed.; CRC Press Inc.Boca Raton, FL, 2010, pp 47-52.

31. Liu, X. F.; Guan, Y. L.; Yang, D. Z.; Li, Z.; De Yao, K., Antibacterial action of chitosan and carboxymethylated chitosan. *J. Appl. Polym. Sci.* **2000,** *79*, 1324-1335.

32. Rabea Entsar, I.; Badawy Mohamed, E. T.; Stevens Christian, V.; Smagghe, G.; Steurbaut, W., Chitosan as antimicrobial agent: applications and mode of action. *Biomacromolecules* **2003,** *4*, 1457-65.

33. Foda, N. H.; El-Iaithy, M.; Tadros, I., Implantable biodegradable sponges: effect of interpolymer complex formation of chitosan with gelatin on the release behavior of tramadol hydrochloride. *Drug Dev. Ind. Pharm.* **2007,** *33*, 7-17.

34. Lee, D. W.; Lim, H.; Chong, H. N.; Shim, W. S., Advances in chitosan material and its hybrid derivatives: a review. *Open Biomater. J.* **2009,** *1*, 10-20.

35. Anitha, A.; Sowmya, S.; Kumar, P. T. S.; Deepthi, S.; Chennazhi, K. P.; Ehrlich, H.; Tsurkan, M.; Jayakumar, R., Chitin and chitosan in selected biomedical applications. *Prog. Polym. Sci.* **2014,** *39*, 1644-1667.

36. Di Martino, A.; Sittinger, M.; Risbud, M. V., Chitosan: A versatile biopolymer for orthopaedic tissue-engineering. *Biomaterials* **2005,** *26*, 5983-5990.

37. Francis Suh, J. K.; Matthew, H. W. T., Application of chitosan-based polysaccharide biomaterials in cartilage tissue engineering: a review. *Biomaterials* **2000,** *21*, 2589-2598.

38. Haipeng, G.; Yinghui, Z.; Jianchun, L.; Yandao, G.; Nanming, Z.; Xiufang, Z., Studies on nerve cell affinity of chitosan-derived materials. *J. Biomed. Mater. Res.* **2000,** *52*, 285-95.

39. Yang, T. C.; Zall, R. R., Absorption of metals by natural polymers generated from seafood processing wastes. *Ind. Eng. Chem. Prod. Res. Dev.* **1984,** *23*, 168-72.

40. Wan Ngah, W. S.; Teong, L. C.; Hanafiah, M. A. K. M., Adsorption of dyes and heavy metal ions by chitosan composites: A review. *Carbohydr. Polym.* **2011,** *83*, 1446-1456.

41. Wu, F.-C.; Tseng, R.-L.; Juang, R.-S., A review and experimental verification of using chitosan and its derivatives as adsorbents for selected heavy metals. *J. Environ. Manage.* **2010,** *91*, 798-806.

42. Bhatnagar, A.; Sillanpaeae, M., Applications of chitin- and chitosan-derivatives for the detoxification of water and wastewater - A short review. *Adv. Colloid Interface Sci.* **2009,** *152*, 26-38.

43. Wei, D.; Sun, W.; Qian, W.; Ye, Y.; Ma, X., The synthesis of chitosan-based silver nanoparticles and their antibacterial activity. *Carbohydr. Res.* **2009,** *344*, 2375-2382.

44. Sugunan, A.; Thanachayanont, C.; Dutta, J.; Hilborn, J. G., Heavy-metal ion sensors using chitosan-capped gold nanoparticles. *Sci. Technol. Adv. Mater.* **2005,** *6*, 335-340.

45. Fuchs, E., Keratins and the skin. *Annu. Rev. Cell Dev. Biol.* **1995,** *11*, 123-53.

46. Chen, W.; Duan, L.; Zhu, D., Adsorption of polar and nonpolar organic chemicals to carbon nanotubes. *Environ. Sci. Technol.* **2007,** *41*, 8295-8300.

47. Khosa, M. A.; Ullah, A., A Sustainable Role of Keratin Biopolymer in Green Chemistry: A Review. *J. Food Processing & Beverages* **2013,** *1*, 8.

48. Nakamura, A.; Arimoto, M.; Takeuchi, K.; Fujii, T., A rapid extraction procedure of human hair proteins and identification of phosphorylated species. *Biol. Pharm. Bull.* **2002,** *25*, 569-572.

49. Yamauchi, K.; Yamauchi, A.; Kusunoki, T.; Kohda, A.; Konishi, Y., Preparation of stable aqueous solution of keratins, and physicochemical and biodegradational properties of films. *J. Biomed. Mater. Res.* **1996,** *31*, 439-444.

50. Tanabe, T.; Okitsu, N.; Tachibana, A.; Yamauchi, K., Preparation and characterization of keratin-chitosan composite film. *Biomaterials* **2002,** *23*, 817-25.

51. Hameed, N.; Guo, Q., Blend films of natural wool and cellulose prepared from an ionic liquid. *Cellulose* **2010,** *17*, 803-813.

52. Vasconcelos, A.; Freddi, G.; Cavaco-Paulo, A., Biodegradable materials based on silk fibroin and keratin. *Biomacromolecules* **2008,** *9*, 1299-305.

53. Koshland, D. E., Jr., The lock-and-key principle and the induced-fit theory. *Angew. Chem.* **1994,** *106*, 2468-72.

54. Steed, J. W.; Atwood, J. L.; Editors, *Supramolecular Chemistry, Second Edition*. 2009; p 970 pp.

55. Pedersen, C. J., Cyclic polyethers and their complexes with metal salts. *J. Amer. Chem. Soc.* **1967,** *89*, 7017-36.

56. Cram, D. J., The design of molecular hosts, guests, and their complexes. *J. Inclusion Phenom.* **1988,** *6*, 397-413.

57. Yahmin, Y.; Pranowo, H. D.; Armunanto, R., Ab Initio Investigation of 12-Crown-4 and benzo-12-crown-4 complexes with Li^{+}, Na^{+}, K^{+}, Zn 2^{+}, Cd $^{2+}$, and Hg $^{2+}$. *Indonesian Journal of Chemistry* **2010,** *10*, 106-109.

58. Tzeng, D. L.; Shih, J. S.; Yeh, Y. C., Adsorption of heavy metal ions on crown ether adsorbents. *Analyst (London)* **1987,** *112*, 1413-16.

59. Radwan, A. A.; Alanazi, F. K.; Alsarra, I. A., Microwave irradiation-assisted synthesis of a novel crown ether crosslinked chitosan as a chelating agent for heavy metal ions (M^{+n}). *Molecules* **2010,** *15*, 6257-6268.

60. Luz Godino-Salido, M.; Santiago-Medina, A.; Arranz-Mascaros, P.; Lopez-Garzon, R.; Gutierrez-Valero, M. D.; Melguizo, M.; Javier Lopez-Garzon, F., Novel active carbon/crown ether derivative hybrid material for the selective removal of Cu(II) ions: The crucial role of the surface chemical functions. *Chem. Eng. Sci.* **2014**, 94-104.

61. Awual, M. R.; Yaita, T.; Taguchi, T.; Shiwaku, H.; Suzuki, S.; Okamoto, Y., Selective cesium removal from radioactive liquid waste by crown ether immobilized new class conjugate adsorbent. *J. Hazard. Mater.* **2014,** *278*, 227-235.

62. Liu, Y.; Zhang, H.-Y.; Bai, X.-P.; Wada, T.; Inoue, Y., Molecular Design of Crown Ethers. 21. Synthesis of Novel Double-Armed Benzo-15-crown-5 Lariats and Their Complexation Thermodynamics with Light Lanthanoid Nitrates in Acetonitrile. *J. Org. Chem.* **2000,** *65*, 7105-7109.

63. Kuzmicz, R.; Kowalska, V.; Domagala, S.; Stachowicz, M.; Wozniak, K.; Kolodziejski, W., X-ray Diffraction, FT-IR, and 13C CP/MAS NMR Structural Studies of Solvated and Desolvated C-Methylcalix[4]resorcinarene. *J. Phys. Chem. B* **2010,** *114*, 10311-10320.

64. Timmerman, P.; Verboom, W.; Reinhoudt, D. N., Resorcinarenes. *Tetrahedron* **1996,** *52*, 2663-704.

65. Tunstad, L. M.; Tucker, J. A.; Dalcanale, E.; Weiser, J.; Bryant, J. A.; Sherman, J. C.; Helgeson, R. C.; Knobler, C. B.; Cram, D. J., Host-guest complexation. 48. Octol building blocks for cavitands and carcerands. *J. Org. Chem.* **1989,** *54*, 1305-12.

66. Hoegberg, A. G. S., Cyclooligomeric phenol-aldehyde condensation products. 2. Stereoselective synthesis and DNMR study of two 1,8,15,22-tetraphenyl[14]metacyclophan-3,5,10,12,17,19,24,26-octols. *J. Am. Chem. Soc.* **1980,** *102*, 6046-50.

67. Erdtman, H.; Hogberg, S.; Abrahamsson, S.; Nilsson, B., Cyclooligomeric phenol-aldehyde condensation products. I. *Tetrahedron Lett.* **1968,** *14*, 1679-82.

68. Kobayashi, K.; Yamanaka, M., Self-assembled capsules based on tetrafunctionalized calix[4]resorcinarene cavitands. *Chem. Soc. Rev.* **2014**. DOI: 10.1039/C4CS00153B.

69. Baechmann, K.; Bazzanella, A.; Haag, I.; Han, K.-Y.; Arnecke, R.; Boehmer, V.; Vogt, W., Resorcarenes as pseudostationary phases with selectivity for electrokinetic chromatography. *Anal. Chem.* **1995,** *67*, 1722-6.

70. Tanaka, Y.; Kato, Y.; Aoyama, Y., Molecular recognition. 8. Two-point hydrogen-bonding interaction: a remarkable chain-length selectivity in the binding of dicarboxylic acids with resorcinol-aldehyde cyclotetramer as a multidentate host. *J. Am. Chem. Soc.* **1990,** *112*, 2807-8.

71. Kikuchi, Y.; Kobayashi, K.; Aoyama, Y., Molecular recognition. 18. Complexation of chiral glycols, steroidal polyols, and sugars with a multibenzenoid, achiral host as studied by induced circular dichroism spectroscopy: exciton chirality induction in resorcinol-aldehyde cyclotetramer and its use as a supramolecular probe for the assignments of stereochemistry of chiral guests. *J. Am. Chem. Soc.* **1992,** *114*, 1351-8.

72. Aoyama, Y.; Tanaka, Y.; Sugahara, S., Molecular recognition. 5. Molecular recognition of sugars via hydrogen-bonding interaction with a synthetic polyhydroxy macrocycle. *J. Am. Chem. Soc.* **1989,** *111*, 5397-404.

73. Ruderisch, A.; Iwanek, W.; Pfeiffer, J.; Fischer, G.; Albert, K.; Schurig, V., Synthesis and characterization of a novel resorcinarene-based stationary phase bearing polar headgroups for use in reversed-phase high-performance liquid chromatography. *J. Chromatogr. A* **2005,** *1095*, 40-49.

74. Ruderisch, A.; Pfeiffer, J.; Schurig, V., Mixed chiral stationary phase containing modified resorcinarene and β-cyclodextrin selectors bonded to a polysiloxane for enantioselective gas chromatography. *J. Chromatogr., A* **2003,** *994*, 127-135.

75. Jain, V. K.; Pillai, S. G.; Pandya, R. A.; Agrawal, Y. K.; Shrivastav, P. S., Selective extraction, preconcentration and transport studies of thorium(IV) using octa-functionalized calix[4]resorcinarene-hydroxamic acid. *Anal. Sci.* **2005,** *21*, 129-135.

76. Plechkova, N. V.; Seddon, K. R., Applications of ionic liquids in the chemical industry. *Chem. Soc. Rev.* **2008,** *37*, 123-150.

77. Austen Angell, C.; Ansari, Y.; Zhao, Z., Ionic Liquids: Past, present and future. *Faraday Discuss.* **2012,** *154* (Ionic Liquids), 9-27.

78. Hurley, F. H.; Wier, T. P., The electrodeposition of aluminum from nonaqueous solutions at room temperature. *Journal of the Electrochemical Society* **1951,** *98* (5), 207-212; Hurley, F. H.; Wier, T. P., Jr., Electrodeposition of metals from fused quaternary ammonium salts. *J. Electrochem. Soc.* **1951,** *98*, 203-6.

79. Graenacher, C. Cellulose solutions. US Patent 1943176A, Jan 9, 1934.

80. Dharaskar, S. A.; Varma, M. N.; Shende, D. Z.; Yoo, C. K.; Wasewar, K. L., Synthesis, characterization and application of 1-butyl-3-methylimidazolium chloride as green material for extractive desulfurization of liquid fuel. *Sci. World J.* **2013**, DOI: 10.1155/2013/395274.

81. Swatloski, R. P.; Spear, S. K.; Holbrey, J. D.; Rogers, R. D., Dissolution of cellulose with ionic liquids. *J. Am. Chem. Soc.* **2002,** *124*, 4974-4975.

82. Kuzmina, O.; Heinze, T.; Wawro, D., Blending of cellulose and chitosan in alkyl imidazolium ionic liquids. *ISRN Polym. Sci.* **2012**, DOI: 10.5402/2012/251950.

83. Li, R.; Wang, D., Preparation of regenerated wool keratin films from wool keratin-ionic liquid solutions. *J. Appl. Polym. Sci.* **2013,** *127*, 2648-2653.

CHAPTER 2

SELECTIVE ADSORPTION OF HEAVY METAL IONS AND ORGANIC POLLUTANTS BY SUPRAMOLECULAR POLYSACCHARIDE COMPOSITE MATERIALS FROM CELLULOSE, CHITOSAN AND CROWN ETHER

2.1. Background

The release of heavy metals into the environment has become a matter of global concern because they are carcinogenic, non-biodegradable (thus very stable and persistent) and they tend to accumulate within the biological system.[1] These heavy metal ions are accidentally or intentionally released into waterways through untreated wastewater discharges from industrial operations such as metal plating, printing, metallurgical alloying, fertilizers, pesticides and alkaline battery manufacturing.[2] Cadmium and zinc are two of the many heavy metal ions which generate a continuing occupational and environmental concern. Cadmium exhibits an extensively long biological half-life and causes serious health disorders including osteoporosis,[3] multi-tissue cancer,[4,5] Parkinson's disease,[6] and Alzheimer's disease,[7] among other health disorders. Although zinc is an essential micronutrient for plant and animal nutrition, it can also be highly toxic to plants, invertebrates and even vertebrate fish when it is available in excess. Specifically, excess quantities of zinc in the blood can cause neuronal degeneration,[8] lung disorders and growth retardation.[9] In addition, when Zn is present in water at concentrations greater than 4 mg per L, it imparts an undesirable astringent taste to the water. Furthermore, at concentrations greater than 3-5 mg per L, the water appears opalescent and develop a greasy film on boiling.[10] Thus, due to these and other emerging evidence about the harmful effects of heavy metals, international regulatory agencies

have enacted laws and set standards to limit their discharge into municipal sewers.[11] For example, World Health Organization (WHO) set the maximum concentration guideline of Cd in drinking water to be 3 µg per L.[12] However, the costs associated with compliance to these stricter regulations are often prohibitively high especially for small companies and cash strapped economies. Thus, there is a growing demand for the design of relatively efficient and economically viable alternatives which require readily available materials. Such a development would help cushion vulnerable communities—those with little financial surplus to spend.

A variety of technologies have been developed to remove heavy metal ions from water and wastewater. These include *inter alia* reverse osmosis, ion exchange, electrodialysis, chemical precipitation and adsorption onto activated carbon.[13-18]Although these technologies are effective, they present serious limitations which make them unsustainable for use in large scale processes. Specifically, chemical precipitation produces sludge which creates further problems for disposal. In addition, it has also been reported that this process is inefficient in the removal of heavy metal ions such as cadmium.[19,20] Reverse osmosis and ion exchange methods are considered to require special membranes and resins that are expensive.[11] During electrodialysis, hydroxides are formed which usually clog the ion selective membranes rendering them inefficient. In addition, this process requires a large input of energy thereby making it economically unsustainable.[13] Thus, there is still a greater demand for better technologies to remove heavy metal ions in a more efficient and sustainable way.

Amongst all the methods employed in the sequestration of heavy metal ions from water, adsorption is receiving considerable attention owing to its low initial cost,

simplicity of design, ease of operation, insensitivity to toxic substances and its ability to completely remove pollutants even from dilute solutions.[15,21] This considerable attention has resulted in a wide variety of materials being investigated for their suitability in adsorbing heavy metal ions from water. Since some of these metal ions are precious metals, they should be selectively adsorbed for the purposes of recovery and reuse. Therefore, the main requirement for metal ion adsorbents is that they should possess binding sites that are specific to particular heavy metal ions. As has been described in section 1.3.1, crown ethers (CRs) exhibit remarkable selectivity towards heavy metal ions of ionic size which closely matches their cavities.[22] Therefore, the selectivity of CRs can be fine-tuned by changing their cavity size. In addition to changing the cavity size, other modifications that can be done to change their selectivity include changing the rigidity of the ring, appending ionizable groups and changing the number and type of donor atoms. This flexibility in tuning the selectivity of CRs enabled them to be used in selective extraction[23,24] and as sensors for metal ions.[25,26] However, in powder form, CRs are difficult to handle. In addition, they are both expensive and cannot be recycled easily.[27] Thus, attempts have been made to chemically graft them onto some polymer support. Such grafted polymers exhibited better metal ion selectivity than their corresponding CRs and polymers.[28] However, these novel systems were still mired by severe limitations. For example, the reactions involved in grafting the CRs are not only complex but they involve the use of volatile organic solvents which pollute the atmospheric environment. In addition, the chemical processes involved could adversely alter the beneficial properties presented by the polymer. For example, chitosan, by itself adsorbs heavy metal ions through complexation using the amine groups. However, grafting is carried out onto

these active sites thereby making them unavailable for adsorption of heavy metal ions. As a result, the adsorption capacity of the polymer is sacrificed through this grafting.[27] It is therefore desirable to encapsulate CRs into the polymer matrix without any chemical modification.

Cellulose (CEL) and chitosan (CS) are two of the most promising biopolymer support for encapsulating CRs because they possess unique features which have already been described in the previous Chapter. Specifically, CEL exhibit superior mechanical properties[29-31] whilst CS exhibit remarkable properties such as hemostasis,[32] wound healing,[33] antibacterial[34,35] and most importantly they are capable of forming complexes with both heavy metal ions and organic pollutants.[36-38] However, their structures are stabilized by wide networks of intra- and inter-molecular H-bonds which render them virtually insoluble in common organic solvents. This limitation has probably delayed the development of novel CR-based supramolecular composites for the adsorption of heavy metal ions.

Recent developments in the field of applications of ionic liquids (ILs) has enabled them to be successfully used to dissolve large biopolymers such as CEL and CS.[30,39-42] As has been described in section 1.4, ILs are widely explored in many applications because they possess unique properties. In addition to having a negligible vapor pressure,[43] ILs exhibit a wide liquid range and they are thermally stable.[44] The most common IL used in dissolving such biopolymers is an imidazolium-based IL namely 1-butyl-3-methylimidazolium chloride ($BMIm^+Cl^-$). In addition to the dissolution of these natural biopolymers, ILs have been shown to dissolve macrocycles such as cyclodextrins.[45] Therefore, it is reasonable to postulate that this IL can also dissolve CRs.

2.2. Adsorption Kinetics Models

2.2.1. The adsorption process

Adsorption involves the accumulation of substances on a suitable surface from a solution. It is considered to be effective in the removal of heavy metal ions from wastewater.[46] Adsorption can be either physisorb or chemisorb in nature.[47] Physical adsorption is non-specific. The adsorbed molecule can move from one adsorption site to the other. In chemical adsorption, strong electrostatic interactions between the adsorbate ion and the adsorbent active site hold the ion at one site. This introduces selectivity because different types of ions might have different affinities for a particular adsorbent site. The adsorption of a metal ion can occur through four steps depicted on Scheme 2-1 below. On the first stage, the metal ion diffuses through the bulk solution to the boundary layer of fixed film of liquid surrounding the adsorbent. Subsequently, the ion diffuses through this thin film before getting to the entrance of the adsorbent pores. The ion then diffuses through the pore liquid and sometimes along the surface of the adsorbent. Finally, the ion then adsorbs onto the available active site on the inner surface of the adsorbent. Due to the small surface area of the outer surface, the amount of material attached to those surfaces is considered to be insignificant.[48]

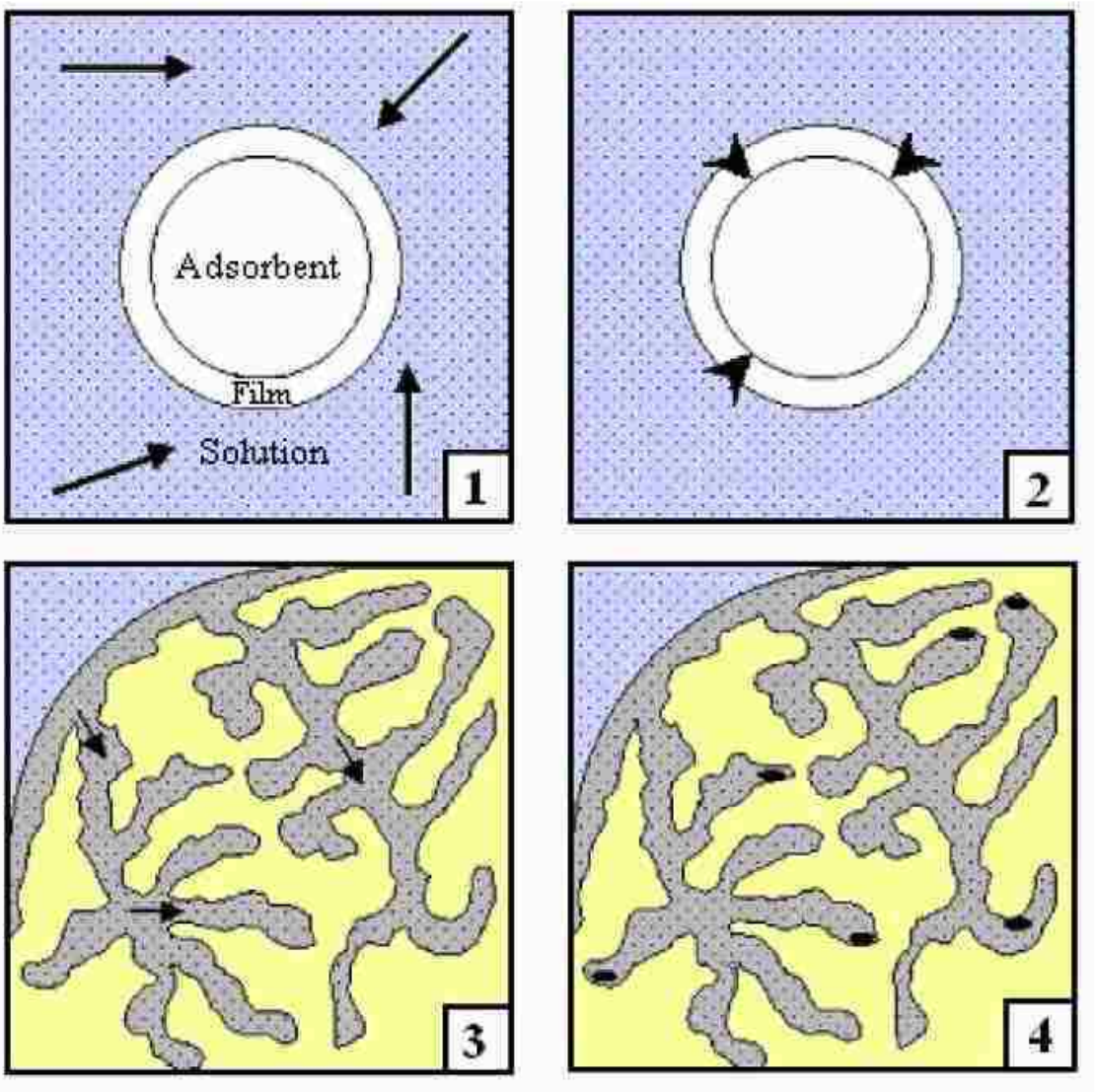

Scheme 2-1 Steps in the adsorption of metal ions onto the adsorbent site; bulk solution transport (1), film diffusion (2), pore diffusion (3) and adsorption (4).[49]

2.2.2. Kinetics Models

Different kinetics models have been used to explain the adsorption of metal ions onto adsorbents such as chitosan, moss peat, activated carbon etc. Amongst these, only

two are the most commonly used; Lagergren's pseudo first order, and pseudo second order model.[50-53] They help to elucidate the mechanism of metal ion adsorption. In addition, the performance of various adsorbents can be assessed using the parameters obtained by fitting experimental data to these models.

2.2.2.1. Pseudo First Order Kinetics

In pseudo first order kinetics, the rate of adsorption is directly proportional to the concentration gradient between the amount adsorbed at equilibrium and the amount still in solution. The derivation of the pseudo first order equation is given below.

$$\frac{dq_t}{dt} = k(q_e - q_t) \qquad \text{Eq. 2.1}$$

Where k is the rate constant of sorption, (g/μmol min), q_e is the amount of divalent metal ion sorbed at equilibrium, (μmol/g), q_t is the amount of divalent metal ion on the surface of the sorbent at any time, t, (μmol/g).

Rearranging Eq. 2.1 leads to Eq. 2.2

$$\frac{dq_t}{(q_e - q_t)} = k\,dt \qquad \text{Eq. 2.2}$$

The integration expression showing the boundary conditions is given in Eq. 2.3

$$\int_0^{q_t} \left(\frac{1}{(q_e - q_t)}\right) dq_t = k. \int_0^t t \qquad \text{Eq. 2.3}$$

By integrating Eq. 2.3, and rearranging results in the linearized form of the pseudo first order equation (Eq. 2.4).

$$\log(q_e - q_t) = \log(q_e) - \frac{k_1}{2.303} t \qquad \text{Eq. 2.4}$$

By plotting log (q_e-q_t) vs time t, the parameters k_1 and q_e which represent pseudo first order rate constant and equilibrium amount adsorbed per unit weight of adsorbent respectively can be determined.

However, in most cases, this linearized equation does not give theoretical q_e comparable with the experimental ones.[54] The plots are found to be linear for only the first few minutes, beyond which the data would not show good correlation. Despite these disadvantages, this model has been used to explain the adsorption of metallic ions onto chitosan.

2.2.2.2. The Pseudo-Second Order Model

Most adsorption kinetics onto polymer adsorbents were found to follow the pseudo second order model. Ho and Mckay applied pseudo second order model on the kinetics of adsorption of divalent metal ions (Pb, Cu, and Ni) onto sphagnum moss peat.[50] The assumption is that the sorption follows the Langmuir equation. The assumptions for Langmuir type of adsorption include:

- There is a monolayer of metal ion on the surface of the adsorbent
- The energy of sorption for each metal ion is the same and is independent of surface coverage
- The sorption occurs only on localized sites and involves no interactions between sorbed ions
- The rate of sorption is almost negligible in comparison with the initial rate of sorption

The pseudo second order rate expression can be represented as below:

$$\frac{dq_t}{dt} = k_2(q_e - q_t)^2 \qquad \text{Eq. 2.5}$$

Where k is the rate constant of sorption, (g/ μmol min), q_e is the amount of divalent metal ion sorbed at equilibrium, (μ mol/g), q_t is the amount of divalent metal ion on the surface of the sorbent at any time, t, (μmol/g).

Separation of variables in Eq. 2.5 gives Eq. 2.6:

$$\frac{dq_t}{(q_e - q_t)^2} = k_2 dt \qquad \text{Eq. 2.6}$$

which has the integration expression represented by Eq. 2.7

$$\int_0^{q_t}\left(\frac{1}{(q_e - q_t)^2}\right) = k_2 . \int_0^t t \qquad \text{Eq. 2.7}$$

$$q_e = \frac{k_2 . q_e^{\,2} . t}{1 + k_2 . q_e . t} \qquad \text{Eq. 2.8}$$

This equation can be linearized to give the following equation:

$$\frac{t}{q_t} = \frac{1}{k q_e^{\,2}} + \frac{1}{q_e} t \qquad \text{Eq. 2.9}$$

A plot of t/q_t against t from experimental data can be used to determine the constants, q_e and k.

2.2.3. Isotherm models

Adsorption isotherm models are used to describe the distribution of adsorbate species between the adsorbent surface and the solution, at equilibrium at a specified temperature. In our study, we used Langmuir, Freundlich, and Dubinin-Radushkevich isotherm models to study equilibrium adsorption of Cd (II) ions onto 100% CS and 50:50 CS:B15C5. Details about their theoretical backgrounds are given in the following subsections 2.2.3.1-2.2.3.3.

2.2.3.1. Langmuir adsorption isotherm

Langmuir adsorption theory is based on monolayer adsorption. The adsorption can only occur at a finite number of sites that are uniformly distributed on the adsorbent surface.[55] Consequently, systems that follow this model are characterized by a theoretical saturation point when all sites are occupied by the analyte species. It is also assumed that there is no interaction and steric hindrance amongst the analyte species. All adsorbent sites exhibit equal affinity for the analyte species. The linearized equation that represents this Langmuir model is shown in Eq.

$$\frac{C_e}{q_e} = \frac{C_e}{q_{\max}} + \frac{1}{K_L q_{\max}} \qquad \text{Eq. 2.10}$$

Where C_e (µmol/L) is the equilibrium concentration; q_e (µmol/g) and $q_{\max}$ (µmol/g) are equilibrium and theoretical adsorption capacity of the adsorbent for the particular

adsorbate respectively; K_L is the adsorption equilibrium constant (L/μmol). The essential characteristics of Langmuir isotherm can be expressed in terms of R_L, a dimensionless constant referred to as separation factor.[56] It is calculated using the following equation:

$$R_L = \frac{1}{1 + K_L C_o} \qquad \text{Eq. 2.11}$$

where C_o is the initial concentration of metal ions in solution. The value of R_L indicates the type of Langmuir isotherm; favorable ($0 < R_L < 1$), irreversible ($R_L = 0$), linear ($R_L = 1$), and unfavorable ($R_L > 1$).

2.2.3.2. Freundlich adsorption isotherm

Freundlich adsorption isotherm is widely applied to multilayer adsorption.[21] It describes adsorption onto heterogeneous surface that exhibit a non-uniform distribution of adsorption enthalpy. Consequently, stronger binding sites are occupied first. It is represented by the expression shown in Eq. 2.12.

$$\log(q_e) = \log(K_F) + (1/n)\log(C_e) \qquad \text{Eq. 2.12}$$

Where K_F is Freundlich constant related to the sorption capacity; n is the heterogeneity factor. As n approaches zero, the surface becomes more heterogeneous. When $n < 1$, the adsorption is considered to be through chemisorption whereas when $n \succ 1$, it is cooperative association.

2.2.3.3. Dubinin-Radushkevich model

Dubinin-Radushkevich model is an empirical model that was initially applied to describe the adsorption of subcritical vapors onto porous solids following a pore filling

mechanism.[21] It is based on the assumption that adsorption enthalpy follows a Gaussian distribution throughout a heterogeneous surface. Its linearized form is represented by Eq. 2.13.

$$\ln q_e = \ln q_{\max,DR} - \beta\varepsilon^2 \qquad \text{Eq. 2.13}$$

Where $q_{\max,DR}$ is the maximum amount of metal ion that can be adsorbed per unit weight of adsorbent; β ($mol^2\ J^{-2}$) is the coefficient related to the free energy of adsorption of the metal ions; ε ($J\ mol^{-1}$) is the Polanyi potential, which is the energy required to overcome the attractive force between the metal ions and the adsorption site. The parameters $q_{\max,DR}$ and β were derived from the intercept and slope of a plot of $\ln q_e$ versus ε^2. Meanwhile, the Polanyi potential can be calculated using the following Eq. 2.14.

$$\varepsilon = RT\ln\left(1+1/C_e\right) \qquad \text{Eq. 2.14}$$

Where R is the molar gas constant ($R=8.314\ J\ mol^{-1}\ K^{-1}$) and T is the temperature of the adsorption solution in Kelvin (T=298 K).

The objective of this study is to report a novel method to synthesize CR-based composites by using $BMIm^+Cl^-$ solvent to dissolve CR, CEL and CS in one-step. This method is described in detail in sections that follow. In addition, we report the characterization of these composite materials using a variety of spectroscopic techniques such as FTIR, UV-Vis, and XRD. These novel composites were then extended towards the selective adsorption of Cd (II) and Zn (II) from synthetic wastewater. Interestingly, interactions between these polysaccharides and the crown ethers led to synergistic adsorption of heavy metal ions. In addition, CS-based composites were able to adsorb

appreciable amounts of the organic pollutant, 2,4,5-trichlorophenol. Details of these adsorption experiments and results are presented in the sections that follow.

2.3. Experimental Methods

2.3.1. Chemicals

Microcrystalline cellulose (with a level-off degree of polymerization, $\overline{D.P.} \approx 300$)[57,58] and chitosan (MW≈310-375 kDa) were purchased from Sigma-Aldrich (Milwaukee, WI). The degree of deacetylation of chitosan, as determined by FT-IR method was 84±2%.[59] Water, purified from a Barnstead Nanopure unit (Dubuque, IA, USA) or double-distilled (~18.2 MΩ cm^{-1}) was used to prepare aqueous solutions of zinc (II) nitrate (J.T. Baker), cadmium (II) nitrate and 2,4,5-trichlorophenol (2,4,5-TCP) (Sigma-Aldrich, Milwaukee, WI, USA). Benzo 15-crown-5 (B15C5), benzo 18-crown-6 (B18C6), dibenzo 18-crown-6 (DB18C6) (Alfa Aesar), and dibenzo 15-crown-5 (Acros) were used as received. The structures of these compounds are presented on Scheme 2-2.

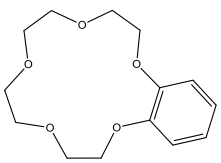

B15C5

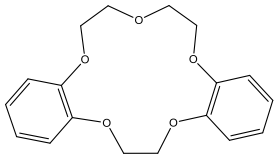

DB15C5

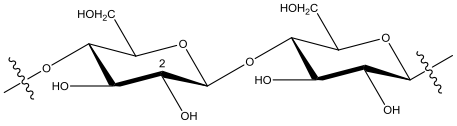

CEL

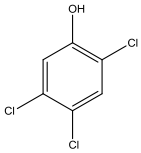

2,4,5-TCP

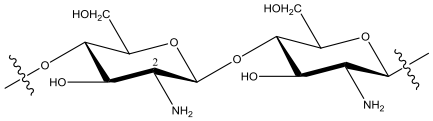

CS

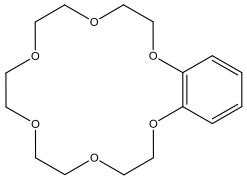

B18C6

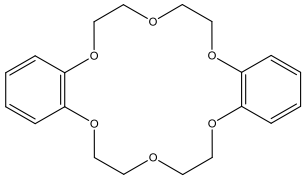

DB18C6

Scheme 2-2 Chemical structures of materials used in this study.

The IL, $BMIm^+Cl^-$ was synthesized according to procedures reported previously.[60] In brief, freshly distilled 1-methylimidazole (350 mL, 4.39 mol) and *n*-butyl chloride (508 mL, 4.83 mol) were allowed to react under argon or nitrogen at 60-70 ^{0}C for 72 h (Figure 2-1). Crude $BMIm^+Cl^-$ was then washed with three 3 X 200 mL dry ethyl acetate to remove any excess reactants and contaminates. Any remaining ethyl acetate was removed by rotavaping the IL at 70 ^{0}C for at least 10 h. The pure IL was then characterized by ^{1}H and ^{13}C NMR spectroscopy. ^{1}H NMR ($CDCl_3$, 400 MHz) δ in ppm: 0.96 (t, 3H,

$NCH_2CH_2CH_2C\underline{H}_3$), 1.38 (m, 2H, $NCH_2CH_2C\underline{H}_2CH_3$), 1.91 (m, 2H, $NCH_2C\underline{H}_2CH_2CH_3$), 4.13 (s, 3H, $NC\underline{H}_3$), 4.34 (t, 2H, $NC\underline{H}_2CH_2CH_2CH_3$), 7.56 (t, 1H, $NC\underline{H}CHN$), 7.72 (t, 1H, $NCHC\underline{H}N$), 10.55 (s, 1H, $NC\underline{H}N$). ^{13}C NMR ($CDCl_3$, 400 MHz) δ in ppm: 13.36 ($NCH_2CH_2CH_2\underline{C}H_3$), 19.35 ($NCH_2CH_2\underline{C}H_2CH_3$), 32.08 ($NCH_2\underline{C}H_2CH_2CH_3$), 36.42 ($N\underline{C}H_3$), 49.63 ($N\underline{C}H_2CH_2CH_2CH_3$), 121.98 ($N\underline{C}HCHN$), 123.67 ($NCH\underline{C}HN$), 137.66 ($N\underline{C}HN$).

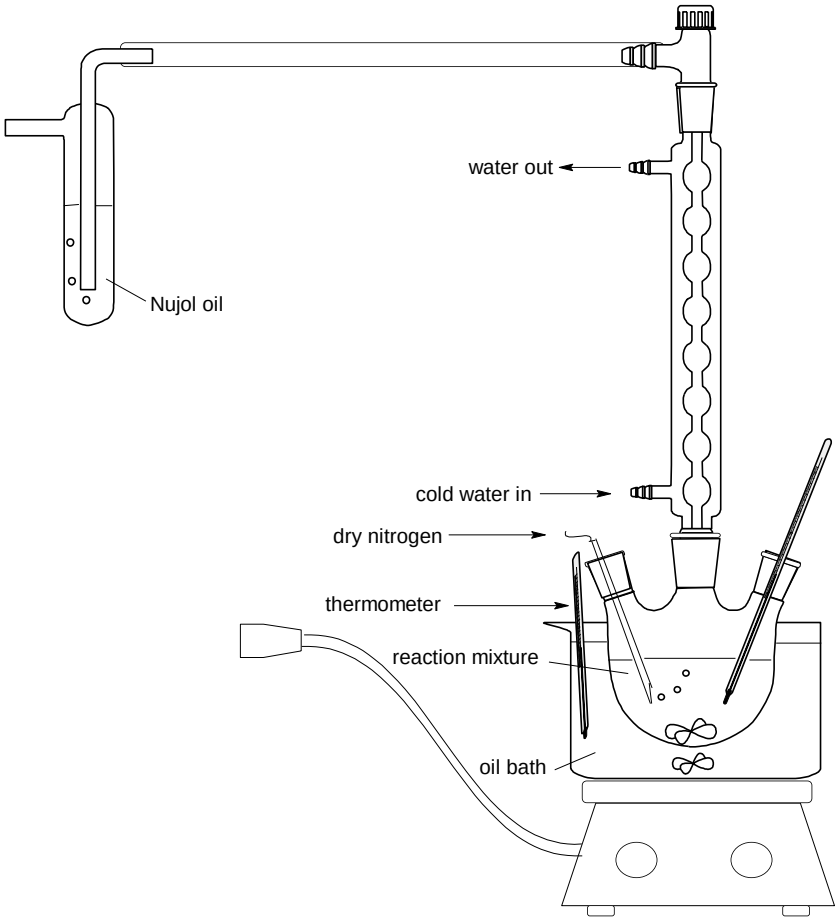

Figure 2-1 Set-up for the synthesis of 1-butyl-3-methylimidazolium chloride.

2.3.2. Instruments

FT-IR spectra of the materials were recorded on a Perkin Elmer 100 spectrometer at 2 cm^{-1} resolution by averaging 64 spectra for each spectrum. These spectra were measured using either KBr or a ZnSe single reflection ATR accessory (Pike Miracle ATR). UV-Visible spectra were measured on a Perkin-Elmer Lambda 35 UV/Vis spectrometer. X-ray diffraction (XRD) measurements were performed on a Rigaku MiniFlex II diffractometer using the Ni filtered Cu Kα radiation (1.54059 Å). The voltage and the current of the X-ray tube were 30 kV and 15 mA respectively. The samples were measured within the 2θ range 2.0 to 40.0^0 with the scan rate being set at 5^0 min^{-1}. Data processing procedures were then performed using the Jade 8 program package.[61] The surface and cross-sectional morphologies of the composite films were examined under vacuum using a Hitachi S-4800 scanning electron microscope (SEM) at accelerating voltage 3 kV. Prior to SEM examination, the film specimens were made conductive by applying a 2 nm iridium-coating onto their surfaces using an Emitech K575x Peltier Cooled Sputter Coater (Emitech Products, TX). Tensile strength of the composite films were evaluated on an Instron 5500R tensile tester (Instron Corp., Canton, MA) equipped with a 1.0 kN load cell and operated at a crosshead speed of 5 mm min^{-1}. Each specimen had a gauge length and width of 25 mm and 10 mm respectively. In order to avoid slippage of the film specimens during measurement, two pieces of sandpaper (20 mm x 20 mm) were folded over the specimen ends and clamped between the jaws of the tensile tester. Figure 2-2shows the image of the tensile tester machine.

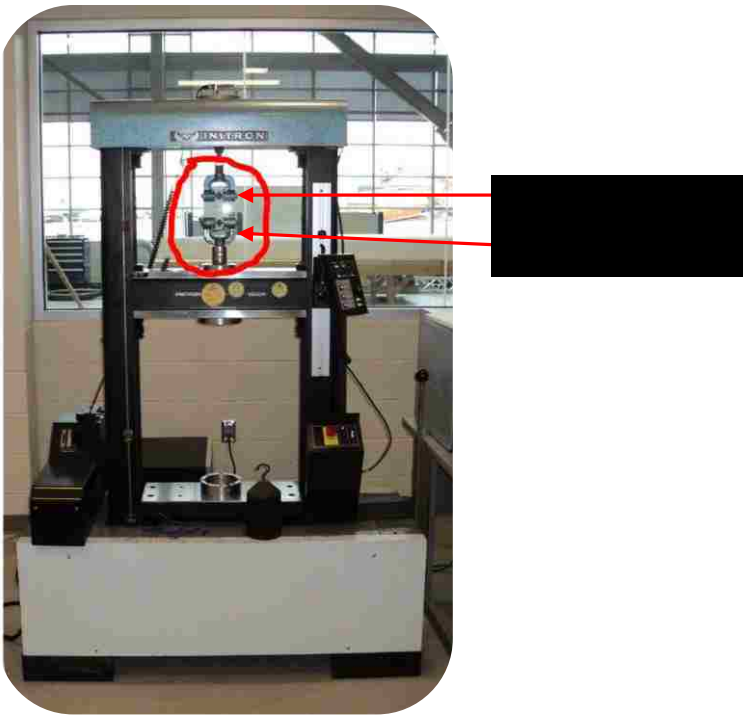

Figure 2-2 Image of the tensile tester machine. The sample is clamped on both ends using the upper and the lower jaws. In this set-up, tensile force is applied by moving the lower jaw vertically downwards whilst the upper jaw remains stationary.

2.3.3. Preparation of polysaccharide/crown ether composite films

The procedure previously developed in our group was slightly modified to adapt to the synthesis of CR-containing composite films.[62] As shown in Scheme 2-3a desired amount of CR (e.g., 0.60 g of B15C5) was dissolved in 30 g of $BMIm^+Cl^-$ at 90-105 ^0C under either argon or nitrogen atmosphere exclude undesirable oxidation of reactants. After the dissolution of B15C5 (~30 min) either CEL or CS was added in portions of 1% (with respect to the weight of $BMIm^+Cl^-$) each time. Each successive 1% portion was added after the previous one had already completely dissolved until a desired amount was reached.

Then, upon complete dissolution (~6 h) of these constituents, homogeneous but viscous solutions of CR and CEL or CS in $BMIm^+Cl^-$ were casted into lab-designed moulds made from Mylar substrates and PTFE. These viscous solutions were left to cool down to room temperature and gel overnight. The ionic liquid, $BMIm^+Cl^-$, was then removed from the films by immersing the films in ~1.8 L water for about 72 h or until all the IL was confirmed absent in the water washing by UV Vis spectroscopy. During this washing period, the washing water was constantly replaced with fresh water each time to maximize and quicken the removal of ionic liquid. Distillation of the water washings enabled us to recover $BMIm^+Cl^-$ for potential reuse. At least 88% of the IL was recovered for reuse.[59] The resultant IL-free wet films were then either air-dried in a home-made drier (for mechanical tests) or they were lyophilized (for adsorption and other characterizations) on a Virtis 2 L freeze drier to afford dried films. Films containing different compositions of either CS and CR, [CS+CR] or CEL and CR, [CEL+CR] and CS and CEL, [CEL+CS] and CEL, CS and CR, [CEL+CS+CR] were synthesized by this same approach. However, when [CEL+CS] composites were made, CEL was dissolved first before adding CS. Also, for the synthesis of [CEL+CS+CR], these components were dissolved in the order CR, then CEL and lastly CS. It should be pointed out that within experimental errors, composite films prepared using either the recovered IL or the fresh IL were similar in terms of their spectroscopic features and their adsorption capacities and behaviors.

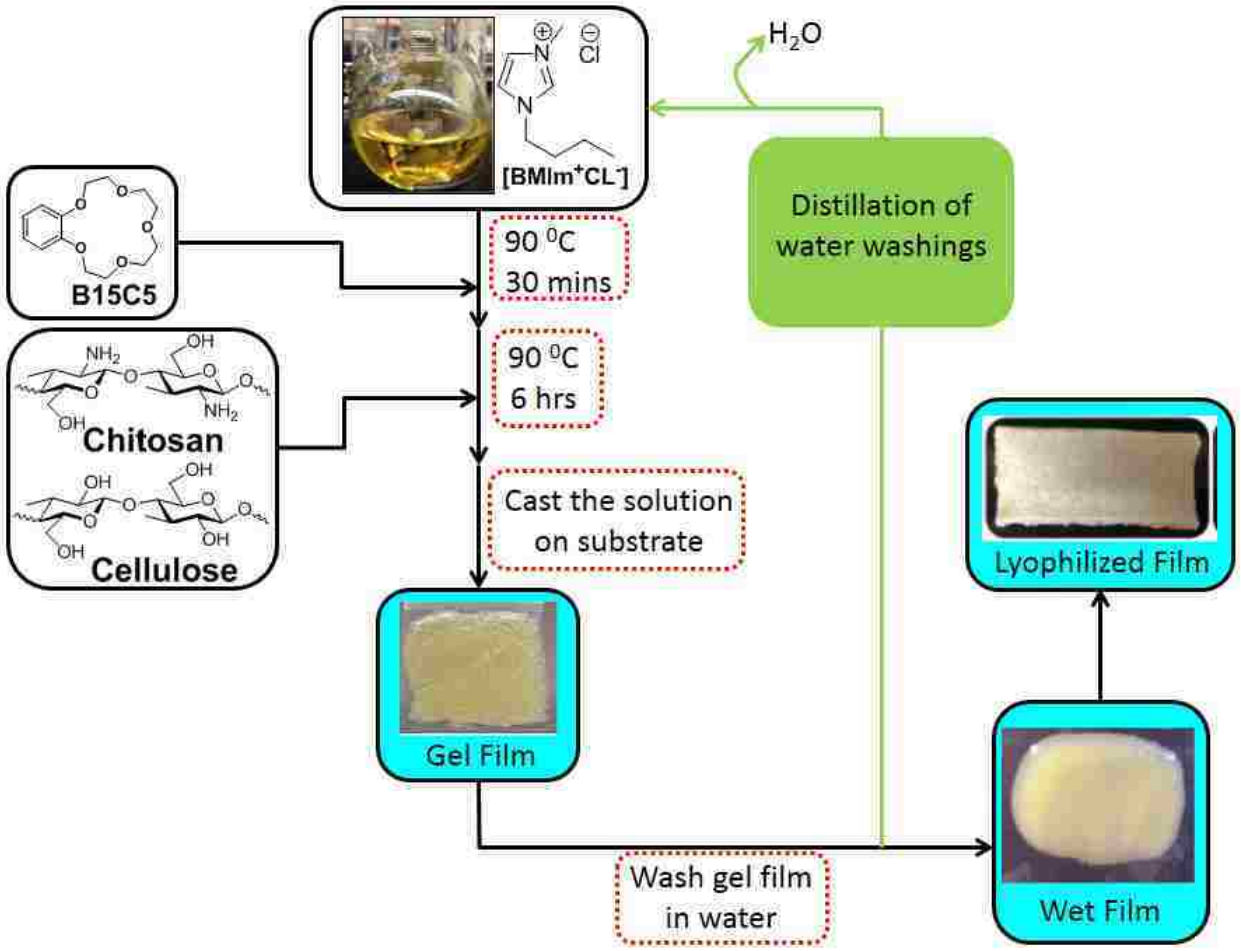

Scheme 2-3 Synthesis of crown ether-based composite films.

2.3.4. Procedure used to measure kinetics of adsorption of heavy metal ions by the composite films

Metal ion solutions of concentration 4.448 mM M^{2+} were prepared by dissolving the desired amount of either cadmium nitrate or zinc nitrate in highly purified water (18.2 MΩ). The pH of these solutions were adjusted to desired pH (pHs studied include 1.9, 3.9, 6.0, 7.1, and 8.0) using either 0.2 M HNO_3 or 0.2 M NaOH. The composite film

(0.20 g) was then added to 100 mL of 4.448 mM metal ion solution in a 250 mL Erlenmeyer flask. The mixture was then shaken at 180 rpm at room temperature (25±1 ^{0}C) using an orbital shaker (Lab-line 1345R, Barnstead). Above this rate, the films would start to break apart, especially those with higher amounts of CR, into small particles making the whole solution turbid. It took ~ 24 h to reach equilibrium adsorption with either Cd^{2+} or Zn^{2+}. An aliquot (50 µL for Cd (II) and 100 µL for Zn (II)) was withdrawn from the flask at predetermined time intervals including the time (t = 0 min), *i.e.*, before adding the film into the metal solution. These aliquots were then diluted with 5% HNO_3. Subsequently, the concentrations of these metal ions were then determined on a Perkimer AAnalyst 100 flame atomic absorption spectrometer at 228.8 nm and 213.9 nm for Cd (II) and Zn (II) respectively.[63] The cumulative amount of metal ions adsorbed up to each time point were calculated by the following mass balance equation:

$$q_t = \frac{(C_i - C_t)V}{W} \qquad \text{Eq. 2.15}$$

where q_t represents the amount of metal ion adsorbed per unit weight of film adsorbent (µmol g^{-1}) at time t (min); C_i and C_t represent the metal ion concentrations (µmol L^{-1}) at time t = 0 min and at time t respectively; V represents the volume (V = 0.1 L) of the metal solution and W is the actual dry weight of the film composite (W ≈ 0.20 g).

The percentage amount of pollutant species adsorbed per unit weight of adsorbent was calculated using the equation below:

$$\%\ adsorbed = \frac{q_e * W}{1000 * C_i * V} * 100\% \qquad \text{Eq. 2.16}$$

Where q_e is the amount of metal ion adsorbed at equilibrium (µmol/g); W, V and C_i are the same as described in Eq. 2.15. It is however worthwhile to mention that the constant 1000 was incorporated into the equation to convert millimmole to micromole.

2.3.5. Procedure used to measure thermodynamics of adsorption of metal ions by composite films

A series of solutions containing Cd (II) ions within the concentration range 100 ppm to 2,000 ppm (0.89- to 17.8 mM) were prepared from a stock solution. Twenty five milliliters of each of these solutions was pipetted into a polyethylene vial. To each of these vials, 25 mg of composite film was added. Another set of vials containing corresponding volumes and concentrations of Cd (II) was also prepared. This acted as blank to account for any adsorption that may occur onto the surfaces of the vials. Subsequently, the vials were stoppered and then they were shaken on the orbital shaker for 96 h to ensure that equilibrium adsorption was achieved. In addition, the experiment was conducted at room temperature, 25 °C. The concentrations of Cd (II) ions in each of the vials were determined using flame AA. The amount adsorbed per unit weight of adsorbent was calculated using the mass balance equation Eq. 2.12. The data obtained was then fitted to three isotherm models; Langmuir, Freundlich and Dubinin-Radushkevich isotherm models.

$$q_e = \frac{(C_o - C_e)V}{W} \qquad \text{Eq. 2.17}$$

Where q_e (µmol/g) is the amount of metal ions adsorbed per unit weight of adsorbent; C_o and C_e represent the initial and equilibrium concentrations (µM) respectively; V is the volume of adsorbate solution; W is the dry weight of adsorbent.

2.3.6. Procedure used to measure adsorption of 2,4,5-trichlorophenol by the composite films

Adsorption of the organic pollutant 2,4,5-trichlophenol (2,4,5-TCP) was measured on a UV Visible spectrometer. Trial experiments indicated that any slight residue of $BMIm^+Cl^-$ left out during the synthesis and washing step could interfere with the absorbance due to 2,4,5-TCP. To avoid such interference, the composite films were washed thoroughly in water until no more IL could be detected at least by UV Vis spectroscopy. Specifically, 2 specimens (each one weighing ~2.7 mg) for each composite to be tested were placed in a thin cell fabricated from PTFE windows sandwiched between two PTFE meshes (). The meshes were clamped together to hold them in place before they were immersed in 1.8 L water. The meshes served a dual function. They allowed free circulation of water and protect the films from possible damage from the stir bar. This washing took 60 h, during which time the water was being constantly replaced (after every 4 h) to optimize the leaching of as much IL as possible. Each time before changing the water, a UV-Vis spectrum was recorded for the water washings. The presence/absence of $BMIm^+Cl^-$ was confirmed by the appearance / disappearance of the peak at 214 nm and 287 nm which are surrogate markers for this IL.

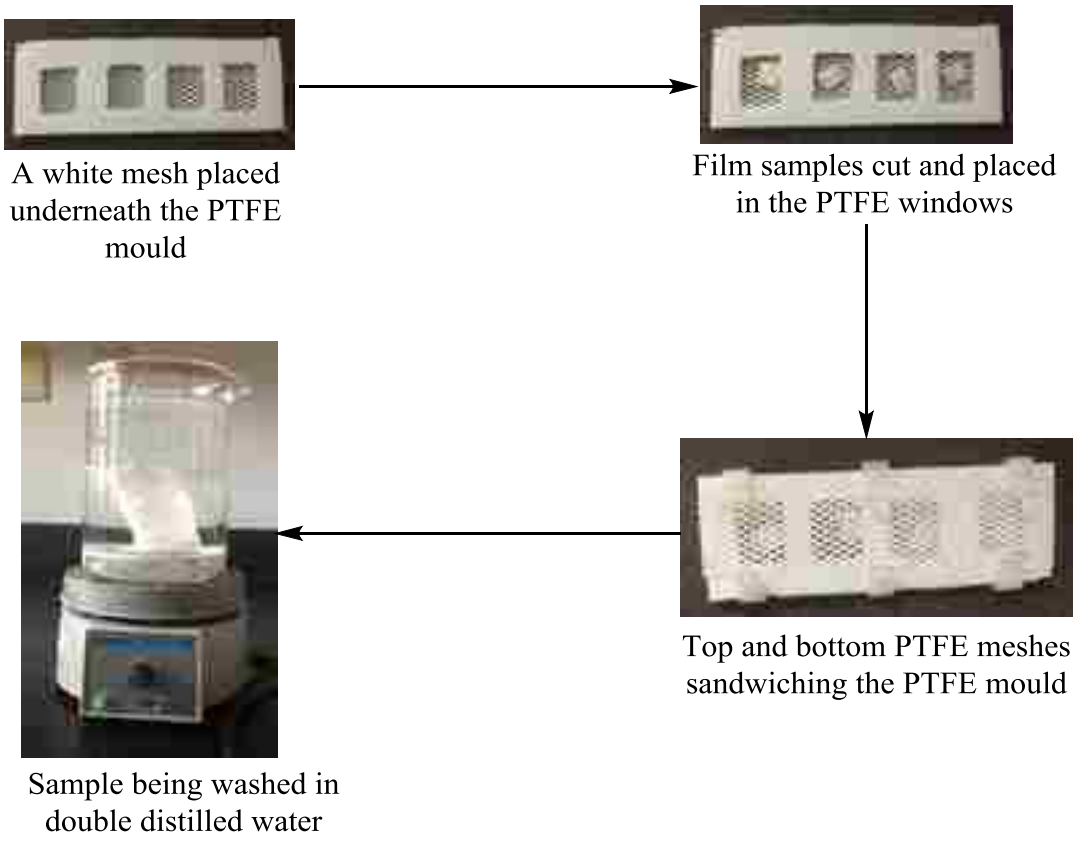

Figure 2-3 Washing samples for adsorption of organic pollutants

After the films were confirmed clean, they were each placed in a separate 10 mm path-length cuvette (Figure 2-4). As shown in this figure, a PTFE mesh (0.8 mm X 0.8 mm) was put into each cuvette before the film was laid flat on this mesh. Another mesh of almost identical dimensions was laid on top of the film. Therefore, the configuration was such that the two meshes sandwiched the film. Then, a spectrophotometric cell spin bar was put on top of the mesh. These two meshes served the same dual functions as during washing i.e. they protected the film from damage from the spin bar and allowed free circulation of the adsorbent solution. Exactly 2.70 mL of 390 µM aqueous solution of 2,4,5-TCP were pipetted into one of the cells. Into the other cell, the blank cell, 2.70 mL of purified water was added. This blank served to correct for any absorbance change unrelated

to the adsorbate. It is noteworthy that in prior experiments, two blanks were used, one with film and water (blank 1) and the other one without film but with aqueous solution of 2,4,5-TCP (blank 2). Blank 2 was used to correct for any insipient adsorption by any component other than the film. It was found that within experimental errors, there was no detectable adsorption by other cell components. Therefore, this blank was not used in subsequent adsorption experiments. Absorbances of the sample cell and blank 1 were then monitored at 289 nm which is the wavelength at maximum absorbance for 2,4,5-TCP. After each measurement, the cell was replaced on a magnetic stirrer and continuous stirred. Then, at each time point, the absorbance due to 2,4,5-TCP unadsorbed was calculated by taking out the difference between the absorbance in sample and blank 1 cells. The amount of 2,4,5-TCP adsorbed (q_t) up to each time point was then calculated using equation 1 with C_i and C_t being the concentrations of 2,4,5-TCP in the solution at t=0 and at time t mins respectively; $V=2.7X10^{-3}$ L; and $W = 2.7X10^{-3}$ g.

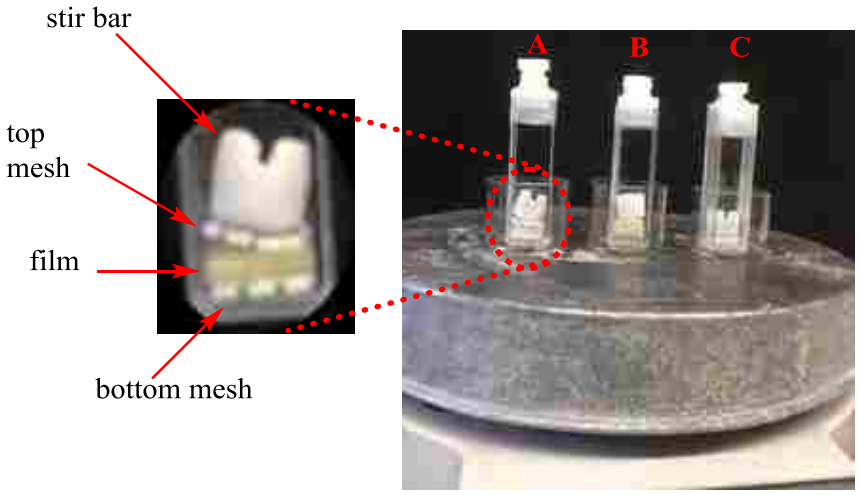

Final setup with the stir bars and the caps on

Figure 2-4 Experimental set-up for evaluating the kinetics of adsorption of organic pollutants. Cuvette (A) contains pollutant solution, film adsorbent, top and bottom meshes, and stir bar, Cuvette (B) contains similar components to (A) except the pollutant solution, film adsorbent, top and bottom meshes, and stir bar, Cuvette (B) contains similar components to (A) except the pollutant solution which is substituted by pure water, Cuvette (C) contains similar components to (A) except the film adsorbent.

2.3.7. Reusability of composite films

Experiments were also designed to determine if these novel composite films could be reused after they adsorb heavy metal ions (Cd^{2+} and Zn^{2+}) and 2,4,5-TCP. Specifically, each of the composite films (i.e. 50:50 CS:B15C5 or 50:50 CEL:B15C5) that had previously adsorbed Cd^{2+} or Zn^{2+} respectively was washed in 100 mL of 5.0 mM aqueous solution of disodium EDTA in an Erlenmeyer flask. The contents were shaken at 180 rpm at room temperature on an orbit shaker. After 2 h of washing, the films were taken out and briefly rinsed in water at least twice before being blotted dry. The films were then put

in fresh EDTA solution and the process repeated two more times. Readsorption of these metal ions was then repeated as described in section 2.3.4.

To test reusability of these polysaccharide crown ether composite films, the film with composition 30:20:50 [CEL+CS+B15C5] was chosen for the adsorption-desorption-readsorption of 2,4,5-TCP. The first adsorption cycle was done as reported earlier. After 24 hours of adsorption, the films were washed in 50 mL of double distilled water for 60 h exchanging water with fresh one every 12 h. Subsequently, the film was put in a cuvette and 2.7 mL of water was added. The absorbance of the water was recorded at 300 nm after 12 h. This was done to confirm that all the previously adsorbed 2,4,5-TCP was desorbed during the 60 h of washing. After the 12 h, the absorbance of the sample and blank were compared and found to be the same thereby confirming that no detectable analyte was still on the film. The film was then taken out of the cuvetted and blotted with filter paper. Adsorption of 2,4,5-TCP was repeated as before.

2.3.8. Analysis of kinetics data

We designed our experiments to determine if our novel polysaccharide composite films can potentially be used to adsorb heavy metal ions (Cd^{2+} and Zn^{2+}) and organic pollutant, 2,4,5-TCP from water. In addition, we sought to evaluate the relative performance of each composite so that the best one could be identified. This was achieved by fitting the kinetics data to three most common kinetics models — pseudo first order, pseudo second order and intra-particle diffusion models. The detailed description and underlying assumptions involved in applying these models has been presented in the previous relevant sections.

2.3.9. Assessment of goodness of fit

We used model selection criteria (MSC) and coefficient of determination, R^2 to estimate the goodness-of-fit of the experimental data to each of the kinetics and thermodynamic models. The MSC was calculated using the equation below:[64]

$$MSC = \ln\left\{\frac{\sum_{i=1}^{n} w_i\left(Y_{obs_i} - \overline{Y}_{obs}\right)^2}{\sum_{i=1}^{n} w_i\left(Y_{obs_i} - Y_{calc_i}\right)^2}\right\} - \frac{2p}{n} \qquad \text{Eq. 2.18}$$

where Y_{obs_i} and Y_{calc_i} are observed and calculated values of the *i-th* point, respectively and w_i is the weight that applies to the *i-th* point, *n* is the number of points and p is the number of parameters. The product moment correlation coefficient was calculated automatically by Excel and Origin.

2.4. Results and Discussion

2.4.1. Synthesis of composite films

Ionic liquid, $BMIm^+Cl^-$ has gained popularity amongst the scientific community due to reasons previously presented in the introductory sections. One of the main advantages of the IL used in this project was that it can dissolve biopolymers such as CEL (MW≈49 kDa)and CS (MW≈310-375 kDa) for up to 10 weight % . In preliminary studies, we found that as high as 10% (with respect to the weight of IL) could be dissolved in $BMIm^+Cl^-$. On the other hand, only 4% CEL could be dissolved in the same amount of IL. These differences in solubility are not surprising because the molecular weights of these biopolymers were different. Also, it is relatively easier to dissolve CS

than CEL. Specifically, CS used in this study has a molecular weight of 310-375 kDa which is at least 6X that of CEL (50 kDa based on D.P. values of 300). However, preparing samples with such high concentrations of CEL or CS was avoided because the solutions became too viscous to stir thus making it difficult to make homogeneous films. After a couple of trials, we eventually chose concentrations of not more than 5% CEL and not more than 3% CS because it was found that these concentrations gave more reproducible samples. Furthermore, CEL dissolved much faster than CS. For example, it took, almost an hour to dissolve 1% CEL whilst it took at 2.5 h to dissolve an equivalent weight of CS. The effect of molecular weight could also be witnessed by the fast dissolution (less than 30minutes to dissolve 5% B15C5); the molecular weight of B15C5 is 222.2 g/mol.

Interestingly, during gelation, drops of the IL were forming at the top surface of the gel samples. This was hardly surprising because during gelation, the polymer chains draw towards one another reforming the intermolecular linkages which were previously disrupted by the IL. This process pushes the IL to the surface. With time (~16 h), the gel films become harder especially those containing CEL. This could be attributed to the homogeneity in the residues making up the CEL chains. Therefore, the chains in CEL tend to pack more tightly than in CS where there are varying ratios of acetyl glucosamine and glucosamine residues.

In some studies, it has been shown that $BMIm^{+}Cl^{-}$ exhibits some level of toxicity against aquatic organisms.[65,66] In view of this, it is necessary to remove this IL from the gel films so as to allay any safety concerns which might arise from using composites containing this IL. To remove this IL from the gel films, we just soaked the films in water

and let the IL leach out. The first wash was yellowish showing the presence of this IL. However, as more water was being replaced with fresh one, this color faded to the extent that it was not visible by the human eye. We therefore used a more sensitive technique, UV Visible spectroscopy to monitor $BMIm^{+}Cl^{-}$ through its absorption bands at 214- and 290- nm. As expected, the intensities of these bands decreased with washing time until the concentration of this IL dropped below the limit of detection of the technique ($3X10^{-5}$ AU). It took ~72 hr for the peaks to disappear (Figure 2-5A and B). Therefore, this amount of time was set as the washing time that is sufficient to remove the IL.

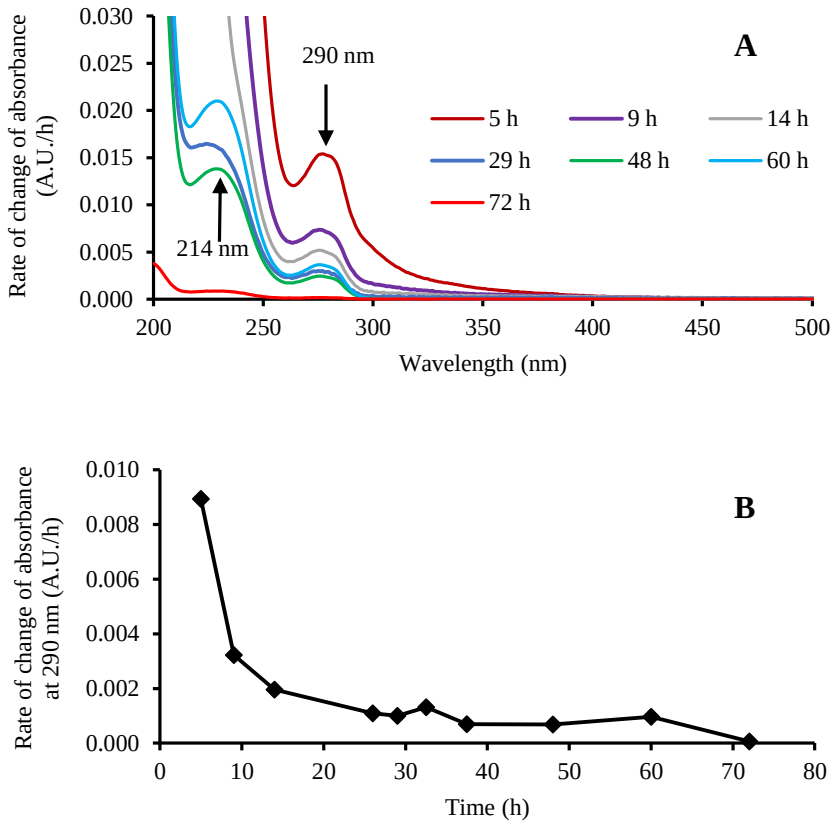

Figure 2-5(A) UV Visible absorption spectra of the aqueous washing solutions at different time points (B) Rate of change of absorbance plotted against time. The molar absorptivity of $BMIm^{+}Cl^{-}$ in water at 290 nm ($\varepsilon_{290\ nm}$) is 2.6 M^{-1} cm^{-1}.

There were differences in the dimensional changes which occurred during drying with either the home-made drier or the lyophilized. Essentially, all films which were air dried contracted in size compared with those that were lyophilized. In some cases, the size would contract as much as 200%. To reduce this effect, we put some weights on top of the films. Specifically, a PTFE mesh was laid on top of the film before putting weights on them.

2.4.2. Characterization of composite films

2.4.2.1. Characterization by FT-IR

We used FTIR spectroscopy to determine if, by any chance, detectable amounts of $BMIm^+Cl^-$ remained within the matrices of the composite films. This is because it could be possible that some $BMIm^+Cl^-$ remain encapsulated in the composites and not get released into the water during washing. Thus, this remaining ionic liquid would not be detected by UV Visible spectroscopy of the water washings because it would not have been released into the water. Therefore, recording FTIR spectra for the films would further confirm the presence/absence of any residual IL within the composites. The FTIR spectrum of $BMIm^+Cl^-$ exhibits a series of spectral features which can be indexed to imidazole ring C-H stretch (3200-3000 cm^{-1}), imidazole ring stretch (1600-1500 cm^{-1}), imidazole H-C-H and H-C-N bending (1168 cm^{-1}), and aromatic C-H vibrations at 756-, 1468-, and 1572-cm^{-1} (Figure 2-6).[67] Of these bands, only the 1600-1500 cm^{-1}, 756-, 1468-, and 1572-cm^{-1} do not overlap with the bands in the spectrum of regenerated CEL. However, only 756-, 1468-, and 1572-cm^{-1} do not overlap with the bands in regenerated CS. Therefore, we could use these bands to check if there was any IL in the films. As expected, these bands were absent in the spectrum of regenerated CEL and CS, thus further confirming the results obtained indirectly by UV Visible spectroscopy of the water washings.

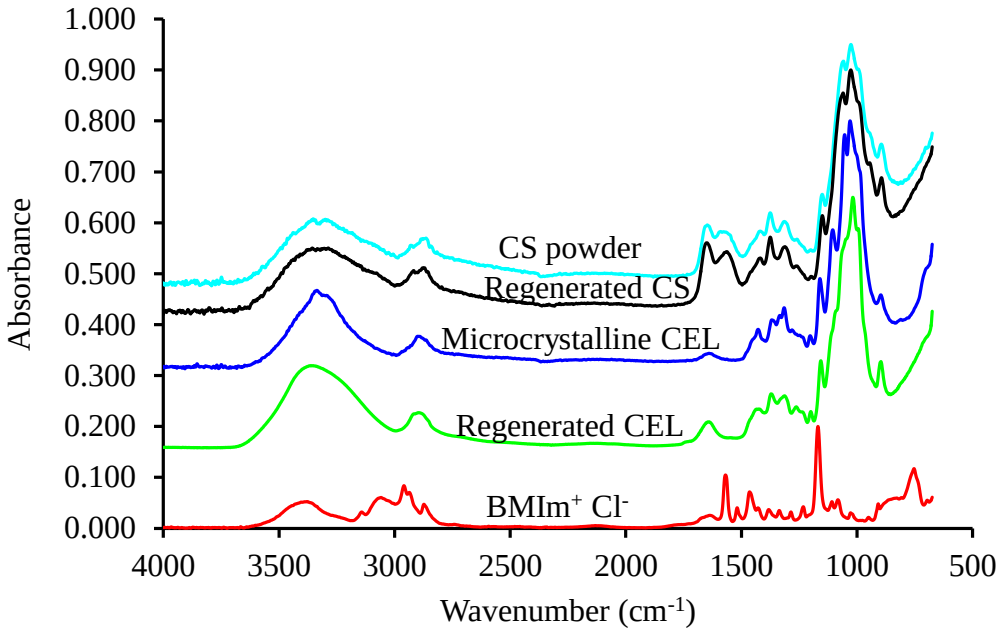

Figure 2-6 FTIR-ATR spectra of 1-butyl-3-methyl-imidazolium chloride (BMIm+Cl-) (red), regenerated CEL (green), microcrystalline CEL (blue), regenerated CS (black), and CS powder (magenta).

We also used FTIR spectroscopy to determine if there was any chemical modifications resulting from the dissolution and regeneration of either CS or CEL. This was accomplished by comparing the spectra of these components before and after regeneration using the IL, $BMIm^{+}Cl^{-}$. As illustrated in Figure 2-6 the spectrum of microcrystalline CEL powder exhibits characteristic bands at 3335 cm^{-1}, 2896 cm^{-1} due to O-H and C-H stretch vibrations in the CEL structure respectively.[68] The bands at 1160 cm^{-1}, 1054 cm^{-1} and 1030 cm^{-1} are associated with C-OH stretch vibrations at C-6.[69] Other bands at 1427-, 1368- and 896-cm^{-1} are assigned to CH_2 symmetric bending vibrations of C-O-C groups, CH/CH_2 bending vibration of C-H, and C-O stretch vibration of C-O-C groups respectively.[68] Interestingly, the spectrum of regenerated CEL is similar

to that of microcrystalline CEL. This suggests that processing CEL in $BMIm^+Cl^-$ did not lead to any chemical alterations, which implies that the IL acted as true solvent. This helps to ensure that the desirable properties of CEL may remain intact whilst fabricating it into a usable form. However, closer inspection of these spectra revealed some minor variations in terms of peak positions. Notably, most bands shifted to lower frequencies implying that the intra- and intermolecular bond network was modified by the regeneration process. For example, bands at 1030- and 1160-cm^{-1} in microcrystalline CEL shifted to 1017- and 1156-cm^{-1} in regenerated CEL respectively. These results suggest that the intra- and intermolecular H-bonding may be affected by the regeneration process. In fact, it has been observed that this change is due to the transition of CEL crystalline structure from the CEL I (highly crystalline) to the CEL II (more amorphous) polymorph. This is possible because $BMIm^+Cl^-$ dissolves CEL through disrupting the intra- and intermolecular H-bonding network in the CEL structure. During regeneration, the more thermodynamically stable CEL II polymorph is produced. The band at 3335 cm^{-1} (in microcrystalline CEL) shifted to a higher frequency, 3340 cm^{-1} (in regenerated CEL). This is due to the same reasons that the intermolecular H-bonding are less pronounced in regenerated than in microcrystalline CEL. However, the band in regenerated CEL is much broader than in microcrystalline CEL. This could be due to adsorbed water in regenerated CEL. This adsorbed water was also confirmed by a more intense band at 1641 cm^{-1} in regenerated material than in microcrystalline CEL.[70]

The FTIR spectra of native CS and regenerated CS were also similar. Since CS structure is similar to that of CEL, except that CS has an amine / acetamide group at C-2, the FTIR spectrum of CS exhibited all of the bands which were observed in the FTIR

spectrum of CEL. These amine and amide groups give rise to bands at 1647 cm^{-1} (amide C=O stretch) and at 1589 cm^{-1} (-NH_2 bending vibrations) in CS powder. Similar bands were observed in regenerated CS; 1649 cm^{-1} and 1575 cm^{-1} bands due to amide C=O stretch and –NH_2 bending vibrations. These results clearly indicate that the chemical structure of CS is retained even after being dissolved and regenerated from the IL, $BMIm^+Cl^-$. Similar results have been reported elsewhere.[62]

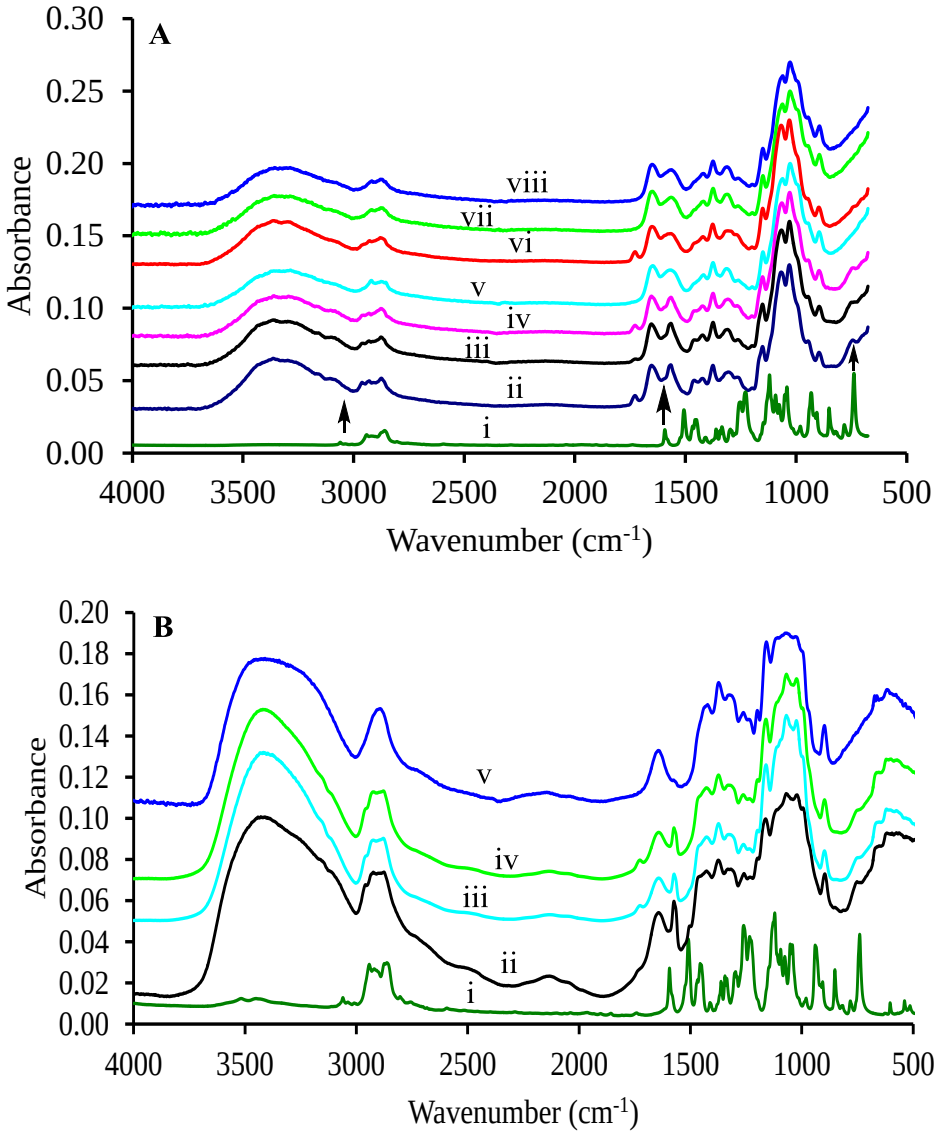

Figure 2-7 FTIR spectra of [CS+B15C5] (A) and [CEL+B15C5] (B) composite films. For (A), (i) B15C5 powder, (ii) 40:60, (iii) 50:50, (iv) 60:40, (v) 70:30, (vi) 80:20, (vii) 90:10 CS:B15C5 and (viii) 100% CS. For (B), (i) B15C5 powder, (ii) 50:50, (iii) 30:70, (iv) 10:90 B15C5:CEL and (v) 100% CEL.

FTIR was also used to investigate the chemical interactions between either CEL or CS and B15C5 in their corresponding composites. As illustrated on Figure 2-7, the FTIR spectrum of B15C5 presents bands that are characteristic of the aromatic C-H vibrations. Specifically, the bands at 1594-, and 1456-cm^{-1} are assigned to aromatic C=C stretching vibrations.[71,72] The bands at 1260- and 1121-cm^{-1} are assigned to aromatic and aliphatic COC stretch vibrations respectively.[71] The bands at 3060- and 739-cm^{-1} are attributed to aromatic C-H stretch vibrations and aromatic C-H out of plane deformation of ortho-disubstituted benzene ring.[73] The presence of this B15C5 crown ether in CS+B15C5 composite was then confirmed by comparing the spectrum of B15C5 with that of the respective composite film. As illustrated in Figure 2-8A, most of the bands for B15C5 are overlapped by those of CS which makes it harder to recognize bands attributed solely to B15C5. However, closer inspection of these spectra show that intensity of the bands at 1589-, 1456- and 739-cm^{-1} are increasing and getting sharper with the concomitant increase in the proportional content of B15C5 in [CS+B15C5] composite films. These results suggest that B15C5 was successfully encapsulated in CS matrix. This same analysis was applied to FTIR spectra of [CEL+B15C5] composite films. As illustrated in the Figure 2-8B, all spectra for [CEL+B15C5] composites contain bands at 1574- and 739-cm^{-1} which are characteristic of B15C5. Therefore, by using FTIR, it was possible to confirm that B15C5 was indeed successfully encapsulated in the polysaccharide matrices.

In addition to B15C5, other crown ethers, DB15C5, B18C6, and DB18C6, were also encapsulated in CS matrices to synthesize [CS+DB15C5], [CS+B18C6] and [CS+DB18C6] respectively. To prove this claim, FTIR spectra of each of these crown

ethers were compared with those of their corresponding CS-composites. As expected, the spectra of these composites contain bands that are characteristic of functional groups in both CS and the respective crown ether (Figure 2-8).

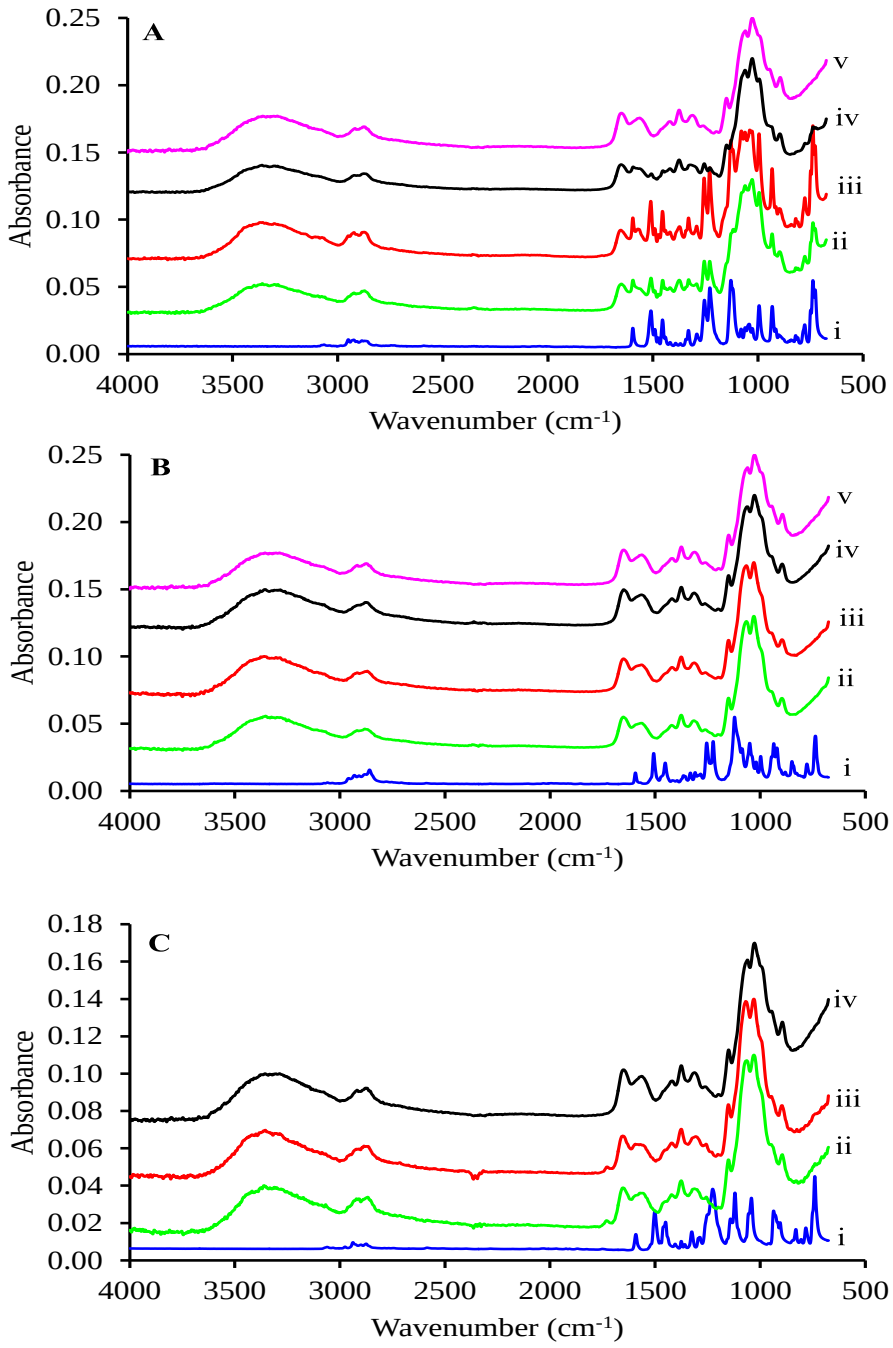

Figure 2-8 FTIR spectra of [CS+DB18C6] (A), [CS+B18C6] (B) and [CS+DB15C5] (C). For (A), (i) DB18C6 powder, (ii) 40:60, (iii) 50:50, (iv) 70:30 CS:DB18C6, and (v) 100% CS, (B) (i) B18C6 powder, (ii) 70:30, (iii) 60:40, (iv) 50:50 CS:B18C6, (C) (i) DB15C5 powder, (ii) 70:30, (iii) 90:10 CS:DB15C5, and (iv) 100% CS.

2.4.2.2. Characterization by UV Visible spectroscopy

UV Visible spectroscopy enabled us to further confirm the presence of B15C5 in both [CS+B15C5] and [CEL+B15C5]. As expected, spectra of 100% CS and 100% CEL exhibit no bands in the UV Visible range because they lack UV-visible chromophores in their structures (Figure 2-9). In fact, their spectra show a sloping background due to the scattering effects. On the other hand, B15C5 exhibit a broad band at 278 nm due to the presence of the benzene ring in its structure. As expected, this band was also present in blend films of this crown ether, B15C5 and CEL/CS. This clearly corroborates the FTIR results that suggest that B15C5 was successfully encapsulated in the polysaccharide matrices.

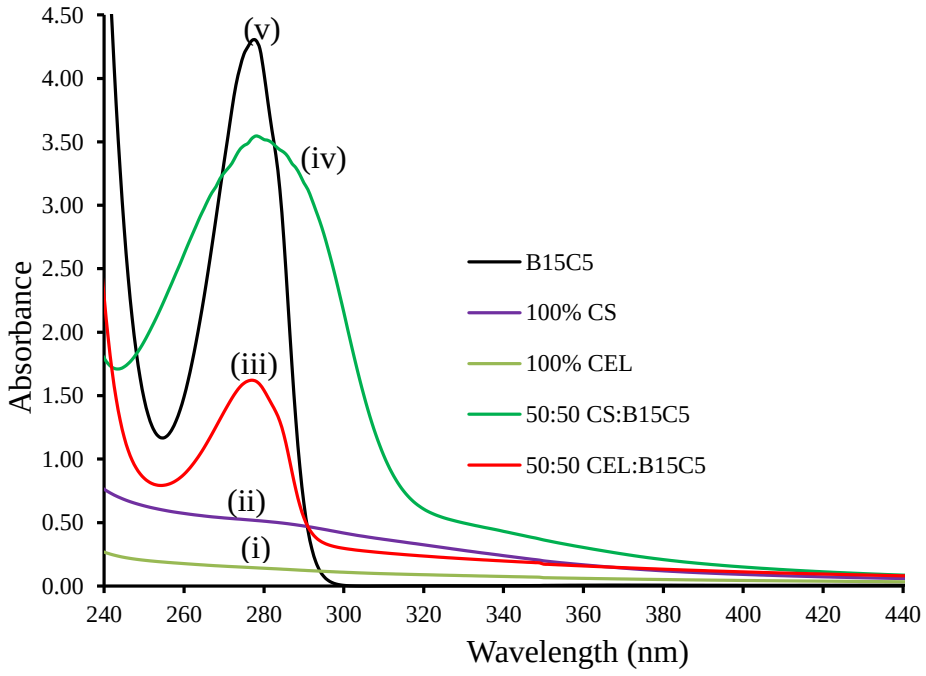

Figure 2-9 UV Visible spectra of 100% CEL (i), 100% CS (ii), 50:50 CEL:B15C5, 50:50 CS:B15C5 and x10^{-4} M B15C5 in chloroform (v).

2.4.2.3. Characterization by X-ray diffraction Spectroscopy

Powder X-ray diffraction spectroscopy was used to investigate the crystal structure of CEL, CS and crown ethers before and after their regeneration from $BMIm^+Cl^-$. As illustrated in Figure 2-10, microcrystalline CEL exhibits diffraction bands at 15.0°, 16.6° (shoulder), 20.7° (shoulder), 22.7°, and 34.7° due to diffraction from planes $1\bar{1}0$, 110, 102, 200 and 004 respectively.[68] These bands are characteristic of cellulose Iβ allomorph. However, upon dissolution and regeneration of this CEL, new broader bands attributed to cellulose II appear at 13.0° and 20.6°. These changes clearly suggest that the crystal structure of microcrystalline CEL was transformed to a relatively amorphous structure. In the CEL Iβ lattice, CEL chains are aligned parallel to each other through H-bonding and van der Waals forces to form a compact structure which comprises predominantly crystalline regions. However, upon dissolution, it was proposed that the IL diffused into the CEL matrix and destroyed the inter- and intra-molecular H-bonding network. Upon regeneration in the water, the solvent molecules were then washed away paving way for reformation of the H-bonding network. However, this reformation is bound to be incomplete because of the transitory nature of regeneration. The shift to lower 2 theta values (i.e. from 15.0° and 22.7° to 13.0° and 20.6° respectively) suggest that the inter-planar distances increased as a result of dissolution and regeneration. These results corroborate previous reports on the dissolution and regeneration of CEL from ILs.[74]

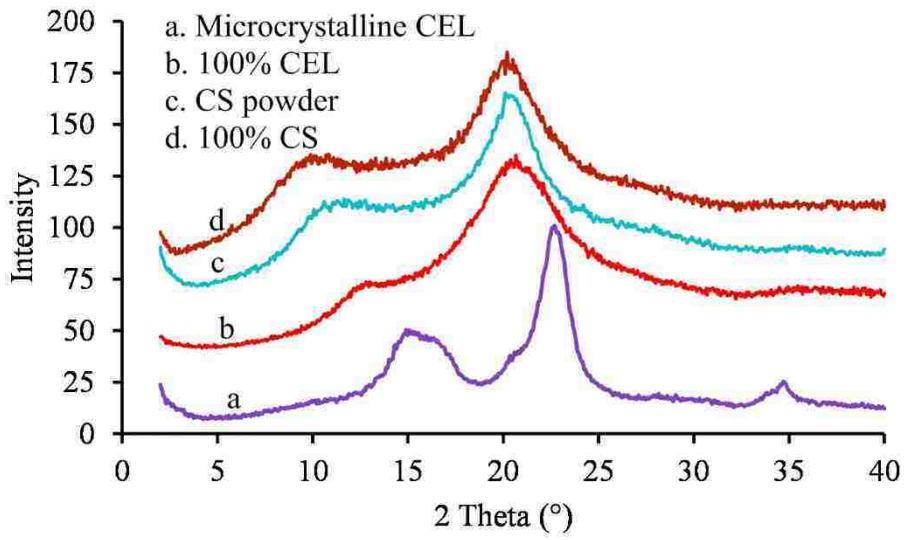

Figure 2-10 XRD spectra of (a) microcrystalline CEL, (b) 100% CEL, (c) CS powder, and (d) 100% CS.

XRD spectra of both CS powder and regenerated CS film exhibit broad bands at 12.0°, 20.4° and 10.8°, 20.2° respectively. These results suggest that the crystal structure of CS was unaffected by the dissolution and regeneration in $BMIm^{+}Cl^{-}$ in stark contrast to the case of microcrystalline CEL. This could be due to the amorphous nature of the CS powder. The CS used in the present study contained 84% deacetylated and 16% acetylated glucosamine residues.[59] As a result, CS chains cannot pack closely thereby leading to long range disorder.

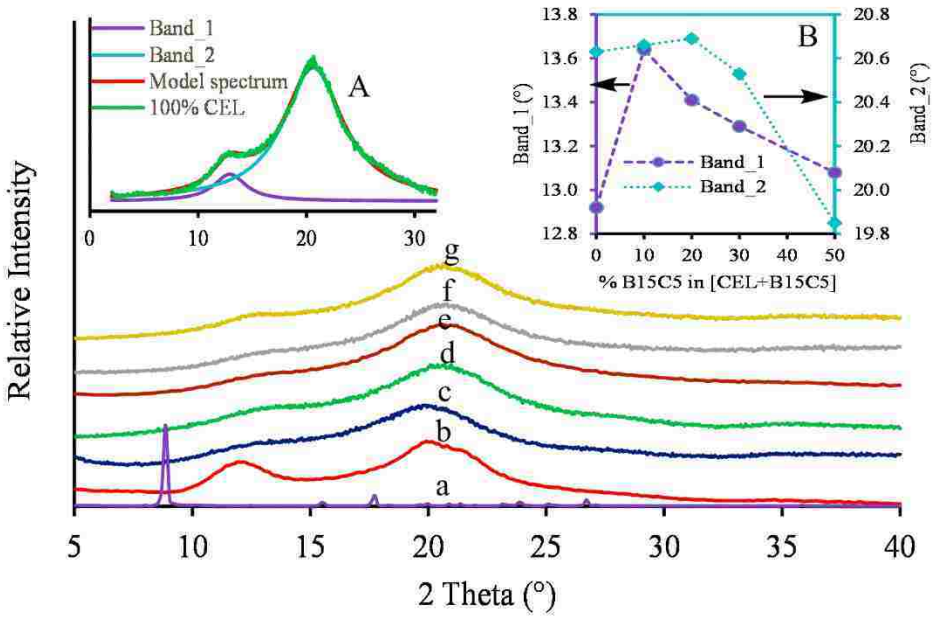

Figure 2-11 XRD spectra of (a) B15C5 powder, (b) 40:60, (c) 50:50, (d) 70:30, (e) 80:20, (f) 90:10 CEL:B15C5, and (g) 100% CEL. (A) Curve fitting for XRD spectrum of 100% CEL. (B) Plot of band positions 1, and 2 against the loading of B15C5 in [CEL+B15C5] composite films

XRD was also invaluable in revealing the structural transformations that take place as a result of blending these polysaccharides (CEL or CS) with crown ethers (B15C5, B18C6, DB15C5, and DB18C6). As illustrated in Figure 2-11, the XRD spectrum of B15C5 reveals a sharp band at 2θ=8.9° and several less intense peaks in the range 15-30° 2θ, which indicate that B15C5 exists in a highly crystalline state. Incorporation of B15C5 into CEL matrix led to some subtle changes in the crystal structure of CEL. These changes were best revealed by fitting two Lorentzian curves to the experimental XRD spectrum of regenerated CEL and [CEL+B15C5] composites (Figure 2-11A). It should be pointed out that attempts were made to fit data to the most widely used Gaussian line shapes resulted in poor fitting results than the Lorentzian line

shapes. For example, fitting the XRD spectrum of regenerated CEL to Gaussian line shapes yielded a coefficient of determination (R2) and chi square (χ2) values of 0.9770 and 2,276.9 respectively. On the other hand, using Lorentzian line shapes improved the R^2 and χ^2 values to 0.9954 and 450.2 respectively. As illustrated, the spectra could be deconvoluted into two bands, one major band at 20.6° and a minor band at 12.9° for 100% CEL. Incorporation of B15C5 in CEL shifted these bands towards smaller 2θ values. For examples; both 20.6° and 12.9° values shifted to 19.8° and 12.5° respectively when 50% B15C5 was incorporated in CEL matrix. The magnitude of the shift correlate positively with the proportional amount of B15C5 (Figure 2-11B). These results suggest that encapsulation of B15C5 causes some structural changes, albeit slightly, in [CEL+B15C5] composite. Since the 2θ values shifted towards smaller values, it can be reasonable to suggest that B15C5 intercalated between the CEL sheets during dissolution thereby pushing these sheets apart. The peaks for crystalline B15C5 disappeared upon encapsulation in CEL probably because the crystalline structure was destroyed or the instrument was not sensitive enough to detect B15C5. The [CS+B15C5] composites also showed the same trend (Figure 2-12).

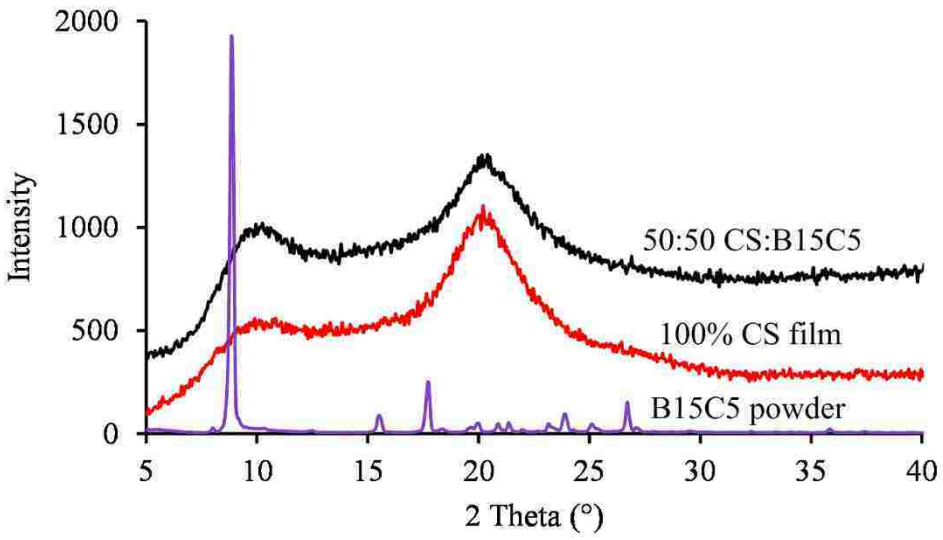

Figure 2-12 XRD spectra of 100% CS film (top spectrum), 50:50 CS:B15C5 (middle spectrum), and B15C5 powder (bottom spectrum).

XRD spectra of DB15C5, DB18C6 and B18C6 powders exhibit sharp bands which are similar to those bands in spectra of B15C5 (Figure 2-13). This indicates that these CRs exist as crystalline powders. After their incorporation in CS matrix, these bands disappear suggesting that their crystalline structures are destroyed. For a composite containing 60% DB18C6 and 40% CS, 40:60 CS:B18C6, the crystalline bands of DB18C6 can be observed suggesting that DB18C6 was still in its crystalline state.

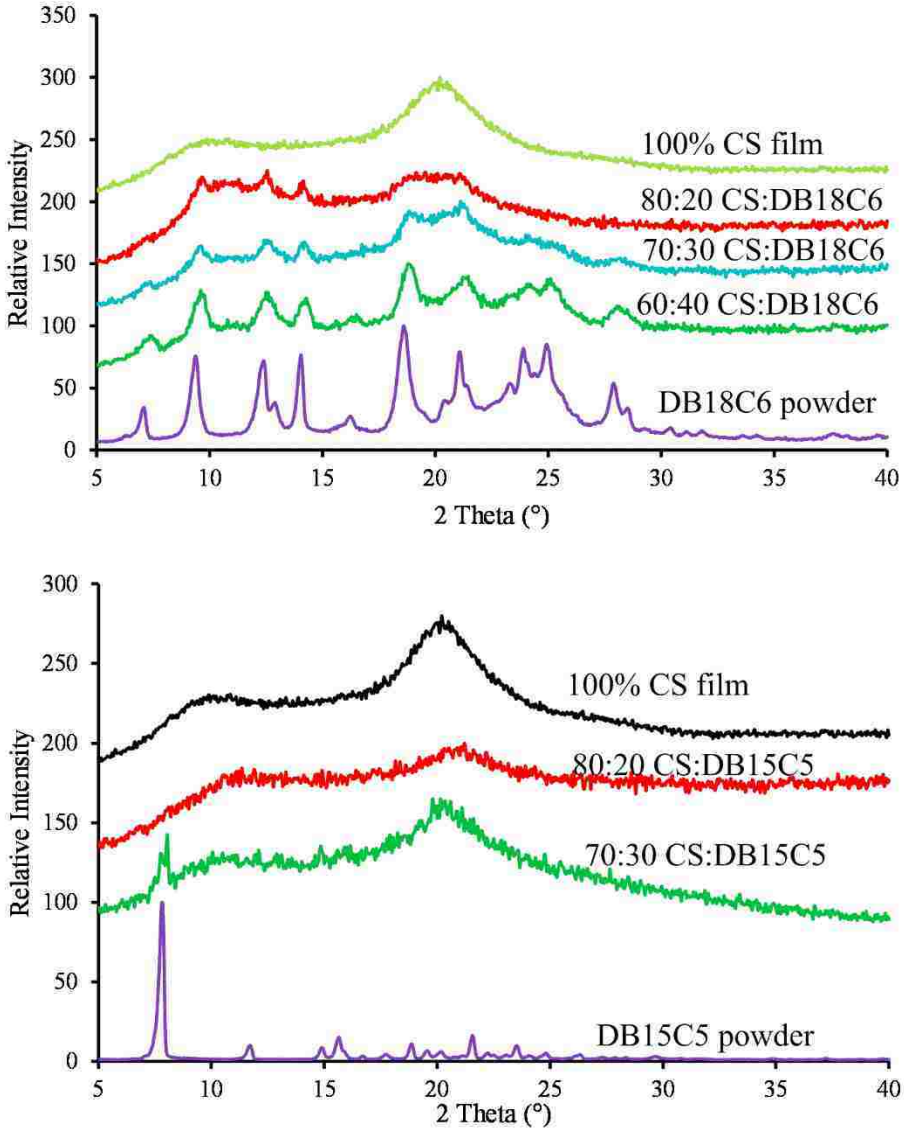

Figure 2-13 XRD spectra of (A) CS:DB18C6 composite films and (B) CS:DB15C5 composite films

2.4.2.4. Characterization by Scanning Electron Microscopy

We used SEM to investigate the texture and morphology of the composite materials, [CEL+B15C5] and [CS+B15C5]. The images shown in Figure 2-14 represent

the surface (four images in the first column) and cross sectional (four images in the second column) images of regenerated 100% CS, 100% CEL, and their respective composites with B15C5. Interestingly, the SEM images of 100% CS and 100% CEL exhibit different morphologies despite having similar chemical structures. While CS exhibits a smooth texture, CEL, on the other hand, exhibits a fibrous texture. Most importantly, their composites with B15C5 exhibit morphologies which are similar to those of CS (for 50:50 CS:B15C5) and CEL (for 50:50 CEL:B15C5). In addition, these images are homogeneous suggesting that the polysaccharides and B15C5 are compatible with each other. This compatibility could be due to favorable intermolecular interactions between CEL/CS and B15C5. These results corroborate XRD and FTIR results.

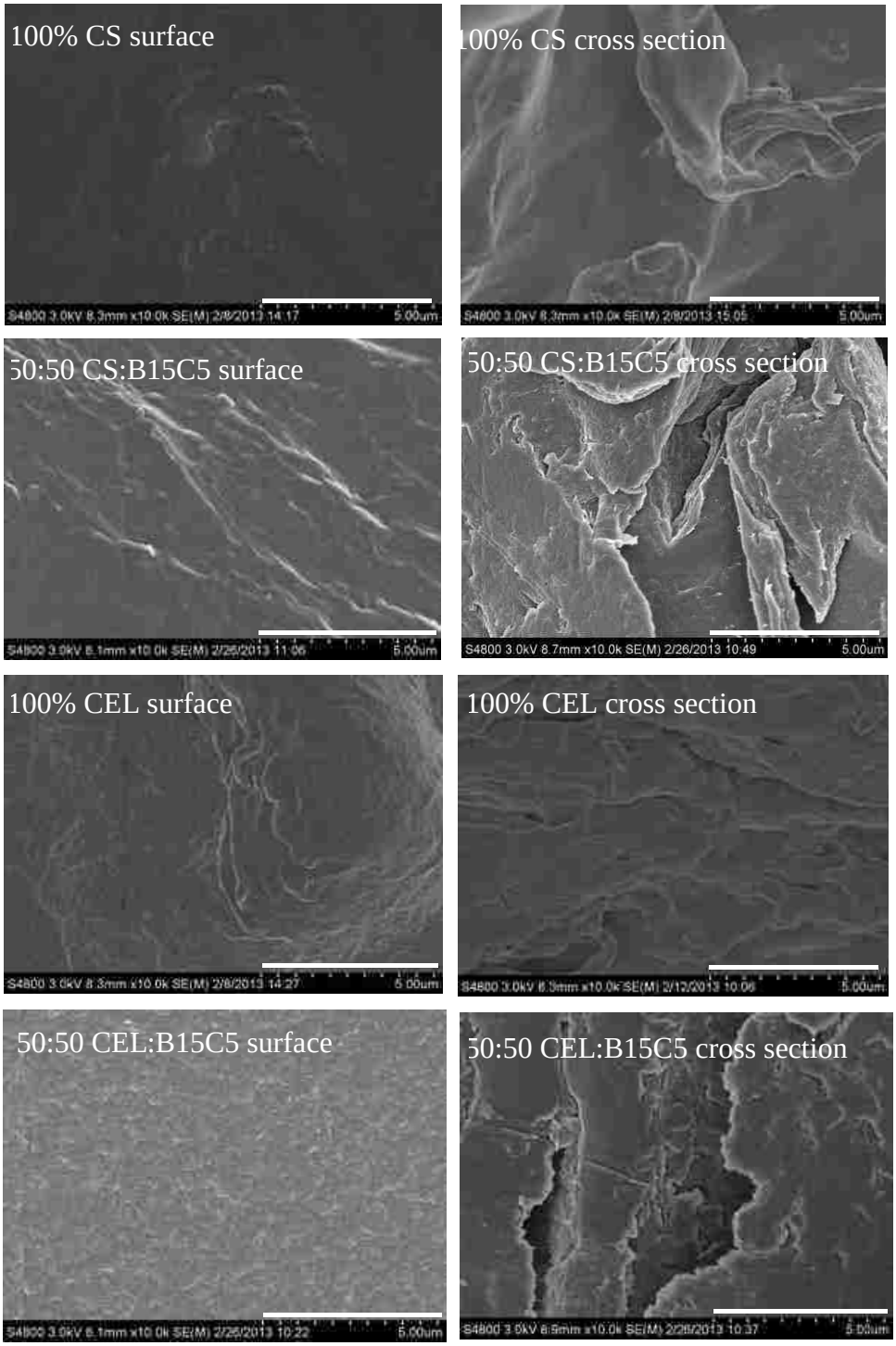

Figure 2-14 SEM images of surface (first column) and cross section (second column) of 100% CS (first row), 50:50 CS:B15C5 (second row), 100% CEL (third row) and 50:50 CEL:B15C5 (fourth row). The scale of the white bar is 5.00 μm.

2.4.2.5. Mechanical Properties of [CEL+B15C5], [CEL+CS] and [CS+B15C5]

We evaluated the mechanical properties of our composites because this property has implications for practical use. If the mechanical properties of the film are poor, it might be difficult to apply them for any practical use. As described earlier, both CS and B15C5 possess poor mechanical properties despite their remarkable potential in adsorbing both heavy metal ions and organic pollutants. Therefore, to improve their mechanical properties, they have to be blended with biopolymers which possess superior mechanical properties. Since CEL is known to possess superior mechanical properties, it is therefore expected that blending either CS or B15C5 with CEL would result in a composite with better mechanical properties, and the mechanical properties of the composite should correlate positively with the concentration of CEL. As illustrated in Figure 2-15, increasing the percentage loading of CEL in either [CEL+CS] or [CEL+B15C5] resulted in a concomitant increase in the tensile strength of the resultant composite. For example, adding 80% CEL to CS resulted in a 5X increase in the tensile strength of 80:20 CEL:CS (72±5 MPa) compared to that of 100% CS (12±4 MPa). Similarly, adding CEL to B15C5 increased the tensile strength of the resultant [CEL+B15C5] composite. However, it is worthwhile to mention that attempts to make [CEL+B15C5] composites containing less than 50% CEL were unsuccessful because the films were too weak to be used in any practical application. Therefore, only films containing at least 50% CEL were prepared. Adding 50% CEL to B15C5 resulted in a film composite with 29±5 MPa tensile strength. As more and more CEL was added to B15C5, the tensile strength increased. For example; the tensile strengths of [CEL+B15C5] composites containing 80% and 90% were found to be 47±5 MPa and

54±4 MPa respectively. The tensile strength of [CEL+CS] increased at a faster rate than that of [CEL+B15C5]. For example, increasing the concentration of CEL from 60% to 80% in [CEL+CS] and CEL+B15C5] resulted in a 74.4% and a 24% increase in tensile strength respectively. This can be rationalized by the similarity in chemical structures between CEL and CS than between CEL and B15C5. Essentially, the only difference between CEL and CS is that CS has an amine group at C-2 whilst the CEL has hydroxyl groups instead. These similar structures enable the formation of favorable intermolecular hydrogen bonding between CEL and CS than between CEL and B15C5 thus strengthening the resultant composite films in the former composite.

We also evaluated the tensile properties of film composites made from CS and B15C5, [CS+B15C5]. With its film forming capability, CS is expected to improve the mechanical properties of its composite with B15C5. Although there was some improvement in the mechanical properties of [CS+B15C5], these were very minor considering the effect caused by CEL. For example, 80:20 CS:B15C5 had a tensile strength of 26±5 MPa whilst 80:20 CEL:B15C5 had a tensile strength of 47±5 MPa. However, the combination of CS and B15C5 is expected to be superior in terms of

adsorption of both heavy metal ions and organic pollutants.

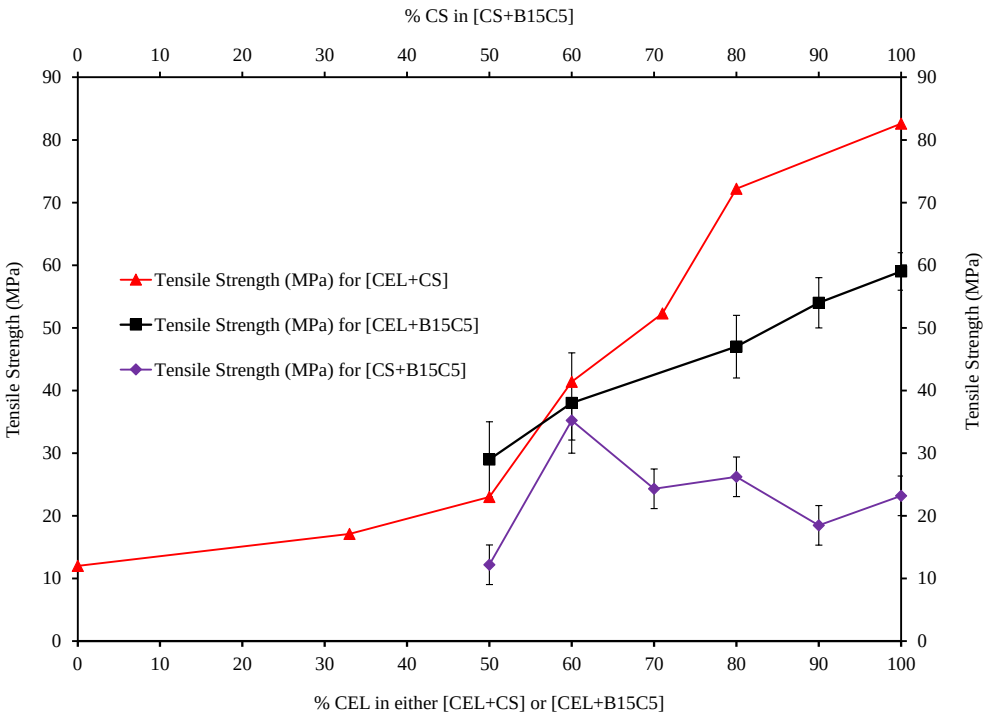

Figure 2-15 Tensile strength properties of [CEL+CS] (red triangles), [CEL+B15C5] (black squares), and [CS+B15C5] (purple diamonds).

In summary, XRD, UV Vis, FT-IR and SEM results presented clearly indicate that supramolecular composite materials containing various proportions of CEL, CS, and B15C5 were successfully synthesized using $BMIm^{+}Cl^{-}$ as the sole solvent. Since the majority of $BMIm^{+}Cl^{-}$ was recovered for reuse, this method is deemed to be recyclable. In addition, adding CEL to the composites substantially increased the mechanical properties of the corresponding composites. Since CEL has retained its superior mechanical properties even after its incorporation in [CEL+CS] and [CEL+B15C5], it is also expected that both CS and B15C5 may retain their desirable properties. Specifically,

composites containing either CS or B15C5 may be good adsorbents for organic and inorganic pollutants (from CS) and selectively form stable complexes with heavy metal ions (from B15C5). In the following sections, we present our investigations of the capability of these composites to adsorb heavy metal ions (Cd^{2+} and Zn^{2+}) and endocrine disruptor (3,4,5-trichlorophenol).

2.4.3. Applications of Composite Films

2.4.3.1. Effect of pH on the adsorption of heavy metal ions (Cd^{2+} and Zn^{2+}).

It is well known that pH is one of the important factors which affect chemical interactions between the binding of the adsorbent and the adsorbate. Experiments were designed to investigate the effect of pH on the adsorption of heavy metal ions. It was not possible to investigate the entire range of pHs, because of limitations on samples. For example, in our preliminary studies, we found out that [CS+B15C5] and 100% CS were unstable in acidic conditions. Specifically, 100% CS and [CS+B15C5] films dissolved completely in solutions of pH 2.0. This is hardly surprising since CS possess amine groups which can easily get protonated and therefore become soluble at this pH. On the other hand, Cd (II) and Zn(II) solutions formed precipitates at pH 8.5 and 7.6 respectively. In addition, although initially the solutions of Cd(II) and Zn(II) at pH 8.0 and 7.1 respectively appeared to be stable, they formed precipitates during the measurements. As a result of these limitations, we carried out our investigations at pH 3.9 and 6.0 (for Cd^{2+}) and pH 1.9 and 6.0 (for Zn^{2+}). We used 50:50 CS:B15C5 sample for adsorption of Cd^{2+} and 50:50 CEL:B15C5 for adsorption of Zn^{2+}. After fitting data to pseudo second order, q_e values were obtained. The rationale for using pseudo second

order model was based on better coefficient of determination (R^2) and MSC values than pseudo first order model fitting *(vide infra)*. Specifically, pseudo first order fits gave R^2 and MSC values in the range 0.7481-0.9937 and 0.0453-4.4040 respectively. However, pseudo second order fits gave higher values of both R^2 and MSC which were in the range 0.9831-0.9998 and 3.6573-7.7901 respectively. It was found that adsorbent efficiency of these composite films were more superior at pH 6.0 than at lower pHs (i.e. pH 3.9 for [CS+B15C5] and pH 1.9 for [CEL+B15C5]). Specifically, whereas [CS+B15C5] adsorbed 363±10 µmol Cd^{2+} per g of film at pH 6.0, the same film adsorbed only 112±6 µmol of Cd^{2+} per g of film at pH 3.9. The film containing 50:50 CEL:B15C5 adsorbed 233±6 µmol Zn^{2+} per g film at pH 6.0. However, reducing the pH of Zn (II) solution to 1.9 decreased the q_e value to 40.6±0.2 µmol Zn^{2+} per g of film. This may be due to the fact that CS has a pKa value of 6.4, and thus at lower pHs (3.9 in this case), most of the amine groups are protonated thereby inhibiting the interactions between these amine groups and the metal ions. In addition, the oxygen atoms in B15C5 are probably coordinated to protons at lower pH leading to a subdued adsorption performance. Furthermore, the hydroxyl groups in CEL may also be protonated in the acidic solution. In view of these results, we conducted all subsequent experiments at pH 6.0 for the adsorption of either Cd^{2+} or Zn^{2+}.

2.4.3.2. Kinetics of adsorption of cadmium (II) ions

The adsorption of Cd^{2+} at various time points were calculated using the mass balance equation (Eq. 2.15) and the results were then graphed. Typical results of such plots are shown in Figure 2-16, Figure 2-17, and Figure 2-18. As illustrated, all the series follow the same general trend. Essentially, these series can be subdivided into three

regions; the region when the rate of adsorption appears to be constant, followed by a slowdown in the rate of adsorption and lastly a region where there is no change in the amount adsorbed. These results suggest that these composite films indeed adsorb Cd^{2+}. This was also the case with adsorption of Zn^{2+} (*vide infra*). To precisely compare the efficiency of these composites towards the adsorption of Cd^{2+} (and Zn^{2+}), these kinetics data were then fitted to both pseudo first order and pseudo second order models. Goodness of fit of these models were determined based on the values of coefficient of determination, R^2 and model selection criteria, MSC. These analyses resulted in q_e values, k_1 value for pseudo first order, k_2 for pseudo second order models, R^2 and MSC values for both of these models (Table 2-1). In all cases, both R^2 and MSC values were higher for pseudo second order than for pseudo first order model. This suggests that pseudo second order model describe well the kinetics of adsorption of Cd^{2+} onto the composites investigated in this study. This was also the same case with the adsorption of Zn^{2+} and 2,4,5-TCP.

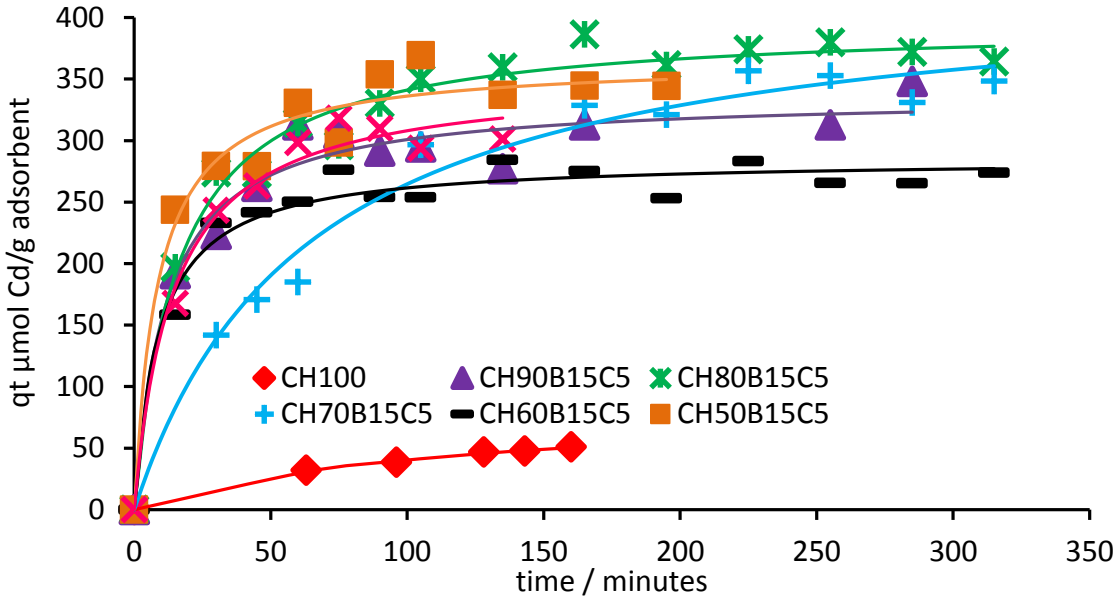

Figure 2-16 Non-linear Pseudo second order fitting for kinetics of Cd^{2+} adsorption onto composite films containing various proportions of CS and B15C5.

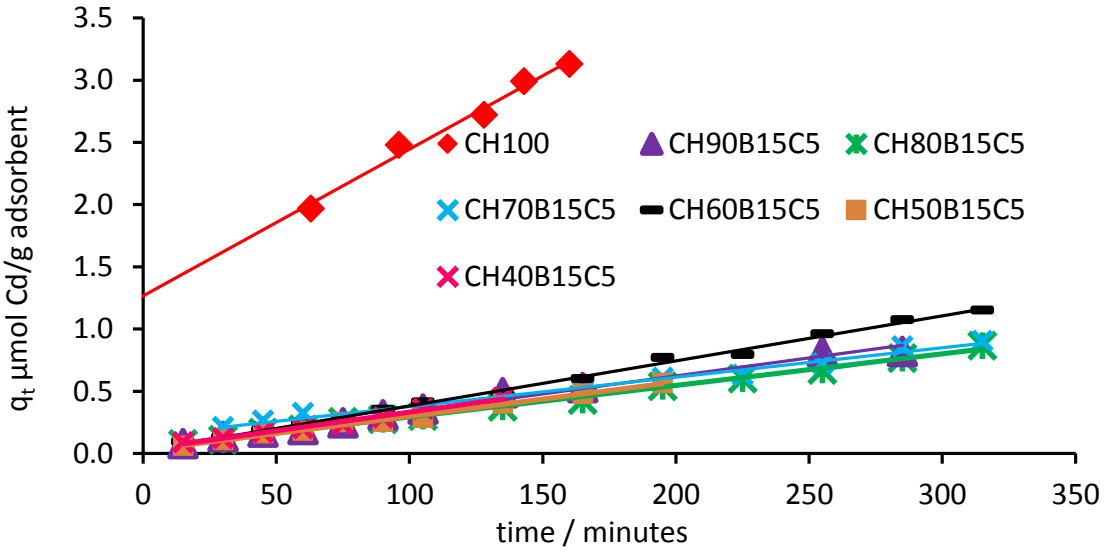

Figure 2-17 Linear Pseudo second order fitting for kinetics of Cd^{2+} adsorption onto composite films containing various proportions of CS and B15C5.

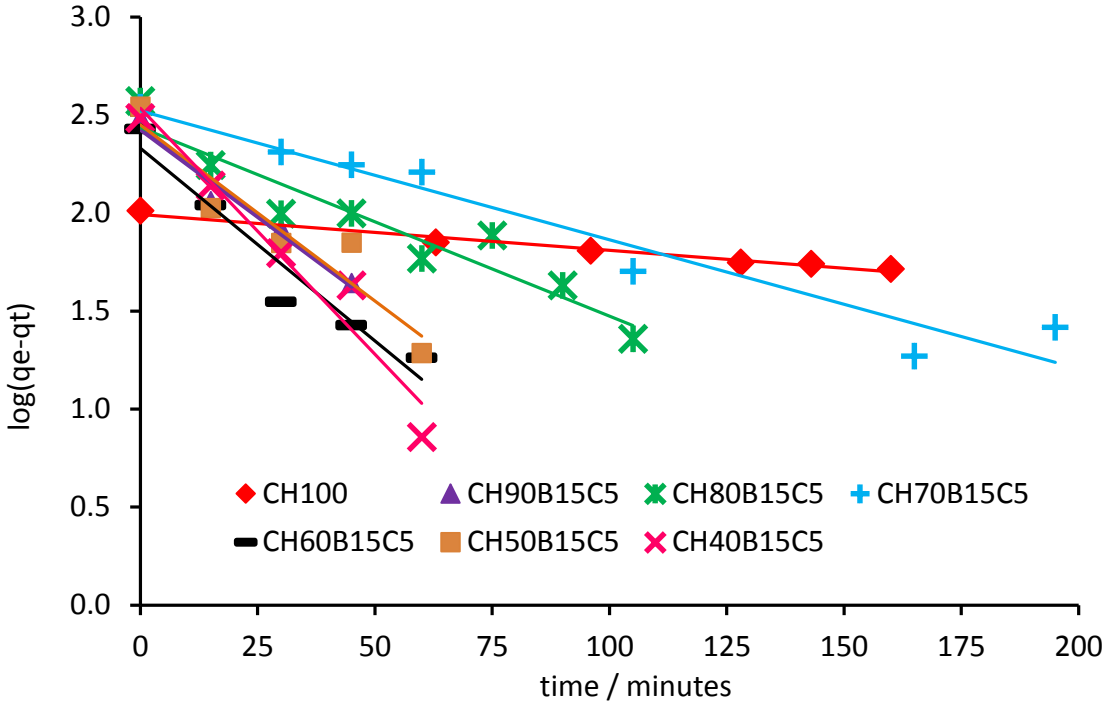

Figure 2-18 Linear Pseudo first order fitting for kinetics of adsorption onto composite films containing various proportions of CS and B15C5.

Table 2-1 Kinetic Parameters for Adsorption of Cadmium onto CS100, [CS+B15C5], [CEL+B15C5] and [CS+CEL].

% Component			Pseudo First-Order Kinetic Model					Pseudo Second-Order Model			
CS	CEL	B15C5	q_e, expt (µmol/g)	q_e, calc (µmol/g)	$K_1 *10^3$ (min^{-1})	R^2	MSC	q_e, calc (µmol/g)	K_2 (g.µmol min^{-1})	R^2	MSC
100			104	98±4	4.2±0.4	0.9729	2.9496	104±4	0.058±0.004	0.9971	4.8337
90		10	306	270±40	41±6	0.9612	2.2493	345±10	0.19±0.06	0.9887	4.1225
80		20	373	270±50	22±3	0.9075	1.8804	394±7	0.16±0.03	0.9966	5.3963
70		30	347	330±60	15±2	0.9420	2.2754	423±20	0.040±0.006	0.9831	3.6573
60		40	268	210±50	45±7	0.9362	1.9520	436±10	0.062±0.008	0.9926	4.6257
50		50	350	280±90	41±8	0.8923	1.4282	363±10	0.3±0.1	0.9922	4.4585
40		60	306	300±100	58±8	0.9445	2.0910	333±10	0.29±0.09	0.9891	5.1487
	90	10	121	122±8	4.3±0.2	0.9910	4.2668	142±4	0.037±0.004	0.9923	4.4713
	80	20	169	178±9	6.9±0.3	0.9937	4.4040	179±7	0.07±0.02	0.9899	4.1533
	70	30	114	100±30	12±1	0.9699	2.5037	115±5	0.4±0.7	0.9921	4.2075
	60	40	47	36±5	1.7±0.2	0.9397	2.1419	48±1	0.15±0.02	0.9985	5.7204
	50	50	22	17±10	30±20	0.7481	0.0453	22.8±0.2	4±1	0.9998	7.7901

We, therefore used pseudo second order fitting results to evaluate the adsorption performance of each of 100% CS, 100% CEL, [CEL+CS], [CEL+B15C5], [CS+B15C5] and [CS+CEL+B15C5] composites. This was achieved by comparing the q_e values obtained from this pseudo second order model fitting. As expected, 100% CS adsorbs up to 104±4 µmol Cd^{2+} per g of film. This may be due to the presence of amine groups which can form complexes with the heavy metal ions. Specifically, the lone pairs on nitrogen atom on ammine group interact via dative bonding with the positive charge on Cd^{2+}. Conversely, 100% CEL could barely adsorb any Cd^{2+}. These results can be rationalized by invoking the hard-soft acid-base (HSAB) theory. This theory suggests that soft acids tend to form stronger complexes with soft bases, and hard acids interact more strongly with hard bases. In this particular case, Cd (II) is considered to be a soft acid. Whereas nitrogen (on $–NH_2$) is considered to be a soft base, oxygen (on –OH of CEL) is considered to be a hard base. Accordingly, Cd (II) is expected to form stronger complexes with amine groups (on CS) than hydroxyl groups (on CEL) thereby explaining the higher q_e value of CS than the q_e value for CEL.

Table 2-2 Equilibrium sorption capacity (q_e) values for adsorption of Cd^{2+} onto [CEL+CS], [CEL+B15C5], [CS+B15C5] and [CS+CEL+B15C5] composites as determined by pseudo second order fitting to kinetics data.

Cellulose	Chitosan	B15C5	Cadmium
			q_e *10^6 mol g^{-1}
100			Not detected
80	**20**		23.0±0.2
71	**29**		98±3
60	**40**		110±10
50	**50**		91±4
20	**80**		110±6
	100		104±4
90		**10**	142±4
80		**20**	179±7
70		**30**	115±5
60		**40**	48±1
50		**50**	22.8±0.2
	90	**10**	345±10
	80	**20**	394±7
	70	**30**	423±20
	60	**40**	436±10
	50	**50**	363±10
	40	**60**	333±10
30	**20**	**50**	250±4
20	**50**	**30**	245±4
35	**35**	**30**	342±8
50	**20**	**30**	161±2

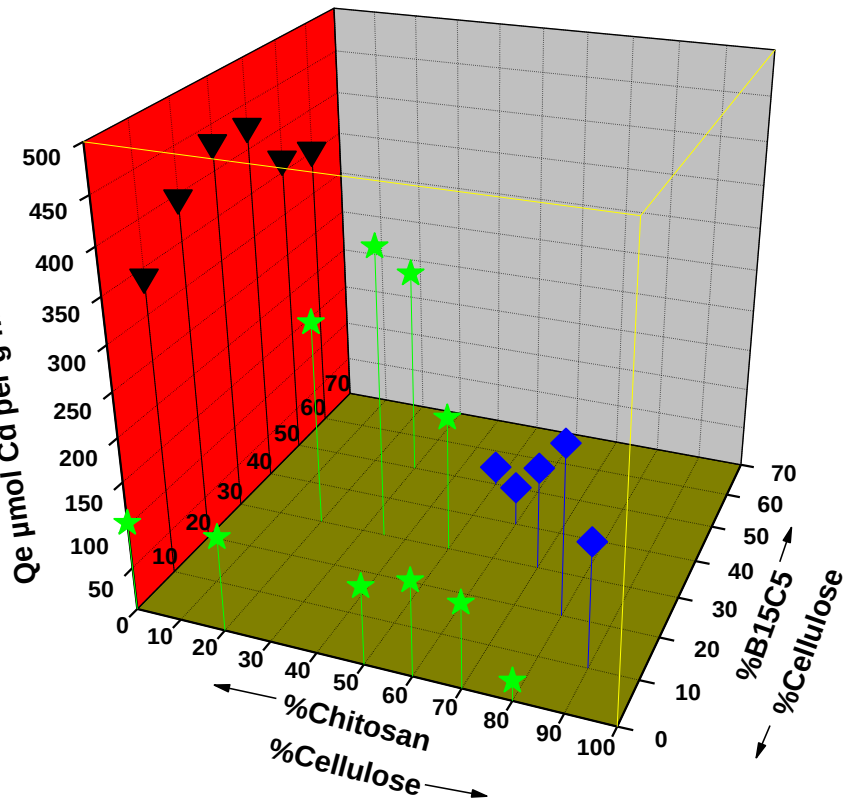

Figure 2-19 3D plot of the amount of Cd^{2+} adsorbed at equilibrium (q_e) as a function of CEL, CS, and B15C5 loading in [CEL+CS], [CEL+B15C5], [CS+B15C5] and [CS+CEL+B15C5] composites. This plot was generated using q_e values obtained by pseudo second order fitting in Table 2-2.

The data in Table 2-2 was then used to construct a 3D graph in order to see clearly the effect of composition of films on the amount of Cd^{2+} adsorbed at equilibrium, q_e. Specifically, q_e was plotted as a function of the composition of [CS+B15C5], [CS+CEL] and [CEL+B15C5] films (Figure 2-19). As illustrated, adding B15C5 to CS substantially increased the adsorption efficiency of the resultant [CS+B15C5] composite films. For example, adding just 10% B15C5 to CS enhanced the q_e value by at least 3X

compared to the q_e value for 100% CS (q_e values for 90:10 CS:B15C5 and 100% CS were found to be 345±10 µmol per g film and 104±4 µmol per g film respectively). This enhancement suggests that B15C5 retains its desirable selective complexation properties even after being encapsulated in the biopolymer matrix. This trend was maintained until it peaked at 436±10 µmol per g [CS+B15C5] when 40% B15C5 was added to CS (i.e. 60:40 CS:B15C5 film). Beyond this level of B15C5 concentration, the efficiency decreased but still remained substantially higher than the efficiency of 100% CS. For example, the lowest q_e value of 333±10 µmol per g film was obtained with 40:60 CS:B15C5 composite film which is at least 3X higher than the q_e value obtained with 100% CS. The decrease in efficiency can be attributed to the poor rheological properties of [CS+B15C5] at higher B15C5 loading. This is corroborated by poor mechanical properties of [CS+B15C5] at B15C5 loading of at least 50%. For example, 50:50 CS:B15C5 had the lowest tensile strength. In addition, the tensile strength of 60:40 CS:B15C5 was too low to be measured precisely.

The effect of B15C5 was also observed in [CEL+B15C5] composite films. Although CEL by itself could barely adsorb any Cd^{2+}, addition of B15C5 to this biopolymer substantially enhanced the efficiency of adsorption of this pollutant. For example, adding 10% B15C5 to CEL resulted in adsorption of up to 142±4 µmol Cd^{2+} per g of film. Interestingly, the effect of B15C5 was more than that of CS. For example, [CEL+B15C5] containing 20% B15C5 adsorbed up to 179±7 µmol Cd^{2+} per g of film. This is at least 7X higher than the amount adsorbed by one g of [CS+CEL] composite film containing 20% CS. Although CS contain softer ligands (from amine groups) than B15C5 (from oxygen atoms), the chelate effect seems to have greater effect than the

HSAB effect. This is hardly surprising because compared to CS, B15C5 has 5 oxygen atoms which can form relatively more stable complexes with Cd(II) ions. However, at higher B15C5 loading in CEL (i.e. 50% and 60%), the efficiency of [CEL+B15C5] became inferior to that of [CS+CEL] containing an equivalent composition (i.e. 50% and 60% CS). For example, one g of 40:60 CS:CEL adsorbed almost 2.3X more Cd^{2+} than that adsorbed by an equivalent weight of 40:60 B15C5:CEL (Table 2-2). This may be due to the poorer mechanical properties of [CEL+B15C5] than those of [CS+CEL] composites.

Interestingly, CS and B15C5 exhibited synergistic adsorption of Cd^{2+} from water. This was confirmed by comparing the q_e values of [CS+B15C5] with the algebraic sum of q_e values of [CS+CEL] and [CEL+B15C5]. This was because 100% CEL was found to not adsorb any Cd^{2+}. Thus, any adsorption of Cd^{2+} by [CS+CEL] and [CEL+B15C5] composites was attributed solely to CS and B15C5 respectively. For example, one g of 80:20 CS:CEL and one g of 80:20 CEL:B15C5 adsorbed 110±6 µmol and 179±7 µmol Cd^{2+} respectively. The algebraic sum of these q_e values (i.e. 289±9 µmol) is expected to be equal to the amount adsorbed by 80:20 CS:B15C5 if these two components CS and B15C5 contribute independently towards the adsorption of this pollutant. However, the q_e value for 80:20 CS:B15C5 was found to be 394±7 µmol Cd^{2+} which is substantially higher than the predicted q_e value based on the algebraic sum (i.e. 289±9 µmol). Similarly, a q_e value of 363±10 µmol found for 50:50 CS:B15C5 is at least 3X higher than the predicted 113.8±4 µmol (obtained by adding 22.8±0.2 µmol and 91±4 µmol for 50:50 CEL:B15C5 and 50:50 CS:CEL respectively). Essentially, all [CS+B15C5] composites adsorbed much higher-than-predicted amounts of Cd^{2+}. These results suggest

that CS and B15C5 interact synergistically to adsorb much higher amounts of Cd^{2+}. It is highly likely that Cd^{2+} might form a 'perched' complex with B15C5 ligand. Specifically, Cd^{2+} is slightly raised above the plane formed by the five oxygen atoms of B15C5 and coordinate to them through dative bonding. Then, nitrogen atom of the amino group of CS coordinates this same Cd (II) ion from the top thus forming a pseudo octahedral structure. Such complexes are known to be more stable than the complexes formed through either coordination to five oxygen atoms of B15C5 or coordination with only amino groups of CS.

An ideal composite is expected to possess properties such as higher adsorption and good mechanical properties. To package these properties into one composite, we synthesized three-component composites containing various relative amounts of CEL, CS and B15C5. We expected that the resultant composite would possess superior mechanical properties (from CEL) and synergistic adsorption of heavy metal ions (Cd^{2+}). The results of adsorption of this metal ion by such composites are presented in Table 2-2. Although these composites adsorbed less Cd^{2+} than adsorbed by [CS+B15C5], these amounts are still satisfactory for practical use. For example, one g of 35:35:30 CS:CEL:B15C5 could adsorb up to 342±8 μmol Cd^{2+} which is similar to 345±10 μmol adsorbed by an equivalent weight of 90:10 CS:B15C5. These results further reaffirm that the desirable properties of the constituents of these composite films are retained even after blending them together.

Table 2-3 Equilibrium sorption capacity (q_e) values for adsorption of Cd^{2+} onto [CS+B15C5], [CS+DB15C5], [CS+B18C6], and [CS+DB18C6] composite films.

Chitosan	B15C5	DB15C5	B18C6	DB18C6	qe µmol/g	K *10³	R^2	MSC	% Adsorbed
90		**10**			285±9	0.065±0.006	0.9937	4.4950	12.8
70		**30**			195±6	0.08±0.01	0.9953	4.7812	8.76
60		**40**			294±7	0.18±0.03	0.9976	5.3609	13.2
40				**60**	26.5±0.6	2.3±0.3	0.9976	5.3827	1.19
50				**50**	460±10	0.020±0.003	0.9888	4.2692	20.47
70				**30**	85±2	0.16±0.02	0.9971	5.3868	3.82
50			**50**		114.0±0.7	0.8±0.2	0.9994	7.2486	5.12
60			**40**		359±4	0.053±0.004	0.9970	5.6719	16.16
70			**30**		306±4	0.08±0.01	0.9969	5.5670	13.75
90	**10**				345±10	0.19±0.06	0.9887	4.1225	15.52
70	**30**				423±20	0.040±0.006	0.9839	3.6573	19.02
60	**40**				436±10	0.062±0.008	0.9926	4.6257	19.59
50	**50**				363±10	0.3±0.1	0.9922	4.4585	16.34
40	**60**				333±10	0.29±0.09	0.9891	5.1487	14.98

Attempts were also made to compare the effects of other crown ethers (i.e. DB15C5, DB18C6, B18C6) in the adsorption of cadmium ions. The results, as determined by fitting kinetics data to pseudo second order model are presented in Table 2-3. As illustrated, CS-based composites containing B15C5 adsorbed the highest amounts of Cd^{2+} as compared to those containing the other crown ethers. This can be rationalized by considering the cavity sizes of these crown ethers. Whereas B15C5 and DB15C5 have the same cavity size of 1.7-2.2 Å, B18C6 and DB18C6 both have a cavity size of 2.6-3.2 Å.[75] Since the size of Cd^{2+} (1.94 Å)[76] closely matches the size of both B15C5 and DB15C5, it is expected that more stable complexes are formed between this ion and these crowns. This is why all composites containing B15C5 adsorbed more Cd^{2+} than composites containing 18C6-based crown ethers. For example, 70:30 CS:B15C5 adsorbed up to 423±20 µmol Cd^{2+} which is substantially higher than the 306±4 µmol adsorbed by 70:30 CS:B18C6 composite. Similarly, 70:30 CS:DB15C5 adsorbed 195±6 µmol which is also substantially higher than 85±2 µmol Cd^{2+} adsorbed by 70:30 CS:DB18C6. In addition, the number of substituents attached to the crown ring had an effect on the efficiency of adsorption. Essentially, for similar crown ring sizes, all singly benzo-substituted CR-based composites adsorbed more Cd^{2+} than the Cd^{2+} adsorbed by dibenzo-substituted composites. For example, whilst 90:10 CS:B15C5 adsorbed 345±10 µmol, 90:10 CS:DB15C5 adsorbed only 285±9 µmol Cd^{2+} per g of film. These results suggest that, in addition to the crown ring size, other factors such as substituent effects also affect the adsorption efficiency of these CR-based composites. The phenyl group is known to decrease the electron density on ethereal oxygen atoms in crown ring thereby weakening the interactions between the crown ether and the metal ion. Thus, this

deactivating effect is expected to be more pronounced in dibenzo-crown ether than in benzo-crown ether of similar crown ring size. In addition, the benzo groups reduce the flexibility of the crown ether ring. Thus, the size of benzo-crown ether is expected to adjust slightly to accommodate the metal ion whereas the size of dibenzo-crown ether is expected to remain fixed.

2.4.3.3.Kinetics of adsorption zinc (II) ions

After showing that our composites could adsorb Cd^{2+}, we extended their applications by investigating their capability to adsorb another heavy metal ion, Zn^{2+}. Similarly to the fitting of kinetics of adsorption of Cd^{2+}, kinetics of adsorption of Zn^{2+} fitted well to the pseudo second order model (Table 2-4). Thus, we used q_e values obtained by fitting data to this model to compare the efficiencies of the composite films. Interestingly, while 100% CEL could not adsorb any Cd^{2+}, it could adsorb up to 46±1 µmol Zn^{2+} per g of film. On the other hand, 100% CS adsorbed more Cd^{2+} than Zn^{2+}. This is hardly surprising because Zn is a harder acid than Cd. Thus, the harder oxygen atoms on hydroxyl groups on CEL interact more favorably with Zn than with Cd.

Interestingly, [CEL+B15C5] also exhibited some level of synergistic adsorption of Zn (II) ions. For example, one g of 100% CEL and 50:50 CS:B15C5 adsorbed 46±1 and 123±3 µmol Zn^{2+} respectively. Thus, 50:50 CEL:B15C5 is expected to adsorb 169±3 µmol (= (46±1)+(123±3)) of Zn^{2+}. However, it turns out that this composite film could adsorb a substantially higher amount of Zn (II) (i.e. 233±6 µmol) than this predicted amount. Furthermore, [CS+CEL] composites also exhibited synergy in adsorbing Zn^{2+}. For example, q_e value for 50:50 CS:CEL was found to be 178±4 µmol which is much higher than the 46±1 µmol which is adsorbed by 100% CEL, assuming that CS does not

adsorb any Zn^{2+}. All these observations can be rationalized by the hard soft acid base theory.

Table 2-4 Kinetic parameters for adsorption of Zn^{2+} onto [CEL+B15C5], [CS+B15C5], and [CS+CEL] composite films.

% Component				Pseudo First-Order Kinetic Model				Pseudo Second-Order Model			
CS	CEL	B15C5	q_e, expt (µmol/g)	q_e, calc (µmol/g)	$K_1 *10^3$ (min^{-1})	R^2	MSC	q_e, calc (µmol/g)	K (g.µmol min^{-1})	R^2	MSC
70		30	156	80±60	3.2±0.8	0.7845	0.8680	157±5	0.4±0.6	0.9941	4.6338
50		50	120	90±20	11±2	0.8997	1.6326	123±3	0.3±0.2	0.9952	4.8432
	100		45.6	20±8	2.5±0.7	0.7728	0.8152	46±1	0.6±0.2	0.9983	5.7102
50	50		165	130±70	4.2±0.9	0.7842	1.0333	178±4	0.05±0.01	0.9928	4.3614
67	33		208	200±40	9.1±0.9	0.9518	2.4611	239±8	0.041±0.005	0.9950	4.7255
70	30		179	160±10	16±1	0.9635	2.9473	186±3	0.16±0.02	0.9962	5.2741
30	70		341	360±70	25±3	0.9287	2.1415	349±5	0.2±0.1	0.9973	5.6424
	50	50	211	180±33	4.0±0.5	0.9383	2.1187	233±6	0.035±0.006	0.9956	4.9386
	70	30	43.6	34±4	19±2	0.9684	2.7872	45.0±0.3	1.2±0.1	0.9998	7.9132
40		60	197	90±30	1.5±0.4	0.5996	0.4709	190±9	0.3±0.1	0.9715	3.4745

2.4.3.4.Adsorption isotherm results

Figure 2-20A, B, and C report the plots of C_e/q_e versus C_e, $\log q_e$ versus $\log C_e$ and $\ln q_e$ versus ε^2 for Langmuir, Freundlich and D-R isotherms respectively. As illustrated in this Figure 2-20 and Table 2-5, equilibrium data for Cd (II) adsorption onto both composites, 100% Cs and 50:50 CS:B15C5, fit very well to each of the three isotherm models with the coefficients of determination lying in the range 0.9165 to 0.9958. Langmuir model fitted better to the adsorption of Cd (II) onto 100% CS (R^2 = 0.9922) than adsorption onto 50:50 CS:B15C5 (R^2 = 0.9165). This is expected because 100% CS is composed of one adsorbing component whereas 50:50 CS:B15C5 is composed of two adsorbing components, CS and B15C5. Therefore, we expect the surface sites on 100% CS to exhibit equal adsorption affinity towards Cd (II) ions. The values of R_L for Langmuir fitting to adsorption of Cd (II) onto both 100% CS (R_L =0.6±0.2) and 50:50 CS:B15C5 (R_L =0.7±0.1) lie between zero and one suggesting favorable adsorption processes. Further insight could be obtained from the values of n from Freundlich fittings. As shown in Table 2-5, n =1.4±0.1 for adsorption of Cd (II) onto each of the composite films, 100% CS and 50:50 CS:B15C5. This suggests that Cd (II) is adsorbed through physical interactions with the adsorbent sites. However, both Langmuir and Freundlich isotherm models cannot give an insight into the mechanism of adsorption. The mechanism can be obtained from D-R model fitting. From this model, the value of mean free energy, E, helps to distinguish between chemisorb and physisorb. This mean free energy can be calculated using the relation: $E = (2\beta)^{-0.5}$.[21] Mean free energy is basically the energy required to overcome the attractive force between the

adsorbate species and the adsorbent site. A value of *E* lying between 8 and 16 kJ/mol is indicative of chemisorb whilst a value of *E* lying below 8 kJ/mol is indicative of physisorb.[77] As illustrated in Table 2-5, *E* values are below 8 kJ/mol for adsorption of Cd (II) onto 100% CS (6.8±0.1 kJ/mol) and 50:50 CS:B15C5 (6.5±0.5 kJ/mol) suggesting that the adsorption was physisorb in both cases.

Table 2-5 Langmuir, Freundlich and Dubinin-Radushkevich isotherm parameters for adsorption of Cd^{2+} onto 100% CS and 50:50 CS:B15C5 composite films

Langmuir isotherm			
	q_{max}(µmol/g)	K_L (L/µmol)	R^2
100% CS	800±40	101±6	0.9922
50:50 CS:B15C5	2,200±300	52±9	0.9165
Freundlich isotherm			
	n	K_F (mol/g)(L/mol)$^{1/n}$	R^2
100% CS	1.4±0.1	10.3±0.3	0.9752
50:50 CS:B15C5	1.4±0.1	20±5	0.9773
Dubinin-Radushkevich isotherm			
	q_{max}(µmol/g)	E (kJ/mol)	R^2
100% CS	1,700±100	6.8±0.1	0.9958
50:50 CS:B15C5	3,500±600	6.5±0.5	0.9697

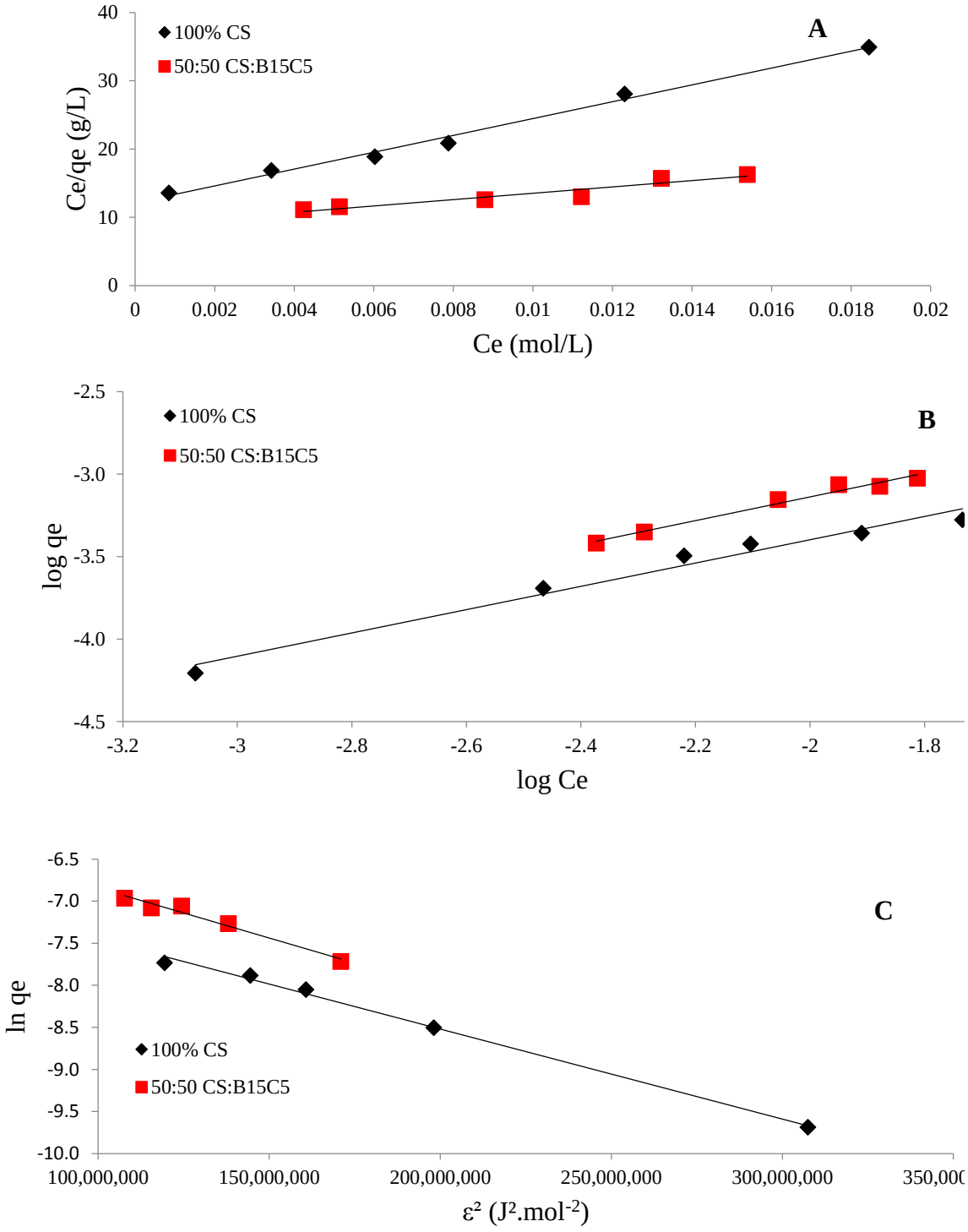

Figure 2-20 Langmuir (A), Freundlich (B) and Dubinin-Radushkevich (C) isotherms for the adsorption of Cd^{2+} onto 100% CS (black diamonds) and 50:50 CS:B15C5 (red squares).

2.4.3.5. Kinetics of adsorption of 2,4,5-trichlophenol, an endocrine disruptor

Endocrine disruptors such as chlorophenols are ubiquitous in wastewaters due to their use in agriculture as biocides. They adversely interfere with the normal functioning of the hormonal systems of mammals. They are eventually washed into waterways during rain. Thus, there is need to design better adsorbents for these toxic substances. In this study, we sought to widen the applications of our composite films by exploring their adsorption capacity towards 2,4,5-trichlorophenol. As was the case with the heavy metal ions (Cd^{2+} and Zn^{2+}), pseudo second order model appears to describe the kinetics of adsorption of 2,4,5-TCP better than pseudo first order model. Thus, it is plausible to use CS-based composites to adsorb 2,4,5-TCP. As shown in the Table 2-6, 100% CS adsorbed up to 32.3±0.2 μmol per g of film. Reducing CS content in the composites led to a reduction in the amount of 2,4,5-TCP adsorbed. For example, adding 80% CEL to CS led to an almost 6X reduction in the amount of 2,4,5-TCP adsorbed per g of film. Essentially, the amount of 2,4,5-TCP adsorbed by these composites correlates positively with CS loading in the composite. Furthermore, adding B15C5 to the composites does not seem to have any effect on the adsorption of this organic pollutant. For example, 50:20:30 CS:CEL:B15C5 adsorbed up to 23.75±0.09 μmol of 2,4,5-TCP which is similar to 24.76±0.07 μmol which is adsorbed by 50:50 CS:CEL. Similarly, 20:30:50 CS:CEL:B15C5 adsorbed 16.1±0.1 μmol 2,4,5-TCP which is similar to 14.34±0.03 μmol adsorbed by 20:80 CS:CEL. These results clearly suggest that the adsorption of the organic pollutant is due solely to CS. These results are hardly suprising because 2,4,5-TCP is known to interact with CS through amino groups.[45] Since CEL and B15C5 lack these groups, they may not form any complexes with these species.

Table 2-6 Equilibrium sorption capacity (qe) values for adsorption of 2,4,5-TCP onto [CS+CEL], [CS+B15C5], [CEL+B15C5] and [CS+CEL+B15C5] composite films.

Cellulose	Chitosan	B15C5	2,4,5-TCP
			q_e *10^6 mol g^{-1}
100			5.40±0.08
80	**20**		14.34±0.03
71	**29**		15.09±0.02
60	**40**		21.68±0.06
50	**50**		24.76±0.07
33	**67**		27.0±0.2
40		**60**	5.97±0.03
	100		32.3±0.2
30	**20**	**50**	16.1±0.1
20	**50**	**30**	23.75±0.09

2.4.3.6. Intra-particle diffusion model

We applied intra-particle diffusion modeling to our adsorption kinetics data to gain more insights into the mechanism of adsorption of these heavy metal ions (Cd^{2+} and Zn^{2+}) and organic pollutant (2,4,5-TCP). The results are presented in Table 2-7 and graphs of q_t against $t^{0.5}$ are presented in Figure 2-21. Generally, there are two stages of adsorption for each of the three adsorbate species. The first linear portion corresponds to the earlier stage when the adsorbate species are rapidly transported to the surface of the adsorbent where they instantaneously get adsorbed onto the available adsorption sites. This stage is characterized by a rate constant, $k_{ip,1}$. Subsequent to this stage, there is a much slower stage characterized by the rate constant, $k_{ip,2}$. As more and more sites on the outer surface of the adsorbent get used up, the adsorbate species have to move further into the pores of adsorbent. This diffusion is very slow, thus $k_{ip,2}$ is always slower than

$k_{ip,1}$. For example, $k_{ip,1}$ for 50:50 CS:B15C5 was calculated to be 22±1 μmol g^{-1} $min^{-0.5}$ whilst $k_{ip,2}$ was calculated to be at less 3.4X less than $k_{ip,1}$ (i.e. 3.4±0.2 μmol g^{-1} $min^{-0.5}$) . Interestingly, both $k_{ip,1}$ and $k_{ip,2}$ obtained for both Cd^{2+} and Zn^{2+} adsorption were at least an order of magnitude higher than those obtained for adsorption of 2,4,5-TCP. This is hardly surprising since the metal ions are much smaller than 2,4,5-TCP, thus the metal ions can diffuse faster than the organic pollutant.

Table 2-7 Intra particle diffusion model rate constants for adsorption of Cd^{2+}, Zn^{2+} and 2,4,5-trichlorophenol (2,4,5-TCP) onto composite materials.

Intra-Particle Diffusion Model Parameter Values for Cd^{2+} and Zn^{2+} Adsorption		
	k_1 (μmol/g.$min^{1/2}$)	**k_2 (μmol/g.$min^{1/2}$)**
CS50B15C5 for Cd^{2+}	22±1	3.4±0.2
CS50B15C5 for Zn^{2+}	7.3±0.4	2.6±0.3
CEL50B15C5 for Cd^{2+}		1.66±0.09
CEL50B15C5 for Zn^{2+}	8±1	0.7±0.2
CS100 for Cd^{2+}		5.3±0.5
Intra-Particle Diffusion Model Parameter Values for 2,4,5-Trichlorophenol Adsorption		
	k_1 (μmol/g.$min^{1/2}$)	**k_2 (μmol/g.$min^{1/2}$)**
CS100	2.5±0.1	0.77±0.06
CEL100	0.68±0.02	0.135±0.005
CEL40B15C5	0.52±0.05	0.049±0.001
CEL30CS20 B15C5 50	1.25±0.04	0.32±0.03
CEL20CS50B15C5 30	1.50±0.03	0.54±0.02

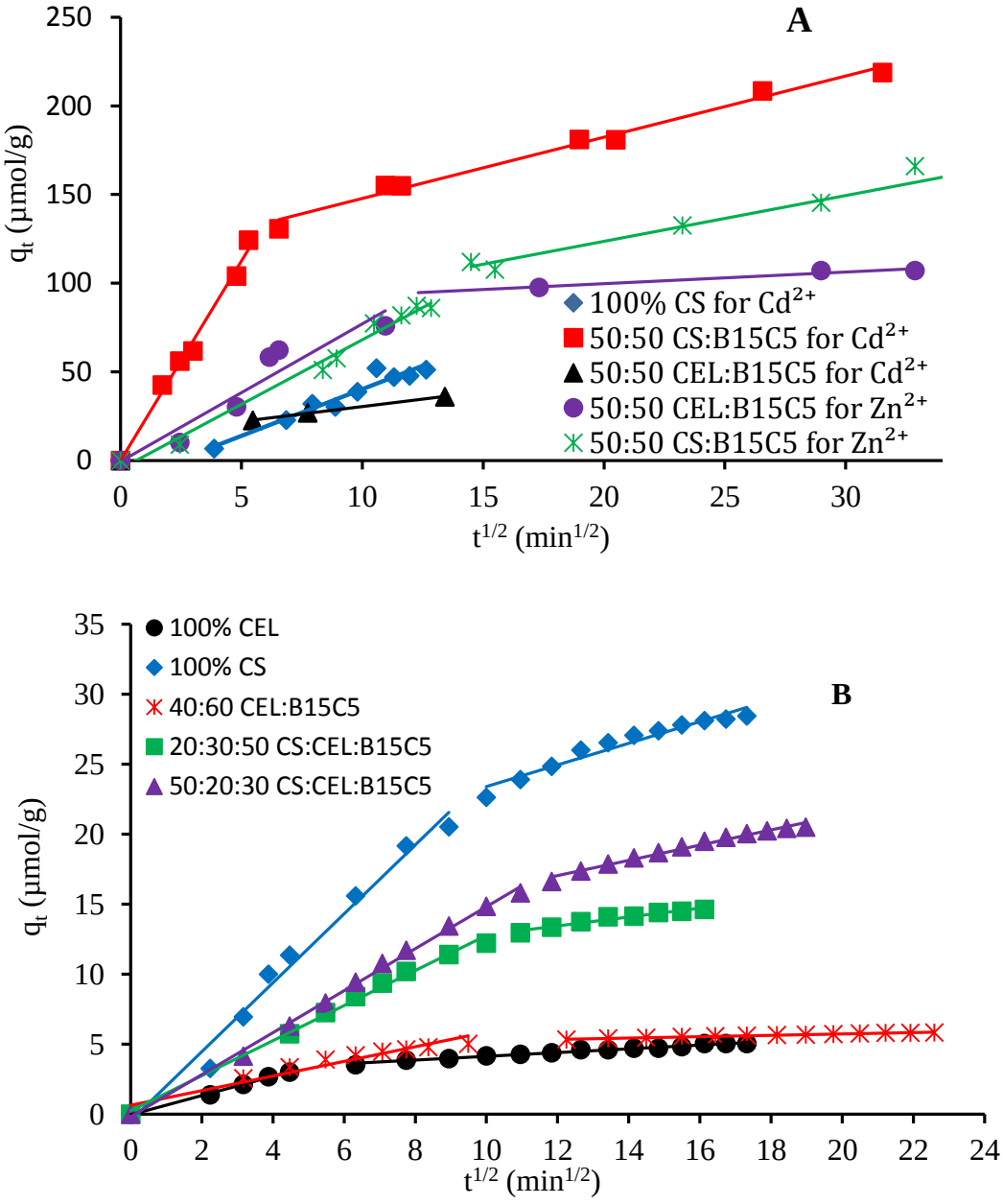

Figure 2-21 Intra particle diffusion plots for adsorption of (A) Cd^{2+} and Zn^{2+}, and (B) 2,4,5-trichlorophenol onto composite materials.

2.4.3.7. Reusability of composite films

One of the most economical benefit of the adsorbents is their ability to be reused for further adsorption experiments. Interestingly, our composites retained their adsorption performance for adsorbing the heavy metal ions (Cd^{2+} and Zn^{2+}) and 2,4,5-TCP. For example, one g of 50:50 CS:B15C5 adsorbed up to 363±10 µmol of Cd^{2+} when used for the first time. After desorption, this same film could adsorb up to 380 µmol Cd^{2+}. Similarly, whereas 233±6 µmol Zn^{2+} was adsorbed by 50:50 CEL:B15C5 when used for the first time, up to 267±3 µmol of this same ion were adsorbed when this film was used for the second time.

Figure 2-22 shows the plot of q_t against time for the two cycles of adsorption of 2,4,5-TCP by 20:30:50 CS:CEL:B15C5. This figure clearly shows that the adsorption profiles for both the first adsorption cycle and the second adsorption cycle are very similar. After fitting the data to pseudo second order model, it was found out that 20.46±0.06 µmol and 20.4±0.1 µmol of 2,4,5-TCP were adsorbed during the first and the second cycles respectively.

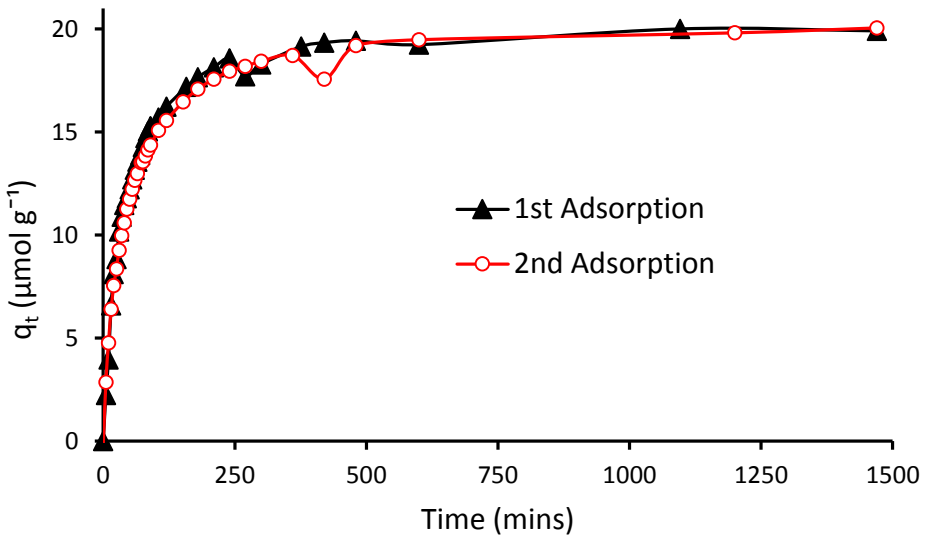

Figure 2-22 Plot of q_t of adsorption of 2,4,5-trichlorophenol (2,4,5-TCP) as a function of time by 20:30:50 CS:CEL:B15C5 composite films. Black curve with solid triangle markers is for first adsorption cycle using freshly prepared films. Red curve with open circle markers is for second adsorption cycle i.e. adsorption by films after desorbing 2,4,5-TCP that had been adsorbed during the first cycle.

2.5. Conclusions

In summary, we successfully synthesized novel composites containing CS, CEL and various crown ethers. Interestingly, these composites retained the native properties of their constituents namely, superior mechanical properties (from CEL), excellent adsorbent capability for heavy metal ions (from crown ethers) and pollutants (from CS). More importantly, these polysaccharides interacted synergistically with crown ether to enhance their adsorption capability for heavy metal ions Zn and Cd. Interestingly, these crown ethers showed size selectivity between these two heavy metal ions. In addition, our composites can be regenerated and reused with similar their adsorption efficiency.

2.6. References

1. Kobya, M.; Demirbas, E.; Senturk, E.; Ince, M., Adsorption of heavy metal ions from aqueous solutions by activated carbon prepared from apricot stone. *Bioresour. Technol.* **2005,** *96*, 1518-1521.

2. Perez-Marin, A. B.; Zapata, V. M.; Ortuno, J. F.; Aguilar, M.; Saez, J.; Llorens, M., Removal of cadmium from aqueous solutions by adsorption onto orange waste. *J. Hazard. Mater.* **2007,** *139*, 122-131.

3. Youness, E. R.; Mohammed, N. A.; Morsy, F. A., Cadmium impact and osteoporosis: mechanism of action. *Toxicol. Mech. Methods* **2012,** *22*, 560-567.

4. Asara, Y.; Marchal, J. A.; Carrasco, E.; Boulaiz, H.; Solinas, G.; Bandiera, P.; Garcia, M. A.; Farace, C.; Montella, A.; Madeddu, R., Cadmium modifies the cell cycle and apoptotic profiles of human breast cancer cells treated with 5-fluorouracil. *Int. J. Mol. Sci.* **2013,** *14*, 16600-16616.

5. Waalkes, M. P., Cadmium carcinogenesis in review. *J. Inorg. Biochem.* **2000,** *79*, 241-244.

6. Okuda, B.; Iwamoto, Y.; Tachibana, H.; Sugita, M. *Parkinsonism after acute cadmium poisoning*; Hyogo College of Medicine, Fifth Department of Internal Medicine, Nishinomiya, Japan: Netherlands FIELD Citation:, 1997; pp 263-5.

7. Basun, H.; Lind, B.; Nordberg, M.; Nordstrom, M.; Bjorksten, K. S.; Winblad, B., Cadmium in blood in Alzheimer's disease and non-demented subjects: Results from a population-based study. *BioMetals* **1994,** *7*, 130-4.

8. Koh, J. Y.; Choi, D. W., Zinc toxicity on cultured cortical neurons: involvement of N-methyl-D-aspartate receptors. *Neuroscience* **1994,** *60*, 1049-57.

9. Duruibe, J. O.; Ogwuegbu, M. O. C.; Egwurugwu, J. N., Heavy metal pollution and human biotoxic effects. *Int. J. Phys. Sci.* **2007,** *2*, 112-118.

10. Cohen, J. M.; Kamphake, L. J.; Harris, E. K.; Woodward, R. L., Taste threshold concentrations of metals in drinking water. *J. - Am. Water Works Assoc.* **1960,** *52*, 660-70.

11. Semerjian, L., Equilibrium and kinetics of cadmium adsorption from aqueous solutions using untreated Pinus halepensis sawdust. *J. Hazard. Mater.* **2010,** *173*, 236-242.

12. World Health, O., Cadmium in drinking-water: background document for development of WHO guidelines for drinking-water quality. 2004, http://www.who.int/water_sanitation_health/dwq/chemicals/cadmium.pdf . (accessed Nov 30, 2014).

13. Ahalya, N.; Ramachandra, T. V.; Kanamadi, R. D., Biosorption of heavy metals. *Res. J. Chem. Environ.* **2003,** *7*, 71-79.

14. Azouaou, N.; Sadaoui, Z.; Djaafri, A.; Mokaddem, H., Adsorption of cadmium from aqueous solution onto untreated coffee grounds: Equilibrium, kinetics and thermodynamics. *J. Hazard. Mater.* **2010,** *184*, 126-134.

15. Agrawal, A.; Sahu, K. K., Kinetic and isotherm studies of cadmium adsorption on manganese nodule residue. *J. Hazard. Mater.* **2006,** *137* (2), 915-924.

16. Shukla, A.; Zhang, Y.-H.; Dubey, P.; Margrave, J. L.; Shukla, S. S., The role of sawdust in the removal of unwanted materials from water. *J. Hazard. Mater.* **2002,** *95*, 137-152.

17. Li, Q.; Zhai, J.; Zhang, W.; Wang, M.; Zhou, J., Kinetic studies of adsorption of Pb(II), Cr(III) and Cu(II) from aqueous solution by sawdust and modified peanut husk. *J. Hazard. Mater.* **2007,** *141*, 163-167.

18. Ayyappan, R.; Sophia, A. C.; Swaminathan, K.; Sandhya, S., Removal of Pb(II) from aqueous solution using carbon derived from agricultural wastes. *Process Biochem. (Oxford, U. K.)* **2004,** *40*, 1293-1299.

19. Babel, S.; Kurniawan, T. A., Low-cost adsorbents for heavy metals uptake from contaminated water: a review. *J. Hazard. Mater.* **2003,** *97*, 219-243.

20. Benjamin, M. M.; Sletten, R. S.; Bailey, R. P.; Bennett, T., Sorption and filtration of metals using iron-oxide-coated sand. *Water Res.* **1996,** *30*, 2609-2620.

21. Foo, K. Y.; Hameed, B. H., Insights into the modeling of adsorption isotherm systems. *Chem. Eng. J. (Amsterdam, Neth.)* **2010,** *156*, 2-10.

22. Hiraoka, M., *Crown compounds: their characteristics and applications*. Kodansha Tokyo: 1982.

23. Visser, A. E.; Swatloski, R. P.; Reichert, W. M.; Griffin, S. T.; Rogers, R. D., Traditional Extractants in Nontraditional Solvents: Groups 1 and 2 Extraction by Crown Ethers in Room-Temperature Ionic Liquids. *Ind. Eng. Chem. Res.* **2000,** *39*, 3596-3604.

24. Dai, S.; Ju, Y. H.; Barnes, C. E., Solvent extraction of strontium nitrate by a crown ether using room-temperature ionic liquids. *J. Chem. Soc., Dalton Trans.* **1999,** *8*, 1201-1202.

25. Takagi, M.; Nakamura, H.; Sanui, Y.; Ueno, K., Spectrophotometric determination of sodium by ion-pair extraction with crown ether complexes and monoanionic dyes. *Anal. Chim. Acta* **1981,** *126*, 185-90.

26. Vaidya, B.; Zak, J.; Bastiaans, G. J.; Porter, M. D.; Hallman, J. L.; Nabulsi, N. A. R.; Utterback, M. D.; Strzelbicka, B.; Bartsch, R. A., Chromogenic and Fluorogenic Crown Ether Compounds for the Selective Extraction and Determination of Hg(II). *Anal. Chem.* **1995,** *67*, 4101-11.

27. Peng, C.; Wang, Y.; Tang, Y., Synthesis of cross-linked chitosan-crown ethers and evaluation of these products as adsorbents for metal ions. *J. Appl. Polym. Sci.* **1998,** *70*, 501-506.

28. Yi, Y.; Wang, Y.; Liu, H., Preparation of new crosslinked chitosan with crown ether and their adsorption for silver ion for antibacterial activities. *Carbohydr. Polym.* **2003,** *53*, 425-430.

29. Yang, Q.; Fujisawa, S.; Saito, T.; Isogai, A., Improvement of mechanical and oxygen barrier properties of cellulose films by controlling drying conditions of regenerated cellulose hydrogels. *Cellulose (Dordrecht, Neth.)* **2012,** *19*, 695-703.

30. Pang, J.; Liu, X.; Zhang, X.; Wu, Y.; Sun, R., Fabrication of cellulose film with enhanced mechanical properties in ionic liquid 1-allyl-3-methylimidaxolium chloride (AmimCl). *Materials* **2013,** *6*, 1270-1284.

31. Abdulkhani, A.; Hojati Marvast, E.; Ashori, A.; Karimi, A. N., Effects of dissolution of some lignocellulosic materials with ionic liquids as green solvents on mechanical and physical properties of composite films. *Carbohydr. Polym.* **2013,** *95* (1), 57-63.

32. Rao, S. B.; Sharma, C. P., Use of chitosan as a biomaterial: studies on its safety and hemostatic potential. *J. Biomed. Mater. Res.* **1997,** *34*, 21-28.

33. Burkatovskaya, M.; Castano, A. P.; Demidova-Rice, T. N.; Tegos, G. P.; Hamblin, M. R., Effect of chitosan acetate bandage on wound healing in infected and noninfected wounds in mice. *Wound Repair Regen.* **2008,** *16*, 425-431.

34. Rabea Entsar, I.; Badawy Mohamed, E. T.; Stevens Christian, V.; Smagghe, G.; Steurbaut, W., Chitosan as antimicrobial agent: applications and mode of action. *Biomacromolecules* **2003,** *4*, 1457-65.

35. Burkatovskaya, M.; Tegos, G. P.; Swietlik, E.; Demidova, T. N.; Castano, A. P.; Hamblin, M. R., Use of chitosan bandage to prevent fatal infections developing from highly contaminated wounds in mice. *Biomaterials* **2006,** *27*, 4157-4164.

36. Wan Ngah, W. S.; Teong, L. C.; Hanafiah, M. A. K. M., Adsorption of dyes and heavy metal ions by chitosan composites: A review. *Carbohydr. Polym.* **2011,** *83*, 1446-1456.

37. Li, N.; Bai, R., Copper adsorption on chitosan-cellulose hydrogel beads: behaviors and mechanisms. *Sep. Purif. Technol.* **2005,** *42*, 237-247.

38. Sun, X.; Peng, B.; Ji, Y.; Chen, J.; Li, D., Chitosan(chitin)/cellulose composite biosorbents prepared using ionic liquid for heavy metal ions adsorption. *AIChE J.* **2009,** *55*, 2062-2069.

39. Zhang, H.; Wu, J.; Zhang, J.; He, J., 1-Allyl-3-methylimidazolium chloride room temperature ionic liquid: A new and powerful nonderivatizing solvent for cellulose. *Macromolecules* **2005,** *38*, 8272-8277.

40. Xie, H.; Zhang, S.; Li, S., Chitin and chitosan dissolved in ionic liquids as reversible sorbents of CO2. *Green Chem.* **2006,** *8*, 630-633.

41. Isik, M.; Sardon, H.; Mecerreyes, D., Ionic liquids and cellulose: dissolution, chemical modification and preparation of new cellulosic materials. *Int. J. Mol. Sci.* **2014,** *15*, 11922-11940, 19.

42. Swatloski, R. P.; Spear, S. K.; Holbrey, J. D.; Rogers, R. D., Dissolution of cellulose with ionic liquids. *J. Am. Chem. Soc.* **2002,** *124*, 4974-4975.

43. Dupont, J.; Suarez, P. A. Z., Physico-chemical processes in imidazolium ionic liquids. *Phys. Chem. Chem. Phys.* **2006,** *8*, 2441-2452.

44. Dharaskar, S. A.; Varma, M. N.; Shende, D. Z.; Yoo, C. K.; Wasewar, K. L., Synthesis, characterization and application of 1-butyl-3-methylimidazolium chloride as green material for extractive desulfurization of liquid fuel. *Sci. World J.* **2013**, 395274/1-395274/10, 10 pp.

45. Duri, S.; Tran, C. D., Supramolecular Composite Materials from Cellulose, Chitosan, and Cyclodextrin: Facile Preparation and Their Selective Inclusion Complex Formation with Endocrine Disruptors. *Langmuir* **2013,** *29*, 5037-5049.

46. Huang, C. P.; Blankenship, D. W., The removal of mercury(II) from dilute aqueous solution by activated carbon. *Water Res.* **1984,** *18* (1), 37-46.

47. Rodriguez-Reinoso, F., *Adsorption by Powders and Porous Solids edited by F. Rouquerol, J. Rouquerol and K.S.W. Sing. Academic*. 1999; Vol. 37, p 1667.

48. Tchobanoglous, G.; Burton, F. L.; Stensel, D. H., *Wastewater Engineering: Treatment and Reuse*. McGraw Hill: New York, 2003.

49. Kelesogu, S. Comparative adsorption studies of heavy metal ions on chitin and chitosan biopolymers. Izmir Institute of Technology, Izmir, July 2007.

50. Ho, Y. S.; McKay, G., The kinetics of sorption of divalent metal ions onto sphagnum moss peat. *Water Res.* **2000,** *34* (3), 735-742.

51. Miretzky, P.; Cirelli, A. F., Hg(II) removal from water by chitosan and chitosan derivatives: A review. *J. Hazard. Mater.* **2009,** *167* (1-3), 10-23.

52. Yang, Z.; Wang, Y.; Tang, Y., Synthesis and adsorption properties for metal ions of mesocyclic diamine-grafted chitosan-crown ether. *J. Appl. Polym. Sci.* **2000,** *75* (10), 1255-1260.

53. Rivera-Utrilla, J.; Bautista-Toledo, I.; Ferro-Garcia, M. A.; Moreno-Castilla, C., Activated carbon surface modifications by adsorption of bacteria and their effect on aqueous lead adsorption. *J. Chem. Technol. Biotechnol.* **2001,** *76* (12), 1209-1215.

54. Gerente, C.; Lee, V. K. C.; Le Cloirec, P.; McKay, G., Application of chitosan for the removal of metals from wastewaters by adsorption-mechanisms and models review. *Crit. Rev. Environ. Sci. Technol.* **2007,** *37* (1), 41-127.

55. Kamari, A.; Yusoff, S. N. M.; Abdullah, F.; Putra, W. P., Biosorptive removal of Cu(II), Ni(II) and Pb(II) ions from aqueous solutions using coconut dregs residue: Adsorption and characterisation studies. *J. Environ. Chem. Eng.* **2014,** *2* (4), 1912-1919.

56. Hall, K. R.; Eagleton, L. C.; Acrivos, A.; Vermeulen, T., Pore- and solid-diffusion kinetics in fixed-bed adsorption under constant-pattern conditions. *Ind. Eng. Chem. Fundam.* **1966,** *5* (2), 212-23.

57. Battista, O. A., Hydrolysis and crystallization of cellulose. *Ind. Eng. Chem.* **1950,** *42*, 502-507.

58. Battista, O. A.; Smith, P. A., Microcrystalline cellulose. *Ind. Eng. Chem.* **1962,** *54*, 20-29.

59. Tran, C. D.; Duri, S.; Delneri, A.; Franko, M., Chitosan-cellulose composite materials: Preparation, Characterization and application for removal of microcystin. *J. Hazard. Mater.* **2013,** *252-253*, 355-366.

60. Frez, C.; Diebold, G. J.; Tran, C. D.; Yu, S., Determination of Thermal Diffusivities, Thermal Conductivities, and Sound Speeds of Room-Temperature Ionic Liquids by the Transient Grating Technique. *J. Chem. Eng. Data* **2006,** *51*, 1250-1255.

61. Duri, S.; Majoni, S.; Hossenlopp, J. M.; Tran, C. D., Determination of Chemical Homogeneity of Fire Retardant Polymeric Nanocomposite Materials by Near-Infrared Multispectral Imaging Microscopy. *Anal. Lett.* **2010,** *43*, 1780-1789.

62. Tran, C. D.; Duri, S.; Harkins, A. L., Recyclable synthesis, characterization, and antimicrobial activity of chitosan-based polysaccharide composite materials. *J. Biomed. Mater. Res., Part A* **2013,** *101A*, 2248-2257.

63. Asencios, Y. J. O.; Sun-Kou, M. R., Synthesis of high-surface-area γ-Al2O3 from aluminum scrap and its use for the adsorption of metals: Pb(II), Cd(II) and Zn(II). *Appl. Surf. Sci.* **2012,** *258*, 10002-10011.

64. Phaechamud, T.; Ritthidej, G. C., Formulation variables influencing drug release from layered matrix system comprising chitosan and xanthan gum. *AAPS PharmSciTech* **2008,** *9*, 870-877.

65. Bailey, M. M.; Townsend, M. B.; Jernigan, P. L.; Sturdivant, J.; Hough-Troutman, W. L.; Rasco, J. F.; Swatloski, R. P.; Rogers, R. D.; Hood, R. D., Developmental toxicity assessment of the ionic liquid 1-butyl-3-methylimidazolium chloride in CD-1 mice. *Green Chem.* **2008,** *10*, 1213-1217.

66. Bernot, R. J.; Brueseke, M. A.; Evans-White, M. A.; Lamberti, G. A., Acute and chronic toxicity of imidazolium-based ionic liquids on Daphnia magna. *Environ. Toxicol. Chem.* **2005,** *24*, 87-92.

67. Rajkumar, T.; Rao, G. R., Investigation of hybrid molecular material prepared by ionic liquid and polyoxometalate anion. *J. Chem. Sci. (Bangalore, India)* **2008,** *120*, 587-594.

68. Oh, S. Y.; Yoo, D. I.; Shin, Y.; Kim, H. C.; Kim, H. Y.; Chung, Y. S.; Park, W. H.; Youk, J. H., Crystalline structure analysis of cellulose treated with sodium hydroxide and carbon dioxide by means of X-ray diffraction and FTIR spectroscopy. *Carbohydr. Res.* **2005,** *340*, 2376-2391.

69. Soheilmoghaddam, M.; Wahit, M. U.; Yussuf, A. A.; Al-Saleh, M. A.; Whye, W. T., Characterization of bio regenerated cellulose/sepiolite nanocomposite films prepared via ionic liquid. *Polym. Test.* **2014,** *33*, 121-130.

70. Han, D.; Yan, L.; Chen, W.; Li, W.; Bangal, P. R., Cellulose/graphite oxide composite films with improved mechanical properties over a wide range of temperature. *Carbohydr. Polym.* **2011,** *83*, 966-972.

71. Shu, J.; Xie, P.; Lin, D.; Chen, R.; Wang, J.; Zhang, B.; Liu, M.; Liu, H.; Liu, F., Two highly stable and selective solid phase microextraction fibers coated with crown ether functionalized ionic liquids by different sol-gel reaction approaches. *Anal. Chim. Acta* **2014,** *806*, 152-164.

72. Zhou, X.; Xie, P.-F.; Wang, J.; Zhang, B.-B.; Liu, M.-M.; Liu, H.-L.; Feng, X.-H., Preparation and characterization of novel crown ether functionalized ionic liquid-based solid-phase microextraction coatings by sol-gel technology. *J. Chromatogr. A* **2011,** *1218*, 3571-3580.

73. Saleh, M. I.; Kusrini, E.; Salhin, A.; Adnan, R.; Rahman, I. A.; Saad, B.; Yamin, B. M., Structure and thermal stability of the benzo-15-crown-5 with lanthanum (III) bromide complex. *Indonesian Journal of Chemistry* **2010,** *4* (3), 139-144.

74. Cheng, G.; Varanasi, P.; Arora, R.; Stavila, V.; Simmons, B. A.; Kent, M. S.; Singh, S., Impact of Ionic Liquid Pretreatment Conditions on Cellulose Crystalline Structure Using 1-Ethyl-3-methylimidazolium Acetate. *J. Phys. Chem. B* **2012,** *116*, 10049-10054.

75. Frensdorff, H. K., Stability constants of cyclic polyether complexes with univalent cations. *J. Amer. Chem. Soc.* **1971,** *93*, 600-6.

76. Tzeng, D. L.; Shih, J. S.; Yeh, Y. C., Adsorption of heavy metal ions on crown ether adsorbents. *Analyst (London)* **1987,** *112*, 1413-16.

77. Samadi, N.; Hasanzadeh, R.; Rasad, M., Adsorption isotherms, kinetic, and desorption studies on removal of toxic metal ions from aqueous solutions by polymeric adsorbent. *J. Appl. Polym. Sci.* **2014**, Ahead of Print.

CHAPTER 3

SYNTHESIS, CHARACTERIZATION AND APPLICATION OF RESORCINARENE-BASED POLYSACCHARIDE COMPOSITE MATERIALS FOR THE SELECTIVE ADSORPTION OF AROMATIC ORGANIC POLLUTANTS

3.1. Background

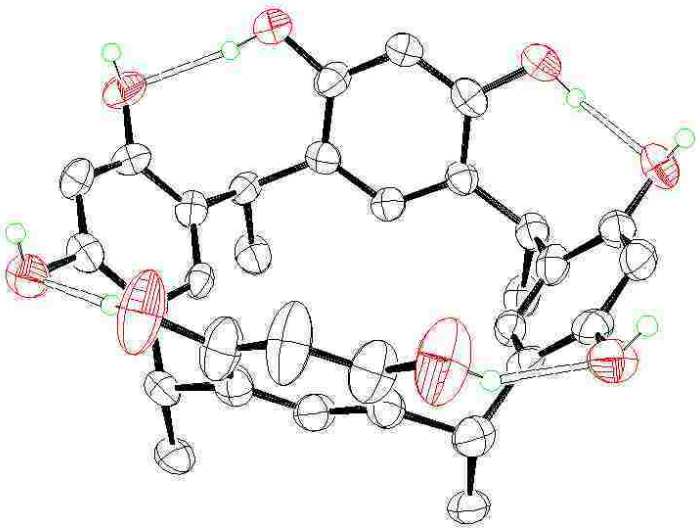

Figure 3-1 X-ray structure of resorcinarene showing its crown conformation (based on coordinates from ref. 1),[1] which is mostly suited to form inclusion complexes with guest species of complementary structure and size. Ortep 3 software was used to draw this structure.[2] Red, black and green spheres represent oxygen, carbon and hydrogen atoms. Some H-atoms and all undecyl chains have been omitted to ensure clarity of presentation. Broken lines show Intramolecular H-bonds formed between oxygen atom from one resorcinol moiety and hydrogen atom from an adjacent resorcinol moiety in the same RES structure.

Macrocycles such as resorcinarenes (RES), calixarenes, cyclodextrins, and crown ethers continue to receive increasing attention due to their ability to form inclusion complexes with organic and inorganic species.[3] Amongst these macrocycles, RES (a

cyclic tetramer synthesized by reacting resorcinol and an aldehyde) represents a fascinating class worthy to study. RES possesses a cavity formed by the four resorcinol moieties, which enable it to form inclusion complexes with guest species of size and shape complementary to that of the inner part of the cavity (Figure 3-1). Thus, the shapes and sizes of guest species are bound to affect the stability of their complexes with RES. In addition to this size-fit requirement, the conformation of the macrocycle also affects the stability of the complexes. For example, RES can exist in five different conformations; crown, boat, chair, diamond, and saddle conformations.[4] In most cases, the crown conformation (Figure 3-1) is most suited to sequester guest molecules of appropriate size into the cavity. As a result of these fascinating properties, RES has found applications in both supramolecular and analytical chemistry. In supramolecular chemistry, it has been used to design complexes which mimic the active site of enzymes thus enabling scientists to gain valuable insights into the nature of kinetics and selectivity of these enzymes.[5,6] In analytical chemistry, RESs have been used in the separation of small organic molecules in reversed phase HPLC[7] and gas chromatography,[8] in selective extraction,[9] and as carriers in polymer inclusion membranes (PIMs).[10-12] In addition, RESs have recently been found to stabilize dispersions of nanoparticles in organic solutions.[13] In all these applications, RES could form selective complexes with a variety of guest compounds (neutral and ionic). However, RES has rarely been used to adsorb organic pollutants. In this study, we explore the use of RES for the removal of organic pollutants from water.

Although water is seemingly an abundant resource, in reality, fresh water suitable for human consumption is becoming scarcer due to pollution from industrial, agricultural

as well as domestic wastes. These wastes contain either organic or inorganic pollutants depending on the nature of the industrial activity being carried out. Organic pollutants such as phenolic and nitro-aromatic compounds are very ubiquitous in these industrial wastes as they are widely used as raw materials in various industries including dyes, explosives, pesticides, etc.[14] Despite their utility in many industrial processes, these organic pollutants are highly toxic to living organisms including humans. For example, phenol, one of the priority listed pollutants, is highly toxic even at lower concentrations.[15] It imparts a bad taste and odor to the water. In addition, it is resistant to biodegradation. In the presence of chlorine in water, phenols are converted to chlorophenols which are implicated in disrupting the endocrine system. As a result of these harmful effects of phenols, Environmental Protection Agency (EPA) lowered the maximum allowable concentration of phenol in wastewaters down to 1 mg per L.[16] Methyl derivatives of phenol (*o*-, *m*-, and *p*-cresol) have also been listed as stable, priority chemical pollutants because of their harmful effects to the biological systems.[17] For example, whereas *o*-cresol causes heart, liver and kidney damages, *m*-cresol is fatal if ingested or if it is absorbed through the skin.[18] *p*-Cresol is a well-known uremic toxin which can easily bind to proteins thereby evading removal from blood during hemodialysis.[19,20] In addition, *p*-cresol can cause central nervous system disorders which result in death.[17] Similarly to phenol and its derivatives, nitro-aromatic compounds (nitrobenzene, *1,2*-, *1,3*- and *1,4*-dinitrobenzene, *o*-, *m*-, and *p*-nitrotoluene) cause a variety of toxicological effects. As a result, they have also been listed as priority pollutants by the EPA.[21-23] Thus, there is need to remove these pollutants from water before discharging it into the water ways.

A variety of techniques have been used to remove organic pollutants from water. These include, but not limited to, photocatalytic degradation over UV irradiated titanium dioxide, microbial degradation, and adsorption. Amongst these techniques, adsorption appears to be the most effective. However, most adsorbents including activated carbon, and other natural sorbents are non-selective in their adsorption of organic species from water. This is a huge limitation given that most aqueous waste contain not only the hazardous species but also the innocuous organics at much higher concentrations. Consequently, the adsorption capacity of these adsorbents is significantly reduced due to competition between the hazardous and the non-hazardous species. Thus, there is need to design selective adsorbents to enhance the capacity to remove more hazardous species. In addition, this selective adsorption will enable recovery of species for their subsequent reuse in valuable industrial processes.

As described earlier, RES represent an interesting class of macrocycles which exhibit excellent selectivity towards binding specific guest species. Although it can selectively recognize of organic pollutants, its practical application is hindered by its inability to form films. As described in the previous Chapter, this limitation can be overcome by immobilizing RES in polysaccharide matrices. This has the advantage of making it easier to separate the pollutant-laden adsorbent from the aqueous solution. In addition, these polysaccharides (CEL and CS) are relatively abundant. Thus, the objective of the present study was to encapsulate RES in either CEL or CS matrix using a green solvent, ionic liquid to dissolve and regenerate the corresponding composite films. In addition, these composite films were evaluated for their ability to show adsorption selectivity towards positional isomers of cresol, toluene and dinitrobenzene. It is expected

that this study will provide more insights into the mechanism of selectivity of the RESs. Details are reported herein for the synthesis, characterization and utilization for the removal of phenolic and nitro-aromatic pollutants.

3.2. Experimental

3.2.1. Chemicals

C-undecylcalix[4]resorcinarene monohydrate, phenol, *o*-cresol, *p*-cresol, 1,2-dinitrobenzene, 1,4-dinitrobenzene were purchased from Sigma-Aldrich (Milwaukee, WI), *m*-cresol, 1,3-dinitrobenzene and *p*-nitrotoluene were purchased from Alfa Aesar (Ward Hill, MA). Nitrobenzene, *o*-nitrotoluene and *m*-nitrotoluene were obtained from Fisher Scientific (Springfield, NJ), Avocado Research Chemicals (Ward Hill, MA), and Acros Organics (Morris Plains, NJ) respectively. All the other chemicals—chitosan, cellulose, 1-butyl-3-methylimidazolium chloride, and double distilled water— used in this study are the same as the ones described in the previous Chapter 2. Scheme 3-1 represents structures of these analytes used in the adsorption study.

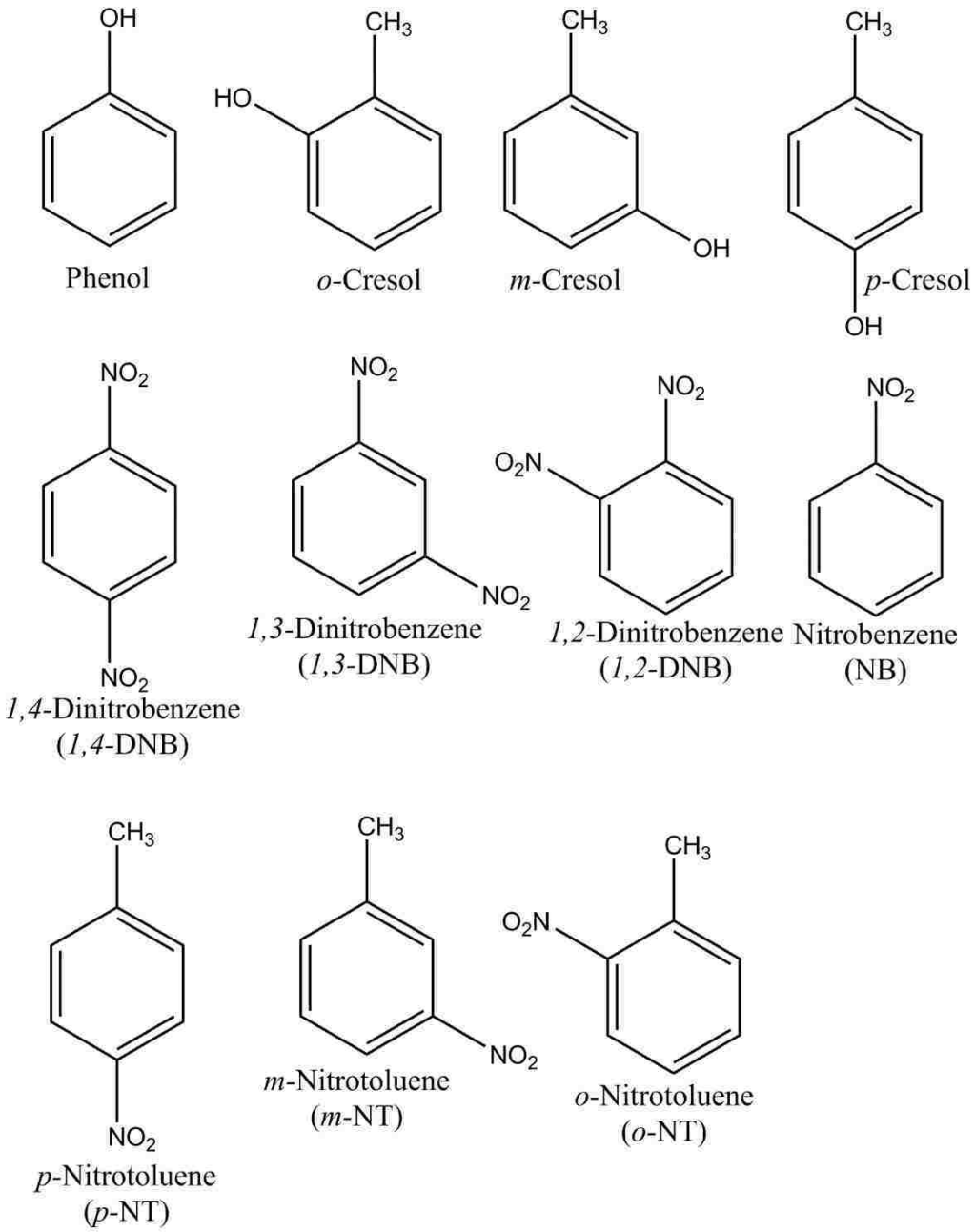

Scheme 3-1 Structures of analytes used in the adsorption study

3.2.2. Synthesis of composite films

The procedure described in the previous Chapter 2 for the synthesis of crown ether based composites was basically followed in the synthesis of RES-based composite films. All the steps have been presented schematically in Scheme 3-2. In brief, in the synthesis of two-component films, either CEL or CS was dissolved first in 1% portions followed by RES. RES dissolved within one hour of addition to the polysaccharide solutions. However, two hours were given to allow complete mixing between the either CEL or CS and RES. It should be pointed however that attempts were made to synthesize composites containing *c*-methylcalix[4]resorcinarene (MRES) without success. This was because during washing, this resorcinarene derivative leached into the aqueous washing solution. RES and this derivative differ in the length of the alkyl groups attached to the lower rim of the macrocycles. Whereas, RES contains undecyl ($CH_3(CH_2)_{10}$-) groups, MRES contains methyl (CH_3-) groups. Therefore, RES is expected to be more hydrophobic than MRES thereby lowering the aqueous solubility of the former.

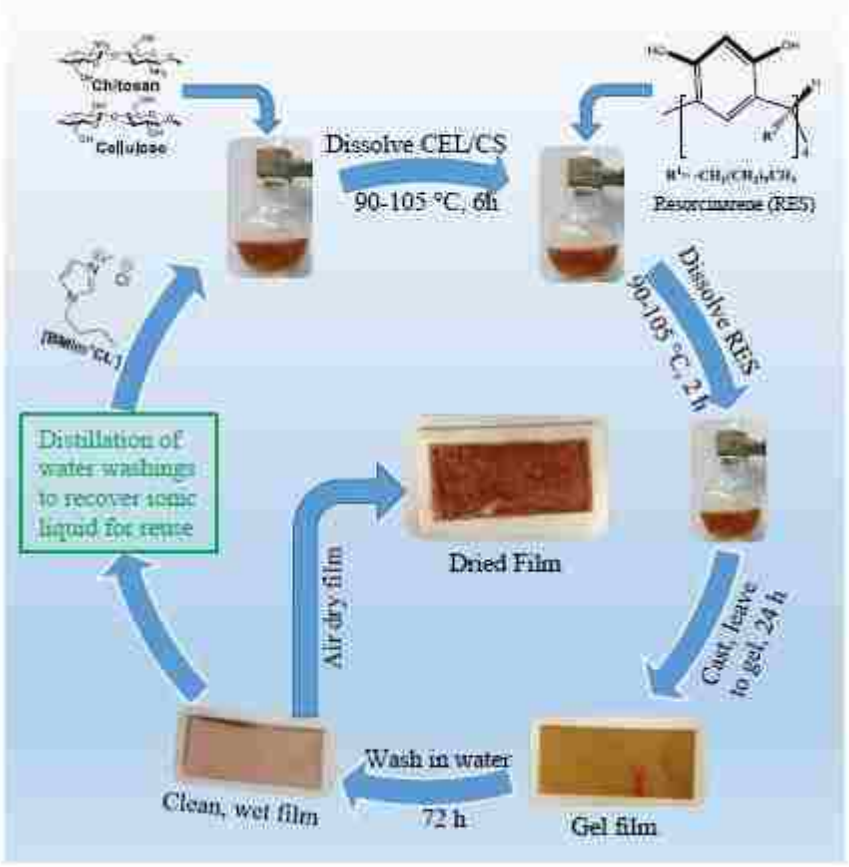

Scheme 3-2 Synthesis of one-(CEL, and CS) and two-component ([CEL+RES] and [CS+RES]) films

3.2.3. Characterization of composite films

The composite films were characterized by FTIR, near IR, powder X-ray diffraction, scanning electron microcopy (SEM), solid state NMR. FTIR was performed on a Perkin Elmer 100 series spectrometer using KBr method. The scan range was 4000-450 cm^{-1}, the resolution was set at 2 cm^{-1}. Sixty four spectra were scanned and averaged for each sample to optimize the signal to noise ratio. Near IR was measured in

transmission mode on a Nicolet 6700 FTIR series (Thermo Electric Corporation) equipped with a KBr beam splitter and an InGaAs room temperature detector. Each spectrum was recorded in the range 10,000-4000 cm^{-1} at resolution 2 cm^{-1} and averaged 64 scans for each sample. To measure the spectrum of RES, the powder was ground and mixed with KBr before being pressed into a pellet which was subsequently presented for measurement. Powder XRD was performed on a Rigaku Miniflex II series diffractometer within the range 2-40° 2θ using Cu Kα radiation, 30 kV, 15 mA with a scan speed of 5° (2θ) per min. Data files from this measurement were then converted to a spreadsheet compatible format using Jade 8 program.[24] SEM images were taken on a Hitachi S4800 field emission SEM with beam energy 3 kV and at a working distance of 7.9-8.4 mm. Before taking the measurements, the samples were made conductive by applying a 2 nm thick iridium coating on the surface and cross sections of the specimens. Solid state ^{13}C cross polarization magic angle spinning (CP-MAS) NMR spectra were recorded at 500 MHz using a Bruker Avance III 500 MHz spectrometer.

3.2.4. Procedure used to measure kinetics of adsorption of organics onto the composite films

We followed the same procedure as described in the previous Chapter 2 for the measurement of kinetics of adsorption of organic pollutants. In brief, all organic solutes were dissolved in double distilled water to make 390 μM solution. Meanwhile, two films for each composition were being washed in water to remove any residual ionic liquid which could interfere with the UV Vis absorption measurements. Details on the washing of the films and the set-up for measurement of kinetics can be found in the relevant section in the previous Chapter 2.

3.2.5. Analysis of kinetics data

Similar to the measurement of kinetics of adsorption in the previous Chapter 2, the amount of solute adsorbed up to each time point, q_t, was calculated using the mass balance equation (*i.e.* $q_t = [(C_o - C_t)V]/W$) where C_o *and* C_t represent the concentration of solute at t=0 and t=t minutes respectively; *V* and *W* represent the volume of solution and weight of film respectively. Then this data was fitted to kinetics models; pseudo first order, pseudo second order, and the intra-particle diffusion models. Again, the details about the theoretical assumptions of these models can be found in the relevant section in the previous Chapter 2. However, only their final linearized expressions are presented in this section.

Pseudo first order model	$\log(q_e - q_t) = \log(q_e) - \left(k_1 / 2.303\right)t$
Pseudo second order model	$\frac{t}{q_t} = \frac{1}{k_2 . q_e^{\,2}} + \frac{1}{q_e}t$
Intra-particle diffusion model	$q_t = k_i . t^{0.5} + I$

3.3. Results and Discussion

3.3.1. Characterization by FTIR and NIR spectroscopy

FTIR and NIR were used to investigate the chemical structural changes which take place on RES as it is blended with the polysaccharides (CEL and CS) (Figure 3-2A). As illustrated in the figure and in Table 3-1, the spectrum of RES powder exhibits unique bands at 1618- and 1505-cm^{-1} due to the vibrations of the aromatic C-H groups.[25] There

is also a band at 1437 cm^{-1} which is due to the vibrations of the methine backbone in RES structure. This spectrum also exhibit bands at 2956-, 2922-, and 2853-cm^{-1}, which could be tentatively assigned to the sp^3 C-H stretch vibrations for the undecyl- groups. These sp^3 C-H stretch vibrations are sensitive to the conformational order or disorder of the alkyl chains.[26-29] A highly ordered chain structure is characterized by low values of υ_s=2850 cm^{-1} and υ_{as}=2918 cm^{-1}, a higher degree of conformational disorder is characterized by higher values of υ_s=2856 cm^{-1} and υ_{as}=2927 cm^{-1}. In this particular case, we observed vibrational frequencies that lie between these two extremes (i.e. υ_s=2853 cm^{-1} and υ_{as}=2922 cm^{-1}. This suggests that the packing of the alky groups is somewhat loose. This structure is more favored by the crown conformation of the macrocycle. In addition to these bands, there was another band appearing as a shoulder at 3492 cm^{-1}. This band can be attributed to the OH stretch vibrations of the resorcinol groups in the macrocycle. The vibrational frequency of this vibrational mode is very sensitive to the nature of H-bonding within the structure of RES. These vibrational frequencies are assigned as follows: 3611 cm^{-1} for free OH groups; 3599 cm^{-1} for OH with oxygen acting as proton acceptor in H-bonding; 3481 cm^{-1} for OHs acting as proton donors in H-bonding; and 3393 cm^{-1} for OH participating in two H-bonds that is both as proton acceptor and as proton donor.[30] The vibrational frequency for RES powder (i.e. 3492 cm^{-1}) lies between the scenario where OH can act as either a proton acceptor or donor. This can be best explained by considering the crown conformation as the most dominant conformation in the structure of RES. In this conformation, OH groups of neighboring resorcinol groups on the same RES molecule participate in H-bonding with one being a proton donor and the other being a proton acceptor. However, these results are not very

conclusive as this RES powder contained one mole equivalent of remnant water. This water could also participate in H-bonding with these resorcinol groups. The participation of water OH in H-bonding is further corroborated by the absence of a peak at 3611 cm^{-1} which is ascribed to free OH groups.

Upon regeneration in the polysaccharide matrix, it is possible that the structure of RES is changed. However, the similarity between the spectra of RES by itself and in either CS or CEL suggests that there were no substantial changes to the structure of RES. In addition, the presence of RES bands in the composite films suggest that RES was successfully encapsulated in either CEL or CS matrix. Despite this similarity, there were some interesting subtle changes which took place as a result of this blending. For example, the band at 3492 cm^{-1} in RES dissappeared in the spectra of the composite films. Instead, broad bands appeared at 3380 cm^{-1} and 3358 cm^{-1} for 50:50 CEL:RES and 50:50 CS:RES composite films. These bands are attributed to vibrations of OH groups involved in extensive hydrogen bonding. This is hardly surprising because CEL and CS possess many OH groups within their structures which can participate in H-bonding between the polysaccharide molecules themselves or with the OH groups in RES. Thus, the disappearance of the 3492 cm^{-1} peak could be ascribed to either disruption of the H-bonding in RES structure or just an overlap between the polysaccharide H-bonded OH vibrations and this band. It is therefore difficult to establish the nature of H-bonding in the composite films. However, monitoring some other changes in the vibrational frequencies of RES in composite films could shed more light on the effects of polysaccharides on the structure of RES. For example, the shift ($\Delta\upsilon = 2$ cm^{-1}) to higher frequencies for the asymmetric and symmetric stretch vibrations of RES in composite

films reflect more disorder in the conformation of the alkyl side chains. However, this shift could be insignificant. Another indication of interactions between RES and the polysaccharides was noticed when the aromatic vibrations became weaker when RES was encapsulated in the polysaccharide matrix. For example, as illustrated in Table 3-1, the band at 1618 cm^{-1} in RES powder shifted to 1615- and 1613-cm^{-1} in [CEL+RES] and [CS+RES] composite films respectively. Similarly, the 1505 cm^{-1} band in RES powder shifted down to 1500cm^{-1} when RES was encapsulated in either CEL or CS matrix. This red shift suggests a reduction in the double bond character of resorcinol rings. Such observations were reported elsewhere.[26]

NIR spectra was used to further confirm that RES was successfully encapsulated in the polysaccharide matrices (Figure 3-2B). As illustrated in this figure, NIR spectrum of RES exhibits bands at 1730-1762 nm which are tentatively assigned to first overtone stretch vibrations of alkyl CH groups. In addition, the bands at 2310- and 2350-nm were ascribed to the combination bands for C-H stretch and deformation. It is however surprising to note that the spectrum of RES did not show the bands ascribed to the aromatic CH vibrations. An explanation to this cannot be given at this time. The spectrum for CEL exhibit bands at: 1466 nm due to the first overtone OH stretch; 2096 nm due to the combination vibrations of OH asymmetric stretch, OH and CH deformation.[31,32] Since the chemical structure of CS is similar to that of CEL, we expect their NIR spectra to be similar as well. This is the case except for additional bands at 1529- and 2096-nm which are ascribable to the first overtone and combination absorptions of the amino groups. The band at around 1930 nm (1928 nm for RES; 1932 nm for 50:50 CEL:CS; 1929 nm for 50:50 CS:RES; 1934 nm for CEL and 1933 nm for CS) are due to the combination of OH

asymmetric stretch and OH deformation of water. Similarly to the observations made with FTIR, the spectra of the composite films exhibit bands that are ascribed to both constituents, i.e. RES and CEL in [CEL+RES] and RES and CS in [CS+RES] composite films. No new bands were observed in the composites suggesting that no covalent bonds were formed between RES and either CEL or CS. Therefore, the only forms of interactions could be the simple van der Waals and H-bonding interactions.

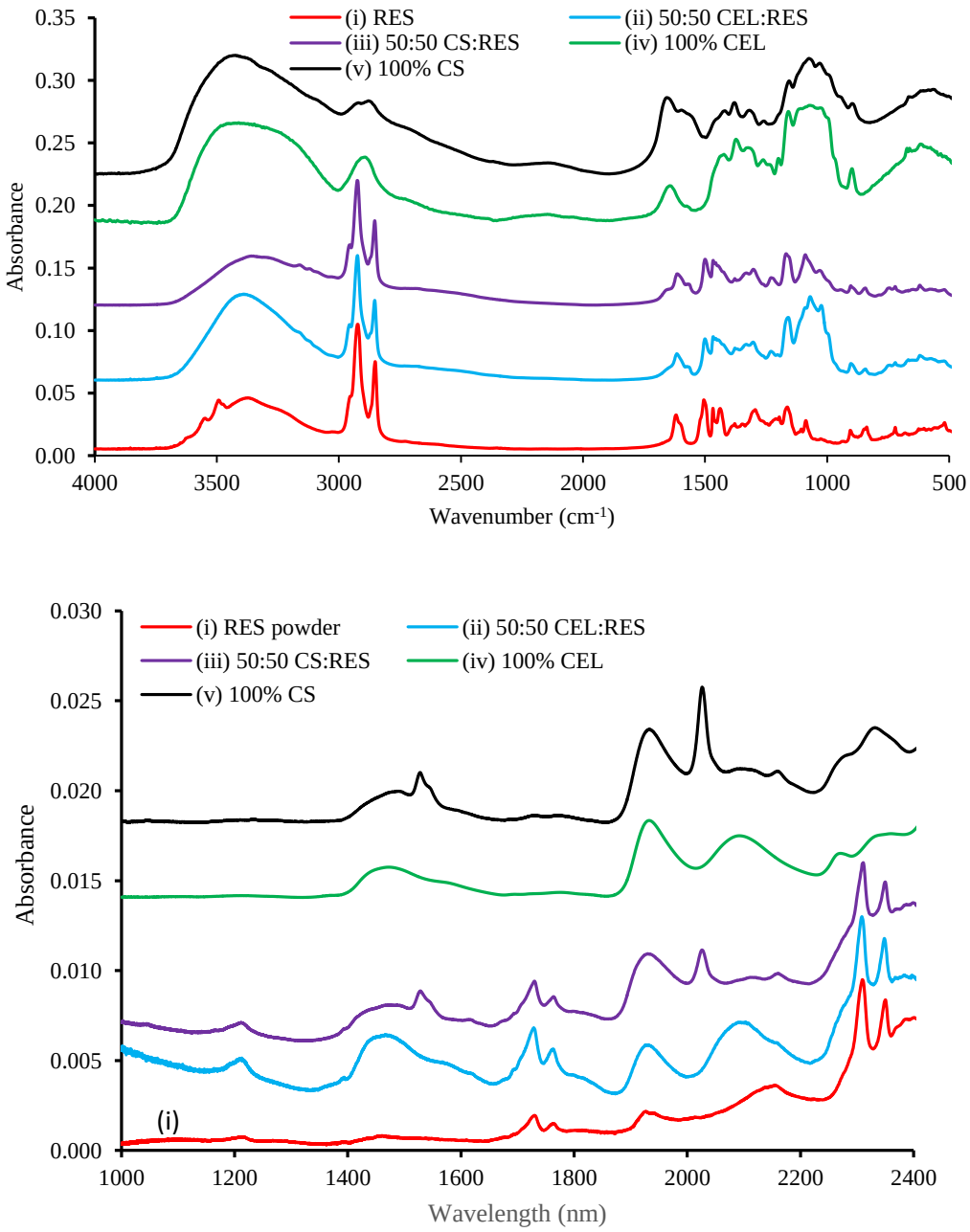

Figure 3-2 FTIR (A) and NIR (B) spectra of composite films. (i) resorcinarene (RES) powder, (ii) 50:50 CEL:RES, (iii) 50:50 CS:RES, (iv) 100% CEL, and (v) 100% CS. The spectra were translated vertically for easier viewing.

Table 3-1 Vibrational frequencies attributed to RES in RES powder, 50:50 CEL:RES and 50:50 CS:RES composite films. The literature values have been included for reference. All frequencies are in wavenumbers (cm^{-1}).

Peak assignment	RES powder	50:50 CEL:RES	50:50 CS:RES	[25]Literature
υ(O-H) H-bonded	3372 broad	3379 broad	3358 broad	3367 broad
υ(CH_3) asym.	2956	2956	2956	2954
υ(CH_2) asym.	2922	2924	2924	2922
υ(CH_2) sym.	2851	2853	2853	2852
υ(C-H) arom.	1618	1615	1613	1620
υ(C-H) arom.	1505	1500	1500	1502
δ(CH_2)	1378	1377	1378	1378
δ(C-H) methine bridge	1163	1159	1167	1154
δ(C-H) ip. arom	1087	1089	1089	1087
δ(C-H) oop. arom.	847	842	843	846

υ-stretch vibration; δ-bending vibration; asym.-asymmetric; sym.-symmetric; arom.-aromatic; ip-in plane; oop-out of plane.

3.3.2. XRD spectroscopy of composite films

XRD is a very valuable technique to investigate the crystal structure of a given compound. In the present case, we used it to investigate the structural changes which could take place to RES as a result of its blending in the polysaccharide matrices. As illustrated in Figure 3-3, the spectrum of RES powder shows typical crystalline peaks at 6.2°, 7.6°, 11.4°, 15.3°, and 18.6° 2θ reflecting the close packing and regular crystallization in its structure. However, XRD spectrum of 100% CEL exhibits typical amorphous bands at 13.0° and 20.6° 2θ which are attributed to cellulose II. Similarly, XRD spectrum of 100% CS exhibits broad bands at 10.8° and 20.2° 2θ. Upon blending RES with these polysaccharides, in addition to the bands attributed to either RES or CS or CEL, new strong bands appeared at 14.7° and 14.6° 2θ in 50:50 CEL:RES and CS:RES respectively. This suggests that the polysaccharides have modified the ordered

packing of RES. This could be due to the establishment of intermolecular interactions between RES and the polysaccharides. These XRD results further reinforce the evidence of compatibility between RES and the polysaccharides which was witnessed in vibrational spectroscopy results. Specifically, as described earlier, RES possesses OH groups which are capable of forming H-bonds with the OH groups from either CEL or CS. More information about these kinds of interactions was obtained from NMR (*vide infra*).

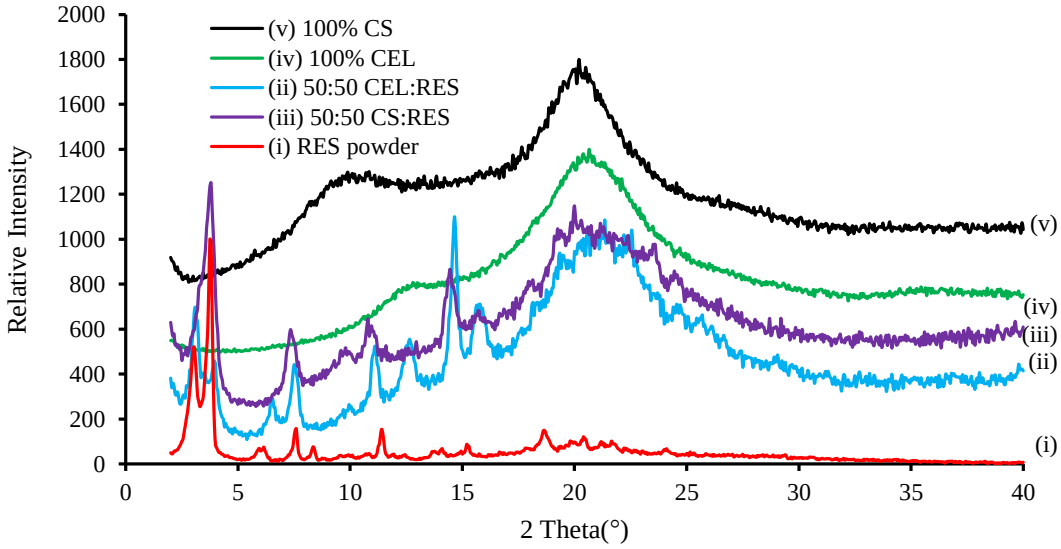

Figure 3-3 X-ray diffraction spectra of (i) RES powder, (ii) 50:50 CEL:RES, (iii) 50:50 CS:RES films; (iv) 100% CEL; and (v) 100% CS films.

3.3.3. ^{13}C CP/MAS NMR spectral studies of RES-based polysaccharide composites

Magic angle spinning (MAS) is a technique commonly used in solid state NMR spectroscopy to increase the resolution of the otherwise broad peaks. Specifically, the sample is spun at the magic angle θ_m=54.74° with respect to the direction of the applied

magnetic field, B_0. This results in narrowing of bands thereby improving the resolution between these bands. However, dilute nuclei such as ^{13}C give rise to very weak signals. To go around this problem, another technique called cross polarization (CP) is used to enhance the signal to noise (S/N) ratio of these dilute nuclei species. In CP, the polarization of abundant spins such as ^{1}H spins is transferred to dilute spins such as ^{13}C. This results in a substantial improvement in the S/N ratio of these naturally dilute spins. Thus, combining CP with MAS results in better S/N ratio and better resolution. For more detailed treatment of this subject, the reader is referred to literature.[33,34]

We, therefore used this combined CP/MAS NMR technique to characterize the miscibility of RES with the polysaccharide (CEL, CS). This was achieved by comparing spectra of composite films with those of pure constituents (i.e. RES, CEL, and CS). Figure 3-4 shows ^{13}C NMR spectra of pure RES, CS, CEL and their composite films. As illustrated in this figure and Table 3-2, RES, CS, and CEL exhibit resonances which are consistent with literature values.[3,35,36] The resonances for RES were consistent with those of the cone conformation. After mixing the RES with either CEL or CS, the resultant composites exhibit bands that are a superposition of those obtained in spectra of the pure constituents. For example, the spectrum for 50:50 CEL:RES show bands that are a mere weighed superposition of those bands obtained for pure CEL and pure RES. This provides further evidence of successful encapsulation of RES in the polysaccharide matrices. However, there were some notable changes which occurred to RES resonances. Specifically, the resonances for alkyl chain underwent an upward shift. The shift was from 33.2 ppm to 29.7 ppm and 30.0 ppm for RES powder, 50:50 CEL:RES and 50:50

CS:RES respectively. This suggests that the conformation of these alkyl chain groups was modified by the polysaccharides.

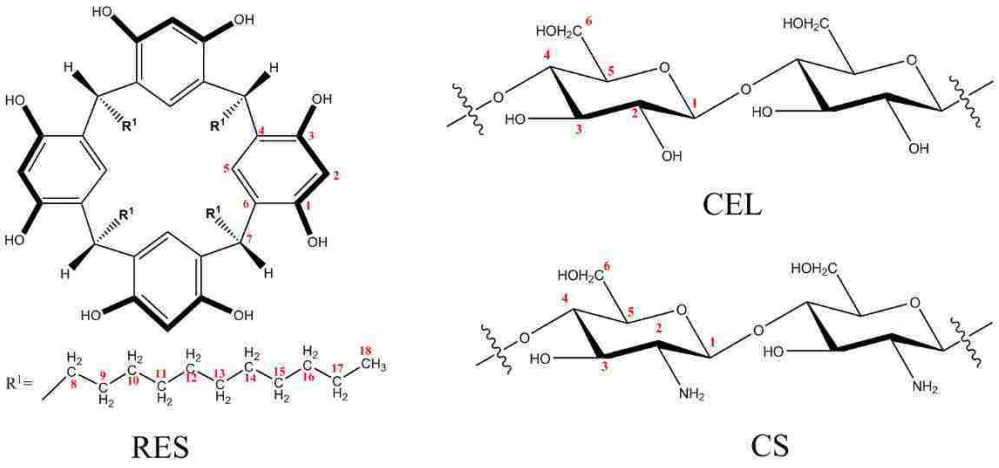

Scheme 3-3 Structures of RES, CEL, and CS used to show numbering in peak assignments in NMR

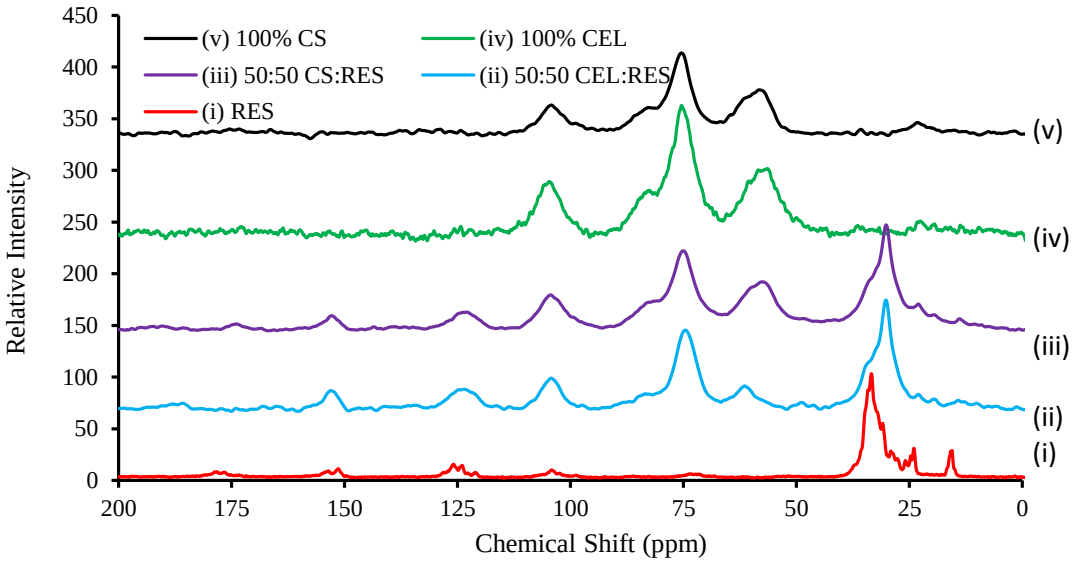

Figure 3-4 ^{13}C CP/MAS NMR spectra of (i) RES powder, (ii) 50:50 CEL:RES, (iii) 50:50 CS:RES, (iv) 100% CEL, and (v) 100% CS films. The spectra have been translated vertically upwards for clarity of presentation.

Table 3-2 ^{13}C solid state NMR chemical shifts of RES powder, 50:50 CEL:RES, 50:50 CS:RES, 100% CEL, and 100% CS films. All chemical shifts are in ppm. The last three columns are literature values of the chemical shifts of RES, 100% CEL and 100% CS.

Peak Assignment	RES powder	50:50 CEL:RES	50:50 CS:RES	100% CEL	100% CS	[a]RES Lit.[3]	[a]100% CEL Lit.[35]	[a]100% CS Lit.[36]
				Resorcinarene (RES)				
C1, C3	152.7, 150.6	152.6	152.2			153.7, 153.1, 151.5, 150.8,		
C2	105.8, 103.3, 101.9	103.6	103.6			103.4, 102.9, 100.9		
C4,C6	127.9, 127.0, 125.0, 123.3	122.4	125.3			123.2, 122.7, 122.3, 121.2		
C5	120.1	122.4	125.3			123.7, 120.0		
C7-C16	33.2, 32.4	29.7, 34.6	30.0, 34.6			33.6, 32.4		
C17	23.1					24.1, 23.4		
C18	14.7, 15.0					16.5, 15.1, 13.9		
				Cellulose/Chitosan				
Peak Assignment	RES powder	50:50 CEL:RES	50:50 CS:RES	100% CEL	100% CS		[a]100% CEL Lit.[35]	[a]100% CS Lit.[36]
C1		103.6	103.6	102.6	102.1		105.7	104.7
C2		73.8	55.7	75.5	57.8		74.8	57.6
C3, C5		73.8	74.7	75.5	75.6		74.8	75.0
C4		83.6	81.8	81.8	83.2		84.4	82.4
C6		60.3	60.8	56.0	62.6		63.0	60.1
CH_3					25.3			23.2

[a]Data was obtained from literature.

3.3.4. Scanning electron microscopy of RES-based composites

The morphology of RES-based composite were analyzed by SEM and the images are presented in Figure 3-5. As illustrated in this figure, the surface and cross sectional images of pure CEL and pure CS exhibit a smooth and homogeneous structure with no signs of phase separation. Although CS and CEL exhibit a similar structure except for the substitutions at C-2, the microstructure of CEL is fibrous as revealed by SEM. Interestingly, the composite films obtained by blending these polysaccharides with RES also exhibit a homogeneous morphology with no areas that could be attributed to either of the constituents. This further corroborates results obtained from vibrational spectroscopy and NMR. In particular, the presence of OH groups in RES enables the formation of H-bonding interactions with the OH of either CEL or CS. The surfaces are dense and non-porous. This dense structure can be rationalized by considering that the films were dried slowly in a home-made drier chamber. During this stage, as water evaporates from the polymer matrix, the polymer chains draw closer to each other and form stronger interactions. In the case of a film containing RES and either CEL or CS, stronger interactions are established between these polysaccharides and RES. The slow speed of this evaporation process ensures that most of the air pockets are closed because the interactions between RES and the polysaccharides are much stronger than those interactions between air and either RES or polysaccharides. However, the cross sectional surfaces of the composite films are rather coarse. This could be due to some crystallization of the RES species inside the polysaccharide matrix. This coarse structure would help in lowering the surface tension of water thereby enhancing the accessibility of the adsorbent sites to the pollutant species.

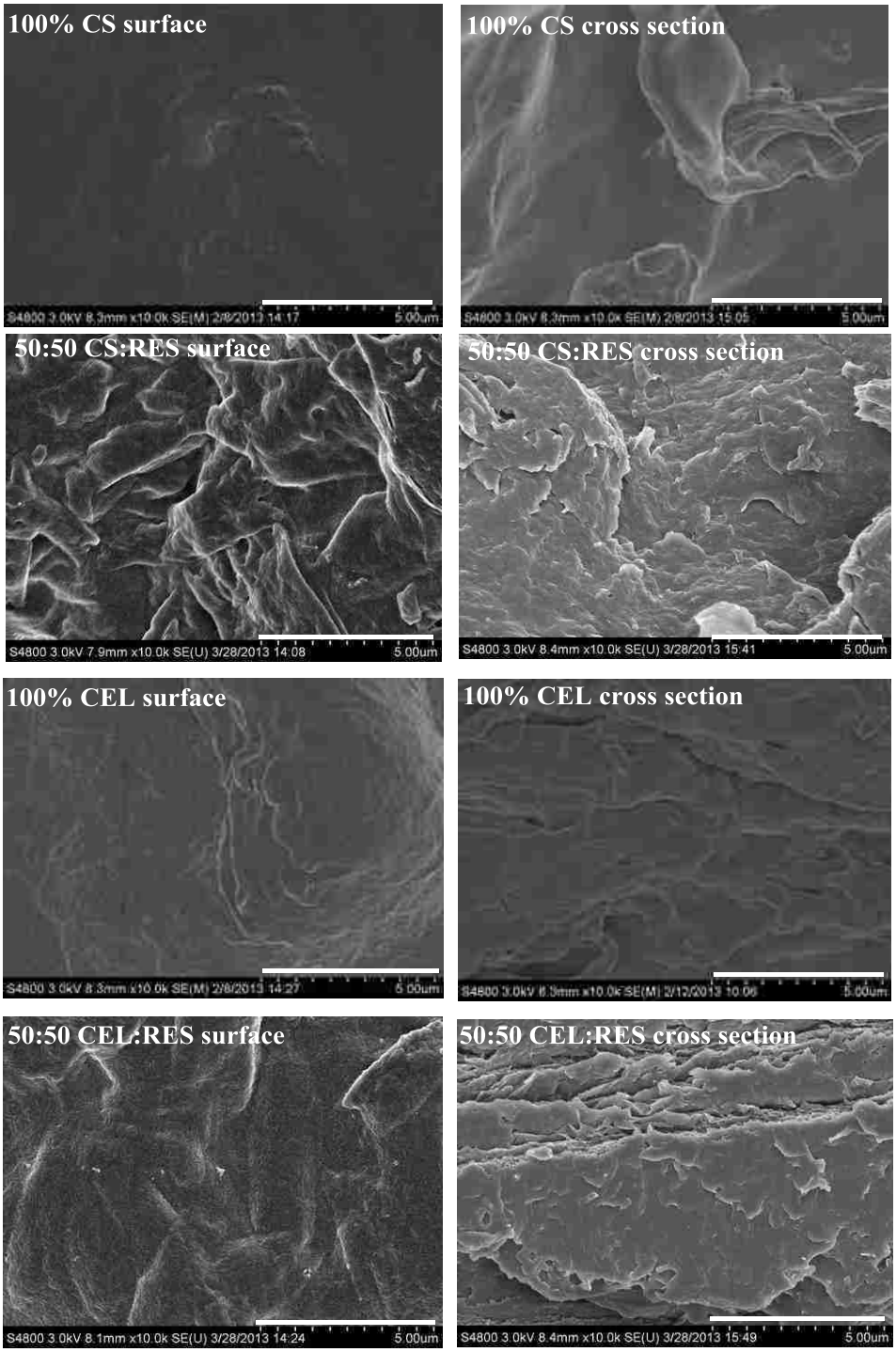

Figure 3-5 SEM images of RES-based polysaccharide composites. First column shows surface images whilst second column shows the cross sectional images of 100% CS (first row), 50:50 CS:RES (second row), 100% CEL (third row), and 50:50 CEL:RES composites (fourth row).

Taken together, FTIR, NIR, XRD, NMR and SEM presented clearly indicate that RES was successfully encapsulated in the polysaccharide matrices. In addition, the evidence presented shows that RES did not undergo any kind of chemical reaction with these polysaccharides or with the ionic liquid. Thus, these novel materials are expected to retain properties of their individual constituents that is they are expected to form host-guest complexes (from RES) with organic species such as phenolic and nitro-aromatic compounds. To test these claims, these novel materials were applied towards adsorption of positional isomers of cresol, toluene, dinitrobenzene, phenol, and nitrobenzene. The results of these experimental studies are presented in the next section.

3.3.5. Applications of RES-based composites

As described earlier, we used UV Vis spectroscopy to monitor the adsorption of phenol, nitrobenzene (NB), and positional isomers of cresol (*o*-, *m*-, and *p*-cresol), dinitrobenzene (*1,2*-, *1,3*-, and *1,4*-dinitrobenzene) and nitrotoluene (*o*-, *m*-, and *p*-nitrotoluene). We monitored the kinetics of adsorption by measuring the absorbance of the analyte solutions at predetermined time points. We chose analytical wavelengths based on the molar absorptivity of the analyte solutions at a concentration of 390 µM. Representative spectra of these analyte solutions and the corresponding analytical wavelengths are shown in Figure 3-6 and Table 3-3 below. As illustrated, these spectra exhibit unique bands in the UV region. The analytical wavelengths were therefore chosen in this region such that the absorbance of a 390 µM solution would be within the range 0.502-0.648 A.U. which lies within the linear range of the UV absorption technique. It should be pointed out however that some of these analytical wavelengths are not necessarily the wavelengths that give the maximum absorbance (λ_{max}). This was because,

at the λ_{max}, the molar absorptivity values were too high to be measured accurately at this 390 µM concentration. This was the case with all substituted nitrobenzene derivatives *i.e.* nitrotoluene and dinitrobenzene isomers. For example, *o*-NT had the lowest molar absorptivity of 5,800 $M^{-1}cm^{-1}$ amongst these nitrobenzene derivatives.[37] At a concentration of 390 µM, it corresponds to an absorbance value of 2.262 A.U. which is outside the validity of Beer's law. Thus, for these analytes, we chose analytical wavelengths which were red-shifted from the λ_{max}. For example, for this *o*-NT, we chose λ_{max}=326 nm with a molar absorptivity of 1,287 $M^{-1}cm^{-1}$ (Table 3-3).

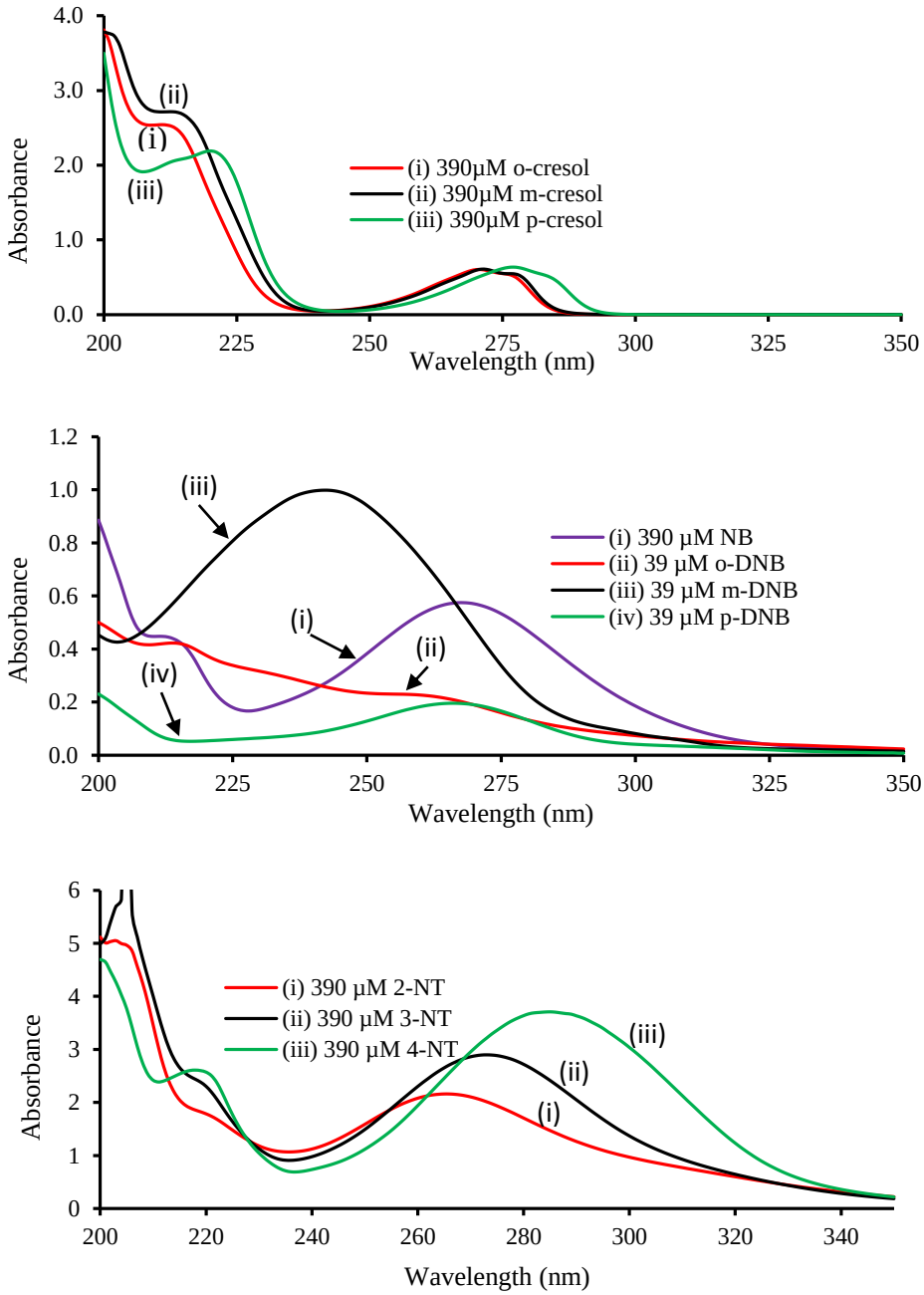

Figure 3-6 UV Visible absorption spectra of the analytes in water. All other analytes were measured at a concentration of 390 µM, except for *o*-, *m*- and *p*-DNB which had a concentration of 39 µM. (A) *o*-, *m*-, and *p*-Cresol; (B) NB, *1,2*-, *1,3*- and *1,4*-DNB; (C) *o*-, *m*-, and *p*-NT.

Table 3-3 Analytical wavelengths together with corresponding molar absorptivity values for aqueous solutions of the aromatic analytes.

Pollutant species	Analytical wavelength λ (nm)	Molar absorptivity ε_λ ($M^{-1}\,cm^{-1}$)
Phenol	270	1492
Nitrobenzene	268	1423
o-Nitrotoluene	326	1287
m-Nitrotoluene	320	1530
p-Nitrotoluene	330	1654
1,2-Dinitrobenzene	304	1661
1,3-Dinitrobenzene	295	1565
1,4-Dinitrobenzene	320	1573
o-Cresol	271	1547
m-Cresol	271	1560
p-Cresol	277	1644

Figure 3-7 shows traces for typical absorption changes for the adsorption of 1,2-DNB onto the different composite films. As illustrated, over time, the absorbance decreases due to the adsorption of the analyte species. This is because as the analyte species are being adsorbed onto a solid surface thereby decreasing there concentration in solution. From these measured absorbances, the amount adsorbed at each up to each time point, q_t, can then be calculated using the mass balance equation (*i.e.* $q_t = [(C_o - C_t)V]/W$) which was introduced in the previous Chapter. Typical curves obtained after this calculation are shown in Figure 3-8. It is clear from such traces that the adsorption profiles of the analytes onto the different composite films follow the same pattern. Specifically, during initial stages of adsorption, the rate of adsorption is almost linear. However, over time, this rate slows down until it reaches equilibrium. It is also clear from Figure 3-7 and Figure 3-8, that the efficiency of the composite films are different. For example, pure 100% CEL and 100% CS adsorb less amount of analyte at

equilibrium than the amount that is adsorbed by those composites containing RES (*i.e.* 50:50 CEL/CS:RES). This suggests that some favorable interactions between the analyte species and RES give rise to stronger complexes which in turn manifest in higher adsorption at equilibrium. This is hardly surprising since RES, with benzene rings in its structure can interact with these aromatic analytes through π-π interactions. More detailed discussion on the nature of these interactions will be discussed later in this section.

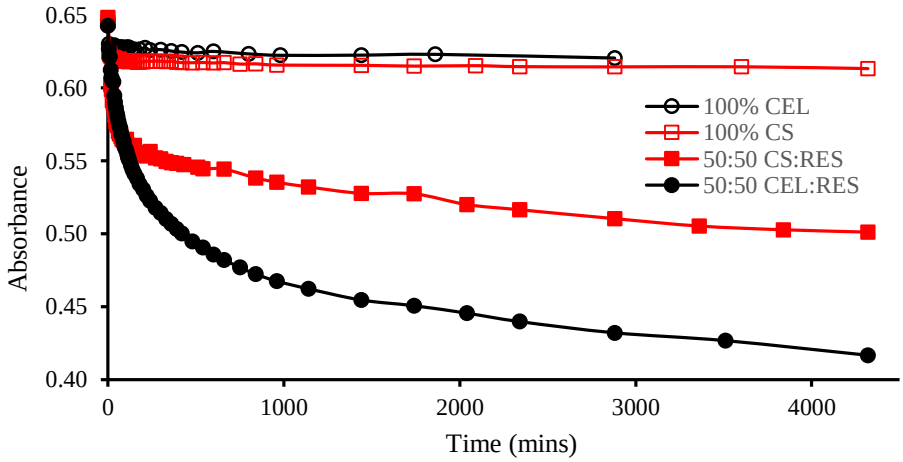

Figure 3-7 Typical absorbance-time profiles for the adsorption of 1,2-DNB onto the different composite films.

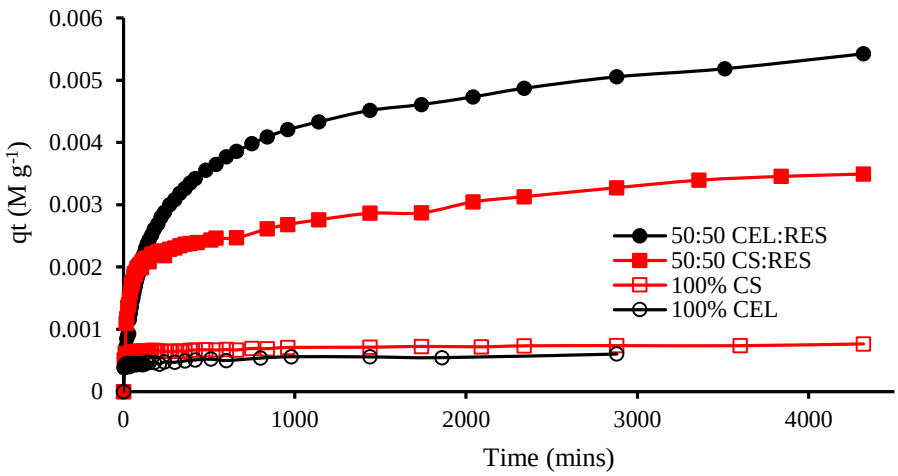

Figure 3-8 Typical q_t vs time profiles for the adsorption of 1,2-DNB onto the different composite films.

Detailed information about the mechanism of adsorption was obtained by fitting the kinetic data to pseudo first order and pseudo second order models. Theoretical treatment of these models have been presented in the previous Chapter 2. Two important parameters can be obtained from these models *viz* amount adsorbed at equilibrium, q_e and rate constants, k. These parameters can then be used to evaluate the efficiency of these different adsorbents. Such information is necessary to design and optimize the conditions for efficient adsorption of these analytes. Typical linearized plots for pseudo first order and pseudo second order are shown in Figure 3-9. It is evident from these plots that data fitted better to pseudo second order than to pseudo first order model. We then used two goodness of fit parameters (R^2 and MSC) to show that the pseudo second order fits relatively better than the pseudo first order model. As was the case in the graphical plots, both R^2 and MSc values for pseudo second order were consistently higher than the corresponding values for pseudo first order model (Table 3-4 and 1-5). In addition,

experimental q_e values matched those obtained from pseudo second order fitting. These results suggests that the adsorption of these analytes onto the studied composite films is described better by the pseudo second order model. Accordingly, we used pseudo second order model fit parameters to evaluate the performance of these composite films. In addition, we could also compare the effect of the introduction of substituent groups to the benzene ring of the analytes. Furthermore, we could compare the effect of substituted position on the adsorption behavior of positional isomers of the analytes.

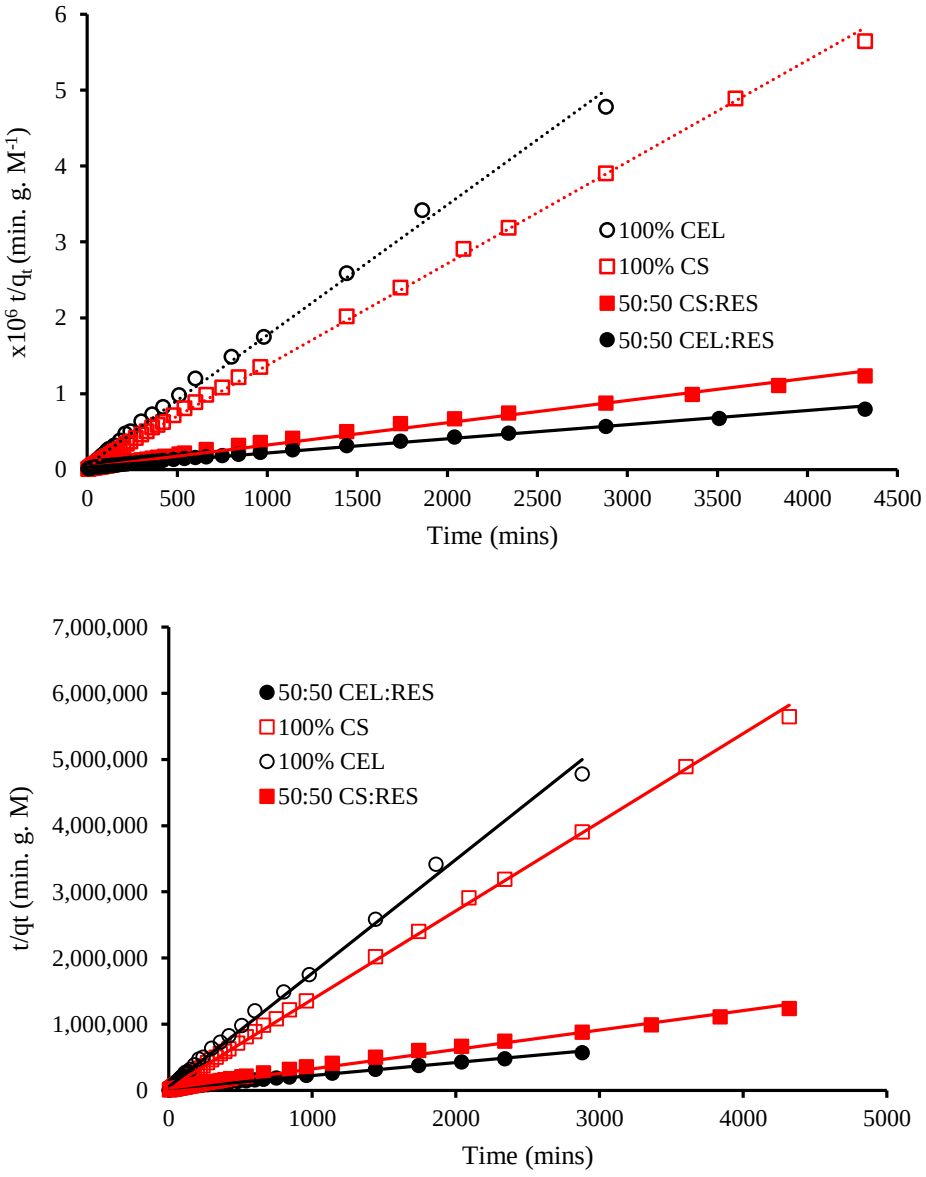

Figure 3-9 Typical linearized plots for (A) pseudo second order and (B) pseudo first order models for the adsorption of 1,2-DNB onto the four different composite films.

Table 3-4 Kinetic parameters obtained by fitting pseudo second order and pseudo first order models to the adsorption of the aromatic analytes to the four composite films.

				Pseudo second order model				Pseudo first order model			
CEL	RES	CS	$q_{e,exp}$ ($M\ g^{-1}$)	$q_{e,calc}$ ($M\ g^{-1}$)	k_1 ()	R^2	MSC	$q_{e,calc}$ ($M\ g^{-1}$)	k_2 ()	R^2	MSC
						1,2-Dinitrobenzene (1,2-DNB)					
100			0.60	0.583(6)	50(10)	0.9964	5.8389	0.18(1)	0.9(1)	0.6576	0.9606
		100	0.765	0.747(3)	46(8)	0.9990	6.8438	0.146(7)	0.59(6)	0.6892	1.0900
50	50		5.4	5.37(5)	1.02(6)	0.9953	5.2814	3.6(1)	0.86(3)	0.9228	2.4865
	50	50	3.49	3.41(4)	2.7(4)	0.9929	4.8678	1.77(6)	0.83(4)	0.9185	2.4641
						1,3-Dinitrobenzene (1,3-DNB)					
100			0.459	0.445(4)	100(30)	0.9968	5.9452	0.094(9)	1.0(2)	0.4074	0.4121
		100	0.72	0.738(2)	190(30)	0.9996	8.4031	0.17(4)	22(3)	0.7172	1.1251
50	50		4.6	4.52(3)	1.7(1)	0.9970	6.1920	2.6(1)	0.86(5)	0.8564	1.8650
	50	50	3.11	3.07(2)	4.2(5)	0.9968	5.6716	1.28(6)	0.94(5)	0.8894	2.1344
						1,4-Dinitrobenzene (1,4-DNB)					
100			0.33	0.324(4)	1000	0.9965	6.0938	0.18(6)	90(10)	0.8807	1.7629
		100	1.38	1.39(2)	19(3)	0.9951	5.6487	0.50(2)	2.0(2)	0.7972	1.4781
50	50		2.96	2.74(4)	3.9(7)	0.9906	4.5928	1.28(5)	0.40(4)	0.6570	0.9960
	50	50	2.92	2.90(2)	4.8(6)	0.9972	5.7952	1.11(6)	1.05(6)	0.8696	1.9569
						Nitrobenzene (NB)					
100			0.82	0.82(4)	10(2)	0.9673	3.1984	0.64(2)	1.65(8)	0.9656	3.1467
		100	1.48	1.48(4)	14(3)	0.9902	4.4034	0.87(4)	2.6(1)	0.9527	2.8288
50	50		8.3	8.45(3)	2.29(7)	0.9995	7.4583	4.6(2)	3.5(2)	0.9353	2.6264
	50	50	5.2	5.25(4)	5.2(4)	0.9986	7.4583	2.6(2)	3.6(3)	0.8284	1.6198

Table 3-5 Kinetic parameters obtained by fitting pseudo second order and pseudo first order models to the adsorption of aromatic analytes to the four composite films.

				Pseudo second order model				Pseudo first order model			
CEL	RES	CS	$q_{e,exp}$ (M g^{-1})	$q_{e,calc}$ (M g^{-1})	k_2 ()	R^2	MSC	$q_{e,calc}$ (M g^{-1})	k_1 ()	R^2	MSC
							o-Nitrotoluene (*o*-NT)				
100			2.27	2.7(2)	1.0(1)	0.9393	2.6020	2.29(9)	2.4(1)	0.9691	3.2780
		100	2.0	2.1(1)	2.8(5)	0.9449	2.6989	1.6(1)	2.9(2)	0.9095	2.1915
50	50		10.6	10.79(6)	2.2(2)	0.9994	7.1615	4.5(4)	3.1(2)	0.9202	2.3174
	50	50	8.0	8.08(5)	3.9(4)	0.9994	7.2987	2.6(3)	2.8(3)	0.8337	1.5834
							m-Nitrotoluene (*m*-NT)				
50	50		11.5	11.68(2)	2.17(8)	0.9999	9.2329	4.4(4)	2.8(2)	0.9409	2.6461
	50	50	8.9	8.96(1)	6.2(2)	0.9999	9.1570	2.4(3)	4.3(3)	0.7810	1.4316
							p-Nitrotoluene (*p*-NT)				
50	50		10.9	10.98(3)	3.0(2)	0.9998	8.5812	3.2(4)	2.7(2)	0.8600	1.7921
	50	50	8.6	8.74(2)	6.3(2)	0.9998	8.6515	5.7(2)	15.0(4)	0.9769	3.6383
							Phenol				
50	50		0.414	0.486(3)	98(7)	0.9985	6.4158	0.23(3)	24(2)	0.8893	2.0528
	50	50	0.846	0.827(7)	37(3)	0.9972	5.7840	0.36(2)	3.0(3)	0.7456	1.2546
							o-Cresol				
50	50		1.01	1.010(3)	25(2)	0.9996	14.7191	0.30(2)	1.22(7)	0.8561	1.8631
							m-Cresol				
50	50		0.98	0.977(3)	14.3(8)	0.9993	7.2594	0.42(3)	1.04(7)	0.8066	1.5674
							p-Cresol				
50	50		1.13	1.143(6)	55(8)	0.9994	7.2812	0.89(9)	20(1)	0.9381	2.5823

The q_e data obtained by pseudo second order model were used to construct a 3D bar chart to illustrate clearly the performance of the different composite films (Figure 3-10). Interestingly, both [CEL+RES] and [CS+RES] composite adsorbed consistently higher amounts of nitro-aromatic species than the amount adsorbed by their pure 100% CEL and 100% CS counterparts. For example, 100% CEL and 100% CS adsorbed 2.7±0.2 $M^{-1}g^{-1}$ and 2.1±0.1 $M^{-1}g^{-1}$ of *o*-NT respectively. On adding 50% RES onto each of CEL and CS, the resultant composites adsorbed almost 4X the amount of *o*-NT that was adsorbed by pure 100% CEL and 100% CS (Table 3-5). This could be rationalized by considering the structures of the analytes in relation to the structures of the adsorbents. All analyte species contain a substituted benzene ring. Their structures only differ in the substituents attached to this benzene ring. On the other hand, the adsorbents exhibit very different structures. Whereas RES contain four benzene rings and eight hydroxyl groups in its macrocyclic structure, both CEL and CS contain anhydroglucose and glucosamine residues in their polymeric structures. Therefore, whereas RES can interact through its π-electrons in addition to H-bonding through its resorcinol hydroxyl groups and van der Waals interactions, both CEL and CS can only interact through van der Waals forces and H-bonding. Compared to the structures of analyte species, RES can form π-π interactions in addition to the VDW and H-bonds. In addition, RES, with its macrocyclic cavity, can form inclusion complexes with the analyte species. Conversely, both CEL and CS can only interact through VDW and H-bonding. Therefore, on this basis, RES is justifiably expected to form stronger complexes with these analyte species than the complexes formed between these species and either CEL or CS. Consequently, RES-containing composite films adsorb more pollutant than either pure 100% CEL or 100% CS.

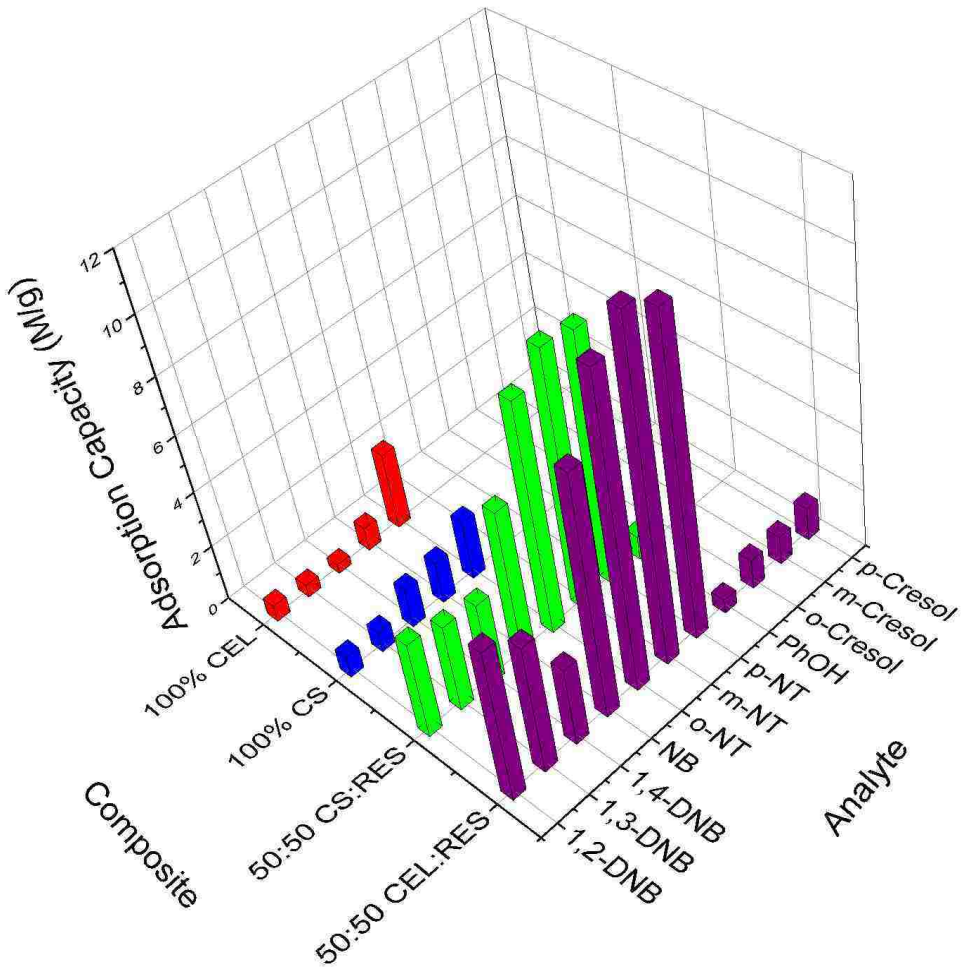

Figure 3-10 3D representation of adsorption capacity of various organic pollutants by 100% CEL (red), 100% CS (blue), 50:50 CS:RES (green) and 50:50 CEL:RES (purple).

It is also interesting to note that in most cases, 100% CS adsorbed more analyte species than 100% CEL. For example, the latter adsorbed 0.82±0.04 $M^{-1}g^{-1}$ of NB, while the former adsorbed 1.48±0.04 $M^{-1}g^{-1}$ which is almost twice as much. These results corroborate previous findings that CS, with its amino groups, can form stronger

complexes than CEL except in the case of *o*-NT, 100% CEL adsorbed slightly higher amount (2.7±0.2 $M^{-1}g^{-1}$) than that by 100% CS (2.1±0.1 $M^{-1}g^{-1}$). There may be large uncertainty associated with these results as R^2 and MSC values for these adsorptions were not very high compared to all the other pseudo second order fits.

In previous studies, it has been reported that nitro-aromatic species can form π-π electron donor acceptor (EDA) complexes with π-electron rich adsorbents. For example, in one study, it was concluded that the strong adsorptive interaction between nitro-aromatics and carbon nanotubes was due to the π-π EDA interaction between nitro-aromatic molecules (electron acceptors) and the highly polarizable grapheme sheets (electron donors) of carbon nanotubes.[38] Since the benzene rings in RES are substituted by –OH groups (two per each benzene ring) which are electron releasing, we expect RES to be rich in π-electrons. Therefore, RES is expected to form stronger π-π interactions with those analytes possessing an electron deficient aromatic system. We therefore investigated this possibility by comparing the adsorption of NB against phenol onto RES-based composite films. Interestingly, RES-based composite films adsorbed consistently higher amounts of nitrobenzene than phenol. Specifically, whereas only 0.486±0.003 $M^{-1}g^{-1}$ of phenol was adsorbed by 50:50 CEL:RES composite films, at least 17X as much NB (8.45±0.03 $M^{-1}g^{-1}$) was adsorbed by the same composite film. In another similar case, whereas 0.827±0.007 $M^{-1}g^{-1}$ of phenol was adsorbed by 50:50 CS:RES composite film, almost 7X as much NB (5.25±0.04 $M^{-1}g^{-1}$) was adsorbed by this same composite film. Such higher selectivity for NB over phenol that is being exhibited by RES-based composites can be attributed to the strength of EDA complexes formed between RES and these aromatic species. Whereas phenol is more electron rich, NB is more electron

deficient due to the activating and deactivating effects of phenol and NB respectively. Consequently, electron deficient NB forms stronger complexes with electron rich RES than the complexes formed between electron rich phenol and electron rich RES. The interactions between RES and NB are more like electrostatic than the more hydrophobic interactions between RES and phenol. These results suggest that H-bonding interactions between RES and phenol are insignificant compared with the EDA interactions between RES and NB.

We also investigated the effect of adding another methyl- and nitro- substituents onto phenol (to make cresols) and nitrobenzene (to make dinitrobenzene, DNBs) respectively. Whereas methyl group is electron releasing, nitro group is electron withdrawing. Therefore, cresols are expected to be more electron rich than phenol. Similarly, DNBs are expected to be more electron deficient than NB. Consequently, if the EDA mechanism still holds, less amount of cresols should be adsorbed than the amount adsorbed for phenol. Likewise, more DNB should adsorbed at equilibrium than NB. However, the results in Table 3-5 seem to contradict these expectations. Essentially, more cresol was adsorbed than phenol and less DNB was adsorbed than NB. For example, at least twice as much cresol as phenol was adsorbed by 50:50 CEL:RES composite film. The same trend was observed for DNBs. These results suggest that other mechanisms could be at play when an additional substituent is added to these benzene derivatives. We propose that cresols could be interacting through their methyl groups, with the more oleophilic undecyl groups in RES. The trend in the adsorption of DNBs compared to NB is still very unclear at this time.

We also investigated the possibility of formation of inclusion complexes between RES and the aromatic analytes. This was accomplished by comparing the q_e values obtained for the different positional isomers of DNB, cresol and NT. Considering the q_e values obtained for cresol and NT isomers, it is clear that RES did not exhibit any discernible selectivity amongst these isomers. For example, one g of 50:50 CEL:RES adsorbed 10.79±0.06 mol L^{-1}, 11.68±0.02 mol L^{-1}, and 10.98±0.03 mol L^{-1} *o*-, *m*-, and *p*-NT respectively. Likewise, one g of 50:50 CEL:RES adsorbed 1.010±0.003 mol L^{-1}, 0.977±0.003 mol L^{-1}, and 1.143±0.006 mol L^{-1} *o*-, *m*-, and *p*-cresol respectively. Interestingly, RES-based composite films show some selectivity amongst the DNB isomers. For example, one g of 50:50 CEL:RES composite film adsorbed more *1,2*-DNB (5.37±0.05 mol L^{-1}) than *1,3*-DNB (4.52±0.03 mol L^{-1}) which was in turn more than *1,4*-DNB (2.74±0.04 mol L^{-1}). Such results seem to suggest that inclusion complexes were formed between RES and DNBs. In this case, only the benzene part is included and not the nitro-substituents. Therefore, a larger part of 1,2-DNB is included than 1,3-DNB. Thus more π-π EDA interactions were formed between the former and RES. Consequently, stronger complexes were formed between RES and 1,2-DNB than between RES and 1,3-DNB. If the *p*-substituted DNB, 1,4-DNB form an inclusion complex with RES, one of the nitro groups would be inserted into the cavity. This is unfavorable given the bulky nature of the nitro groups. Thus, 1,4-DNB exhibited the lowest q_e values for both [CEL+RES] and [CS+RES].

In all these studies, NT exhibited the highest q_e values than the other analytes (NB, DNB, cresol and phenol) for adsorption onto 50:50 CEL:RES composite films. This seems to suggest that the methyl group and the nitro group act synergistically to enhance

the interactions between RES and NT. The exact mechanism of adsorption of these NT isomers is still unclear at this time. However, these results help to advance valuable knowledge in the design of better adsorbents for such kinds of analyte species. An additional observation was that despite 100% CS being more superior to 100% CEL in terms of adsorption of these analytes, [CS+RES] composite film was inferior to [CEL+RES]. For example, whereas one g 50:50 CS:RES adsorbed 8.08±0.05 mol L^{-1} *o*-NT, the equivalent amount of 50:50 CEL:RES adsorbed 10.79±0.06 mol L^{-1} of this *o*-NT pollutant species. Such behavior suggest that CEL and RES interact synergistically to adsorb more pollutant than CS and RES. Nevertheless, both composites exhibited the highest q_e values than those composites containing pure 100% CEL and 100% CS.

Intra-particle diffusion model was used to gain more insight into the stages involved in the adsorption of these aromatic species. This model assumes that the rate limiting step in adsorption is the diffusion of analyte species into the pores of the adsorbent to access the inner adsorbent sites. This model is represented by the equation ($q_t = k_i t^{0.5} + I$) where k_i is the diffusion rate constant and I is a constant that gives information about the thickness of the boundary layer.[39] According to this model, if the plot of q_t vs square root of t is linear over the whole range, then the adsorption process is controlled by intra-particle diffusion, while, if the data exhibit multi-linear regions, then at least two steps are determining the rate of adsorption. As can be seen from the representative plots of qt vs $t^{0.5}$ (Figure 3-11) and the data in Table 3-6, all the data exhibit two linear regions except for 100% CEL and 100% CS. Thus, in those cases when there was only one linear region, the adsorption process was solely controlled by intra-particle diffusion. In cases where there were two linear regions, the first region was

characterized by higher slope than the second region. Such observations have been reported in many adsorption studies. The first region is attributed to the instantaneous utilization of adsorption sites on the surfaces of the composite films. The second region is characterized by slow diffusion of the analyte species onto the inner pores of the composites. It is interesting to note that all the cresols and phenols exhibited the slowest rates than NB, DNB and NT species.

Table 3-6 Intra particle diffusion data for adsorption of pollutant species onto the composite films.

CEL	RES	CS	k_{i1}	R^2	k_{i2}	R^2
			1,2-Dinitrobenzene (1,2-DNB)			
100			0.0037(2)	0.8945		
		100	0.017(2)	0.8717	0.0022	0.9310
50	50		0.205(2)	0.9966	0.036(1)	0.9905
	50	50	0.250(9)	0.9924	0.0262(4)	0.9942
			1,3-Dinitrobenzene (1,3-DNB)			
100			0.0018(2)	0.6497		
		100	0.026(2)	0.9490		
50	50		0.240(5)	0.9890	0.0269(8)	0.9902
	50	50	0.244(5)	0.9963	0.0169(2)	0.9951
			1,4-Dinitrobenzene (1,4-DNB)			
100						
		100	0.060(5)	0.9534	0.0127(4)	0.9853
50	50		0.227(6)	0.9918	0.0241(4)	0.9911
	50	50	0.25(1)	0.9821	0.0171(2)	0.9964
			Nitrobenzene (NB)			
100			0.191(1)	0.9462		
		100	0.0250(5)	0.9933		
50	50		0.60(1)	0.9964	0.058(5)	0.9519
	50	50	0.46(1)	0.9907	0.078(5)	0.9617

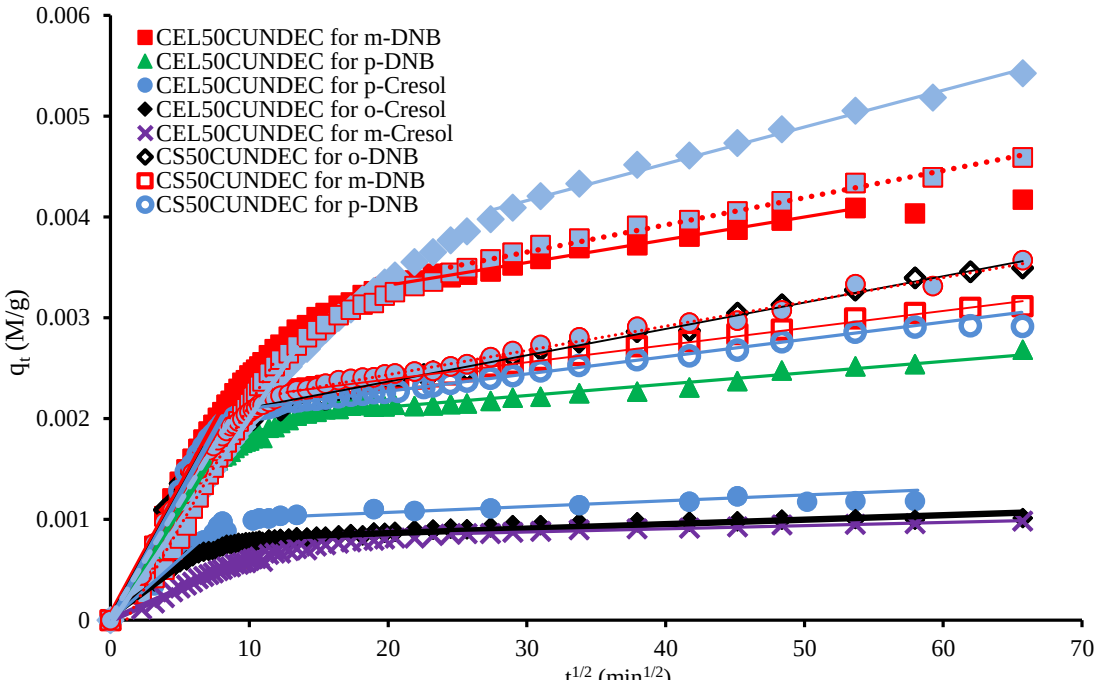

Figure 3-11 Intra-particle diffusion plot for the adsorption of 1,2-DNB onto 100% CEL, 100% CS, 50:50 CEL:RES and 50:50 CS:RES composite films

3.4. Conclusions

The findings of this study reaffirms the possibility of packaging the desirable properties of two individual components into one composite. This was achieved by using a non-derivatizing solvent, $BMIm^{+}Cl^{-}$ to dissolve and regenerate RES-based polysaccharide composite s. The resultant composites exhibited properties of their individual constituents. Specifically, polysaccharides, CEL and CS enabled the formation of films whilst RES imparted selectivity to the corresponding composites. These RES-containing composites were found to be more selective than pure CEL and CS for the adsorption of NB, DNB, and NT isomers. These results are consistent with the formation

of π-π EDA complexes between the π electron rich RES and the π electron deficient analytes. In addition, RES-based composites exhibited selectivity amongst the positional isomers of DNB. Such differences could be rationalized by considering the formation of inclusion complexes between RES and each of *1,2*- and *1,3*-DNB. It was also found out that nitro and methyl groups are prerequisites for better adsorption of benzene-substituted analyte species by RES-based composites. Thus, the information presented in this report will set a platform for understanding that the mechanism of adsorption of aromatic species depends on the type of substituents and the position of aromatic substitution. Such information is vital in developing robust adsorbents for removal and recovery of the potentially toxic organic species from water.

3.5. References

1. MacGillivray, L. R.; Diamente, P. R.; Reid, J. L.; Ripmeester, J. A., Encapsulation of two aromatics by a carcerand-like capsule of nanometer-scale dimensions. *Chem. Commun. (Cambridge)* **2000,** (5), 359-360.

2. Farrugia, L. J., ORTEP-3 for windows - a version of ORTEP-III with a graphical user interface (GUI). *J. Appl. Crystallogr.* **1997,** *30* (5, Pt. 1), 565.

3. Pietraszkiewicz, M.; Pietraszkiewicz, O.; Kolodziejski, W.; Wozniak, K.; Feeder, N.; Benevelli, F.; Klinowski, J., x-ray Diffraction and 13C Solid-State NMR Studies of the Dimethylformamide Solvate of Tetra(C-undecyl)calix[4]resorcinarene. *J. Phys. Chem. B* **2000,** *104*, 1921-1926.

4. Timmerman, P.; Verboom, W.; Reinhoudt, D. N., Resorcinarenes. *Tetrahedron* **1996,** *52* (8), 2663-704.

5. Rebilly, J.-N.; Reinaud, O., Calixarenes and resorcinarenes as scaffolds for supramolecular metallo-enzyme mimicry. *Supramol. Chem.* **2014,** *26*, 454-479.

6. Lawrence, D. S.; Jiang, T.; Levett, M., Self-Assembling Supramolecular Complexes. *Chem. Rev. (Washington, D. C.)* **1995,** *95*, 2229-60.

7. Ruderisch, A.; Iwanek, W.; Pfeiffer, J.; Fischer, G.; Albert, K.; Schurig, V., Synthesis and characterization of a novel resorcinarene-based stationary phase bearing polar headgroups for use in reversed-phase high-performance liquid chromatography. *J. Chromatogr. A* **2005,** *1095*, 40-49.

8. Ruderisch, A.; Pfeiffer, J.; Schurig, V., Mixed chiral stationary phase containing modified resorcinarene and β-cyclodextrin selectors bonded to a polysiloxane for enantioselective gas chromatography. *J. Chromatogr., A* **2003,** *994*, 127-135.

9. Boerrigter, H.; Verboom, W.; Reinhoudt, D. N., Novel Resorcinarene Cavitand-Based CMP(O) Cation Ligands: Synthesis and Extraction Properties. *J. Org. Chem.* **1997,** *62*, 7148-7155.

10. Benosmane, N.; Hamdi, S. M.; Hamdi, M.; Boutemeur, B., Selective transport of metal ions across polymer inclusion membranes (PIMs) containing calix[4]resorcinarenes. *Sep. Purif. Technol.* **2009,** *65*, 211-219.

11. Ugur, A.; Sener, I.; Hol, A.; Alpoguz, H. K.; Elci, L., Facilitated Transport of Zn(II) and Cd(II) Ions Through Polymer Inclusion Membranes Immobilized With a Calix[4]resorcinarene Derivative. *J. Macromol. Sci., Part A Pure Appl. Chem.* **2014,** *51*, 611-618.

12. Benjjar, A.; Eljaddi, T.; Kamal, O.; Touaj, K.; Lebrun, L.; Hlaibi, M., The development of new supported liquid membranes (SLMs) with agents: Methyl cholate and resorcinarene as carriers for the removal of dichromate ions (Cr2O2-7). *J. Environ. Chem. Eng.* **2014,** *2*, 503-509.

13. Wei, A.; Kim, B.; Pusztay, S. V.; Tripp, S. L.; Balasubramanian, R., Resorcinarene-encapsulated nanoparticles: Building blocks for self-assembled nanostructures. *J. Inclusion Phenom. Macrocyclic Chem.* **2001,** *41*, 83-86.

14. Mu, Y.; Rozendal, R. A.; Rabaey, K.; Keller, J., Nitrobenzene Removal in Bioelectrochemical Systems. *Environ. Sci. Technol.* **2009,** *43*, 8690-8695.

15. Keith, L.; Telliard, W., ES&T special report: priority pollutants: Ia perspective view. *Environ. Sci. Technol.* **1979,** *13*, 416-423.

16. Busca, G.; Berardinelli, S.; Resini, C.; Arrighi, L., Technologies for the removal of phenol from fluid streams: A short review of recent developments. *J. Hazard. Mater.* **2008,** *160*, 265-288.

17. Singh, R. K.; Kumar, S.; Kumar, S.; Kumar, A., Biodegradation kinetic studies for the removal of p-cresol from wastewater using Gliomastix indicus MTCC 3869. *Biochem. Eng. J.* **2008,** *40*, 293-303.

18. Kennedy, L. J.; Vijaya, J. J.; Sekaran, G.; Kayalvizhi, K., Equilibrium, kinetic and thermodynamic studies on the adsorption of m-cresol onto micro- and mesoporous carbon. *J. Hazard. Mater.* **2007,** *149*, 134-143.

19. Brunet, P.; Dou, L.; Cerini, C.; Berland, Y., Protein-bound uremic retention solutes. *Adv. Ren. Replace Ther.* **2003,** *10*, 310-20.

20. Wernert, V.; Schaef, O.; Faure, V.; Brunet, P.; Dou, L.; Berland, Y.; Boulet, P.; Kuchta, B.; Denoyel, R., Adsorption of the uremic toxin p-cresol onto hemodialysis membranes and microporous adsorbent zeolite silicalite. *J. Biotechnol.* **2006,** *123*, 164-173.

21. Majumder, P. S.; Gupta, S. K., Hybrid reactor for priority pollutant nitrobenzene removal. *Water Res.* **2003,** *37*, 4331-4336.

22. Guo, D.; Ma, J.; Li, R.; Guo, C., Genotoxicity effect of nitrobenzene on soybean (Glycine max) root tip cells. *J. Hazard. Mater.* **2010,** *178*, 1030-1034.

23. Boyd, S. A.; Sheng, G.; Teppen, B. J.; Johnston, C. T., Mechanisms for the Adsorption of Substituted Nitrobenzenes by Smectite Clays. *Environ. Sci. Technol.* **2001,** *35*, 4227-4234.

24. Duri, S.; Majoni, S.; Hossenlopp, J. M.; Tran, C. D., Determination of Chemical Homogeneity of Fire Retardant Polymeric Nanocomposite Materials by Near-Infrared Multispectral Imaging Microscopy. *Anal. Lett.* **2010,** *43*, 1780-1789.

25. Moreira, W. C.; Dutton, P. J.; Aroca, R., Langmuir-Blodgett Monolayers and Vibrational Spectra of Calix[4]Resorcinarene. *Langmuir* **1994,** *10*, 4148-52.

26. Sapper, H.; Cameron, D. G.; Mantsch, H. H., The thermotropic phase behavior of ascorbyl palmitate: an infrared spectroscopic study. *Can. J. Chem.* **1981,** *59*, 2543-9.

27. De Miguel, G.; Pedrosa, J. M.; Martin-Romero, M. T.; Munoz, E.; Richardson, T. H.; Camacho, L., Conformational Changes of a Calix[8]arene Derivative at the Air-Water Interface. *J. Phys. Chem. B* **2005,** *109*, 3998-4006.

28. Byrd, H.; Whipps, S.; Pike, J. K.; Ma, J.; Nagler, S. E.; Talham, D. R., Role of the template layer in organizing self-assembled films: zirconium phosphonate monolayers and multilayers at a Langmuir-Blodgett template. *J. Am. Chem. Soc.* **1994,** *116*, 295-301.

29. Porter, M. D.; Bright, T. B.; Allara, D. L.; Chidsey, C. E. D., Spontaneously organized molecular assemblies. 4. Structural characterization of n-alkyl thiol monolayers on gold by optical ellipsometry, infrared spectroscopy, and electrochemistry. *J. Am. Chem. Soc.* **1987,** *109*, 3559-68.

30. Kuzmicz, R.; Kowalska, V.; Domagala, S.; Stachowicz, M.; Wozniak, K.; Kolodziejski, W., X-ray Diffraction, FT-IR, and 13C CP/MAS NMR Structural Studies of Solvated and Desolvated C-Methylcalix[4]resorcinarene. *J. Phys. Chem. B* **2010,** *114*, 10311-10320.

31. Yan, J.; Villarreal, N.; Xu, B., Characterization of Degradation of Cotton Cellulosic Fibers Through Near Infrared Spectroscopy. *J. Polym. Environ.* **2013,** *21*, 902-909.

32. Tsuchikawa, S.; Siesler, H. W., Near-infrared spectroscopic monitoring of the diffusion process of deuterium-labeled molecules in wood. Part I: Softwood. *Appl. Spectrosc.* **2003,** *57*, 667-674.

33. Lowe, I. J., Free induction decay of rotating solids. *Phys. Rev. Lett.* **1959,** *2*, 285-7.

34. Watt Eric, D.; Rienstra Chad, M., Recent advances in solid-state nuclear magnetic resonance techniques to quantify biomolecular dynamics. *Anal. Chem.* **2014,** *86* (1), 58-64.

35. Tran, C. D.; Duri, S.; Delneri, A.; Franko, M., Chitosan-cellulose composite materials: Preparation, Characterization and application for removal of microcystin. *J. Hazard. Mater.* **2013,** *252-253*, 355-366.

36. Heux, L.; Brugnerotto, J.; Desbrieres, J.; Versali, M. F.; Rinaudo, M., Solid State NMR for Determination of Degree of Acetylation of Chitin and Chitosan. *Biomacromolecules* **2000,** *1*, 746-751.

37. Haderlein, S. B.; Schwarzenbach, R. P., Adsorption of substituted nitrobenzenes and nitrophenols to mineral surfaces. *Environ. Sci. Technol.* **1993,** *27*, 316-26.

38. Chen, W.; Duan, L.; Zhu, D., Adsorption of polar and nonpolar organic chemicals to carbon nanotubes. *Environ. Sci. Technol.* **2007,** *41*, 8295-8300.

39. Furusawa, T.; Smith, J. M., Intraparticle mass transport in slurries by dynamic adsorption studies. *AIChE J.* **1974,** *20*, 88-93.

CHAPTER 4

SYNTHESIS AND CHARACTERIZATION OF A POTENTIAL BONE TISSUE ENGINEERING MATERIAL FROM CELLULOSE, CHITOSAN AND HYDROXYAPATITE

4.1. Background

The human skeletal system performs a variety of vital functions including structural support to the body, protecting vital organs and also serving as a reservoir of minerals. Interestingly, this system is capable of regenerating itself throughout the whole life of an individual. However, in the event of traumatic injuries, the system may fail to heal properly necessitating the intervention of surgical procedures. The common surgical procedure for such severe injuries involve bone grafting to restore the normal function of the skeletal system. Bone grafting involves transplanting bone tissue from either the patient's body (autografts) or cadavers (allografts) or from other species (xenografts) to the defect site.[1-5] Although bone grafting has helped to restore the normal functioning of the skeletal system, its continued use is threatened by major challenges. For example, the major challenge facing autografts is the limited amount of bone stock in a patient's body. In addition, the invasive nature of obtaining autografts leaves a wound at the donor site which would oftentimes take longer times to heal thereby adding misery to the quality of life of the patient. Furthermore, the bone graft may be resorbed at the surgical site.[6] Allografts pose the risk of eliciting immunogenic response, which result in their rejection and attack by the patient's own immune system.[7] Furthermore, there is the risk of transfer of diseases and other health complications from the donor.[8,9] While xenografts share the same risks as allografts, they also pose the risk of failing to meet the biomechanical

properties required especially at load bearing sites. Therefore, to circumvent these shortcomings, efforts have been focused on developing unique artificial scaffolds that mimic the extracellular matrix.

Scaffolding remains the most promising strategy to provide temporary support to the load bearing site to allow successful repair of lost bone tissue. The prerequisite for success of a given scaffolding system is its mimicry to the bone tissue. Thus, the design of the best scaffold requires understanding of the biological, chemical and mechanical properties of the bone tissue. Bone tissue is a very complex and dynamic tissue which is made up of a mineral phase, an organic phase and water. The mineral phase is mainly composed of calcium (Ca^{2+}), and phosphate (PO_4^{3-}) and constitute up to 60% of the mass or 40% of the volume of bone.[10] In addition, other mineral ions such as carbonate (CO_3^{2-}) and fluoride ions exist in small fractions. The main form of the bone mineral is hydroxyapatite (HAp) with the general chemical formula $Ca_{10}(PO_4)_6(OH)_2$. This mineral provides stiffness and strength to the bone. The organic phase (occupies 40% of the volume of bone) of the bone is mainly composed of type I collagen with a small but important fraction of non-collagenous proteins such as osteonectin, osteopontin, osteocalcin, etc.[10] Collagen provides strength and flexibility to the bone. In addition, it provides surfaces for the nucleation and growth of hydroxyapatite crystals. Non collagenous proteins mediate the events associated with cell attachment, deposition of hydroxyapatite and its maturation. Water acts as a medium in which important biochemical reactions take place. Therefore, the structural organization of HAp, collagen, and water play a vital role in determining the properties of bone, such as mechanical and biological properties. Consequently, a scaffold meant to correct for bone defects should

mimic these constituents of bone in order to enhance the chances of success in repairing defected tissue.

An ideal bone scaffold should therefore be able to (1) withstand mechanical forces experienced at the defect site, (2) allow the diffusion of nutrients and waste products to and from the defect site, (3) degrade at a rate that matches the regeneration of the bone tissue, and (4) to control delivery of therapeutics to the site. Most importantly, the scaffold should be osteoconductive, osteoinductive and biocompatible. In an attempt to achieve this goal, a variety of materials have been investigated with various levels of success. For example, metal implants have been used to replace defective bone completely because they possess superior mechanical properties. However, in some isolated cases, the tissue surrounding the prosthesis fails to attach to the metal leading to some complications which would require another costly and painful surgery.[11-16] These problems have urged research into the use of synthetic polymers such as polyesters and polyurethanes. Although these polymers can be engineered to possess a wide range of mechanical properties, their use is precluded by the impending crisis in the petroleum industry. This is because these synthetic polymers are made from the non-renewable petroleum resource which faces the risk of running out due to its widespread use without adequate replenishment. Thus, efforts have been focused on naturally derived biopolymers such as polysaccharides (e.g. cellulose, chitosan), hyaluronic acid, and proteins (such as keratin, collagen, elastin, etc).

Several studies have focused on the use of natural biopolymers to design successful scaffolds to correct for bone defects. Amongst these biopolymers, cellulose (CEL) and chitosan (CS) hold much promise. These biopolymers are not only

biocompatible but they can also degrade into non-toxic products which can be easily excreted from the body.[17-23] Most importantly, CS exhibits antibacterial activity against a wide range of bacteria usually implicated in implant-associated infections.[24-26] Thus, its use as a scaffold constituent would ensure a bacteria-free implant site which in turn improves the chances of successful reconstruction of the damaged bone tissue. Cellulose is well known for its superior mechanical properties.[27] Thus, it can potentially be used to make scaffolds that are intended to be used at load bearing sites. Although CS and CEL possess desirable properties for their potential use in bone tissue scaffolds, there is still room to improve their osteoconductive and mechanical properties by blending them with HAp.

Hydroxyapatite is widely used as an orthopedic implant coating because it is similar to bone mineral and therefore it is expected to be osteoconductive. However, by itself, HAp is difficult to apply as a bone scaffold because it is too brittle and difficult to process.[28] In addition, HAp exhibit poor tensile strength and poor impact resistance. Furthermore, it tends to migrate from the implant site potentially causing irritation or damage to surrounding healthy tissues.[29] Also, crystalline HAp tends to degrade more slowly than the normal healing rate of bone.[30] To go around this problem while still retaining its osteoconductive properties, HAp is often combined with either CS or CEL among other biopolymers to fabricate composite scaffolds. The resultant scaffolds often possess properties of their constituents. For example a scaffold containing chitosan and hydroxyapatite was found to be both osteoconductive (from HAp) and antibacterial (from CS);[31] a scaffold containing cellulose and HAp was found to be both osteoconductive (from HAp) and mechanically superior (from CEL).[32]

Despite the potential of these HAp-based biopolymer scaffolds, there exist challenges in their fabrication. The low solubility of HAp in both aqueous (except in acidic solutions) and organic solvents precludes *in situ* fabrication of HAp/biopolymer scaffolds. In addition, the synthesis of the HAp involves post-heat treatment at temperatures in excess of 1100 °C.[33] Such high temperatures prevents the possibility of synthesizing HAp/biopolymer scaffolds *in situ* because the biopolymers would undergo thermal degradation at such high temperatures. Furthermore, blending powdered HAp with either CS or CEL can lead to weak bonding between these components which oftentimes would result in implant failure. *In situ* precipitation of calcium phosphate in biopolymer matrix can be achieved by soaking the biopolymer film in a simulated body fluid (a solution with ion concentration close to that of human blood plasma kept under physiological pH and temperature conditions) for several days.[34] A modified version of this biomimetic method involves soaking the film alternately in separate solutions of calcium and phosphate ions.[35,36] This modified procedure takes less time than the conventional biomimetic technique; it takes just a couple of hours to complete.

Fabricating the biopolymer films prior to the *in situ* deposition of HAp is hampered by the low solubility of both CS and CEL in conventional solvents. This recalcitrance to conventional solvents is due to the existence of extensive networks of intra- and inter-molecular H-bonds in the structures of CEL and CS. This low solubility makes it more difficult to process and functionalize these two polysaccharides. Until recently when ionic liquids were discovered, *N*-methyl morpholine *N*-oxide[37] and acetic acid[38] were widely used to dissolve and regenerate CEL and CS films respectively. However, these solvents potentially cause degradation of these biopolymers. Worse still,

they cannot dissolve both CEL and CS, thus limiting the possibility of synthesizing [CEL+CS] composite films. These challenges have been alleviated by the introduction of ionic liquids which can dissolve both CEL and CS simultaneously in the same solvent system. For example, 1-butyl-3-methylimidazolium chloride, $BMIm^{+}Cl^{-}$, an IL was found to dissolve both CS and CEL and regenerate their composite films.[39] This enabled the possibility of synthesizing [CEL+CS] containing various proportions of these components in one step. The resultant composite films were found to possess combined properties from each of the components. For example, as expected, [CEL+CS] composite materials exhibited superior mechanical properties (from CEL) and excellent antibacterial properties (from CS).

To the best of our knowledge, there are no reports published about combining the regeneration of [CEL+CS] composites from ionic liquid with their subsequent *in situ* mineralization by the fast alternate soaking technique. Therefore, in this study, we seek to close this knowledge gap by combining the advantages of these two seemingly unrelated developments to synthesize novel HAp polysaccharide composites for potential use in bone tissue engineering. Results on the detailed characterization of these composite materials are reported in the following sections.

4.2. Experimental Procedure

4.2.1. Chemicals

High molecular weight chitosan (M_w≈310 to 375 kDa, 84±2% degree of deacetylation),[27] microcrystalline cellulose (DP≈300),[40] ammonium persulfate and potassium antimonyl molybdate were obtained from Sigma-Aldrich (Milwaukee, WI).

Ammonium molybdate tetrahydrate was supplied by J.T. Baker. Methylimidazole and chlorobutane used to make the ionic liquid, 1-butyl-3-methylimidazolium chloride, were sourced from Fisher Scientific. HAp standard was obtained as a gift from Professor J. M. Toth from department of Biomaterials and Tissue Engineering at Marquette University. All other reagents were of analytical grade and were sourced from commercial suppliers (Sigma Aldrich and Fisher Scientific). The water that was used throughout the experiments was double distilled (18.2 MΩ cm^{-1}).

4.2.2. Instrumentation

A variety of spectroscopic techniques were used to characterize the polysaccharide composite films. Specifically, the following techniques were used; X-ray diffraction (XRD), FTIR, and SEM. X-ray photoelectron spectra were taken on a HP 5950A ESCA spectrometer with Al monochromatic source and a flood gun was used for charge suppression. In addition, the composites were evaluated for their tensile properties. Details on the conditions and instruments used to carry out these analyses have already been presented in previous chapters.

4.2.3. Preparation of polysaccharide composite materials

All films containing various proportions of CEL and CS were prepared according to the method that was developed in our group.[39] In brief, as shown in Scheme 4-1, the required amounts of either CEL or CS were dissolved in $BMIm^+Cl^-$ to enable the regeneration of composite materials containing various proportions of these two components. The IL-laden gels were then washed with distilled water to remove the IL.

This washing took about three days. Subsequent distillation facilitated the recovery of the IL for reuse.

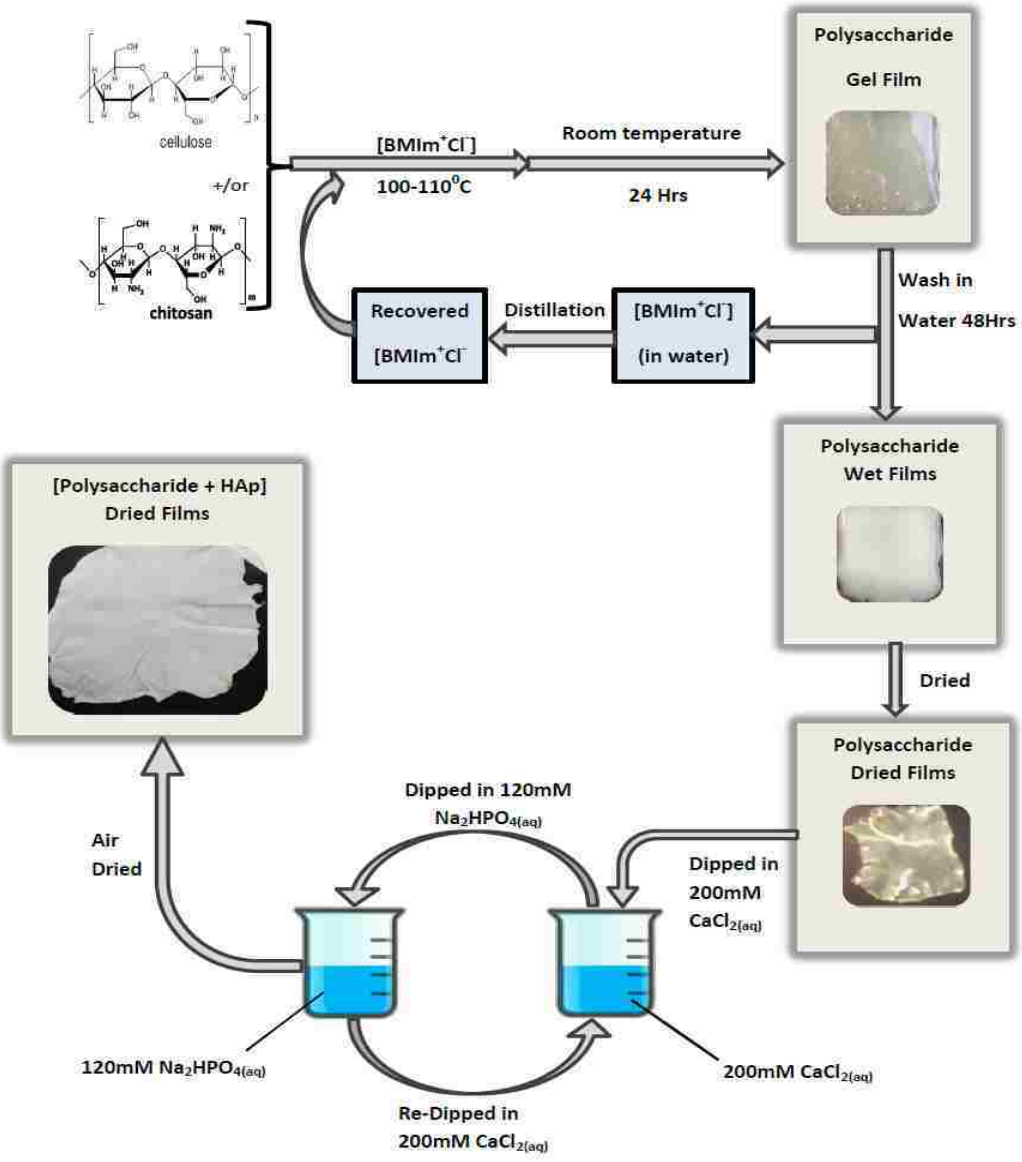

Scheme 4-1 Synthesis of [CEL+CS] composites and their mineralization in aqueous solutions of $CaCl_2$ and Na_2HPO_4.

4.2.4. Mineralization of polysaccharide composite films by the dipping method

Calcium phosphate was template onto the polysaccharide matrix by the well-known alternate soaking technique (Scheme 4-1).[36] In details, the rectangular film (7.0 cm x 3.5 cm L x W) was soaked in an aqueous solution of $CaCl_2$ (50.0 mL of 200 mM Ca^{2+}) for 60 seconds. During this time, the cations diffused and got encapsulated into the polysaccharide matrix. The film was then taken out of this solution and rinsed twice in double distilled water to remove physisorbed Ca^{2+}. The film was subsequently soaked in an aqueous solution of Na_2HPO_4 (50.0 mL of 120.0 mM HPO_4^{2-} for another 60 seconds during which time the anions diffused into the biopolymer matrix. After the lapse of the 60 seconds, the film was rinsed in double distilled water to remove unbound mineral ions. Then, the film was soaked again in a fresh solution of 50.0 mL of 200.0 mM $CaCl_2$. The whole series of operations was then replicated 20 times. The wet films were then air dried in a custom-designed drier.

4.2.5. Procedure used to estimate the molar ratio of calcium and phosphorus in [CEL/CS+HAp] composite films

4.2.5.1. Digestion of [CEL/CS+HAp] films for analysis of their composition

Flame atomic absorption spectrometry[41] and the ascorbic acid[42] method were used to determine the bulk molar content of the HAp-containing polysaccharide composite films. Exactly 50.0 mg of film specimen was suspended in 50.0 mL of double distilled water. One milliliter of 11.0 N sulfuric acid and 0.400 g ammonium persulfate were added successively. The mixture was boiled gently on a hot plate until volume decreased to *ca.* 10 mL. It took *ca.* 1.5 hours to reach this 10 mL level. It should be pointed that

[CS+HAp] composite dissolved completely to give a clear solution in this acidic solution. The composites containing CEL produced some white particles suspended in the solution. These were then filtered using a 20-25 µm filter paper. The solution was then cooled to room temperature and the volume was adjusted to *ca.* 30.0 mL with double distilled water. One drop of phenolphthalein indicator was added to the resultant solution. Color remained colorless because the solution was still acidic. The solution was then neutralized to a faint pink color using 1.0 N aqueous NaOH. The whole neutralized solution was transferred quantitatively to a 100 mL volumetric flask. This solution denoted as *Stock* was then used for the determination of both phosphorus and calcium.

4.2.5.2. Ascorbic acid protocol for determining phosphorus in [CEL/CS+HAp] films

The following protocol was then followed for determining the molar content of phosphorus in the films. One milliliter of the *Stock* solution prepared in section 4.2.5.1 was further diluted to 100 mL with double distilled water. Ten milliliters of this dilute sample were measured into each of 6X25 mL volumetric flasks. Different volumes (0.0-10.0 mL) of 2.50 ppm P were added into each of these flasks and the volume in each flask was adjusted to the mark using double distilled water. Subsequently, these solutions were transferred into six Erlenmeyer flasks and 4.0 mL of the combined reagent were added to each of the six solutions. The combined reagent was prepared fresh each time by mixing 50.0 mL of 5.0 N H_2SO_4, 5.0 mL of 8.2 M potassium antimonyl tartrate, 15.0 mL of 32.4 mM ammonium molybdate and 30.0 mL of 0.1 M ascorbic acid solutions. A blue colored complex was formed within a minute of adding the combined reagent. After 10 minutes absorbance of each sample was measured at 880 nm using a Perkin Elmer Lambda 35 UV/Vis spectrometer. A standard addition curve of absorbance against the

volume of standard added to each flask was subsequently generated from this collected data. This was then fitted to a general linear model (Y = mX + C where Y is the absorbance of the solution, X is the volume of added standard; m and C represent the fitted parameters slope and intercept respectively). Extrapolation of this line to the X-axis (i.e. absorbance = 0) gives the concentration of the phosphorus in the diluted sample solution. Taking into account the dilution factors facilitates the calculation of the concentration of phosphorus in the original *Stock* solution prepared in section 4.2.5.1 above. Knowing the amount (50.0 mg) of film sample that was digested in the acidic solution allowed the calculation of the percentage of phosphorus in the film.

4.2.5.3. Atomic absorption spectrometric determination of calcium in the films

Calcium was determined by the reported flame atomic absorption method with minor modifications. Specifically, ten milliliters of the *Stock* solution prepared in 4.2.5.1 was diluted further to 100 mL with double distilled water. Subsequently, ten milliliters of this dilute sample solution were pipeted into each of the 6x25 mL volumetric flasks. Systematically varied amounts (0.0-5.0 mL) of 10.0 ppm Ca^{2+}were added to these flaks. Three milliliters of 0.18 M La_2O_3 were added to these flasks to alleviate any possible interference from sulfate ions. The volumes were then adjusted to the marks using 0.2 M HNO_3 solution. The absorbance of each solution was measured at 422.7 nm on a Perkin Elmer AAnalyst 100 flame atomic absorption spectrometer. Air and acetylene were used as oxidant and fuel respectively. Similarly to the calculations of P content, a standard calibration curve was constructed and subsequently used to calculate the percentage of calcium in the film that was digested in4.2.5.1. Then the weight percentages of CA and P

were converted to moles to produce Ca/P mole ratio in each HAp polysaccharide composite.

4.3. Results and Discussion

4.3.1. X-ray diffraction spectroscopy

We used XRD spectroscopy to monitor the crystal structural changes which took place after calcium phosphate was deposited in the polysaccharide matrixes. This was achieved by comparing the spectra of polysaccharide films before (Figure 4-1A) and after (Figure 4-1B) deposition of the calcium phosphate. As can be seen from Figure 4-1A, the spectrum of 100% CS presents unique diffraction peaks at 2θ=~10.9° and 18.8° 2θ which can be assigned to **101** and **002** planes respectively.[43] On the other hand, the spectrum of 100% CEL presents unique bands at 2θ=10.9° and 20.0° 2θ, which are tentatively ascribed to reflections from **101** and **002** planes respectively.[43] As expected, spectra for blend films containing both CEL and CS (i.e. 50:50 CEL:CS, and 60:40 CEL:CS) contain bands that represent an algebraic sum of the bands observed in individual spectra of 100% CEL and 100% CS. This suggests that CEL and CS were successfully blended together without detectable changes in their crystal structures. This is hardly surprising given that the structures of CEL and CS are similar. The only difference between their structures is that CEL has an OH group on C-2 whereas CS has an amine group bonded to that same C-atom. Therefore, the two biopolymers can form hydrogen bonds through -OH and -NH_2 groups.

Precipitation of calcium phosphate in situ on the polysaccharide films led to substantial changes in their corresponding XRD spectral traces (Figure 4-1A and B). In

the composites containing calcium phosphate, in addition to the bands ascribed to the polysaccharides, new bands appeared at 2θ=6.1±0.3° and 32.0±0.6°. Since our goal was to synthesize HAp *in situ* on polysaccharide matrixes, we compared these new bands to those of HAp standards and HAp reference JCPDS# 72-1243.[44] These two standards show matching bands at various positions with the most pronounced peaks located at 2θ=25.9° (**002**), 31.7° (**211**), 32.2° (**112**), 32.9° (**300**), and 34.0° (**202**) 2θ. Thus, the band at 26.1±0.3° in mineralized composite films can be tentatively assigned to the **002** plane of crystalline HAp.[45] The band at 32.0±0.6° in mineralized composites was so broad that it could be a result of overlapping contributions from the planes **211**, **112**, **300**, and **202**. These results suggest that HAp was successfully deposited in situ in the polysaccharide matrices. However, HAp deposited on these polysaccharides was less crystalline than the standard HAp because compared to the peaks for XRD of standard HAp, the corresponding peaks in mineralized composites were broader. This is a significant finding because biological apatite is known to have a less crystalline form of HAp. Therefore, it is expected that the composites synthesized in this current study should behave similarly to the HAp *in vivo*. Specifically, they should be osteoconductive and be able to degrade at the same rate as the normal healing of the bone.

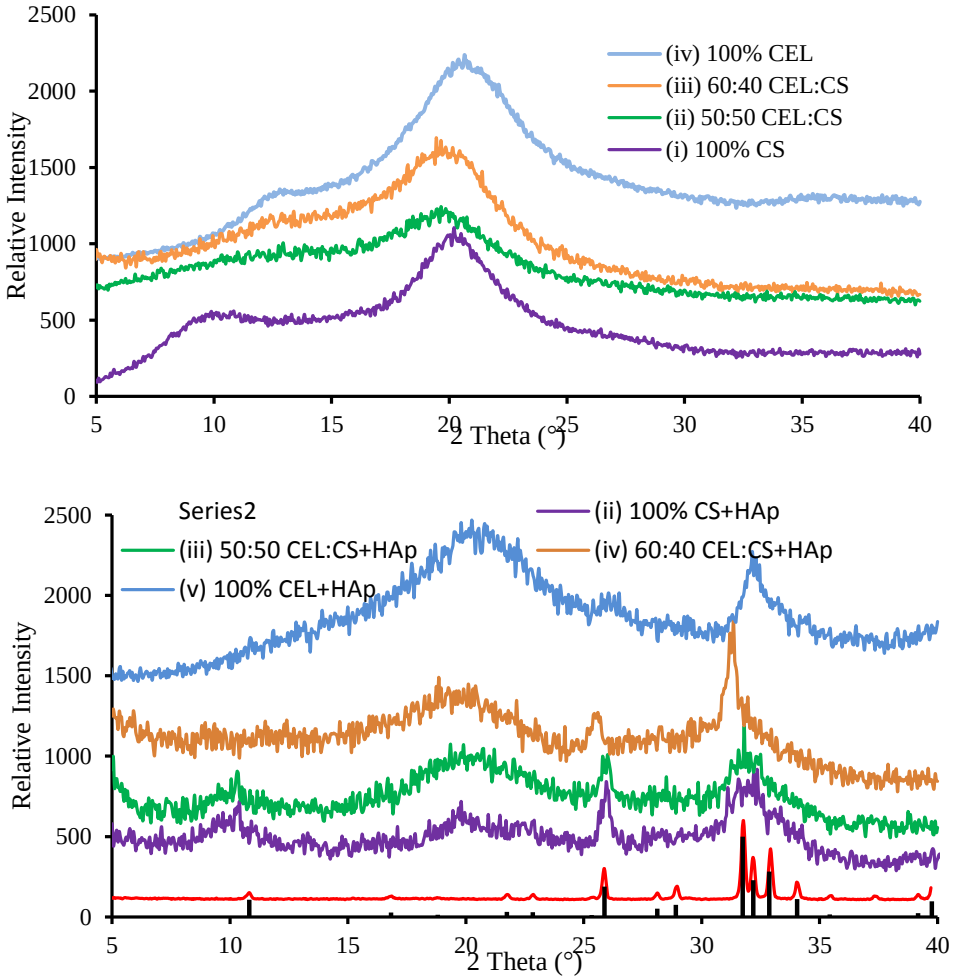

Figure 4-1 XRD spectral traces of polysaccharide films before (A) and after (B) deposition of calcium phosphate. For A: (i) 100% CS, (ii) 50:50 CEL:CS, (iii) 60:40 CEL:CS, and (iv) 100% CEL. For B: (i) HAp standard, (ii) 100% CS+HAp, (iii) 50:50 CEL:CS+HAp, (iv) 60:40 CEL:CS+HAp, (v) 100% CEL+HAp. The black bar graph at the bottom in (B) represents the indexed HAp peaks according to JCPDS# 72-1243.

4.3.2. Characterization by FTIR

FTIR was used to confirm both the regeneration of CEL and CS and their mineralization with calcium phosphate. As illustrated, regenerated CS film (Figure 4-2

(iii)) exhibited at bands around 3700-3250 cm^{-1} (overlapping O-H stretching vibrations and symmetric N-H stretching vibrations), 2900-2850 cm^{-1} (symmetric C-H stretch vibrations), 1657 cm^{-1} (C=O stretch, amide I), 1580 cm^{-1} (N-H deformation, amide II), 1380 cm^{-1} (amide CH_3 symmetrical deformation), 1319 cm^{-1} (C-N stretch, amide III), and 1150-890 cm^{-1} (C-O-C bending vibrations).[43] Regenerated CEL film (Figure 4-2 (vii)) exhibited a broad band at ~3400 cm^{-1} due to stretching vibrations of H-bonded O-H groups. In addition, this spectrum exhibited bands at 2900-2850 cm^{-1} and 1150-890 cm^{-1} due to sp^3 C-H and deformations of the saccharide structure respectively.[43] These bands for CEL and CS films were similar to the ones for their corresponding unprocessed powders suggesting that there were no chemical reactions that took place during the dissolution and regeneration from the ionic liquid. Similarly, the spectral traces of composites containing both CEL and CS exhibited bands that are a weighted sum of those bands observed in their pure component spectra. This further confirms compatibility between CEL and CS. This is beneficial especially in bone tissue engineering because the resultant composite is expected to possess properties derived from each one of these components. For example, as described in the previous sections, CEL and CS can impart tensile strength and antibacterial properties to the resultant composite film.

Deposition of calcium phosphate led to substantial changes in the spectral traces of these polysaccharide composite films (Figure 4-2). Clear changes are noticed in the 650-520 cm^{-1} region where the phosphate bands are well resolved from the polysaccharide bands.[45,46,47] Essentially, whereas mineralized composites exhibited sharp peaks at 604 cm^{-1} and 563 cm^{-1}, the same composites before mineralization do not show

any definitive peaks within this range. These bands are due to the υ_4 or bending vibrational mode of OPO group (Figure **4-3**). Although the band at 1038 cm^{-1} (v_3) for HAp is overlapped by those attributed to the deformations of the saccharide structure, it is apparent that the intensity of this peak after mineralization has increased as compared to the intensity before mineralization. This further confirms that HAp was successfully mineralized onto the polysaccharide films. The band expected at 962 cm^{-1} was probably overlapped by those bands that appeared at the same position in the spectra of polysaccharides. The band at 1400 cm^{-1} in the mineralized films could be due to the v_3 vibrations from CO_3^{2-}.[47] This carbonate could have come from the atmospheric CO_2. Biological apatites have been found to contain different amounts of carbonate. This carbonate substitutes either OH (type A) or phosphate (type B) ions in the structure of hydroxyapatite. Overall, FTIR has shown that indeed HAp was successfully mineralized onto either CEL or CS or their corresponding composites. In addition, the nature of the HAp deposited is similar to the biological apatite. Therefore, these composite films represent the best platform to template HAp in a way that reflects the natural process. Consequently, these composites could also exhibit properties that are similar to the ones that are exhibited by natural bone.

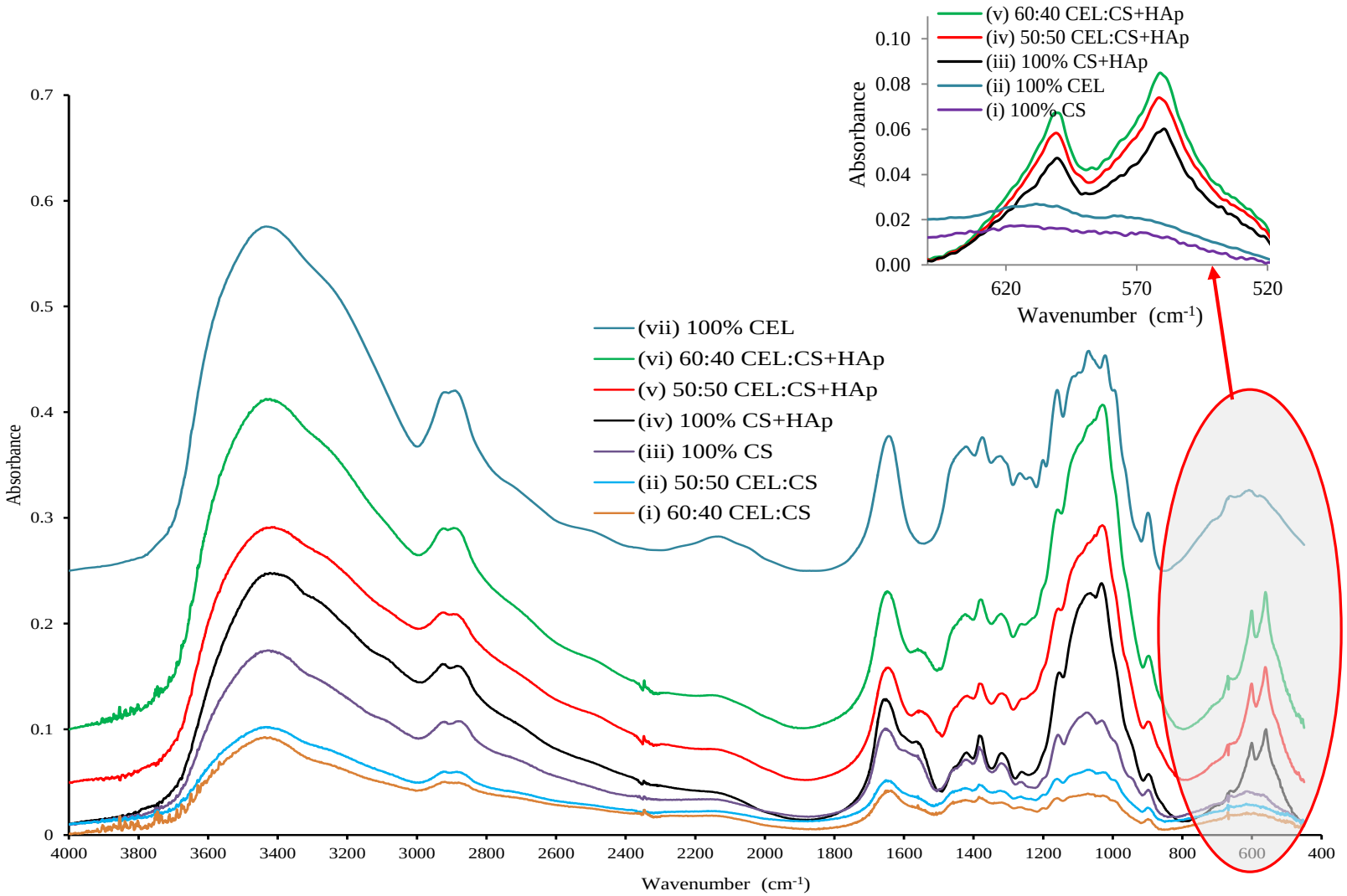

Figure 4-2 FTIR spectral traces of polysaccharide films before and after deposition of calcium phosphate. (i) 60:40 CEL:CS, (ii) 50:50 CEL:CS, (iii) 100% CS, (iv) 100% CS+HAp, (v) 50:50 CEL:CS+HAp, (vi) 60:40 CEL:CS+HAp, and (vii) 100% CEL. The inset shows a 650-520 cm^{-1} snapshot of the spectral traces of 100% CS (i), 100% CEL (ii), 100% CS+HAp (iii), 50:50 CEL:CS+HAp (iv), 60:40 CEL:CS+HAp (v).

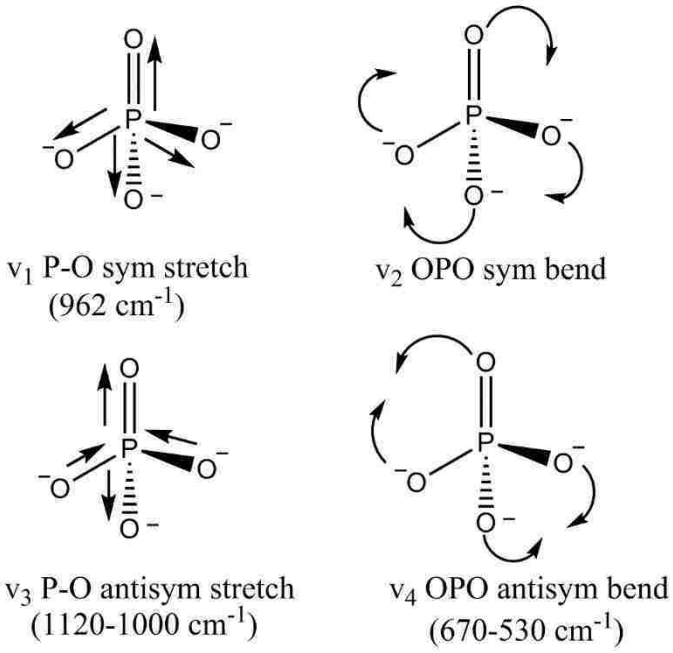

Figure 4-3 Vibrational modes of vibration of phosphate group. The arrows show the deformation of P-O and OPO bonds and angle respectively. Data given in brackets indicate the vibrational frequency for phosphate in HAp.

4.3.3. SEM images of the composite films

SEM was used to reveal the texture and morphological changes that took place as a result of deposition of calcium phosphate onto the polysaccharide composite films (Figure 4-4). As illustrated, the SEM images of pure component films i.e. CEL and CS are homogeneous without any noticeable features or any signs of phase separation. Closer inspection of these two images reveals some fibrous-like structures with diameters of about 0.5-1.0 µm in CEL. The CS image shows a smoother texture. In addition, this CS image showed a dense surface without any signs of micro porous structure. This could be due to reformation of more H-bonds within CEL structure than within the CS structure. Chitosan contains bulky acetyl and amino groups compared to only OH groups in CEL.

Thus, CEL can reform more extensive H-bonds than those formed in CS. Consequently, CEL chains interact to form a fibrous structure. Interestingly, 50:50 CEL:CS composite film was not only homogeneous but its morphology is more similar to that of pure CS film. Specifically, it has a smooth structure without any visible fibrous structures. This suggests that the formation of H-bonding in CEL is inhibited by the presence of CS chains. In fact, CEL chains probably formed new H-bonds with CS to give a composite which is more disordered than pure CEL film.

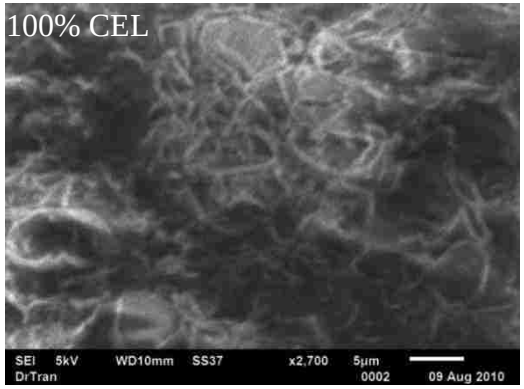

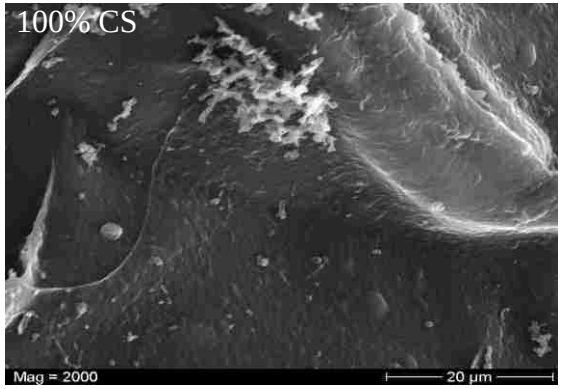

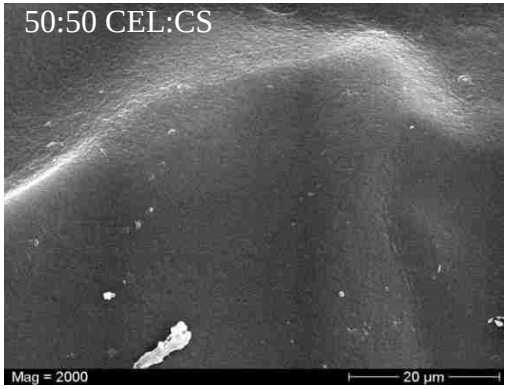

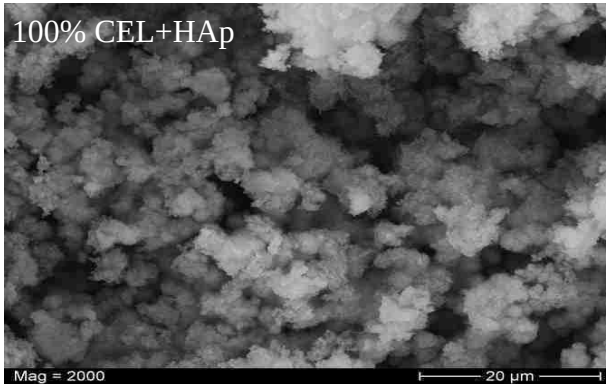

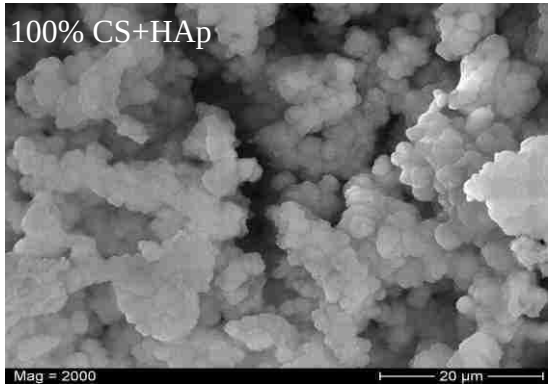

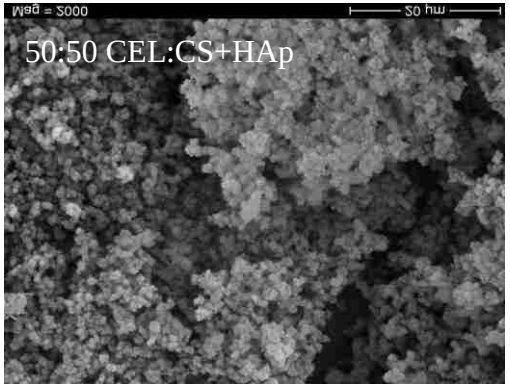

Figure 4-4 SEM Images of 100% CEL, 100% CS, 50:50 CS:CEL and their corresponding calcium phosphate composites.

After mineralization with calcium phosphate, both the texture and morphologies of corresponding polysaccharide composites changed substantially. All mineralized films exhibited micro porous structure. In addition, the surfaces became very rough due to the formation of irregular particles on the surfaces of the polysaccharide composites. The particles formed on these polysaccharide surfaces tended to be spherical with a very wide distribution of sizes. In addition, the sizes of HAp particles tend to vary with the type of templating material. For example, the particles formed on these polysaccharide films seem to decrease in the order 100% CEL>100% CS> 50:50 CEL:CS. This can be rationalized by considering the steps involved in the formation of HAp onto these templates. It is well know that the initial step in the formation of HAp involves nucleation. Subsequently, these nuclei grow in size as more HAp gets deposited on top of them.[36,48] Soaking the films in $CaCl_2$ enables Ca^{2+} to bind to the lone pairs of either O in OH and N in NH_2 in CEL and CS respectively. This provides a local super saturation of Ca^{2+} in the tiny hollow spaces in the polysaccharide structure. Then, when these films are dipped in phosphate solution, these ions diffuse into the polysaccharide structure where upon meeting the Ca^{2+}, they form an insoluble precipitate of calcium phosphate. This acts as an initial nucleus for subsequent growth. These nuclei grow by up taking more Ca^{2+} and PO_4^{3-} from the solution. On one hand, CEL, with its fibrous structure, would have small hollow spaces which would ease the nucleation of HAp. CS, with its dense and non-porous structure, would not have such spaces. Consequently, there is more room for nucleation and growth of particles on CEL than on CS. Interestingly, when these two polysaccharides were blended together, the resultant composite film (50:50 CEL:CS) seems to inhibit the growth of HAp particles. The reduced growth in HAp particles could

be due to the presence of two different structures of the two different polysaccharides. Therefore, it is clear that the size of HAp deposited on different templates will vary with the type of the templating material. This may have implications in the applications of these composites for different types of bone tissue.

4.3.4. Tensile tests for the composites

Tensile strength is a very crucial property that has to be considered in designing scaffolds meant to be used in bone tissue engineering/implants. This is so because any mismatch between the tensile properties of the scaffold and the bone to be regenerated can be catastrophic. If the implant material is too strong, the bone tissue in close proximity to the implant may get resorbed thereby creating more problems. If the material is too weak, it may break under load and this would delay the healing process. We, therefore, evaluated the tensile properties of our mineralized films. It should be noted that CS is so mechanically weak that it is difficult to use it by itself for any load bearing applications such as bone tissue implants. However, its innate antibacterial activity makes it more attractive to use in bone tissue scaffolds to keep the implant site free from bacteria thereby speeding the rate of bone healing. Since CEL is known to possess superior mechanical strength,[39] its combination with CS is expected to improve the mechanical properties of the latter. This would be very attractive because the resultant composite would have desirable properties of the individual components that is superior mechanical strength and antibacterial efficacy.

To confirm this possibility, we measured the tensile properties of our mineralized composite films. As illustrated in Figure 4-5, adding CEL into [CS+HAp] composite films resulted in a substantial increase in tensile strength. For example, the tensile

strength of [CEL+CS+HAp] composite with 80% CEL is 1.9X higher than that of the [CEL+CS+HAp] with 20% CEL. Furthermore, the tensile strength of these composites can be a systematically adjusted by varying the proportional content of CEL in the [CEL+CS+HAp] composite films. Thus, the composite films developed in this study helps to overcome the major limitation that was precluding the use of CS in load bearing applications.

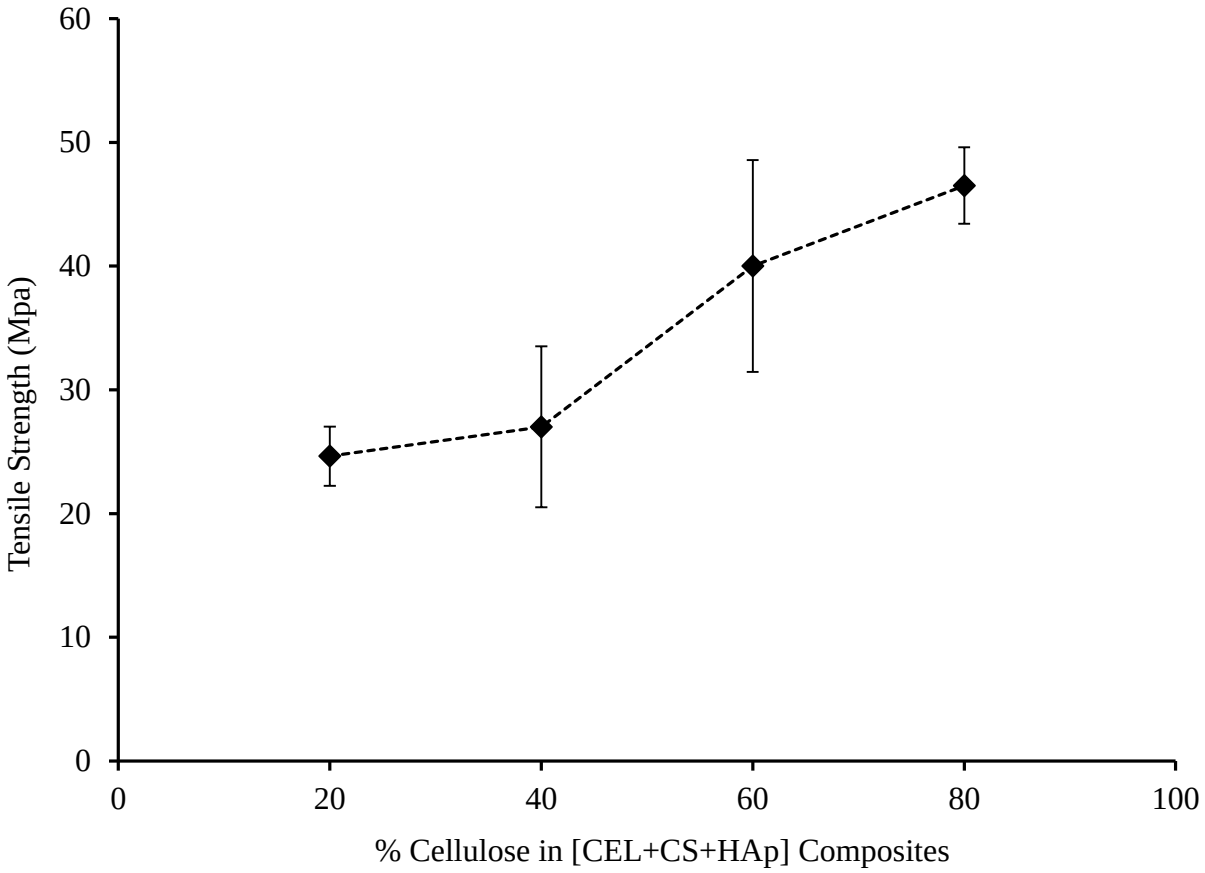

Figure 4-5 Tensile strength of mineralized composite films

4.3.5. Determination of Ca/P molar ratio in the composite films

The molar ratio of Ca/P helps in elucidating the structure of Ca and P in the calcium phosphate precipitate. Stoichiometric apatite has Ca/P ratio of 1.67. However, this ratio varies in biological apatite depending on the species from which the bone was taken.[49] We therefore, determined this ratio by two methods. The first one involved the determination of Ca and P in the bulk sample. The second one involves the determination of this ratio on calcium phosphate which is basically on the surface of the film composites. Both the surface and bulk ratios are important in the design of bone tissue scaffolds. This is so because during the early stages the surface chemistry determines the osteoconductivity of the implant. As the implant gets biodegraded, the inner surfaces get exposed and also get to interact with the biological environment.

Initially, the concentration of Ca and P were determined by flame AA and by UV Visible spectroscopy techniques respectively. In each of these techniques and for each composite, the determination was performed in triplicate and the average values together with their associated standard deviations are presented in Table 4-1. As illustrated, the Ca/P values for all the composites were equal, within experimental error, to the theoretical 1.67 value. This represents the bulk ratio of Ca/P in the films.

Table 4-1 Ca/P Values of Composite Materials Determined by Atomic Absorption (AA) and X-ray Photoelectron Spectroscopy (XPS).

Composite Material	Ca/P by AA	Ca/P by XPS
100% CS+HAp	1.60±0.03	1.28±0.09
100% CEL+HAp	1.7±0.2	1.4±0.1
50:50 CEL:CS+HAp	1.7±0.2	
60:40 CEL:CS+HAp	1.5±0.2	

X-ray photoelectron spectroscopy (XPS), an essentially a surface technique was also used to determine the chemical composition of these films.

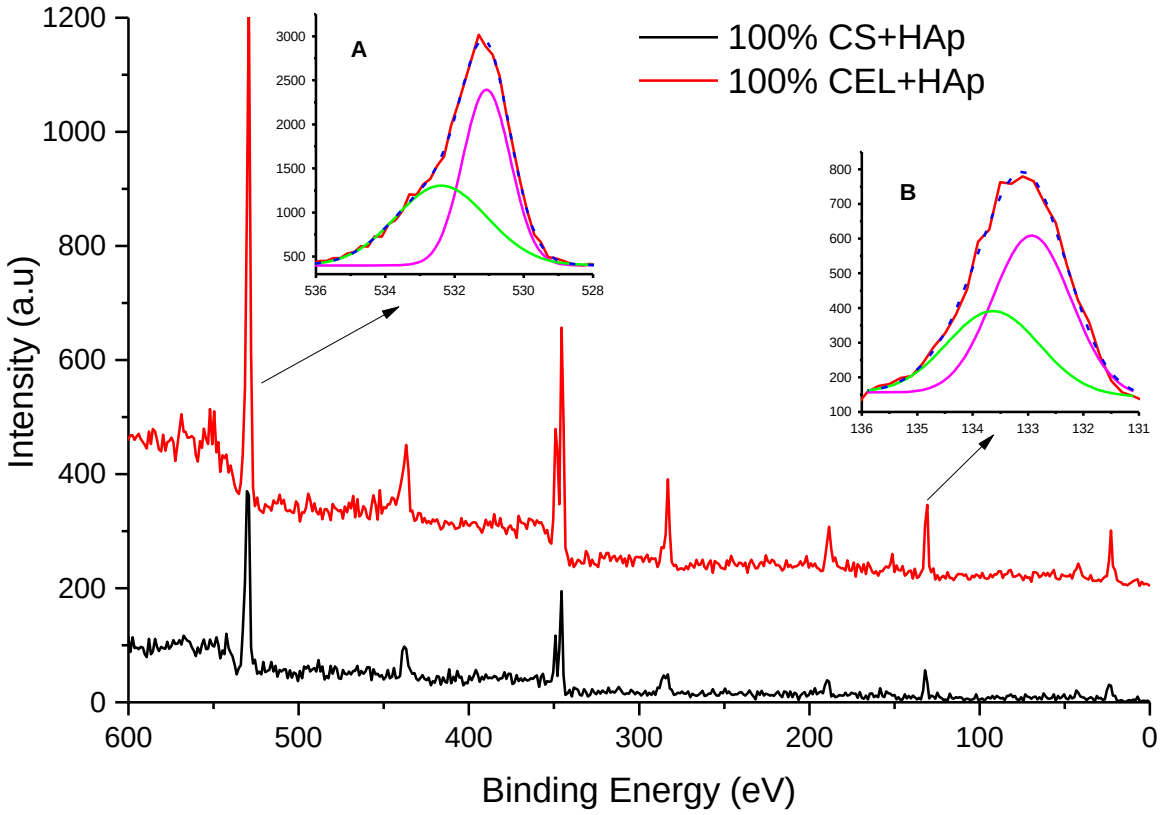

Figure 4-6 X-ray photoelectron spectra (XPS) of mineralized pure [CEL+HAp] and [CS+HAp] films. Insets show deconvolution of (A) O1s band at 532 eV and (b) P2p band at 133 eV in [CEL+HAp].

Table 4-2 Assignments of XPS bands for survey scans of [CEL+HAp] and [CS+HAp].

100% CEL+HAp (eV)	100% CS+HAp (eV)	Peak Assignment	Species
132.9	132.8	$P_{2p3/2}$	PO_4^{3-}
133.6	133.8		HPO_4^{3-}
531.1	531.0	O_{1s}	PO_4^{3-}
532.4	532.2		HPO_4^{3-} / -C-O-
347.2	347.0	$Ca_{2p3/2}$	
350.7	350.5	$Ca_{2p1/2}$	Ca^{2+}
284.9	284.8	C1s	-C-C-
286.3	286.2		C-O (CS or CEL backbone)
287.9	287.8		-O-C-O-

As illustrated in Figure 4-6 and Table 4-2, the XPS spectra of both [CEL+HAp] and [CS+HAp] composites exhibit HAp bands at 350 eV (Ca_{2p}), 439 eV (Ca_{2s}), 133 eV (P_{2p}), 191 eV (P_{2s}), and 532 eV (O_{1s}).[50,51] However, to gain more insights into the nature of bonding in HAp, the bands at 532 eV for O_{1s} and at 133 eV for P_{2p} were resolved into two contributing spectra for each band. The band at 531.1 eV for 100% CEL+HAp (or 533.0 eV for 100% CS+HAp) was assigned to O_{1s} from PO_4^{3-} whilst the band at 532.4 eV for 100% CEL (or 532.2 eV for 100% CS+HAp) was assigned to O_{1s} from HPO_4^{2-} or ether bond in the polysaccharide. The presence of HPO_4^{2-} is not surprising because the phosphate precursor, Na_2HPO_4, was used. In addition to bands confirming the presence of HAp, the bands corresponding to the presence of the polysaccharides were also observed in the XPS survey scans of the composites. For example, the bands at 286.3 eV and 287.9 eV for 100% CEL+HAp correspond to C_{1s} for C-O and –O-C-O- in the polysaccharide structure respectively. Although these results

suggest that calcium phosphate was precipitated on the surfaces of the polysaccharides, they cannot determine the exact form of the calcium phosphate. This is because calcium phosphate exists in up to six different biologically relevant forms; hydroxyapatite (HAp), dicalcium phosphate dihydrate (DCPD), dicalcium phosphate (DCP), monocalcium phosphate (MCP), β-tricalcium phosphate (β-TCP) and octacalcium phosphate (OCP). These six forms differ in the molar ratio of Ca to P. For example, HAp has the highest ratio of 1.67 followed by β-TCP with a ratio of 1.5. Therefore, we used XPS to determine these ratios so that we could confirm the predominant form of calcium phosphate.

The Ca/P molar ratios as determined by XPS are shown in Table 4-1. The integrated areas of Ca and P signals were scaled with the atomic sensitivity factors before the percentage composition was calculated. As illustrated in this table, the Ca/P molar ratios were found to be 1.4±0.1 and 1.28±0.09 in 100% CEL+HAp and 100% CS+HAp respectively. These values are consistently less than those found by AA and UV-Vis spectroscopy. This discrepancy may be due to the nature of these measurement techniques. Whereas XPS is a surface analysis technique, AA and UV-Vis measure the average amount in the whole sample. Thus, if the surface composition is different from the bulk composition, these two techniques are bound to give different values. This was indeed the case in this study. The differences in the surface and bulk compositions of these samples suggest that there were at least two forms of calcium phosphate in these composites. In fact, it has already been reported that films mineralized by the alternate soaking technique exhibit different molar ratios of Ca to P between the bulk and surface. This could be due to the initial formation of OCP with a theoretical Ca/P molar ratio of

1.3. Since new layers of calcium phosphate are formed on the surface, this form should therefore be predominant on the surface of these composites.

4.4. Conclusion

In summary, we have shown that it is possible to synthesize HAp-based polysaccharide composites by the novel alternate soaking technique. Unlike the other methods reported in literature, this currently developed method is simple, environmentally friendly and fast. XRD, FTIR, SEM, and XPS helped to confirm that a dense layer of HAp particles was formed via this efficient technique. In addition, as expected, CEL enhanced the mechanical properties of the [CS+HAp] composites. These results help to provide a platform for the development of potential bone tissue engineering materials. More interestingly, now by using CEL, the composites hold potential in their use in load bearing applications whereas HAp is to improve the osteoconductive properties of the composites.

4.5. References

1. Kim, J.; McBride, S.; Dean David, D.; Sylvia Victor, L.; Doll Bruce, A.; Hollinger Jeffrey, O., In vivo performance of combinations of autograft, demineralized bone matrix, and tricalcium phosphate in a rabbit femoral defect model. *Biomed. Mater.* **2014,** *9*, 035010.

2. Albert, A.; Leemrijse, T.; Druez, V.; Delloye, C.; Cornu, O., Are bone autografts still necessary in 2006? A three-year retrospective study of bone grafting. *Acta Orthop Belg* **2006,** *72* (6), 734-40.

3. Putzer, D.; Coraca-Huber, D.; Wurm, A.; Schmoelz, W.; Nogler, M., Optimizing the grain size distribution of allografts in bone impaction grafting. *J Orthop Res* **2014,** *32* (8), 1024-9.

4. Araujo, M.; Linder, E.; Lindhe, J., Effect of a xenograft on early bone formation in extraction sockets: an experimental study in dog. *Clin. Oral Implants Res.* **2009,** *20*, 1-6.

5. Scabbia, A.; Trombelli, L., A comparative study on the use of a HA/collagen/chondroitin sulphate biomaterial (Biostite) and a bovine-derived HA xenograft (Bio-Oss) in the treatment of deep intra-osseous defects. *J. Clin. Periodontol.* **2004,** *31* (5), 348-355.

6. Grant, G. A.; Jolley, M.; Ellenbogen, R. G.; Roberts, T. S.; Gruss, J. R.; Loeser, J. D., Failure of autologous bone-assisted cranioplasty following decompressive craniectomy in children and adolescents. *J Neurosurg* **2004,** *100* (2 Suppl Pediatrics), 163-8.

7. Stevenson, S.; Horowitz, M., The response to bone allografts. *J. Bone Joint Surg. Am.* **1992,** *74*, 939-50.

8. Mankin, H. J.; Hornicek, F. J.; Raskin, K. A., Infection in massive bone allografts. *Clin Orthop Relat Res* **2005,** (432), 210-6.

9. Lord, C. F.; Gebhardt, M. C.; Tomford, W. W.; Mankin, H. J., Infection in bone allografts. Incidence, nature, and treatment. *J Bone Joint Surg Am* **1988,** *70* (3), 369-76.

10. Robinson, R. A.; Elliott, S. R., Water content of bone. I. The mass of water, inorganic crystals, organic matrix, and carbon dioxide space components in a unit volume of dog bone. *J. Bone and Joint Surg.* **1957,** *39A*, 167-88.

11. Langton, D. J.; Jameson, S. S.; Joyce, T. J.; Hallab, N. J.; Natu, S.; Nargol, A. V. F., Early failure of metal-on-metal bearings in hip resurfacing and large-diameter total hip replacement: A consequence of excess wear. *J Bone Joint Surg Br* **2010,** *92* (1), 38-46.

12. Kinsel, R. P.; Lin, D., Retrospective analysis of porcelain failures of metal ceramic crowns and fixed partial dentures supported by 729 implants in 152 patients: Patient-specific and implant-specific predictors of ceramic failure. *J. Prosthet. Dent.* **2009,** *101*, 388-394.

13. Guyer, R. D.; Shellock, J.; MacLennan, B.; Hanscom, D.; Knight, R. Q.; McCombe, P.; Jacobs, J. J.; Urban, R. M.; Bradford, D.; Ohnmeiss, D. D., Early failure of metal-on-metal artificial disc prostheses associated with lymphocytic reaction: diagnosis and treatment experience in four cases. *Spine (Phila Pa 1976)* **2011,** *36* (7), E492-7.

14. Beaule, P. E.; Dorey, F. J.; Le, D. M. J.; LeDuff, M.; Gruen, T.; Amstutz, H. C., Risk factors affecting outcome of metal-on-metal surface arthroplasty of the hip. *Clin. Orthop. Relat. Res.* **2004,** *418*, 87-93.

15. Ollivere, B.; Darrah, C.; Barker, T.; Nolan, J.; Porteous, M. J., Early clinical failure of the Birmingham metal-on-metal hip resurfacing is associated with metallosis and soft-tissue necrosis. *J Bone Joint Surg Br* **2009,** *91* (8), 1025-30.

16. Fisher, J., Bioengineering reasons for the failure of metal-on-metal hip prostheses: an engineer's perspective. *J. Bone Joint Surg. Br.* **2011,** *93*, 1001-1004.

17. Martson, M.; Viljanto, J.; Hurme, T.; Saukko, P., Biocompatibility of cellulose sponge with bone. *Eur Surg Res* **1998,** *30* (6), 426-32.

18. Barbie, C.; Chauveaux, D.; Barthe, X.; Baquey, C.; Poustis, J., Biological behavior of cellulosic materials after bone implantation: preliminary results. *Clin. Mater.* **1990,** *5*, 251-8.

19. Miyamoto, T.; Takahashi, S.; Ito, H.; Inagaki, H.; Noishiki, Y., Tissue biocompatibility of cellulose and its derivatives. *J. Biomed. Mater. Res.* **1989,** *23* (1), 125-33.

20. Benesch, J.; Tengvall, P., Blood protein adsorption onto chitosan. *Biomaterials* **2002,** *23*, 2561-2568.

21. Chenite, A.; Chaput, C.; Wang, D.; Combes, C.; Buschmann, M. D.; Hoemann, C. D.; Leroux, J. C.; Atkinson, B. L.; Binette, F.; Selmani, A., Novel injectable neutral solutions of chitosan form biodegradable gels in situ. *Biomaterials* **2000,** *21*, 2155-2161.

22. Bourtoom, T.; Chinnan, M. S., Preparation and properties of rice starch-chitosan blend biodegradable film. *LWT--Food Sci. Technol.* **2008,** *41*, 1633-1641.

23. Mathew, A. P.; Oksman, K.; Sain, M., Mechanical properties of biodegradable composites from poly lactic acid (PLA) and microcrystalline cellulose (MCC). *J. Appl. Polym. Sci.* **2005,** *97*, 2014-2025.

24. Liu, N.; Chen, X.-G.; Park, H.-J.; Liu, C.-G.; Liu, C.-S.; Meng, X.-H.; Yu, L.-J., Effect of MW and concentration of chitosan on antibacterial activity of Escherichia coli. *Carbohydr. Polym.* **2006,** *64* (1), 60-65.

25. Zhang, Z.; Chen, L.; Ji, J.; Huang, Y.; Chen, D., Antibacterial properties of cotton fabrics treated with chitosan. *Text. Res. J.* **2003,** *73*, 1103-1106.

26. Liu, X. F.; Guan, Y. L.; Yang, D. Z.; Li, Z.; De Yao, K., Antibacterial action of chitosan and carboxymethylated chitosan. *J. Appl. Polym. Sci.* **2000,** *79* (7), 1324-1335.

27. Tran, C. D.; Duri, S.; Delneri, A.; Franko, M., Chitosan-cellulose composite materials: Preparation, Characterization and application for removal of microcystin. *J. Hazard. Mater.* **2013,** *252-253*, 355-366.

28. He, L.-H.; Standard, O. C.; Huang, T. T. Y.; Latella, B. A.; Swain, M. V., Mechanical behaviour of porous hydroxyapatite. *Acta Biomater.* **2008,** *4* (3), 577-586.

29. Wittkampf, A. R., Fibrin glue as cement for HA-granules. *J Craniomaxillofac Surg* **1989,** *17*, 179-81.

30. Balasundaram, G.; Sato, M.; Webster, T. J., Using hydroxyapatite nanoparticles and decreased crystallinity to promote osteoblast adhesion similar to functionalizing with RGD. *Biomaterials* **2006,** *27*, 2798-2805.

31. Kong, L.; Gao, Y.; Lu, G.; Gong, Y.; Zhao, N.; Zhang, X., A study on the bioactivity of chitosan/nano-hydroxyapatite composite scaffolds for bone tissue engineering. *Eur. Polym. J.* **2006,** *42* (12), 3171-3179.

32. Yoshida, A.; Miyazaki, T.; Ashizuka, M.; Ishida, E., Bioactivity and mechanical properties of cellulose/carbonate hydroxyapetite composites prepared in situ through mechanochemical reaction. *J. Biomater. Appl.* **2006,** *21*, 179-194.

33. Ferraz, M. P.; Monteiro, F. J.; Manuel, C. M., Hydroxyapatite nanoparticles: a review of preparation methodologies. *J. Appl. Biomater. Biomech.* **2004,** *2*, 74-80.

34. Wan, Y. Z.; Hong, L.; Jia, S. R.; Huang, Y.; Zhu, Y.; Wang, Y. L.; Jiang, H. J., Synthesis and characterization of hydroxyapatite-bacterial cellulose nanocomposites. *Compos. Sci. Technol.* **2006,** *66*, 1825-1832.

35. Tachaboonyakiat, W.; Serizawa, T.; Akashi, M., Hydroxyapatite formation on/in biodegradable chitosan hydrogels by an alternate soaking process. *Polym. J. (Tokyo, Jpn.)* **2001,** *33*, 177-181.

36. Taguchi, T.; Kishida, A.; Akashi, M., Apatite formation on/in hydrogel matrixes using an alternate soaking process: II. Effect of swelling ratios of poly(vinyl alcohol) hydrogel matrixes on apatite formation. *J. Biomater. Sci., Polym. Ed.* **1999,** *10*, 331-339.

37. Shih, C.-M.; Shieh, Y.-T.; Twu, Y.-K., Preparation and characterization of cellulose/chitosan blend films. *Carbohydr. Polym.* **2009,** *78* (1), 169-174.

38. Duan, B.; Dong, C.; Yuan, X.; Yao, K., Electrospinning of chitosan solutions in acetic acid with poly(ethylene oxide). *J. Biomater. Sci., Polym. Ed.* **2004,** *15*, 797-811.

39. Tran, C. D.; Duri, S.; Harkins, A. L., Recyclable synthesis, characterization, and antimicrobial activity of chitosan-based polysaccharide composite materials. *J. Biomed. Mater. Res., Part A* **2013,** *101A*, 2248-2257.

40. Battista, O. A.; Smith, P. A., Microcrystalline cellulose. *Ind. Eng. Chem.* **1962,** *54*, 20-29.

41. Cali, J. P.; Bowers, G. N., Jr.; Young, D. S., A referee method for the determination of total calcium in serum. *Clin Chem* **1973,** *19* (10), 1208-13.

42. Drummond, L.; Maher, W., Determination of phosphorus in aqueous solution via formation of the phosphoantimonylmolybdenum blue complex Re-examination of optimum conditions for the analysis of phosphate. *Anal. Chim. Acta* **1995,** *302*, 69-74.

43. Stefanescu, C.; Daly, W. H.; Negulescu, I. I., Biocomposite films prepared from ionic liquid solutions of chitosan and cellulose. *Carbohydr. Polym.* **2012,** *87* (1), 435-443.

44. Posner, A. S.; Perloff, A.; Diorio, A. F., Refinement of the hydroxyapatite structure. *Acta Crystallogr.* **1958,** *11*, 308-9.

45. Chen, F.; Wang, Z.-C.; Lin, C.-J., Preparation and characterization of nano-sized hydroxyapatite particles and hydroxyapatite/chitosan nano-composite for use in biomedical materials. *Mater. Lett.* **2002,** *57* (4), 858-861.

46. Chang, M. C.; Tanaka, J., FT-IR study for hydroxyapatite/collagen nanocomposite cross-linked by glutaraldehyde. *Biomaterials* **2002,** *23*, 4811-4818.

47. Panda, R. N.; Hsieh, M. F.; Chung, R. J.; Chin, T. S., FTIR, XRD, SEM and solid state NMR investigations of carbonate-containing hydroxyapatite nano-particles synthesized by hydroxide-gel technique. *J. Phys. Chem. Solids* **2003,** *64* (2), 193-199.

48. Ge, H.; Zhao, B.; Lai, Y.; Hu, X.; Zhang, D.; Hu, K., From crabshell to chitosan-hydroxyapatite composite material via a biomorphic mineralization synthesis method. *J. Mater. Sci.: Mater. Med.* **2010,** *21* (6), 1781-1787.

49. Tzaphlidou, M., Bone architecture: collagen structure and calcium/phosphorus maps. *J. Biol. Phys.* **2008,** *34*, 39-49.

50. Casaletto, M. P.; Kaciulis, S.; Mattogno, G.; Mezzi, A.; Ambrosio, L.; Branda, F., XPS characterization of biocompatible hydroxyapatite-polymer coatings. *Surf. Interface Anal.* **2002,** *34*, 45-49.

51. Lu, H. B.; Campbell, C. T.; Graham, D. J.; Ratner, B. D., Surface characterization of hydroxyapatite and related calcium phosphates by XPS and TOF-SIMS. *Anal. Chem.* **2000,** (13), 2886-94.

CHAPTER 5

SYNTHESIS AND CHARACTERIZATION OF POTENTIAL ANTIBIOTIC RELEASE PLATFORMS CONTAINING CELLULOSE, CHITOSAN AND KERATIN

5.1. Background

Optimum wound healing follows a well-orchestrated sequence of events that encompasses hemostasis, inflammation, migration, proliferation and maturation.[1] However, a condition such as a compromised immune function in HIV/AIDS and diabetic patients often disturbs this ordered progression of events.[2-4] Consequently, the wound healing process would be prolonged. The delay poses a high risk of bacterial infection through the wound site, further impeding the wound healing process.[5] In most cases, infection of these chronic wounds can be life threatening.[4] Thus, wound healing can be facilitated by maintaining a bacteria-free wound site using antibiotics such as fluoroquinolones. Ciprofloxacin (CPX), a fluoroquinolone, is used widely in wound healing therapy. It exhibits excellent bacteriostatic and bactericidal activity against a wide range of bacteria that are implicated in wound infections such as *Staphylococcus aureus*, *Enterococcus coli*, and *Pseudomonas aeruginosa*.[6]

Controlled release of the antibiotic to the wound site remains an elusive goal, which requires continued attention. Achievement of this goal would be accompanied by major clinical, social and economic benefits. Clinical benefits are derived from the capability of these platforms to potentially maintain therapeutic concentrations of the drug at the wound site for a prolonged period throughout the wound healing process. This helps to reduce or eliminate the chances of antibiotic resistance.[7] Incidentally, controlled

drug delivery obviates the need for frequent administration of the drug which ultimately helps to improve patient comfort and compliance to the prescribed regimen. These serve as social benefits derived from using controlled drug delivery formulations. Since therapeutic amounts can be maintained for a prolonged period, the cost of repeated administration is either reduced considerably or eliminated. Despite all these benefits, the design of controlled drug delivery platforms continues to be a challenge.

Synthetic and natural biopolymers exhibit great potential in controlling the release of encapsulated drugs over a prolonged period. However, synthetic polymers are becoming less attractive because they are derived from non-renewable petroleum reserves. Furthermore, synthetic polymers exhibit slow levels of biodegradation which pose a high risk of pollution. In contrast, natural biopolymers such as polysaccharides (e.g. cellulose and chitosan) and proteins (e.g. keratin and silk) are not only biocompatible but they tend to biodegrade into regular metabolites. Furthermore, they are naturally abundant, which help to guarantee an inexhaustible supply if they are used in any application. For example, cellulose is the most abundant natural biopolymer on earth followed by chitin. Most importantly, these biopolymers are generated as by-products in other industrial processes. For example, whereas chitin is a waste by-product of the sea-food industry keratin is a by-product from the textile industry.

Chitosan (CS), cellulose (CEL) and keratin (KER) have been evaluated, with positive outcomes, for their suitability in controlling drug release.[8-21] Nevertheless, the use of either CS-only or KER-only films is precluded by their poor mechanical properties. Specifically, whereas CS-only film swells extensively in water,[22] KER-only film is too brittle to be used conveniently in such applications.[23] In contrast, CEL is well-

known to exhibit superior mechanical properties.[24] Therefore, it is conceivable that blending CEL with either CS or KER would improve the mechanical properties of the later. In fact, such composites have been synthesized and evaluated for their tensile properties. In all cases, it was found that increasing CEL loading resulted in a concomitant increase in tensile strength.[24-26]

Hence, the aim of this study was to prepare CPX-loaded composite films containing various amounts of CEL, CS and KER. This was achieved by using 1-butyl-3-methylimidazolium chloride, an ionic liquid, as a sole solvent to dissolve these biopolymers. Subsequently, these composites were evaluated for their suitability in controlling release of the drug, CPX. The results of these experiments and characterization are reported herein.

5.2. Experimental Methods

5.2.1. Chemicals

Chitosan (MW≈310-375 kDa), derived from chitin from crustacean shells and microcrystalline cellulose (DP≈300),[27] derived from cotton linters, were purchased from Sigma-Aldrich (Milwaukee, WI). The degree of deacetylation of chitosan (CS) was determined by an FT-IR method to be 84±2%.[28] Raw sheep wool, obtained from a local farm, was cleaned by Soxhlet extraction with a 1:1 (v/v) acetone/ethanol mixture for 48 h. The wool was then rinsed with distilled water and dried at 100±1 °C for 12 h.[29] 1-Methylimidazole and *n*-chlorobutane (both from Alfa Aesar, Ward Hill, MA) were distilled prior to using for the synthesis of [$BMIm^+CL^-$].[28] Ciprofloxacin (Scheme 5-1)

(TCI America) was used as the model drug. Double-distilled deionized water (18 MΩ cm^{-1}) was used to prepare 1.0 mM phosphate buffer (pH 7.2).

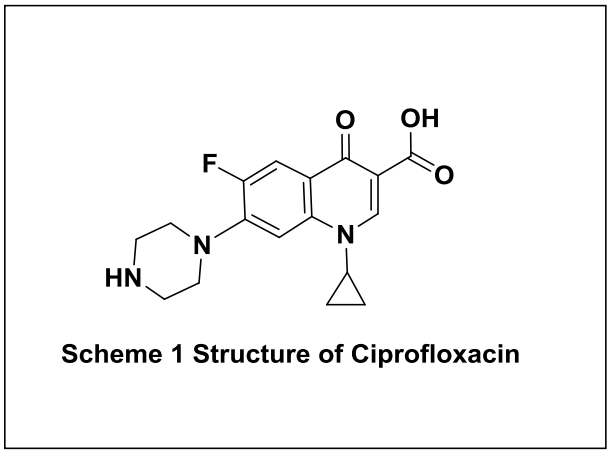

Scheme 1 Structure of Ciprofloxacin

Scheme 5-1 Chemical structure of ciprofloxacin

The protein standards, used to build a PLSR model to estimate the secondary structure of KER included: albumins (bovine serum albumin, BSA and human serum albumin, HSA); hemoglobin (horse, HEM); lysozyme (egg white, LYZ); myoglobin (horse skeletal muscle, MYO); pepsin A (porcine stomach, PEP); ribonuclease A (bovine pancrease, RNASE A); and trypsin inhibitor (soybean, SOY). Except for PEP and SOY, which were purchased from Worthington Biochemical Corporation (Lakewood, NJ), all the other protein standards were purchased from Sigma Aldrich (St Louis, MO). In addition, all the proteins were received in lyophilized powder form and they were used without further purification.

5.2.2. Instruments

FT-IR spectra were recorded on a Spectrum 100 Series FTIR spectrometer (Perkin Elmer, USA) by the KBr method. Specifically, each composite film was cut into small pieces and ground into a fine powder. This powder (1.0 mg) was blended with oven-dried KBr (100.0 mg) in an agate mortar and pestle. The resultant blend was compressed into a disc which was in turn presented for FTIR measurement within the range 4,000-450 cm^{-1} at resolution of 2 cm^{-1}. Each spectrum was an average of 64 individual spectra. Near IR spectra of films were collected on an NIR spectrometer built in our lab. Each spectrum, measured in transmission mode, was an average of 1,000 scans taken at 2 nm intervals within the range 1300-2350 nm. X-ray diffraction (XRD) measurements were taken on a Rigaku MiniFlex II diffractometer utilizing the Ni filtered Cu Kα radiation (1.54059 Å). The voltage and current of the X-ray tube were 30 kV and 15 mA respectively. The samples were measured within the 2θ angle range from 2.0 to 40.0° at scan rate of 5° per minute. File conversion to a spreadsheet compatible type were accomplished using the Jade 8 program package.[30] The surface and cross-sectional morphologies of the film composites were examined under vacuum with a Hitachi S-4800 scanning electron microscope (SEM) at accelerating voltage 3 kV. Prior to SEM examination, the film specimens were made conductive by applying a 2 nm iridium-coating onto their surfaces using an Emitech K575x Peltier Cooled Sputter Coater (Emitech Products, TX). The tensile strength of the composite films were evaluated on an Instron 5500R tensile tester (Instron Corp., Canton, MA) equipped with a 1.0 kN load cell and operated at a crosshead speed of 5 mm min^{-1}. Each specimen had a gauge length and width of 25 mm and 10 mm respectively. In order to avoid slippage of the film

specimens during measurement, two pieces of sandpaper (20 mm x 20 mm) were folded over the specimen ends and clamped between the jaws of the tensile tester. Thermogravimetric analyses, TGA (TG 209 F1, Netzsch) of the composite films were investigated at a heating rate of 10 °C min^{-1} from 30-600 °C under a continuous flow of 20 mL min^{-1} nitrogen gas.

5.2.3. Preparation of Polysaccharide/Keratin/Ciprofloxacin Composite Films

The procedure previously developed in our group,[24] with slight modifications, was adopted to prepare Ciprofloxacin (CPX)-doped composite films containing varying weight proportions of CS, CEL and KER. Scheme 5-2 shows the typical steps followed in synthesizing the CPX-doped composite films. For the synthesis of composites containing KER, the clean wool was dissolved first before the dissolution of either CS or CEL. In a typical experiment, for the synthesis of CPX-doped 25:75 CS:KER film, 6X0.400 g portions of pre-cut wool pieces were dissolved in 40 g of [$BMIm^+Cl^-$] at oil bath temperature of 125±5 ^{0}C under nitrogen atmosphere. Each portion was being added after the previous one had completely dissolved. It took about 6 h to dissolve the 6 portions of wool. After the dissolution of wool, the temperature was lowered to 90 ^{0}C before 2X0.400 g portions of CS were also dissolved in the same solution. This took a further 4 h. Subsequently, 16 mg CPX (equivalent to 0.5% with respect to total weight of biopolymers) was added and allowed to dissolve for a further 2 h. The viscous solution was then cast onto Mylar sheet. The solution was left to gel at room temperature for 24 h. [$BMIm^+CL^-$] was then removed by washing the gel film in 2 L CPX-saturated water. Fresh CPX-saturated water was replaced every 24 h for 72 h. CPX-saturated water was chosen to minimize the dissolution of CPX from the film. The [$BMIm^+CL^-$]-free film

samples were then air dried in a custom-designed air chamber with relative humidity controlled at around 60%. All the other compositions were synthesized the same way.

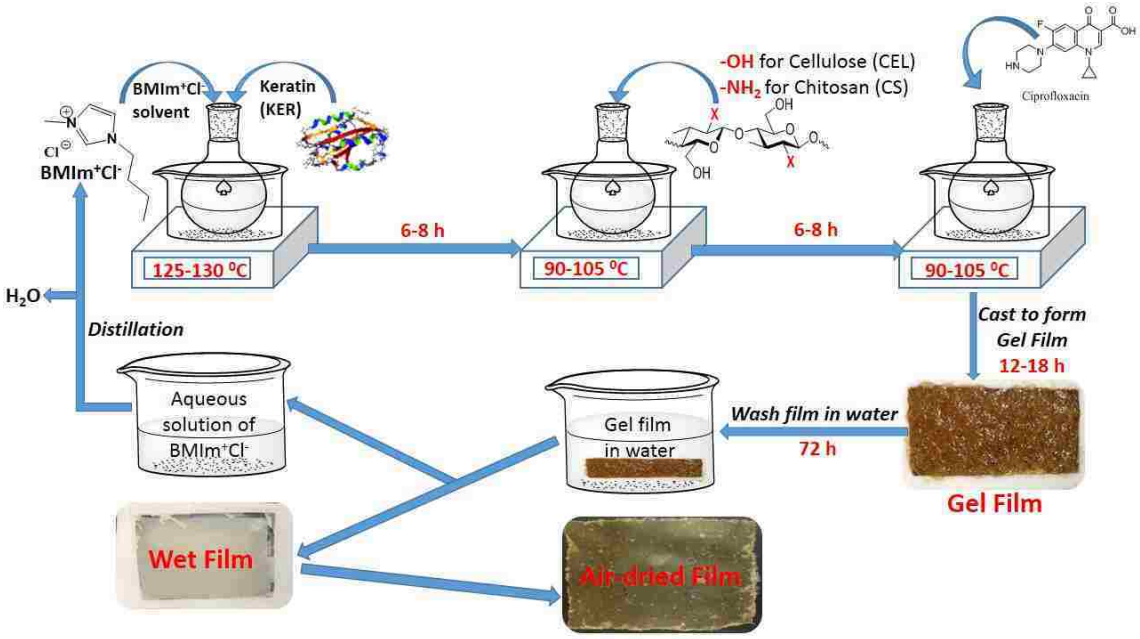

Scheme 5-2 Synthesis of ciprofloxacin (CPX)-loaded composite films containing CEL, CS, and KER.

5.2.4. Procedure used to measure *in vitro* release of ciprofloxacin from CPX-doped CEL/CS/KER composite films

In vitro CPX release from the CPX-doped composite films was monitored by the fluorimetric method. The method, initially designed in our group for the measurement of organic pollutant adsorption,[28] was modified to suit the measurement of *in vitro* CPX release. Specifically, 3.0-3.5 mg composite film, cut into a rectangular shape (4.3±0.2 mm X 4.1±0.3 mm X 0.18±0.02 mm length X width X thickness), was put into a standard 10-mm fluorescence cell. A PTFE mesh, cut to fit in the cell, was laid flat on top of the

composite film. A tiny stir bar (7 mm x 2 mm x 2 mm L x W x H) was then placed on top of the mesh. Exactly 3.5 mL of 1.0 mM phosphate buffer pH 7.2 was added into the cell. The cell was closed with a cell stopper before being immediately presented to the PTI QuantaMaster 40 spectrofluorometer (PTI, Birmingham, NJ). The release of CPX was then monitored by recording fluorescence spectrum (excitation wavelength, λ_{exc} = 324 nm; emission range 350-520 nm; 2 nm interval; 0.4 sec integration time; 0.50 nm and 0.25 nm entrance and exit slit widths respectively) of the buffer solution at specific time intervals for 10 h. The samples were then left to stir for a further 14 h before the last measurement was taken. This final measurement was considered to correspond to the amount of CPX released at equilibrium. The amount of CPX released at each time point, M_t, was calculated by using a calibration curve generated at emission wavelength 418 nm. As an example, the following linear relation $\left(I_{418nm} = 168{,}390 * [CPX] + 6{,}227; r = 0.999\right)$ was used to calculate the concentration of CPX in ppm. The calibration standards covered the concentration range 0.0 to 4.0 ppm. A preliminary experiment was carried out using placebo films (that is, sample without CPX) to determine the background effects from the biopolymer (either CEL or CS or KER) matrix alone. It was found that, besides a vertical offset in background, no emission bands appeared in the emission spectra. Thus, simple background correction was applied to all spectra before reading off the emission intensity at 418 nm. Another experiment was designed to determine the stability of CPX released within the entire 24 hours. For this, we measured the fluorescence of a buffer solution containing the same concentration as the one released at equilibrium (i.e. the concentration corresponding to the amount released within the entire 24 h). The signal intensity remained constant

throughout the entire period. The results suggests that CPX was stable during the entire releasing period.

5.2.5. Analysis of kinetics data

In vitro release data were fitted to four different kinetic models; zero order,[31,32] first order,[31-34] Higuchi,[35,36] and Korsmeyer-Peppas[37-40] models. Zero order model is based on the assumption that the rate of drug release is independent of its concentration. It is represented by the equation:

$$\frac{M_t}{M_\infty} = K_o t \qquad \text{Eq. 5.1}$$

where M_t/M_∞ is the fractional release of the drug at time, t in hrs and K_o is the zero order rate constant. The first order model describes a system where the release rate is concentration dependent; it is represented by the equation:

$$\ln\left(1-\frac{M_t}{M\infty}\right) = -K_1 t \qquad \text{Eq. 5.2}$$

where K_1, the first order rate constant, is taken as the slope of a plot of $\ln(1-M_t/M_\infty)$ against time, t. Higuchi model, sometimes referred to as the square root law because of the square root of time dependence of drug released, is based on Fickian diffusion of the drug from the matrix. This relation is valid only during the early times of drug release; namely the time up to 60% release of the drug. However, not all systems can be described by the Higuchi model. Thus, a more general model, the Korsmeyer-Peppas model or Power law, was developed to describe models including those deviated from Fickian

diffusion. The model relates fractional release to time through an empirical exponent, n and a rate constant, K_p. The model is represented by the following equation:

$$\frac{M_t}{M_\infty} = K_p t^n \qquad \text{Eq. 5.3}$$

Data is fitted using the relation above in the early releasing time is as in the Higuchi model. Higuchi model is a special type of Korsmeyer-Peppas model with n=0.5 for the former. The value of n is used to describe the mechanism of drug release.[37-40] According to this Korsmeyer-Peppas model, for drug release from films, when n=0.5 release is governed solely by Fickian diffusion. A value of n=1.0 is considered to be due to Case II transport of the drug. Values of n between 0.5 and 1.0 are considered to be due to anomalous transport of the drug which is basically a superposition of Fickian diffusion and Case II drug transport.

5.2.6. Quantitative analysis of secondary structure of proteins

5.2.6.1. Partial Least Squares Regression (PLSR)

Partial least squares regression (PLSR) analysis was performed using Unscrambler X 10.1 software (CAMO Inc., Oslo, Norway). A detailed treatise of this subject matter has been presented in the following sections. Briefly, PLSR builds a linear model that relates two data matrices, the predictors (X) and the response (Y) matrices to each other by using an advanced form of least squares fitting technique. In the present study, X contains the spectra of each of the eight protein standards from 1696- to 1623 cm^{-1}; this frequency range was chosen because it was reported to contain much

information about the secondary structure of the proteins.[41-44] *Y* contains information about the secondary structure of the standard proteins. Cross model validation coupled to Jack-knifing was used for selecting X-variables that were strongly correlated to the secondary structure of the proteins.[45,46] Before applying PLSR, data was pretreated by baseline correction, autoscaling by standard normal variate (SNV) and then mean centering, in that order. All these routines are already embedded in Unscrambler software that was used in this study.

The X-ray structures of the eight proteins, constituting our reference set, were taken from the Protein Data Bank (PDB).[47] The secondary structure of these proteins was then evaluated using the algorithm Define Secondary Structure of Proteins (DSSP), which is integrated in the PDB program. The DSSP algorithm works by assigning secondary structure to the amino acids of a protein given the atomic resolution coordinates of the protein. Details on this method are presented elsewhere.[48] Based on this algorithm, eight types of secondary structure are assigned. However, in the present study, only three groups were considered *viz* α-helix, β-sheet and the remainder was assigned to unordered group. The proteins used together with their PDB IDs and the assigned secondary structures are presented in

Table 5-1 Table of secondary structure of standard proteins as determined by the DSSP algorithm integrated in PDB program.

Protein	PDB ID	Custom Code	Source	fα	f_β	f_r
Albumin	4F5T	BSA	Bovine serum	0.727	0.000	0.280
Hemoglobin	1Y8K	HEM	Horse	0.770	0.000	0.230
Albumin	1BJ5	HAS	Human serum	0.710	0.000	0.290
Lysozyme	1LYZ	LYS	Chicken egg white	0.380	0.100	0.520
Myoglobin	205T	MYO	Horse skeletal muscle	0.750	0.000	0.250
Pepsin A	3PEP	PEP	Porcine stomach	0.150	0.430	0.420
Ribonuclease A	2AAS	RNASE A	Bovine pancreas	0.200	0.330	0.470
Trypsin inhibitor	1AVU	SOY	Soy bean	0.010	0.400	0.590

5.2.6.1.1. Notation

X is an m x n matrix where m represents the number of observations or standard samples and n represents the total number of dependent variables or frequency/wavenumber variables. Y is an m x p matrix of m samples and p response variables or secondary structure motifs. B represents an n x p matrix of regression coefficients.

5.2.6.2. Theory

Partial least squares regression (PLSR) is a multivariate regression technique that has found an ever increasing use in a wide range of applications including the objective determination of the secondary structure of proteins.[49-53] As a multivariate technique, it is based on the assumption that there is a linear relationship between spectral data and component concentration as represented by the equation $Y = X * B$, where Y is a response matrix containing the information about the secondary structure motifs (i.e. α-

helix and β-sheet) for each sample; X is a predictor matrix containing information about the spectra of each sample; and B is a matrix containing regression coefficients obtained by PLSR.

The objective in PLSR is to estimate B-matrix by taking into account the covariance between X - and Y -variables simultaneously. Its main advantage over multivariate linear regression (MLR) technique is that PLSR can analyze data with strongly collinear (correlated), noisy, and numerous X -variables.[54] In addition, in PLSR, one does not need to know all the components contributing to the signal, only the significant ones are needed. Furthermore, PLSR outperforms principal components regression (PCR) in that the former models the systematic variation in both X - and Y -matrices whereas the latter models just the X -variance. Thus, the principal components (PCs) obtained in PCR may be sub-optimal in predicting Y -variables.[55]

In PLSR, just like in any other multivariate analysis technique, the first step is to build the model and then use the model to predict the unknown Y -matrix. Building the model involves estimating B -matrix (a matrix regression coefficients) using a training or calibration set. This is achieved by finding a few "new" variables, X -scores (represented by T -matrix), which are estimates of the latent (non-observable) factors. These latent factors are extracted from X -matrix in order to explain as much variation in reference Y as possible and at the same time accounting for the variation in X . Most importantly, the X -scores obtained by PLSR are orthogonal which helps to overcome multicollinearity problem.[56] The X -scores are estimated as linear combinations of the original X -variables with the weight matrix, W . These are represented in the form, $T = X * W$.[56] The common form of PLSR is represented by the equation $\hat{X} = T * P'$ where T and P are

the scores and the loadings matrices respectively. The apostrophe (‘) symbol represent the transpose operation. Likewise, Y-scores, (represented by the matrix U) can also be multiplied by C, the weight matrix of Y-scores to give the relation, $\hat{Y} = U * C'$. Since X-scores are good predictors of Y, $\hat{Y} = T * C'$. The relation $T = X * W$ can then be substituted for T in $\hat{Y} = T * C'$ to give $\hat{Y} = X * W * C'$. By comparing this relation with the multivariate relation, $\hat{Y} = X * B$, B-matrix can be estimated from the relation, $\hat{B} = W * C'$.[56] This estimated matrix of regression coefficients is then used to estimate Y-matrix of the unknown sample.

5.2.6.3. Non-linear iterative partial least squares algorithm (NIPALS)

Non-linear iterative partial linear least squares (NIPALS) algorithm is used to develop the PLSR model. The details of this algorithm are described elsewhere.[54,55] In short, it involves, 1) estimating X weights, W; 2) estimating X-factor scores; 3) estimating Y weights, C and 4) estimate Y-scores, U in an iterative manner. After each factor, *l*, is extracted, the X-matrix is “deflated” by subtracting $t_l * p_l$ from X-matrix. The result is a matrix of residuals, E_{l-1}. The second latent factor is then extracted from this matrix of residuals rather than from the original X-variables themselves. The whole process is repeated until a predetermined number of components has been extracted.

5.2.6.4. Evaluating the quality of the model

The quality of the model can be affected by the number of latent factors and the significance of the X-variables chosen to build the model.

5.2.6.4.1. Choosing the optimum number of latent vectors

The optimum number of latent factors helps to prevent over-fitting, which is a case whereby the information that was used to build the model was not useful to predict responses for the new observations.[55,57] Cross validation and bootstrap techniques are usually used to prevent over-fitting.[58] In the present study, cross validation was used to choose the optimum number of latent factors to build the PLSR model. Specifically, leave-one-out cross validation was used. In this technique, observations or samples are separated into two subsets, the training set and the test set (Figure 5-1). A PLSR model is built on the training set and subsequently used to predict the test set. A different observation is left out and the previously left-out observation is added back to the training set. Another PLSR model is built on this new training set and subsequently used to predict the new test set. This is repeated until all the observations had a chance to be left out from the training set and used as the test set. All these predicted observations are stored in the matrix, $\hat{Y}$.

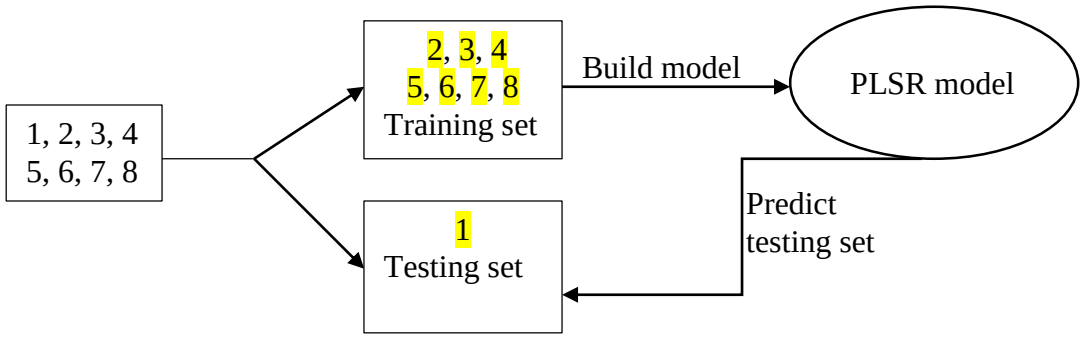

Figure 5-1Diagram to show the flow of operations during cross validation.

The quality of the PLSR sub-models is evaluated using the parameter root mean squared error of cross validation (RMSECV) (Eq. 5.4) where *l* represents the number of latent factors; *i* represents the i^{th} CV segment. The smaller the value of RMSECV the better the model. The number of latent factors that gives the lowest RMSECV is thus chosen as the optimum number of latent factors.

$$RMSECV_l = \sqrt{\frac{\sum_{i=1}^{n}\left(y_{il} - \hat{y}_{il}\right)^2}{n}} \qquad \text{Eq. 5.4}$$

Another parameter, the coefficient of determination, R^2, is also used to assess the model quality. This is calculated for *l*-number of factors, as shown in Eq. 5.5. The higher the value of R^2 the better the model. Using this parameter together with $RMSECV$ ensures the optimum latent factors.

$$R^2 = 1 - \frac{\sum_{i=1}^{n}(y_{il} - \hat{y}_{il})^2}{\sum_{i=1}^{n}\left(y_{il} - \bar{y}\right)^2} \qquad \text{Eq. 5.5}$$

5.2.6.4.2. Choosing the optimum X-variable set

It is essential to identify those X -variables that are relevant for predicting the response matrix, Y . To this end, several approaches have been developed to choose the optimum set of variables that are strongly correlated with the response variable (s).[52,59-62] We chose cross model validation (CMV) for variable selection.[61] In this CMV, one sample is left out whilst the remaining sample set is subjected to PLSR with cross validation (CV). In CV, each sample in the CMV sub-model is left-out in turn and PLSR

is used to generate regression coefficients, b_i on the remaining set. The uncertainty for each regression coefficient, s^2 (b) is calculated by Jack-knifing as illustrated in Eq. 5.6

$$s^2(b) = \left(\sum_{i=1}^{n} (b - b_i)^2 \right) \left(\frac{i-1}{n} \right) \quad \text{Eq. 5.6}$$

These variances can then be used to calculate the *t*-statistic, $t_b = b/s(b)$. These *t*-statistic are then converted to *p*-value. Any X-variable that gives a *p*-value less than 0.05 is considered significant. Each time an X-variable is found to be significant, it is given a score of one (1). Therefore, the maximum possible score for each X-variable corresponds to the number of CMV segments. The X-variables exhibiting the highest score are combined into a new set which is then used to build a PLSR model. Another set of variables exhibiting the next highest score is added to this highest-frequency set. Another PLSR model is generated. This is continued until all the X-variables with a score of at least one (1) is included to make a PLSR model. These models are then compared using RMSECV and R^2 values. The X-variable set giving a PLSR model with the lowest RMSECV and highest R^2 value is then considered to be the optimum set. This is then used to build a PLSR model which is later used to predict unknown Y-response matrix. The steps involved in CMV are described in point form below.

1) Leave out one sample. The rest constitute a cross model validation (CMV) set
2) Generate regression coefficients of each CV segment of this CMV set by using PLSR
3) Compute p-values for each X-variable corresponding to each Y-variable by using Jack-knifing

4) Assign a score to of one (1) each time an X-variable appears significant ($p<0.05$) in predicting at least one of the Y-variables
5) Add back the sample that was previously left out in the previous CMV model. Leave out a different sample. The rest constitute a new CMV set.
6) Repeat steps 2-5 until each one of the samples had a chance to be left out of the CMV model
7) Total the scores for each X-variable
8) Build a PLSR model using only X-variables that exhibit the highest frequency of significance and calculate R^2 and RMSECV
9) Add X-variable set that gave the next highest frequency of significance and calculate R^2 and RMSECV as before
10) Repeat step 9 by adding an X-variable set with the next highest significance each time until an X-variable set with the frequency of significance of at least one (1) is included in the PLSR models
11) Choose a set of X-variables giving PLSR model with the highest R^2 and lowest RMSECV.

5.3. Results and Discussion

5.3.1. Synthesis of [CEL/CS+KER] blend films using ionic liquid solvent

We successfully synthesized one- (CEL, CS, and KER), two- ([CEL+KER], [CS+KER], and [CS+KER]) and three- ([CEL+KER+CS]) component films using $BMIm^+Cl^-$ to dissolve CEL, CS and KER. As shown in Scheme 5-2, wool dissolution was carried out at a higher temperature than the temperature that was used in dissolving

either CEL or CS. This can be rationalized by considering the bond network that is present in these bio-macromolecules. The three dimensional structures of CEL, CS, and wool are stabilized by both intra- and inter-molecular hydrogen bonding. However, wool has additional type of bonding network, namely it has an extensive network of disulfide (-S-S-) linkages both within and between its protein chains. This additional bond network is responsible for the tightness texture of wool fibers. This close structure impedes the penetration of solvent molecules into the wool fibers. As a result, more thermal energy is required to disrupt the secondary structure of wool before it can dissolve the wool. In the early stages after adding wool to the IL, the wool fibers swelled. It seems that, during this stage, IL molecules slowly diffuse into the wool fibers from the outer into the inner layers thereby weakening the interactions between the polymer chains. Subsequently, the chains would disentangle and eventually the IL breaks the disulfide linkages by reducing them to thiol (-SH) form. However, upon exposure to air, these thiol groups can easily be re-oxidized back to the disulfide linkages. In addition, oxygen radicals form, which in turn react with the biopolymers leading to undesirable side products. To eliminate the possibility of formation of these undesirable products, the dissolution was carried out under nitrogen atmosphere. When synthesizing two- or three-component films, the polymers addition order is very critical. For example, all KER-based composites were synthesized by first dissolving the wool. This was primarily because the dissolution of wool required a high temperature whilst the dissolution of the polysaccharides required lower temperature conditions. Therefore, to reduce any possible thermal degradation of CEL or CS (which can adversely affect the desirable properties of these components), the temperature was reduced from 125 °C to 90-105 °C before either CEL or CS was added.

It should be pointed out that when CEL was added in 1% weight portions to KER, the latter enwrapped around the former. This led to the formation of small lumps of CEL, which were found to be difficult to dissolve. This was avoided by adding as low as 0.5% weight portions of CEL. For the synthesis of [CEL+CS] composites, CEL was dissolved first before adding CS. If CS was to be dissolved first, it would form a very viscous solution which would make it difficult to dissolve CEL. This could have an adverse effect on the homogeneity of the resultant composite material. The drug, CPX was added last and it took about 2 hr to dissolve.

The gel films were then washed with water to allow the IL to diffuse from the biopolymer into the water. However, this was only done for composites that did not have any CPX. For samples that contained CPX, a CPX-saturated aqueous solution was used in place of water to minimize the risk of losing the drug by leaching into the water.

5.3.2. Spectroscopic characterization

5.3.2.1. FTIR spectroscopy

We used FTIR spectroscopy to 1) confirm that the chemical structures of the biopolymers remained intact during regeneration from the IL; 2) confirm that the IL was quantitatively removed from the composite films by washing in water; 3) study the chemical interactions amongst the different biopolymers forming the composite films; and 4) determine the secondary structure of keratin in wool, regenerated KER, [CEL+KER] and [CS+KER] composite films.

5.3.2.1.1. Qualitative assessment of the chemical structures of the composite films

FTIR spectra of wool exhibited characteristic bands that are primarily assigned to the vibrational modes of peptide bonds in proteins. For examples; the bands at 1700-1600 cm^{-1} and 1550 cm^{-1} are due to amide C=O stretch (amide I) and C-N stretch (amide II) vibrations respectively.[63] In addition, a band at 3280 cm^{-1} is ascribed to N-H stretch vibration (amide A), and a band at 1300-1200 cm^{-1} is ascribed to the in-phase combination of N-H bending and the C-N stretch vibrations (amide III). This finding is expected since wool contains more than 95% of the protein keratin.[64] Interestingly, the FTIR spectrum of wool lacks a band at 1745 cm^{-1}, which is known to be due to lipid ester carbonyl vibrations.[65] This suggests that Soxhlet extraction quantitatively removed all residual lipids from wool. Interestingly, upon regenerating KER from wool no new IR signatures were observed in the FTIR spectrum of regenerated KER. The results seem to suggest that wool was dissolved by IL without any chemical modifications.

As described above, the regenerated KER film has rather limited applications if used by itself, because it possesses poor mechanical properties *(vide infra)*. Therefore, it is desirable to use either CEL or CS to improve the mechanical properties of KER-based composites. We therefore, prepared blend films containing varying proportional amounts of KER with CS and /or CEL. FTIR analyses of raw and regenerated CS and CEL and their blend films have been covered in detail in Chapter 2 and in an article published by our group.[28] Therefore, their detailed discussion will not be the focus of this section. However, we report on the FTIR analyses of composites containing each of these polysaccharides (CS and CEL) and KER *i.e.* [CEL+KER] and [CS+KER]. Figure 5-2 shows the FTIR spectra of [CEL+KER] (A) and [CS+KER] (B) with different

compositions. As expected, the spectra of these blend films exhibit bands that are characteristic of their respective components. Furthermore, the intensities of these bands tend to correlate well with the concentration of the respective constituents in the films. For example; the band between 1200- and 900- cm^{-1} (due to sugar ring deformations) increased in relative intensity as the proportional amount of CEL increased in the [CEL+KER] composite films (Figure 5-2A). Similarly, the intensity of the amide I and amide II bands increased with concomitant increase in the relative amount of KER in the same [CEL+KER] composite films. Similar trend was noticed in the spectra of [CS+KER] composite films (Figure 5-2B). It is noteworthy that, in all composite films ([CEL+KER], [CS+KER] and [CEL+KER+CS]), no new peaks were observed in their FTIR spectra. Essentially, their spectra are a superposition of the spectra of their corresponding individual components. This, as noted earlier, helps to maintain the desirable properties of these three components in the composites. Specifically, these composites are expected to retain their ability to control drug release (due to KER), to kill bacteria (due to CS) and to be mechanically strong (due to CEL).

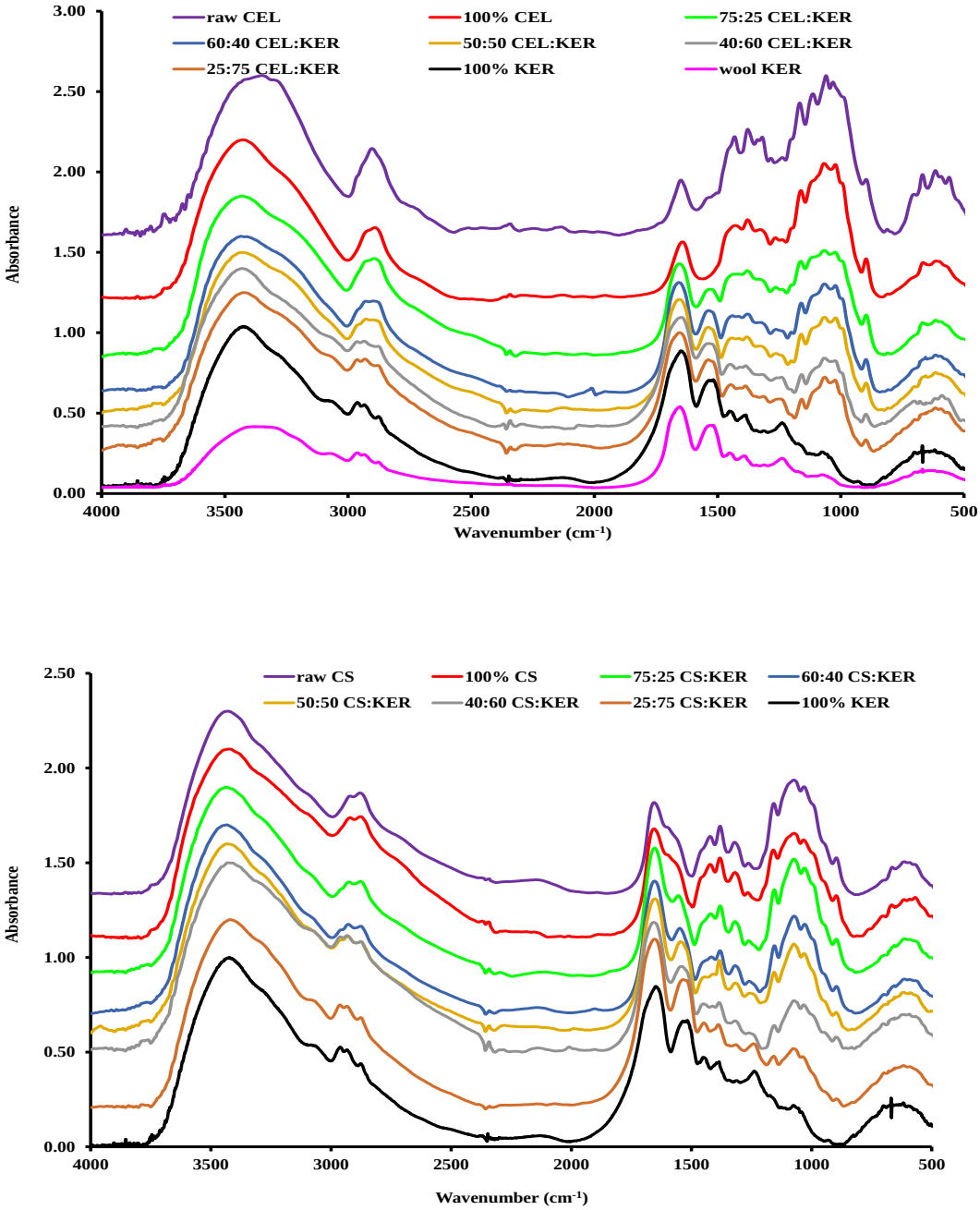

Figure 5-2 FTIR spectra of (A) [CEL+KER] and (B) [CS+KER] composites. The spectra of CEL powder (A, purple) and CS powder (B, purple curve) were included for reference.

The FTIR of composite films containing the drug, CPX exhibited no characteristic bands for CPX. This was hardly surprising considering that the ratio of biopolymer to CPX (200:1) was too high. Therefore, it is surmise to suggest that the CPX content was too low to be detected by FTIR. However, when fluorescence, a relatively more sensitive technique is used, the results show that CPX was indeed present in the composite films. This was confirmed during drug release because over time, the fluorescence of the solution in its CPX-doped composite was present, increased as more CPX was released from the composite films.

5.3.2.1.2. Determination of secondary structure of keratin protein

As stated in the previous section, the main chemical framework of KER remained intact throughout the regeneration process. Nevertheless, the secondary structure of KER could have been modified during this process. Such conformational changes could adversely affect the desirable properties of KER including its ability to control the drug release and the corresponding mechanism.[65] Thus, it is essential to determine the secondary structure of the KER composites. Many techniques have been used to accomplish this task with various levels of success. X-ray diffraction (XRD) has emerged as the most accurate given that it gives precise atomic coordinates. Nevertheless, this technique is limited to crystalline samples. XRD cannot be used because the composites synthesized here are amorphous. Thus, we considered the use of FTIR to probe the secondary structure of KER. This is possible because amide I band in FTIR spectra of proteins is known to be sensitive to the secondary structure of proteins.[66-68] Each conformation gives rise to somewhat different C=O stretching frequency due to variation in the H-bonding pattern. However, amide I band is broad and featureless due to

extensive overlap of the underlying component bands which are both broad and too close to be resolved by FTIR spectroscopy. Thus, mathematical methods based on narrowing the component bands, thereby making them resolvable, have been used to determine the secondary structure of proteins.[68] We, therefore initially evaluated the possibility of using this method to estimate the secondary structure of KER. This was accomplished by deconvoluting the bands, amide I and II (1750-1450 cm^{-1}) using Peak Analyzer tool embedded in the Origin Pro 9.0 software (OriginaLab, USA). The amide bands were resolved into individual Gaussian shaped peaks. Typical results obtained for deconvoluting amide I band for wool and 100% KER are illustrated in Figure 5-3A and B. As illustrated, amide I band was resolved into three separate bands that are assignable to α-helix, β-sheet and random conformations. The proportional content of each of these conformations was then calculated by dividing the integrated area of the corresponding conformation by the total integrated area for all the three bands. These results are shown in Table 5-2. We included results for calculation made by changing the amide spectral region by either 1 cm^{-1} or 2 cm^{-1} in either direction. This was done to investigate the sensitivity of this deconvolution approach to the changes in the spectral region. As shown in this table, it is evidently clear that changing the spectral region has a substantial effect on the results obtained. For examples; by changing the region by 1 cm^{-1} from 1750-1450 to 1751-1451 cm^{-1} for wool led to a 15% increase in the content of α-helix whereas β-sheet content decreased by 31%; Likewise, for 100% KER, α-helix increased by 5.55 whereas β-sheet content decreased by 23%. Similar trends were observed when the spectral ranges were changed by 2 cm^{-1}. These results show that deconvolution of the

amide bands is very subjective and varies with even slight changes in the spectral region studied.

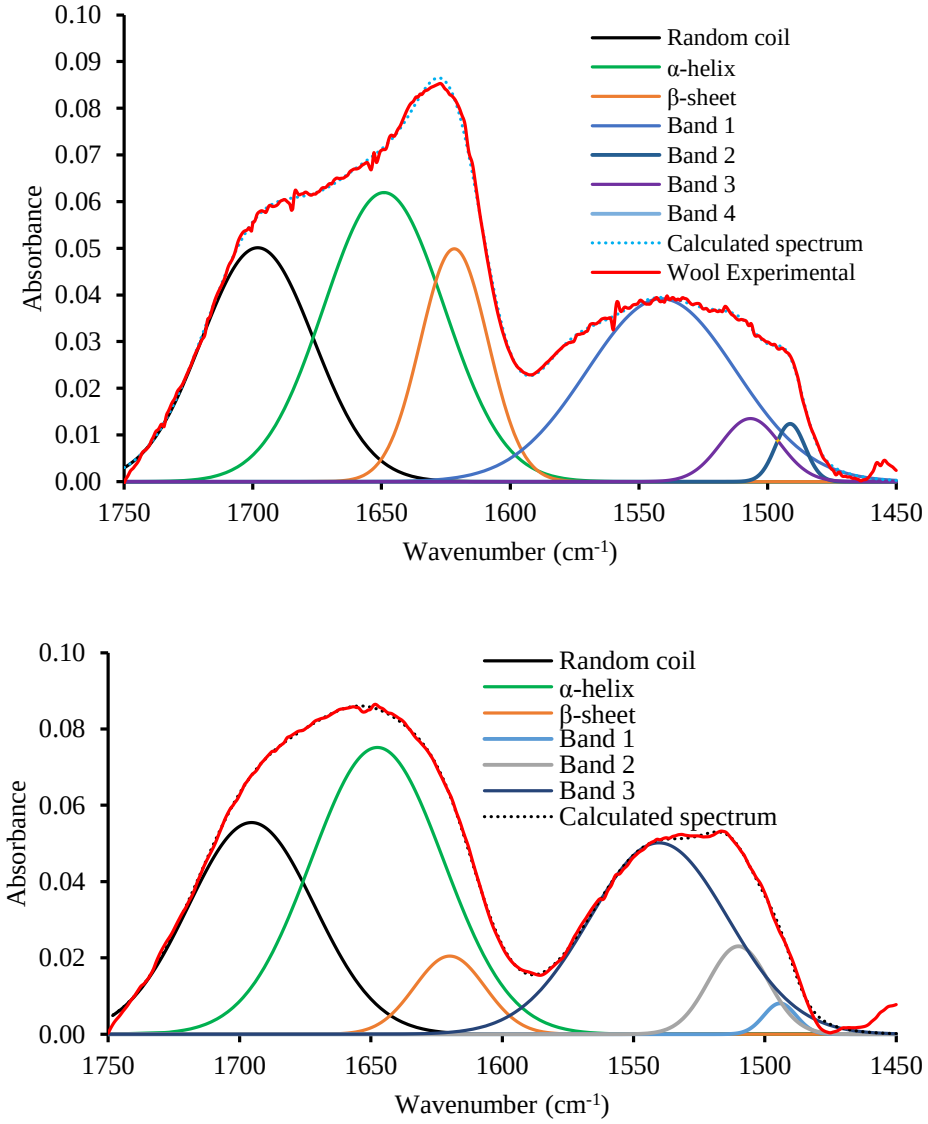

Figure 5-3 Resolution enhancement of the amide I band of wool (A) and 100% KER (B)

Table 5-2 Secondary structure of wool and regenerated KER as determined by curve fitting.

	Spectral range (cm^{-1})	α-helix	β-sheet	Random coil	R^2
Wool, this work	1750-1450	0.454	0.206	0.341	0.9984
Wool, this work	1751-1451	0.522	0.132	0.336	0.9947
Wool, this work	1752-1452	0.519	0.139	0.342	0.9945
Wool, this work	1749-1449	0.541	0.153	0306	0.9945
Wool, this work	1748-1448	0.547	0.157	0.296	0.9943
Wool, Ref 1	1750-1450	0.34	0.25		
Wool, Ref 2	1740-1580	0.47	0.33	0.19	
Wool, Ref 3	1750-1450	0.582	0.379	0.039	
100% KER	1750-1450	0.544	0.079	0.378	0.9976
100% KER	1751-1451	0.574	0.060	0.366	0.9950
100% KER	1752-1452	0.589	0.067	0.344	0.9951
100% KER	1749-1449	0.598	0.074	0.328	0.9950
100% KER	1748-1448	0.611	0.086	0.303	0.9950

Although deconvolution is widely popular due to the ease of carrying out, it falls as being very subjective. Thus, it is important to use a more objective method that is robust. To this end, we investigated the possibility of using partial least squares regression (PLSR), a multivariate technique that has been applied in the determination of the secondary structure of proteins other than keratin. We modeled only two structural motifs, α-helix and β-sheet although the structure of proteins also contains random coil or disordered. Only α-helix and β-sheet were selected because their FTIR spectra are more defined than the spectra linked to random coil. Furthermore, the spectra linked to random coil vary from protein to protein making it difficult to accurately model this motif. Therefore, the remaining fraction, that is the fraction not attributed to any of α-helix and β-sheet, was assumed to be associated with random structures.

The first stage in any multivariate technique is to select a set of predictor (X) variables which correlate well with the response (Y) variables under study. In our case, we used cross model validation (CMV) with Jack-knifing to estimate p-values for each X-variable as described in the previous sections.[69] Only X-variables with p-values less than 0.05 on either α or β were retained in the model. We then recorded the number of times each X-variable was found to be significant in the eight inner models of CMV (Figure 5-4). A set with variables exhibiting the highest frequency (that is eight in the current case) was used to build another model. To this set, we added the set exhibiting the next highest frequency (that is seven). This was continued until all the X-variables with frequency of at least one were used to make the PLS model. Then, the quality of these models were evaluated based on root mean square error of cross validation (RMSECV), coefficient of determination (R^2) and the optimal number of latent variables (LVs). The model with the lowest RMSE, optimal number of LVs and highest R^2 was selected for use in predicting the secondary structure of KER in wool, regenerated KER, CS:KER and CEL:KER composites. The best model that fulfilled these criteria consisted of X-variables with a frequency of significance of at least seven.

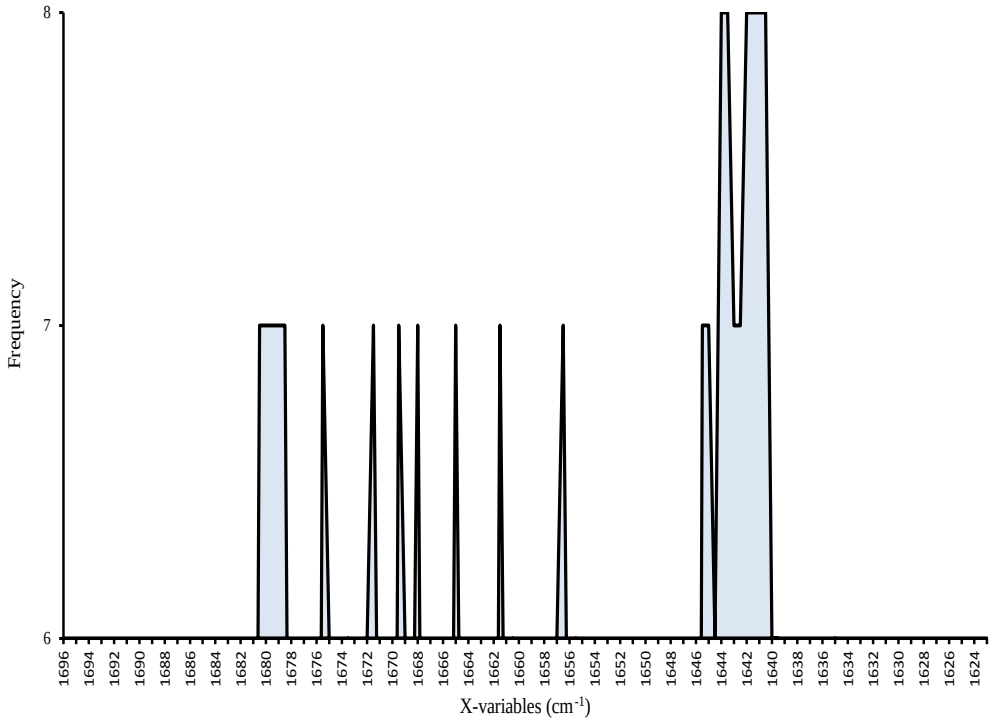

Figure 5-4 Frequency of significance obtained using cross model validation (CMV).

Figure 5-5 summarizes the PLSR results for the chosen PLSR model. As expected, residual validation variance decreases with more factors being incorporated into the model (Figure 5-5A). This is because as more factors get incorporated into the model, more systematic variation gets to be accounted for. However, beyond three factors, the residual validation variance started increasing. This shows that the model is now incorporating noise. Since only factors describing systematic variation should be used in the model, only three factors were used to build the calibration model, which was later used for predictions of unknowns. It was also necessary to check the relative amount of variation explained when this optimum number of factors was used. Figure 5-5B

shows that the three factors accounted for 89% variance which is evidently clear that three factors account for a decent amount of systematic variation in the variables. The scores plot (Figure 5-5C) shows that the first factor (F1) is able to differentiate the protein standards based on their α-helix and β-sheet composition. Along this factor, protein standards with more than 0.3 α-helix and at most 0.1 β-sheet (*i.e.* MYO, HEM, HAS, BSA, LYZ) group together on the right hand side (within the red box) whilst those standards with less than 0.2 α-helix and more than 0.3 β-sheet (RNASE A, SOY, PEP) group together on the left hand side (within the purple box). These differences are further confirmed when the correlation loadings plot was considered (Figure 5-5D). Along the first factor, α- variable tends to appear on the right hand side whilst β- variable appears on the opposite side. By comparing this correlation loadings plot with the scores plot, it becomes apparent that α-variable is positively correlated with proteins containing more α-helix. Similarly, β-variable is positively correlated with proteins containing more β-sheet. In addition, the correlation loadings plot shows the correlation between the Y-variables (α and β) and the X-variables (frequency). As expected, α-helix is positively correlated to the variable 1656.5 cm^{-1} which is consistent with the previous findings.[41-44,52,67] On the other hand, β-sheet is positively correlated to variables 1642.0-1640.5 cm^{-1}.

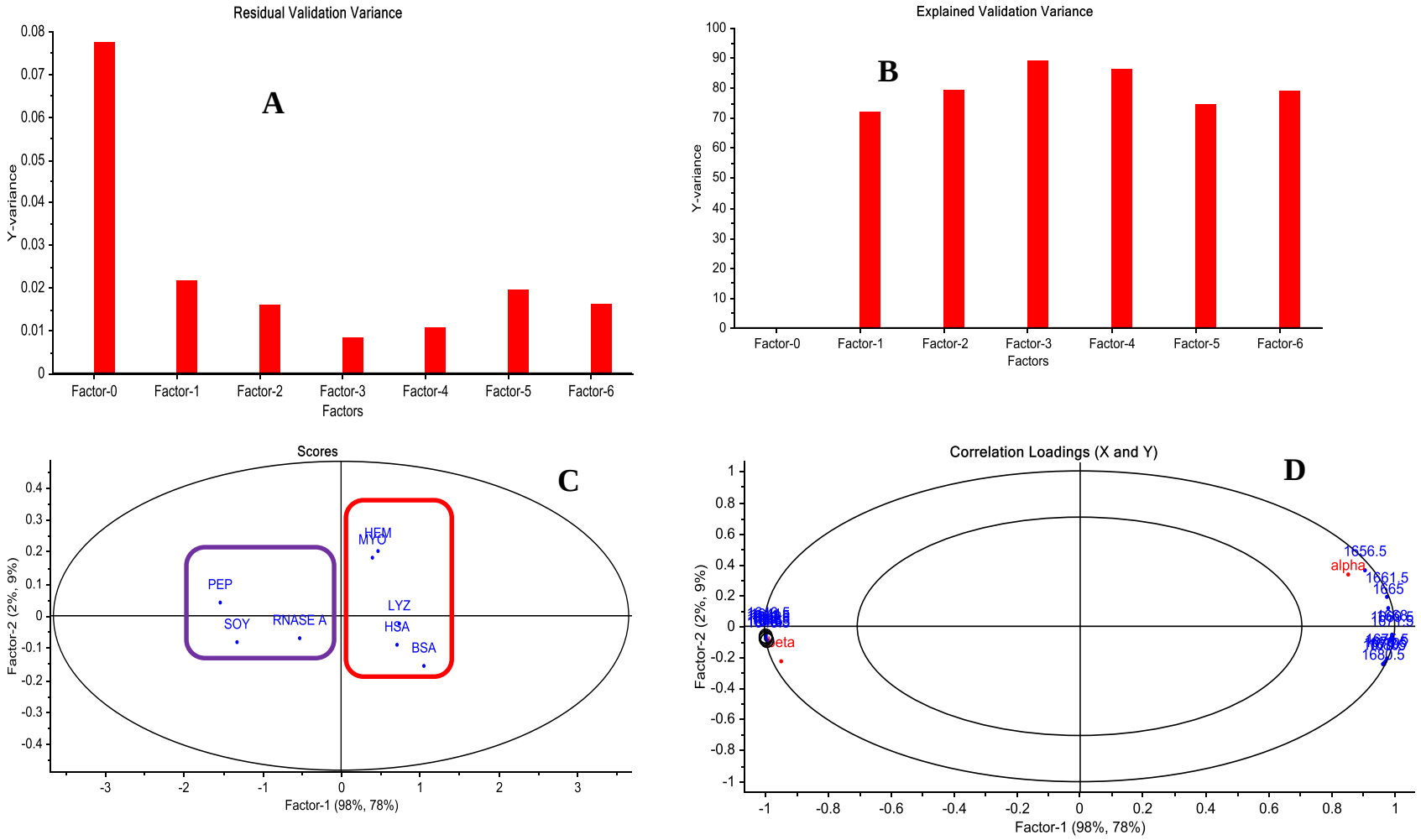

Figure 5-5 Residual validation variance plot (A), Explained validation variance (B), scores plot (C), and the correlation loadings plot (D) obtained after PLSR calibration

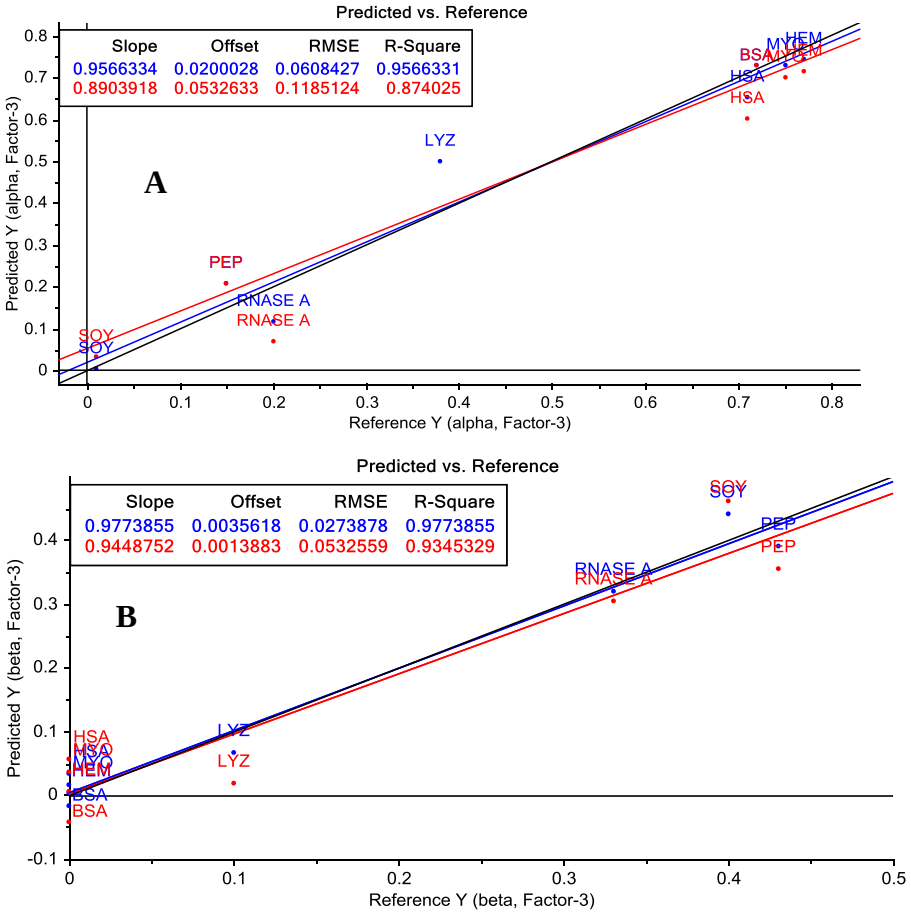

Figure 5-6 Predicted vs reference plots for α-helix (A) and β-sheet (B) obtained by PLSR

The model was then applied to predict the α-helix and β-sheet contents of KER in wool, regenerated KER, CS:KER and CEL:KER composites. After the PLS prediction, wool was found to contain 0.3±0.1 α-helix and 0.18±0.05 β-sheet (Table 5-3). These results corroborate the previous findings that sheep wool contains more α-helix than β-sheet.[70-72] Upon dissolving in the IL and regenerating from water, KER was found to contain 0.3±0.1 α-helix and 0.22±0.06 β-sheet. These results suggest that regeneration of KER helps to retain the same conformation as that of wool but with a slight increase in the β-sheet content. Similar results were reported by elsewhere.[73] Subsequently, an attempt was made to predict the secondary structure of KER in the CS/CEL:KER

composites. It is noteworthy that the FTIR spectra of CEL and CS possess interfering bands in the amide I region. For examples, the spectrum of CEL shows an O-H band from adsorbed water at 1640 cm^{-1}. CS, being partially deacetylated (84±2% degree of deacetylation), contains residual amide bonds which result amide I bands. Consequently, the results obtained in predicting the secondary structure in KER composites containing either CEL or CS are believed to be unreliable. However, it is expected that the interference is minimal when KER is present in high concentrations. As a consequence, we carried out the prediction in composites containing 75% KER, namely the 25:75 CS:KER and 25:75 CEL:KER. As shown in Table 5-3, 25:75 CS:KER was found to contain 0.1±0.2 α-helix and 0.31±0.07 β-sheet whilst its CEL:KER counterpart contains 0.3±0.3 α-helix and 0.3±0.1 β-sheet. Based on these results, it can be concluded that the polysaccharides tend to stabilize β sheet- than α helix- conformation. These results can better be explained by considering the whole process of dissolution and regeneration. During dissolution, the inter- and intra-molecular forces in KER are broken thereby destroying its secondary structure but maintaining its primary structure. During gelation, regeneration from water and drying, these interactions are reestablished thereby partially reforming the same secondary structure as in wool. However, in the presence of the polysaccharides (either CEL or CS), the chains are maintained in the extended form thereby hindering a significant reformation of the α-helix. Consequently, the KER in these matrices adopt structures with lower content of α-helix and higher content of β-sheet.

Table 5-3 Secondary structure of wool, regenerated KER and its composites with CEL and CS as predicted by the PLSR technique

	α-helix	β-sheet
Wool	0.33±0.02	0.181±0.004
100% KER	0.31±0.08	0.21±0.03
25:75 CS:KER	0.18±0.04	0.31±0.04
25:75 CEL:KER	0.32±0.09	0.25±0.04

5.3.2.2. Near IR

Near infrared spectroscopy (NIR) was used to provide further confirmatory evidence for the successful synthesis of [CEL/CS+KER] composite films and to provide qualitative information about the secondary structure of KER. Figure 5-7 shows the NIR spectral traces for the pure and blend films. The spectrum for 100% CEL exhibits characteristic bands at 1490 nm (due to the first overtone of the O—H stretch modes of free and hydrogen bonded –OH groups of cellulose), and the band at 2090 nm (combination band of the first overtone of the O—H deformation vibration and the first overtone of the C—O stretch mode).[65,69,74] In addition, the spectrum also exhibits additional bands between 2200 and 2350 nm which can be tentatively ascribed to the combination of the O—H stretch and C—C/C-O stretch modes.[75,76] An additional band appearing at 1920 nm was due to a combination of the O—H stretch mode and H—O—H bending mode for free and adsorbed water in the cellulose film.[77] In addition to the bands assignable to O–H, C—C, C—O, and C—H, the NIR spectrum of 100% KER exhibits bands characteristic of peptide bonds (—CONH—). For examples, the band at 1530 nm is tentatively assigned to the first overtone of N—H stretch mode while the band at 1978 nm is assigned to a combination of N—H stretch and amide II vibrational modes.[78-80] The doublet at 1700- and 1760-nm is due to the

first overtone C–H stretch for protein side chains.[81,82] To gain an insight into the secondary structure of KER, the region between 2000- and 2350-nm was subjected to second derivative analysis. This revealed two bands, one at 2166 nm (representing α-helix) and another one at 2204 nm (representing β-sheet).[83,84] This suggests that the regenerated KER exhibited both α-helix and β-sheet structures; this concurs with the results obtained elsewhere.[63]

As illustrated on Figure 5-7A, the NIR spectra for the [CEL+KER] blend films containing 75%-, 50%-, and 25%- KER exhibit bands of both CEL and KER. For example, 50:50 CEL:KER contains bands assignable to both KER (doublet between 1690 nm and 1800 nm; bands between 2000 nm and 2350 nm) and CEL (band at 2090 nm). The intensities of the bands ascribable to KER decrease concomitantly with the decrease in KER content in [CEL+KER] composite films. The same trend was observed in the case of [CS+KER] composite films (Figure 5-7B). It is worth noting that the band attributed to water appears at shorter wavelength in 100% CEL (1920 nm) than in 100% KER (1934 nm). This suggests that the water structure in these two biomolecules is different. In addition, adding CEL to KER results in this water band shifting from 1934 nm to 1920 nm. The shift correlates well with the amount of CEL added to KER. Two distinct bands in NIR spectrum of 100% CS appear at 1528 nm and 2020 nm. The former is tentatively assigned to the first overtone of the N—H stretch of the free amine group whilst the latter band is assigned to the combination of C=O and NH stretches in acetylated units of CS.[85]

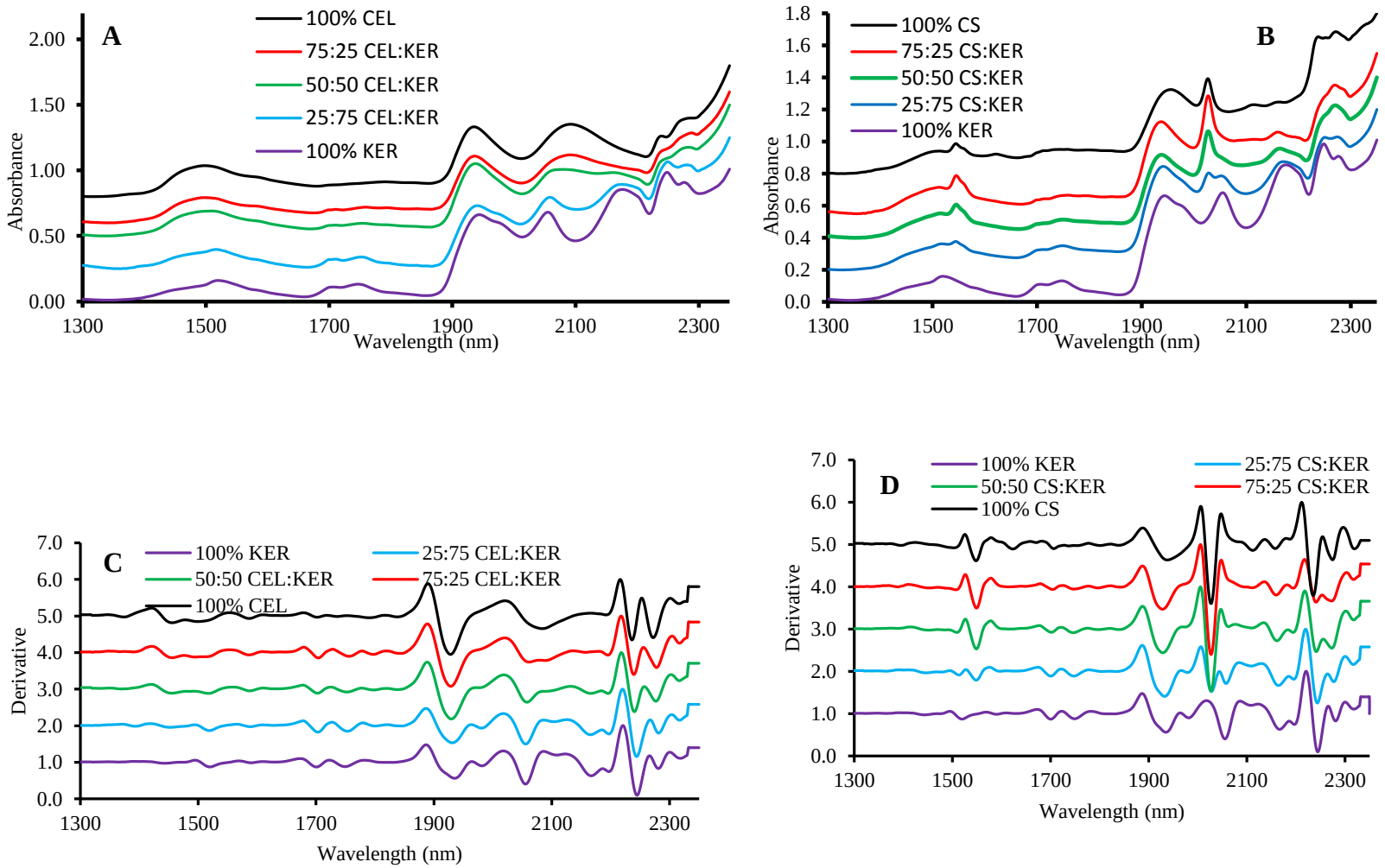

Figure 5-7 NIR spectral traces (A and B) and their second order derivatives (C and D) of (A, C) [CEL+KER] and (B, D) [CS+KER] composite films.

5.3.2.3.Powder X-ray diffraction spectroscopy

The crystal structure of wool, regenerated KER and [CS/CEL+KER] composites were studied using X-ray diffraction. As illustrated in Figure 5-8, the spectral trace of wool exhibits two well resolved peaks at 2θ of about 9° and 20° corresponding to the α-helix and β-sheet structures respectively.[86-88] The presence of both configurations in wool concurs with the results obtained by using FTIR, NIR (*vide supra*) and solid state NMR (*vide infra*) in this study. In addition, there were sharp peaks located at 32° and 36° 2θ, which confirms other crystalline structures within wool. Interestingly, substantial structural changes occurred after dissolving wool in IL and then regenerating it from water. Specifically, the peak at 9° 2θ not only decreased in relative intensity but also became broader. It is evidently clear from these results that α-helix decreased as a result of the dissolution and regeneration process. This is expected since IL is known to destroy the secondary structure of KER in wool during dissolution. On regeneration from water, the secondary structure is partially regenerated leading to an amorphous structure. The peak at about 20° 2θ effectively increased in intensity relative to the peak at 9° 2θ. These results suggest that the resultant regenerated KER contained more β-sheet than α-helix content. When the KER was blended with either CS or CEL, the XRD spectra of the resultant composites were quite similar to the spectrum of regenerated KER alone. This suggests that the polysaccharides (CS and CEL), helped to maintain the polypeptide chains in an extended form thereby hindering a significant reformation of the α-helix conformation. Furthermore, this confirms the compatibility between either CEL or CS and KER.

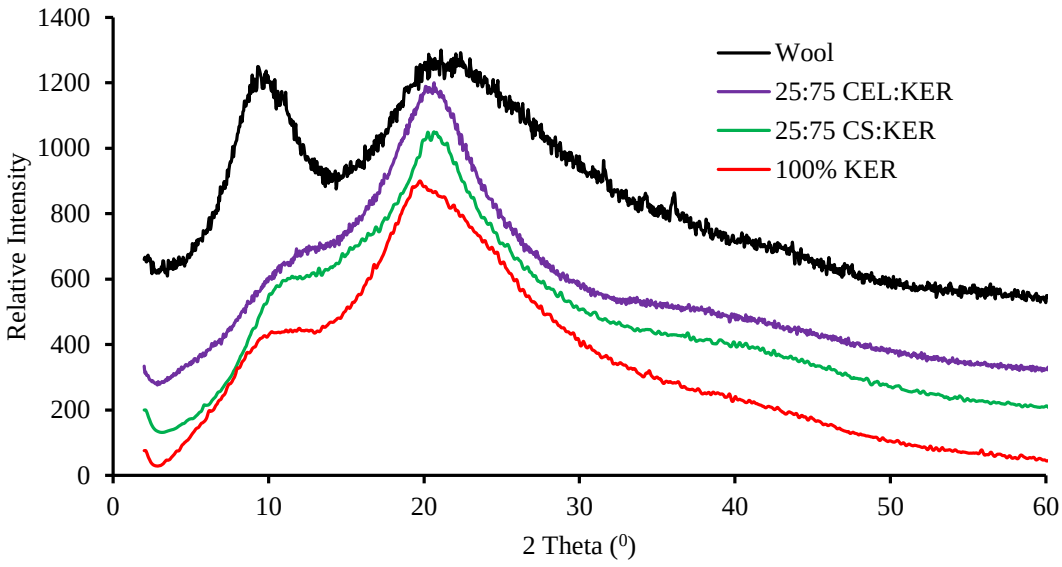

Figure 5-8 X-ray diffraction spectra of wool, regenerated KER, 25:75 CS:KER and 25:75 CEL:KER composites.

5.3.2.4. ^{13}C Solid state Cross Polarization Magic Angle Spinning (CP-MAS) NMR spectroscopy

We used ^{13}C CP/MAS NMR spectroscopy to study the interactions between CEL/CS and KER. The spectra are shown in Figure 5-9(A). For the spectrum for wool, the peaks appearing in the ranges 172-180 ppm, 115-158 ppm, 45-65 ppm and 10-40 ppm can be assigned to carbonyl, aromatic carbons, C^{α} methane and side chain aliphatic carbon atoms respectively.[89] Upon regeneration, KER retained its chemical structure because no new bands appeared in its spectrum. This shows that the ionic liquid dissolved the wool without any chemical modifications. The spectrum for CEL film contained all the peaks assignable to each carbon atom of its anhydroglucose units. Specifically, the peaks appeared at 61.9 ppm (C-6), 74.6 ppm (C-3 and C-5), 83.2 ppm

(C-4), 104.2 ppm (C-1). A composite film containing 75:25 CEL:KER appeared to lack peaks attributed to KER. This could be due to having less amounts of KER which in turn become undetectable by NMR. However, 25:75 CEL:KER contained peaks assignable to either CEL or KER. Similar results were obtained for [CS+KER] composite films. Similarly, spectra of 25:75 CS:KER and 37.5:62.5 CS:KER composites contain bands that correspond to both CS and KER (Figure 5-9B).

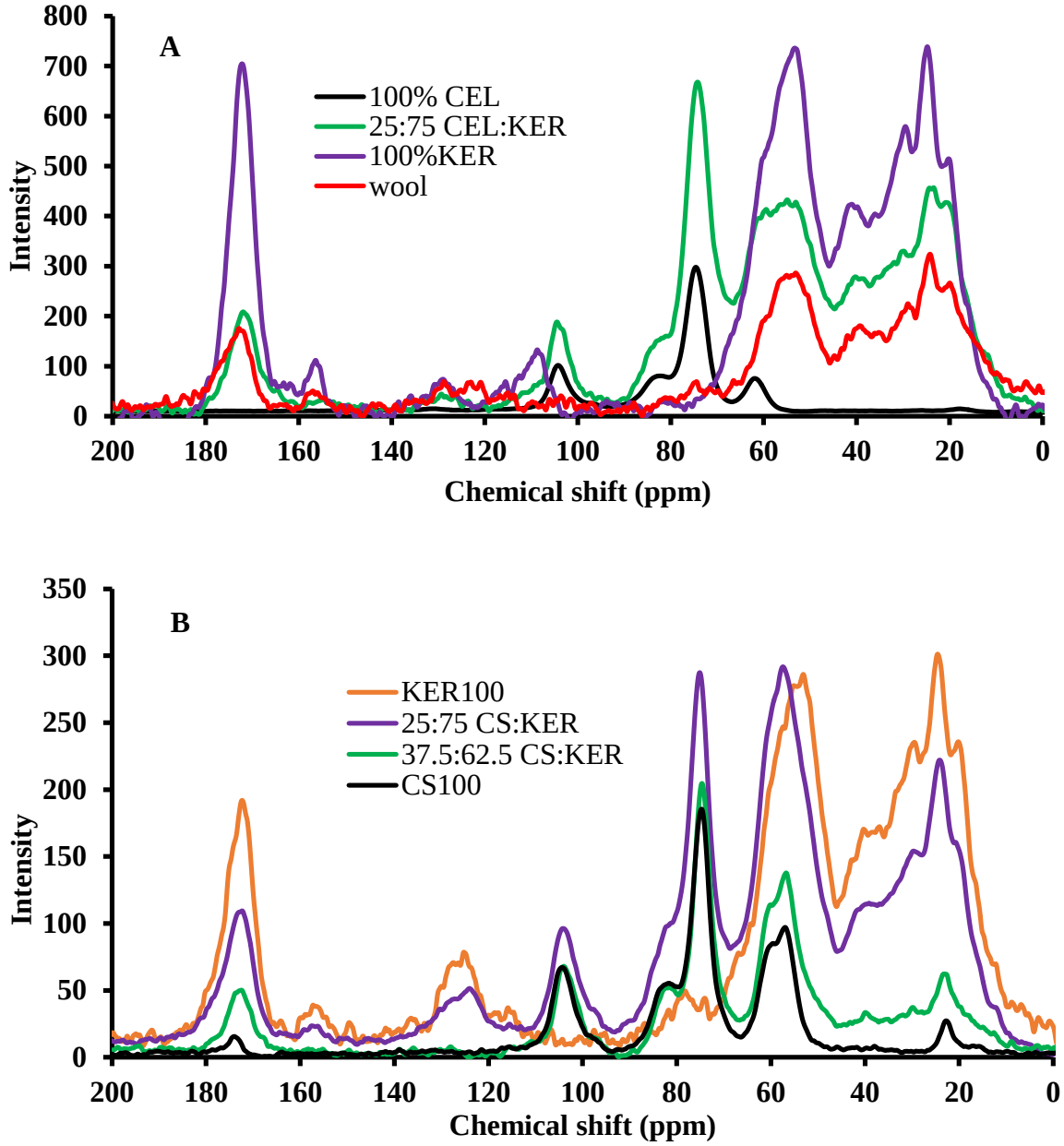

Figure 5-9 ^{13}C CP-MAS spectra of [CEL+KER] (A) and [CS+KER] (B) composites

5.3.2.5. Scanning Electron Microscopy (SEM)

Figure 5-10 shows SEM micrographs of the surfaces and cross sections of [CEL/CS+KER] composite films. While micrographs for 100% CS and 100% CEL surfaces exhibit smooth and homogeneous morphologies without any pores, the micrograph of 100% KER exhibit a rough and porous structure with a three dimensional interconnection throughout the film surface. This porous structure has implications on the physical properties of KER films. For example, the brittleness of 100% KER film can be partly attributed to this porous microstructure. To improve the mechanical properties of KER whilst harnessing its controlled drug-release properties, KER was blended with either CEL or CS. As can be seen, incorporation of the polysaccharides (CEL and CS) in KER matrix leads to significant changes in the microstructures of the resultant composite films. However, the microstructures of these composite films are noticeably different. While incorporation of CS in the KER matrix results in composite films which present smooth and homogeneous surfaces with no evidence for phase separation, incorporation of CEL results in somewhat rough surfaces. This suggests that KER is more compatible with CS than it is with CEL. This is so despite the similarity in the chemical structures of CEL and CS; the only difference in their chemical structures is that CS has an amine group at C-2 whilst CEL has a hydroxyl group. These results seem to predict that [CS+KER], being more densely packed, should be mechanically stronger than [CEL+KER]. However, the results from mechanical tests, described in the next section, indicate that [CEL+KER] composites are much stronger than [CS+KER]. Upon considering that 100% CEL has a fibrous structure, these fibers could still be embedded in the KER matrix thereby leading to stronger composites.

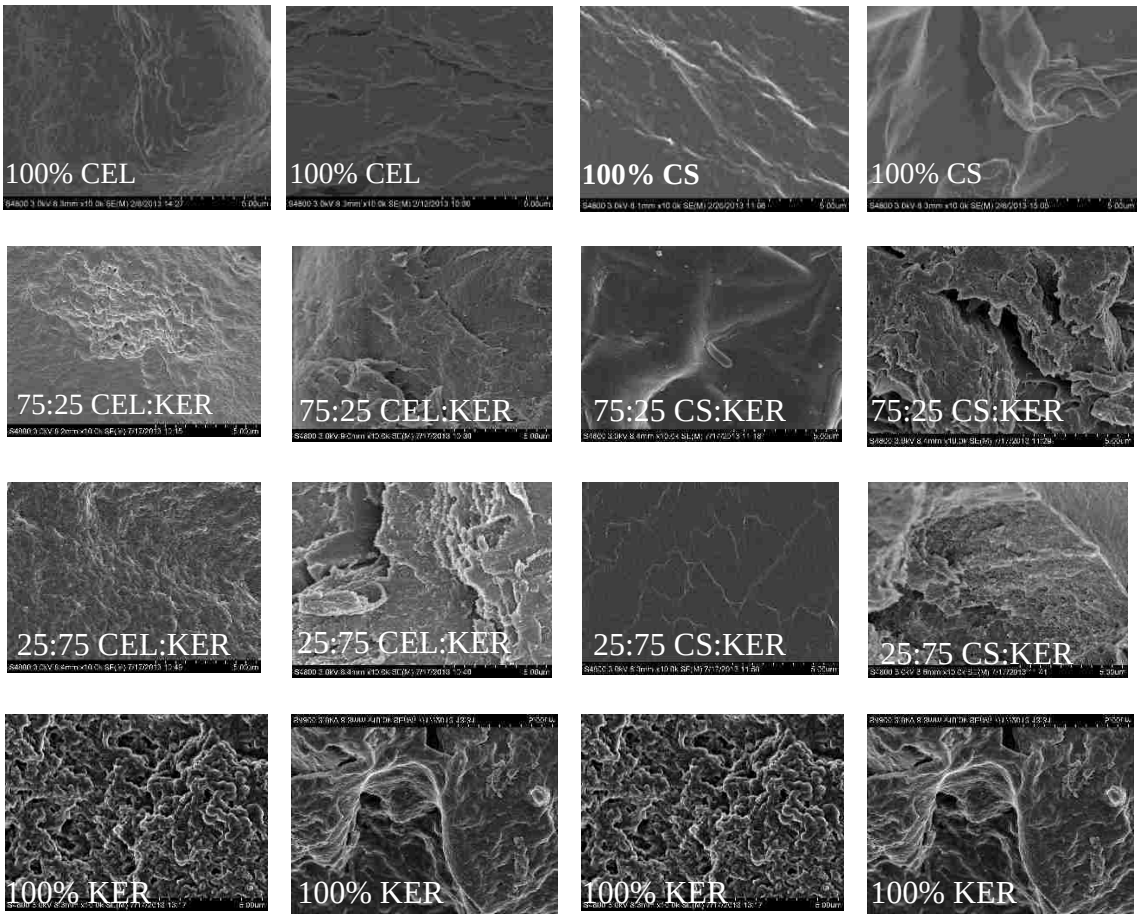

Figure 5-10 SEM images of surcae and cross sections of 100% CEL, 100% CS, 100% KER, 25:75 CEL:KER and 25:75 CS:KER composite films.

5.3.2.6. Mechanical Properties

KER has been shown to induce controlled release of drugs.[26] Nevertheless, its poor mechanical properties continue to hamper its potential applications. For example, in other studies,[90] regenerated KER film was found to be too brittle to be reasonably used in any application. One noble solution would be to chemically blend KER with CEL, which

is known to possess remarkably high mechanical strength. In light of this attractive property of CEL, experiments were designed to verify its effect on the tensile strength of the resultant [CEL+KER] composite films. Figure 5-11 shows the variation of tensile strength of [CEL+KER] as a function of cellulose content. As expected, the tensile strength of [CEL+KER] composite films showed a nearly linear increase as the proportional content of CEL was increased. For example, the tensile strength of [CEL+KER] increased by at least 4X when CEL loading was increased from 25% to 75%. This behavior has also been reported elsewhere when CEL was used as a reinforcement in other composites.[26] One possible explanation could be that the flat surface of CEL serves as a template on which KER molecules, through their hydrogen bonding interactions, coagulate into a β-sheet which in turn lead to stronger composites. It is worth noting that [CEL+KER] composite films were much weaker than [CS+CEL].[24] For example, [CEL+KER] and [CEL+CS] containing 75% and 71% CEL had tensile strengths 36±3 MPa and 52 MPa respectively. This could be attributed to the fact that CEL structure is more similar to that of CS than KER structure. Therefore much stronger interactions are established between CEL and CS than between CEL and KER. Although CS also leads to an increase in the tensile strength of [CS+KER], its effect is noticeably lower than that of CEL of comparable loading. For example, [CEL+KER] and [CS+KER] had tensile strength values of 37±6 MPa and 20±1 MPa respectively for a 40% KER loading. This could be due to the fact that CS is inherently weaker than CEL as reflected by the tensile strengths of 100% CS (36±9 MPa) and 100% CEL (82±4 MPa).

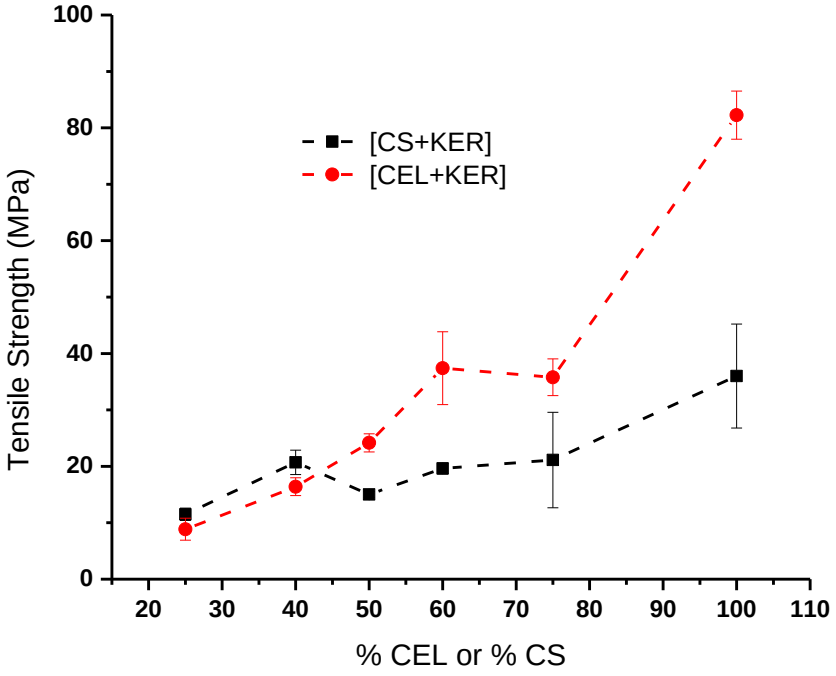

Figure 5-11 Plots of tensile strength as a function of concentration of CEL in [CEL+KER] composites (red circles) and CS in [CS+KER] composites (black squares).

5.3.2.7. Thermal properties of [CEL/CS+KER] composite films

We performed thermo gravimetric analysis (TGA) to determine the effect of each component on the thermal properties of the resultant composite film. In addition, we also studied the effect, on the thermal properties, of processing biopolymers (CS, CEL and KER) in ionic liquid. TGA curves of wool, CEL powder, CS powder, regenerated KER (*i.e.* 100% KER), regenerated CEL (*i.e.* 100% CEL), regenerated CS (*i.e.* 100% CS), [CEL+KER] and [CS+KER] composite films (Figure 5-12). The comparison was achieved by using onset decomposition temperature as a surrogate measure of the thermal

stability of a component. It is probable that the dissolution process could reduce the thermal stability of the biopolymer. Therefore, we compared the onset decomposition temperature of unprocessed biopolymers with those of their corresponding regenerated films. The onset decomposition temperature for wool KER decreased by 0.5% from 246.8- to 245.5 °C upon regenerating from the ionic liquid. Similarly, the onset decomposition temperature for CS powder decreased by 2% from 269.9- to 264.2-°C. The onset of decomposition for CEL powder also decreased by 1.26% from 318.4- to 314.0 °C. These changes are somewhat negligible which suggests that minimal changes in the chemical structure of the biopolymers occurred as a result of regenerating them from ionic liquid. This allows us to study the effect of adding one component to another. Figure 5-13 shows plots of onset decomposition temperature of [CS+KER] and [CEL+KER] composite films. As shown, 100% KER was the least thermally stable followed by CS and then CEL. Interestingly, blend films of KER with each of the polysaccharides show an improvement in the thermal stability as the proportional content with respect to either CEL or CS is increased. Therefore, by changing the composition of the [CEL/CS+KER] composites, the thermal properties can be objectively tuned. All composites and powders showed a transition in the region 30- to 100-°C except for CEL powder. This transition is attributed to residual water. In addition, the water content of the films were found to be between 0% and 6.0%, with CS film having the highest water content. This is expected since CS absorbs water easily.

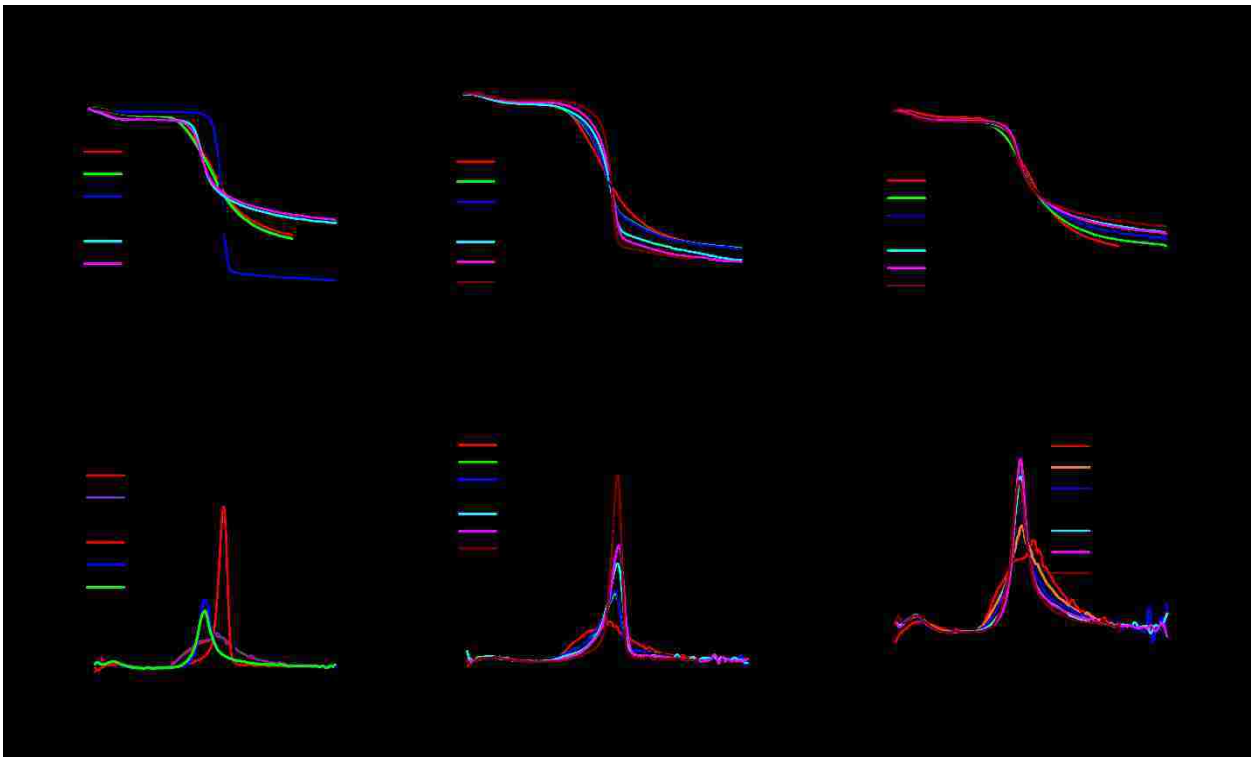

Figure 5-12 TGA curves (first row) and their corresponding derivatives (second row) of wool, CS powder, CEL powder, 100% KER, 100% CEL, 100% KER, [CS+KER] and [CEL+KER] composite films.

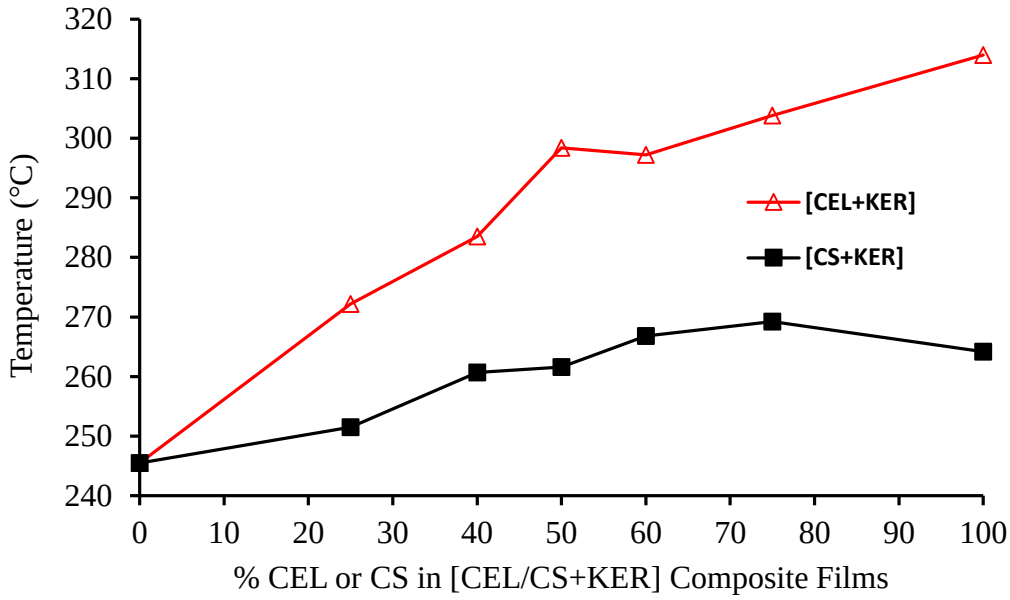

Figure 5-13 Plots of onset decomposition temperatures for [CEL+KER] (red curve with open triangles) and [CS+KER] (black curve with solid squares).

In summary, we have successfully synthesized composites containing various proportions of CEL, CS, and KER in one step using a recyclable ionic liquid, $BMIm^{+}Cl^{-}$. The results obtained by analysis using FTIR, NIR, XRD, NMR and SEM confirm that KER, CS, and CEL remain chemically intact and are compatible with each other. Most importantly, we have developed a PLSR method and successfully used it to accurately and objectively predict the secondary structures of KER in wool, regenerated KER and in its composites with either CEL or CS. Results obtained by NIR, XRD and NMR corroborate PLSR findings. Specifically, all the techniques indicate that KER in wool has a higher α-helix content than β-sheet. However, upon regenerating KER, the proportional content of α-helix decreased compared to the β-sheet content. These results suggest that

during dissolution, the secondary structure of KER is destroyed. During gelation and regeneration from water, α-helix conformation is partially reformed whereas the β-sheet conformation is stabilized. As expected, both CS and CEL improved the tensile and thermal properties of KER. However, in both cases, CEL had a higher effect than CS. The improved mechanical and thermal properties enable the possibility of exploiting the desirable properties of KER in various applications such as drug release in wound control. This is the focus of the next few sections.

5.3.3. Drug Release

5.3.3.1. Qualitative assessment of the release assay

The main goal of this study was to evaluate the suitability of CEL, KER, and CS as matrix platforms for controlling the release of the drug, CPX. This was achieved by carrying out drug release assays using films containing different relative amounts of CEL, KER and CS. The concentration of the drug was fixed at 0.5% of the total weight of biopolymers in each formulation. It is noteworthy that sink conditions should be maintained throughout the experiment to ensure that the release medium is not saturated by the drug. Therefore, the experimental conditions were chosen such that the drug concentration was always less than 10% of the saturation solubility in the release medium; the solubility of CPX in phosphate buffer is 73±7 ppm at 21±1 °C.[91] In our case, 3.5 mg of film would theoretically contain 0.0174 mg (equivalent to 0.5% CPX per total weight of polymers) CPX which in 3.5 mL release medium would translate to ~5 ppm CPX. This represents the maximum concentration that can be released by a typical film in this present study. By comparing this value (5 ppm) with the solubility (73±7 ppm), it is

clear that CPX concentration could stay below 10% of the solubility thereby maintaining the required sink conditions.

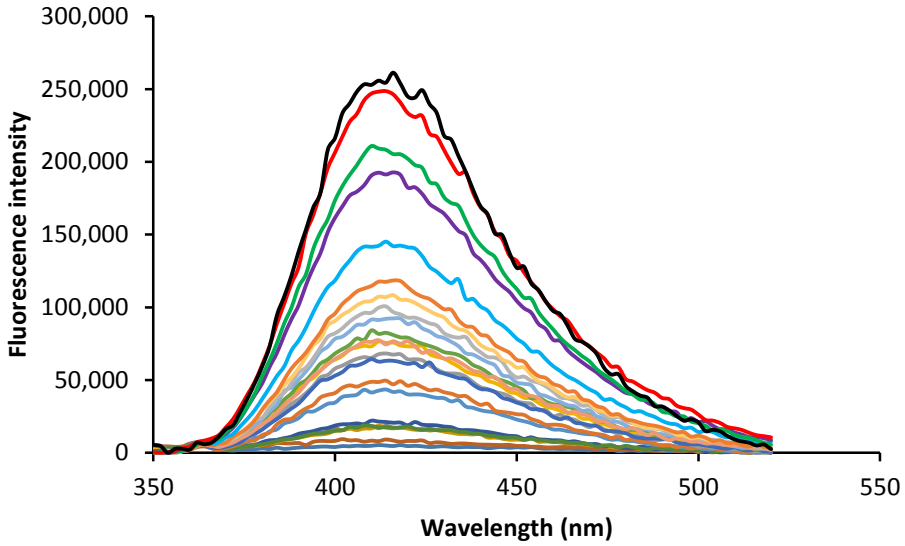

Figure 5-14 Time dependent fluorescence spectra of ciprofloxacin (CPX) release from regenerated KER (100% KER)

Figure 5-14 shows the typical time-dependent fluorescence spectra obtained during drug release from a 100% KER film. This figure illustrates what was generally observed with other formulations. As illustrated on this figure, the band at 418 nm appears to grow over time as a result of progressive increase in the amount of drug being released into the buffer medium. Furthermore, the peak position and peak shape were invariant throughout the study suggesting that the drug remained stable over the whole assay period. In addition, these time dependent spectra appeared to be identical to the calibration spectra *(not shown)*. This suggests that CPX maintained its structure throughout the entire process of its incorporation in the biopolymer matrices. Therefore,

the CPX-doped composite, synthesized by the present method, are expected to retain antimicrobial properties of the CPX.

The time-dependent fluorescence spectra of CPX assay were used to generate plots of fraction of drug released, M_t/M_∞ as a function of time, t in hours for each formulation. As can be seen on Figure 5-15, the release profiles are characterized by two stages: an initial burst release (Stage I) followed by a slow release (Stage II) that eventually reaches a plateau. The burst release could be due to the instantaneous dissolution of the physically bound drug from the surface of the films. Stage II could be due to the diffusion of the encapsulated drug from the interior of the film matrix. This profile is particularly desirable in situations such as the initial stages of wound treatment where it offers immediate relief by delivering therapeutic amounts of the drug to the wound site. Stage II helps to maintain this therapeutic level of drug by delivering a low, but sustainable amount of drug to keep the drug level in the plasma within the therapeutic window.

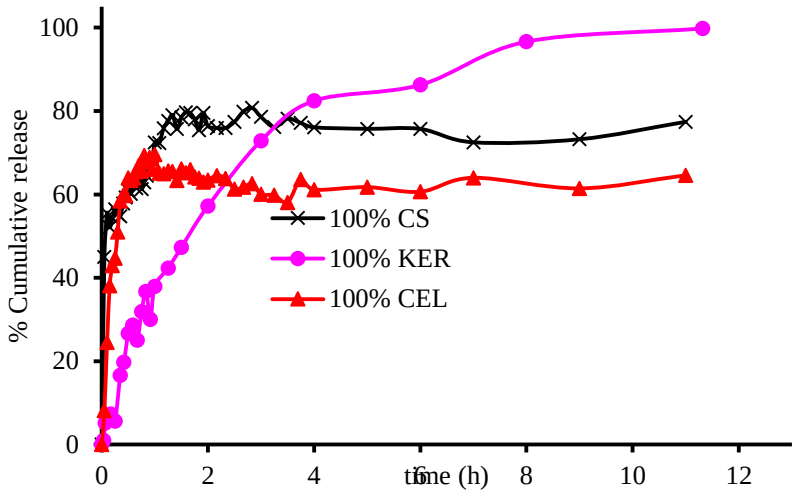

Figure 5-15 Plots of release of CPX as a function of time from 100% CS (black curve with stars), 100% KER (purple curve with solid circles), and 100% CEL (red curve with solid triangles)

Although these formulations (100% KER, 100% CS, and 100% CEL) exhibit two-stage release profiles, the duration and the amount of drug released at each stage varies from biopolymer to biopolymer. For example, it took *ca.* 30 minutes for 100% CEL and 100% CS to release 60% of the encapsulated drug. In contrast, it took 4X (120 minutes) longer for 100% KER to release the same percentage of drug. These results suggest that 100%- CEL and –CS films contained relatively equal but more physi-sorbed drug than 100% KER. As a result, the early release rates for the polysaccharides (CEL or CS) appear to be faster than KER. During Stage II, water diffuses into the biopolymer matrix thereby dissolving the drug. In addition, this water swells the biopolymer matrix leading to more drug being released into the solution medium. From the results of swelling studies, previously published by our group,[28] it was found that CS absorbs at least 3X more water than CEL owing to the more rigid structure of CEL. Therefore, CS

is expected to eventually release more drug than CEL at equilibrium. In fact, the results obtained in the present study concurs with this finding. Specifically, 100% CS released a total of 77% CPX whilst 100% CEL released only 65%. KER, possessing a different chemical structure from that of both CS and CEL, is expected to show different kinetics profile. It has been reported that KER hardly swells in water.[92] As a result, drug release from KER matrix is much slower than from either CS or CEL. Even though KER swells to a lesser extent in water, the phosphate ions in the buffer may adsorb onto the protein thereby making it more ionic Consequently, KER would absorb more water over time. Therefore, with time, its structure would collapse and lead to the release of more drug at equilibrium albeit at a slower pace than either CEL or CS. This could explain why 100% KER released up to 91% drug at equilibrium.

Although 100% KER exhibits a profile which is more desirable for long-term applications like in wound treatment, its poor mechanical properties hinders its adoption for any practical use. Therefore, an attempt was made to reinforce KER by mixing it with either CEL or CS at different proportions. Thereafter, these formulations were evaluated for their drug delivery capabilities. The results, presented in Figure 5-16 show some interesting release profiles of each formulation. In all cases 100% CEL released the least total amount of drug at equilibrium for reasons explained above. All samples containing KER showed some level of controlled drug release, especially at high level of KER. On the other hand, higher levels of either CEL or CS tend to diminish this effect. This was most apparent when formulations containing only the two biopolymers, CEL and CS, were evaluated. As can be seen in Figure 5-16B, all the [CS+CEL] formulations reached equilibrium within the first hour of the assay study. However, when each of CEL or CS

was mixed with KER, there was a substantial slowdown in the rate of drug release. These results illustrate the crucial role which KER can play in controlling the release of the drug.

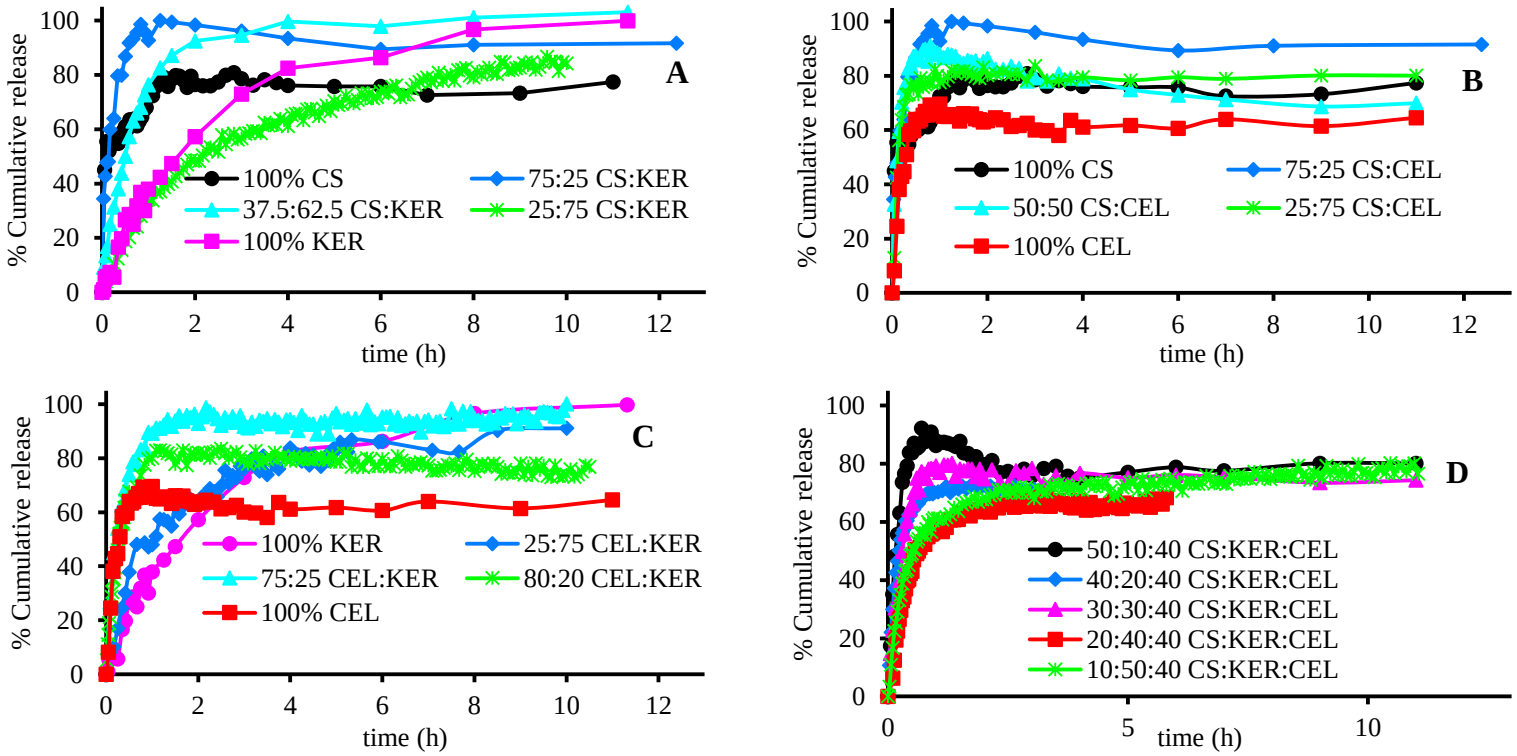

Figure 5-16 Plots of release of ciprofloxacin as function of time from [CS+KER] (A), [CS+CEL] (B), [CEL+KER] (C), [CS+KER+CEL] (D) composite films

5.3.3.2. Quantitative assessment of the release profiles

A more quantitative assessment needed to be done in order to compare the performance of each formulation. We achieved this by fitting release kinetic data to the four widely adopted models; zero order model, first order model, Higuchi model and Korsmeyer Peppas (KP) model. The performance of each model was evaluated by comparing the R^2 and the MSC values.[93] As illustrated in Table 5-3 and Figure 5-17, zero order model consistently gave the lowest R^2 and MSC values for every formulation. This strongly confirm that zero order model cannot be reliably used to describe CPX release from [CEL/CS/KER] composite films. Although first order model gave higher R^2 and MSC values for some formulations, this trend was inconsistent. For examples; first order model gave the highest R^2 and MSC values for only 100% KER, 25:75 CEL:KER, 50:10:40 and 30:30:40 CS:KER:CEL. Therefore, first order can only fit 24% (=4/17x100) of the formulations under this current study. As a result of this inconsistency, zero and first order models are not suitable for this study.

Table 5-4 Results of modeling the release of ciprofloxacin from [CEL/CS/KER] composites.

%			Zero order model			First order model			Higuchi model			Korsmeyer-Peppas model			
CS	KER	CEL	K_0 (t^{-1})	R^2	MSC	K_1	R^2	MSC	K_H ($t^{0.5}$)	R^2	MSC	K (t^{1-n})	n	R^2	MSC
100			1.8(1)	0.9460	0.9469	2.7(1)	0.9731	1.8366	1.063(2)	0.9999	9.3389	1.06(1)	0.500(6)	0.9999	8.9400
75	**25**		4(1)	0.8266	1.2521	6(2)	0.8788	1.6103	1.5(2)	0.9772	3.2792	1.10(6)	0.35(2)	0.9976	5.1588
37.5	**62.5**		0.91(4)	0.9806	3.7409	1.36(4)	0.9938	4.8756	0.76(4)	0.9746	3.4721	0.82(2)	0.70(2)	0.9961	5.2623
25	**75**		0.163(8)	0.9198	2.4752	0.265(8)	0.9663	3.3441	0.370(8)	0.9835	4.0579	0.313(5)	0.58(2)	0.9800	2.4478
	100		0.29(2)	0.9668	3.2502	0.42(1)	0.9932	4.8381	0.43(2)	0.9789	3.7045	0.357(6)	0.72(3)	0.9922	4.6356
	75	**25**	0.49(4)	0.9650	3.1034	0.74(2)	0.9938	4.8290	0.56(4)	0.9664	3.1444	0.53(1)	0.72(3)	0.9918	4.4557
	25	**75**	2.3(4)	0.9433	2.3700	3.2(3)	0.9823	3.5359	1.16(6)	0.9944	4.6790	1.3(1)	0.62(6)	0.9941	4.5319
	20	**80**	1.19(6)	0.9123	0.5700	1.98(5)	0.9740	2.1964	0.92(1)	0.9937	3.1844	1.13(2)	0.65(2)	0.9934	4.9095
		100	0.93(6)	0.9129	0.2323	1.50(8)	0.9447	0.9290	0.92(2)	0.9973	4.0715	1.04(7)	0.60(5)	0.9926	4.4566
25		**75**	2.0(2)	0.9275	0.6798	3.6(2)	0.9624	1.5482	1.42(2)	0.9991	5.2532	1.6(2)	0.57(6)	0.9975	5.3904
50		**50**	2.1(2)	0.9185	0.3182	4.5(2)	0.9753	1.9323	1.53(2)	0.9997	6.2460	1.67(6)	0.54(2)	0.9996	7.2202
75		**25**	2.0(2)	0.9342	0.8145	3.6(2)	0.9657	1.6932	1.35(3)	0.9981	4.4624	1.6(3)	0.6(1)	0.9923	4.2671
50	**10**	**40**	1.8(1)	0.9504	1.0529	3.8(1)	0.9904	3.0892	1.17(7)	0.9857	2.6328	2.0(3)	0.77(8)	0.9897	4.0657
40	**20**	**40**	0.73(2)	0.9642	1.5739	1.06(3)	0.9820	2.4761	0.62(1)	0.9967	3.8935	1.06(4)	0.55(2)	0.9935	5.8134
30	**30**	**40**	1.29(6)	0.9749	1.8596	2.17(4)	0.9952	3.8445	0.86(3)	0.9886	2.7842	1.16(6)	0.62(2)	0.9965	5.4192
20	**40**	**40**	0.117(4)	0.9084	0.1321	0.183(4)	0.9534	1.2089	0.317(3)	0.9978	2.7774	0.92(2)	0.53(4)	0.9950	5.1612
10	**50**	**40**	1.02(6)	0.9321	0.4274	1.82(6)	0.9806	2.1153	0.97(1)	0.9984	4.3130	0.76(3)	0.43(2)	0.9941	4.8179

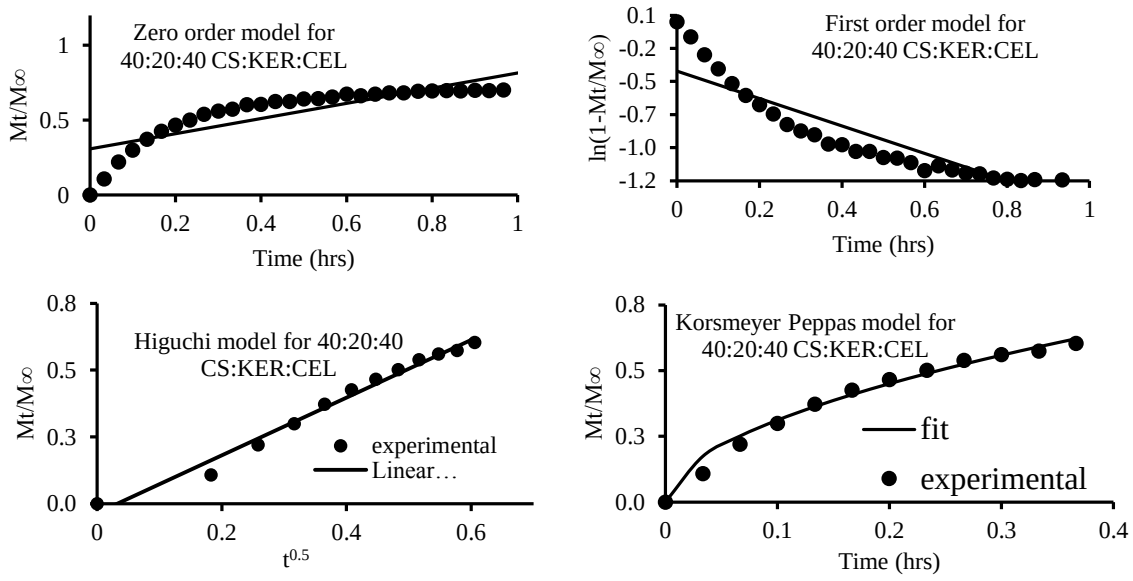

Figure 5-17 Kinetics of release of ciprofloxacin (CPX) from 40:20:40 CS:KER:CEL plotted as zero order, first order, Higuchi, and Korsmeyer-Peppas models

As illustrated in Table 5-3, both Higuchi and Kormeyer Peppas models have high values for R^2 with the former having higher values 64% (=11/17x100) of the time while the later model has higher R^2 values 36% (=6/17x100) of the time. This suggests that Higuchi model represent the release profiles more accurately. However, when MSC values are also taken into account, Higuchi model gives hives higher values of MSC only 24% (=4/17x100) of the time with the remainder 76% being given by Korsmeyer Peppas model. These two results seem to be contradictory at first. However, upon close scrutiny, it is clear that the R^2 values of both models are very close whereas the differences in MSC are larger. Therefore, MSC carries more weight. Consequently, Korsmeyer Peppas model was chosen as it appears to describe all release profiles adequately.

Although the results obtained from Korsmeyer Peppas model are illustrated in Table 5-3 for better visualization, the k_p-values were used to generate a 3D plot (Figure

5-18). As illustrated, 100% KER has the lowest K-values (0.357±0.006) compared to either 100% CEL or 100% CS. In addition, 100% CEL and 100% CS gave almost identical K-values with the former giving K-value 1.04±0.07 whilst the latter gave K-value 1.06±0.01. These results seem to contradict the results obtained from the swelling studies of these two biopolymers in water.[28] From the swelling studies, 100% CS was found to adsorb 3.4X as much water as adsorbed by 100% CEL. Therefore, 100% CS is expected to release more drug faster than 100% CEL. However, upon closer inspection, it was found that during the early stages (which correspond to the time period used to fit drug release data that is the region spanning the first 60% cumulative drug released), both CEL and CS adsorb at almost the same rate. Therefore, they should also release the drug at the same rate. In addition, it took 30 minutes for both CEL and CS to release 60% drug. This amount could correspond to the physi-sorbed drug, hence faster release.

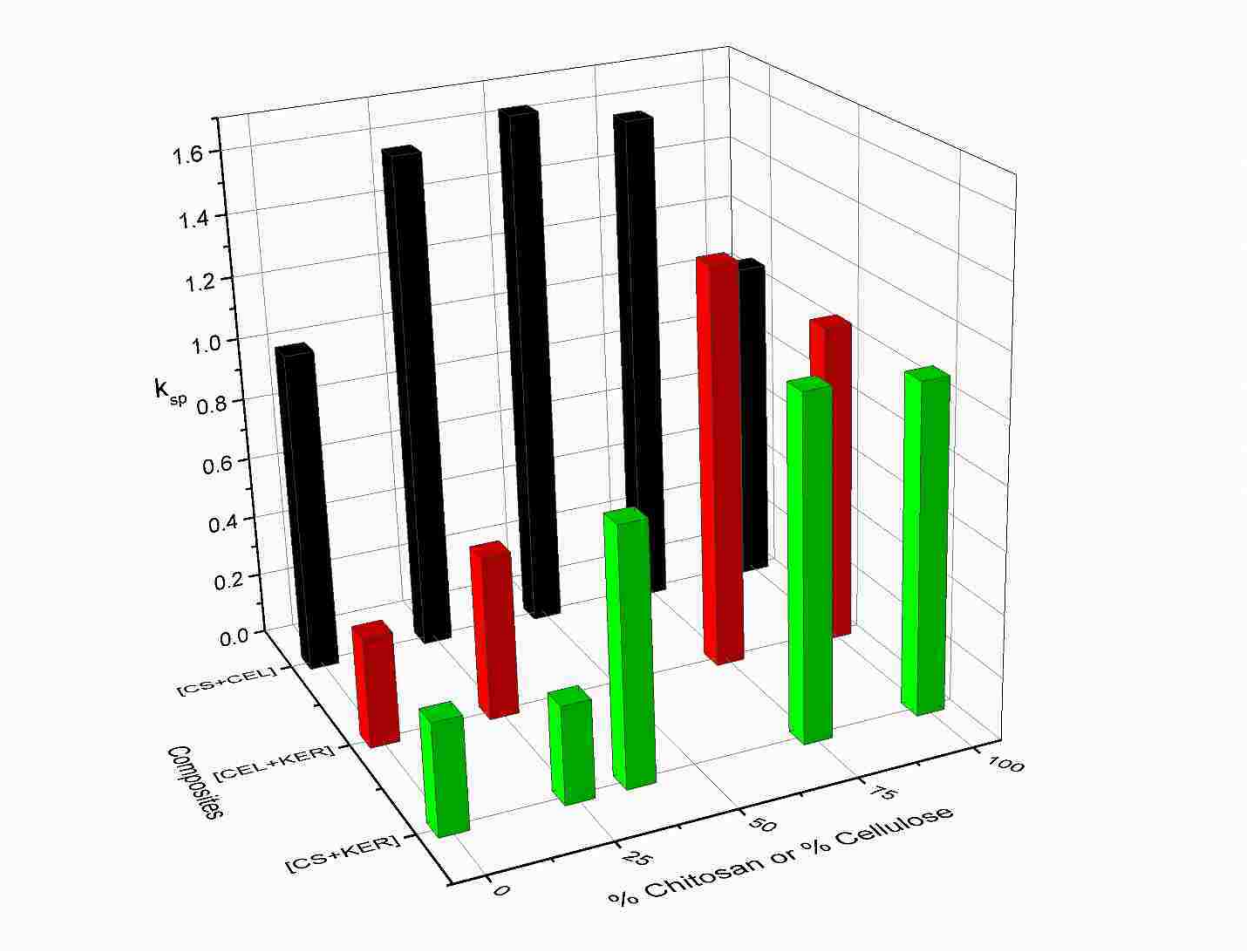

Figure 5-18 3D plot for release rate constants, k_p, obtained by fitting release data to Korsmeyer Peppas model for two-component composites ([CEL+CS] (black), [CEL+KER] (red), and [CS+KER] (green).

Although KER can adequately control release of the drug, it is difficult to handle considering that it is very brittle. Therefore, we decided to blend it with inherently strong biopolymers that is CEL and CS. As illustrated in Table 5-3, for [CS+KER] composites, K-values decreased concomitantly with the increase in proportional content of KER. For example, adding 62.5% KER to CS reduced K-value by 33%. A further 48% reduction was observed when a further 12.5% KER was added to the 62.5:37.5 KER:CS composite

film. The blending of CS and KER is attractive because CS not only improves the mechanical properties but also add some biomedical benefits thereby widening the applications of KER. For examples; CS has been used widely as bactericide,[94-97] and in bone tissue engineering.[98-101] In fact, in our previous publications, we proved that CS inhibits growth of a wide variety of bacteria specifically MRSA, VRE, *S. aureas*, and *S. aeruginosa*.[96,97] This implies that lesser doses of the drug, CPX could be required to combat bacteria at the wound site because some of the bacteria would be controlled by the CS component. Drug release from [CS+KER] was found to be similar to that from [CEL+KER]. This is hardly surprising since CEL and CS possess similar chemical structure except for the presence of an amino group at C-1 in CS. However, for a particular KER content, the [CEL+KER] composite film gave a somewhat higher K-value than the corresponding [CS+KER]. For example, composites containing 75% KER gave K-values 0.53±0.01 for [CEL+KER] and 0.313±0.005 for [CS+KER]. To verify that KER was indeed responsible for slowdown in drug release, we synthesized CPX-doped composite films containing only the two polysaccharides, CEL and CS. The results are also included in Table 2. It is interesting to note that when these two polysaccharides were blended, the resultant composites gave K-values higher than the K-values obtained from either 100% CEL or 100% CS. In addition, the K-values for the [CS+CEL] composites appeared insensitive to the amount of either CS or CEL in the composites. This behavior could be a result of similarity in the chemical structures of these two polysaccharides. The K-values obtained from [CEL+CS] composites were consistently higher than the K-values obtained for either [CEL+KER] and [CS+KER]. This further confirm the utility of KER in controlling drug release.

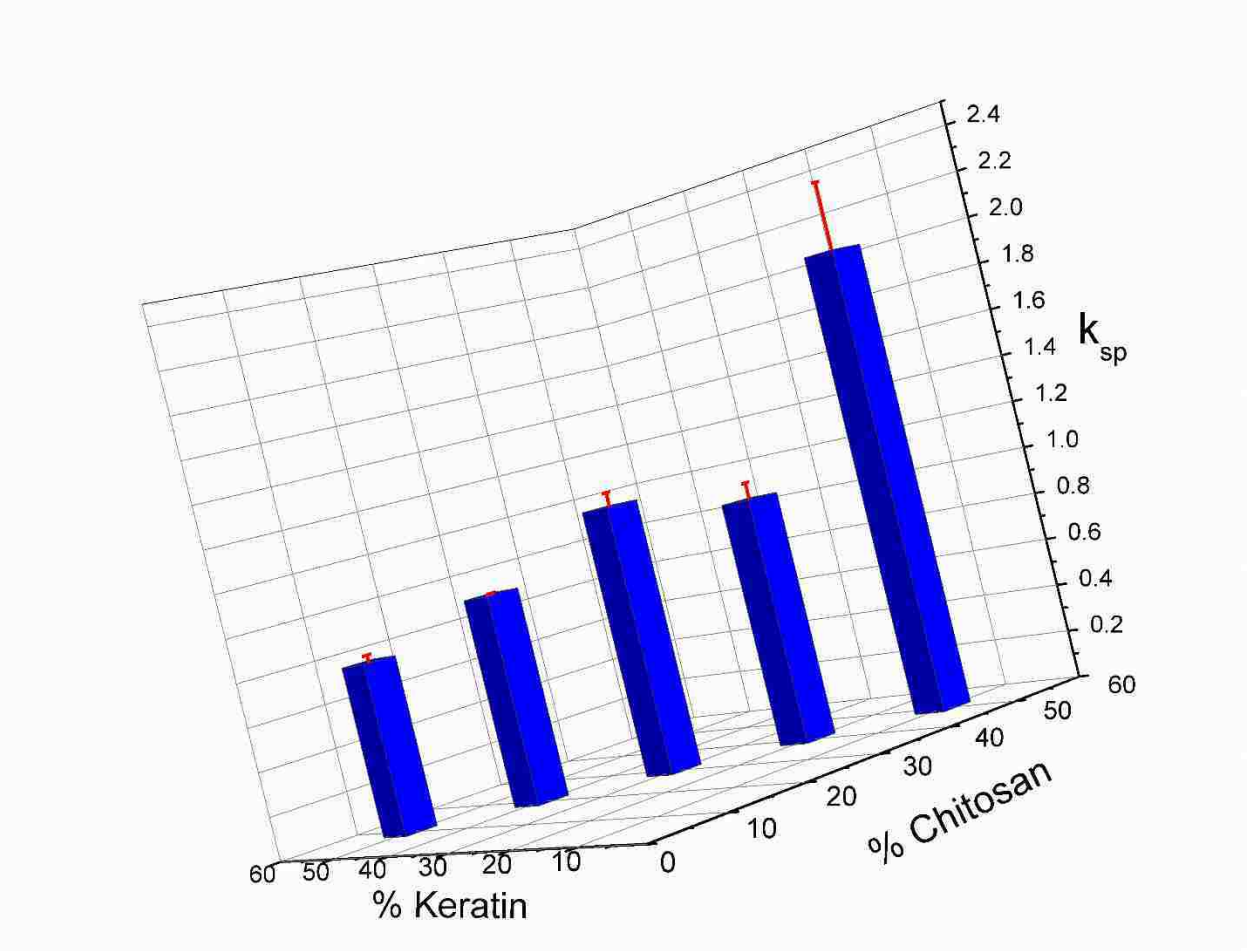

Figure 5-19 3D plot of release rate constants, k_p, obtained by fitting release data to Korsmeyer Peppas model for three-component composites (*i.e.* [CS+KER+CEL])

An attempt was also made to test whether KER can still slow down drug release from a composition containing all the three biopolymers (i.e. KER, CEL and CS). Five composites were synthesized in which the concentration of CEL was fixed at 40% whilst the concentrations of CS and KER were varied from 10% to 50%. The results of fitting the release data to Korsmeyer Peppas model are listed in Table 5-3 and plotted in Figure 5-19. As illustrated, increasing the concentration of KER resulted in a substantial

decrease in the rate of CPX release. For example, when the concentration of KER was increased from 10% to 50%, the release rate slowed down by 62% (i.e. from 2.0±0.3 to 0.76±0.03). It is therefore, evidently clear that the ability of KER to slow down CPX drug release remains intact even in the three-component composites. Thus, the release properties of the composites can be tuned by judiciously adjusting the concentration of KER in the composites. In addition, [CEL+CS+KER] composites are more superior to all the one- (100% CEL, 100% CS, 100%KER) and two-component composites ([CEL+KER], [CS+KER], [CS+CEL]). For example, [CEL+CS+KER] composites have combined properties of their individual components namely superior mechanical properties (from CEL), ability to stop bleeding, inhibit the growth of bacteria and adsorb pollutants (from CS) and controlled release of drugs (from KER).

A particular advantage of Korsmeyer Peppas model over the other three models is that the exponent, n, can give an insight into the mechanism of drug release. These values are given for each composite film, in Table 5-3 As has been described earlier, when n=0.5, the release is described by Fickian diffusion whilst n=1.0 describes the zero order release. As can be seen in Table 5-3, n-values were found to be between 0.5 and 1.0 which suggests that the release from most formulations was an anomalous type (non-Fickian). This suggests that more than one mechanism could be involved in the release of the drug. These mechanisms could be a combination of diffusion and erosion of the films over the course of the assay period. The effect of secondary structure on drug release mechanism can also be studied using Korsmeyer Peppas model. Although CEL and CS enhanced the formation of more β-sheet component in KER, this change seem not to affect the release mechanism. Both 25:75 CS:KER and CEL:KER composites gave K-

and n-values of (0.313±0.005, 0.53±0.01) and (0.58±0.02, 0.72±0.03) respectively. Pure KER film gave K- and n-values of 0.357±0.006 and 0.72±0.03 respectively. Therefore, these formulations are expected to be robust.

5.4. Conclusions

Overall, we have shown that it is indeed possible to preserve the desirable properties of CEL, CS and KER by dissolving them in an ionic liquid and subsequently regenerating them from water. This was confirm by using FTIR, NIR and CP MAS NMR spectroscopy techniques. However, the secondary structure of KER was affected by the regeneration process. This was found out after developing a PLSR model to predict the secondary structure of KER. Specifically, regeneration led to a decrease in the α-helical content of KER with an increase in β-sheet content. In addition, this PLSR method was proved to be more accurate and objective than the conventional curve fitting procedure. More importantly, CEL and CS improved the mechanical and thermal properties of KER-based composite films. These findings provided an impetus for us to apply these composites in drug release. Ciprofloxacin was chosen as a model antibiotic drug. Interestingly, all the composites were found to be able to encapsulate and control the release of this drug. Most importantly, KER was found to substantially slow down the release of CPX. Varying its concentration in the composites enabled us to tune the release of this drug. Therefore, these composites can be used successfully as cheaper and more effective platforms for the release of drugs such as CPX.

5.5. References

1. Falanga, V., Wound healing and its impairment in the diabetic foot. *Lancet* **2005,** *366*, 1736-43.

2. Norrish, A. R.; Lewis, C. P.; Harrison, W. J., Pin-track infection in HIV-positive and HIV-negative patients with open fractures treated by external fixation: a prospective, blinded, case-controlled study. *J Bone Joint Surg Br* **2007,** *89* (6), 790-3.

3. Aird, J.; Noor, S.; Lavy, C.; Rollinson, P., The effect of HIV on early wound healing in open fractures treated with internal and external fixation. *J Bone Joint Surg Br* **2011,** *93* (5), 678-83.

4. Cavanagh, P. R.; Lipsky, B. A.; Bradbury, A. W.; Botek, G., Treatment for diabetic foot ulcers. *Lancet* **2005,** *366*, 1725-35.

5. Waldorf, H.; Fewkes, J., Wound healing. *Adv Dermatol* **1995,** *10*, 77-96; discussion 97.

6. Han, F.; Dong, Y.; Song, A.; Yin, R.; Li, S., Alginate/chitosan based bi-layer composite membrane as potential sustained-release wound dressing containing ciprofloxacin hydrochloride. *Appl. Surf. Sci.* **2014,** *311*, 626-634.

7. Schierholz, J. M.; Steinhauser, H.; Rump, A. F. E.; Berkels, R.; Pulverer, G., Controlled release of antibiotics from biomedical polyurethanes: morphological and structural features. *Biomaterials* **1997,** *18* (12), 839-844.

8. Mi, F.-L.; Wu, Y.-B.; Shyu, S.-S.; Schoung, J.-Y.; Huang, Y.-B.; Tsai, Y.-H.; Hao, J.-Y., Control of wound infections using a bilayer chitosan wound dressing with sustainable antibiotic delivery. *J. Biomed. Mater. Res.* **2002,** *59* (3), 438-449.

9. Inouye, K.; Machida, Y.; Sannan, T.; Nagai, T., Buoyant sustained-release granules based on chitosan. *Drug Des. Delivery* **1988,** *4* (1), 55-67.

10. Chandy, T.; Sharma, C. P., Chitosan beads and granules for oral sustained delivery of nifedipine: in vitro studies. *Biomaterials* **1992,** *13*, 949-52.

11. Chandy, T.; Sharma, C. P., Chitosan matrix for oral sustained delivery of ampicillin. *Biomaterials* **1993,** *14*, 939-44.

12. Felt, O.; Buri, P.; Gurny, R., Chitosan: a unique polysaccharide for drug delivery. *Drug Dev. Ind. Pharm.* **1998,** *24*, 979-993.

13. Kennedy, J. F.; Tun, H. C., Active insolubilized antibiotics based on cellulose and cellulose carbonate. *Antimicrob. Agents Chemother.* **1973,** *3* (5), 575-9.

14. Mori, R.; Nakai, T.; Enomoto, K.; Uchio, Y.; Yoshino, K., Increased antibiotic release from a bone cement containing bacterial cellulose. *Clin Orthop Relat Res* **2011,** *469* (2), 600-6.

15. Jackson, J. K.; Letchford, K.; Wasserman, B. Z.; Ye, L.; Hamad, W. Y.; Burt, H. M., The use of nanocrystalline cellulose for the binding and controlled release of drugs. *Int. J. Nanomed.* **2011,** *6*, 321-330.

16. Chaosri, P.; Thonpho, A.; Srihanam, P., Keratin/sericin blend films as a model system for controlled hydrophilic drug release. *Int. J. Appl. Chem.* **2013,** *9*, 185-196.

17. Nakata, R.; Tachibana, A.; Tanabe, T., Preparation of keratin hydrogel/hydroxyapatite composite and its evaluation as a controlled drug release carrier. *Mater. Sci. Eng., C* **2014,** *41*, 59-64.

18. Yin, X.-C.; Li, F.-Y.; He, Y.-F.; Wang, Y.; Wang, R.-M., Study on effective extraction of chicken feather keratins and their films for controlling drug release. *Biomater. Sci.* **2013,** *1*, 528-536.

19. Li, F.-Y.; Wang, R.-M.; He, Y.-F.; Li, X.-X.; Song, P.-F.; Ying, X.-C.; Mao, C.-W., Keratin films from chicken feathers for controlled drug release. *J. Controlled Release* **2011,** *152* (Suppl. 1), e92-e93.

20. Saul, J. M.; Ellenburg, M. D.; de Guzman, R. C.; Van Dyke, M., Keratin hydrogels support the sustained release of bioactive ciprofloxacin. *J. Biomed. Mater. Res., Part A* **2011,** *98A* (4), 544-553.

21. Belcarz, A.; Ginalska, G.; Zalewska, J.; Rzeski, W.; Slosarczyk, A.; Kowalczuk, D.; Godlewski, P.; Niedzwiadek, J., Covalent coating of hydroxyapatite by keratin stabilizes gentamicin release. *J. Biomed. Mater. Res., Part B* **2009,** *89B*, 102-113.

22. Wu, F. C.; Tseng, R. L.; Juang, R. S., Comparative adsorption of metal and dye on flake- and bead-types of chitosans prepared from fishery wastes. *J. Hazard. Mater.* **2000,** *73* (1), 63-75.

23. Li, J.; Zhang, R.; Zhou, X.; Li, D., Preparation and characterization of wool-keratin films based on SMS nonwovens. *Adv. Mater. Res. (Zuerich, Switz.)* **2011,** *194-196* (Pt. 2, Advanced Engineering Materials), 1529-1535.

24. Tran, C. D.; Duri, S.; Harkins, A. L., Recyclable synthesis, characterization, and antimicrobial activity of chitosan-based polysaccharide composite materials. *J. Biomed. Mater. Res., Part A* **2013,** *101A*, 2248-2257.

25. Wu, Y.-B.; Yu, S.-H.; Mi, F.-L.; Wu, C.-W.; Shyu, S.-S.; Peng, C.-K.; Chao, A.-C., Preparation and characterization on mechanical and antibacterial properties of chitosan/cellulose blends. *Carbohydr. Polym.* **2004,** *57* (4), 435-440.

26. Hameed, N.; Guo, Q., Blend films of natural wool and cellulose prepared from an ionic liquid. *Cellulose (Dordrecht, Neth.)* **2010,** *17*, 803-813.

27. Battista, O. A.; Smith, P. A., Microcrystalline cellulose. *Ind. Eng. Chem.* **1962,** *54*, 20-29.

28. Tran, C. D.; Duri, S.; Delneri, A.; Franko, M., Chitosan-cellulose composite materials: Preparation, Characterization and application for removal of microcystin. *J. Hazard. Mater.* **2013,** *252-253*, 355-366.

29. Xie, H.; Li, S.; Zhang, S., Ionic liquids as novel solvents for the dissolution and blending of wool keratin fibers. *Green Chem.* **2005,** *7*, 606-608.

30. Duri, S.; Majoni, S.; Hossenlopp, J. M.; Tran, C. D., Determination of Chemical Homogeneity of Fire Retardant Polymeric Nanocomposite Materials by Near-Infrared Multispectral Imaging Microscopy. *Anal. Lett.* **2010,** *43*, 1780-1789.

31. Varelas, C. G.; Dixon, D. G.; Steiner, C. A., Zero-order release from biphasic polymer hydrogels. *J. Controlled Release* **1995,** *34* (3, br273), 185-92.

32. Costa, P.; Sousa Lobo, J. M., Modeling and comparison of dissolution profiles. *Eur. J. Pharm. Sci.* **2001,** *13*, 123-133.

33. Gibaldi, M.; Feldman, S., Establishment of sink conditions in dissolution rate determinations. Theoretical considerations and application to nondisintegrating dosage forms. *J. Pharm. Sci.* **1967,** *56*, 1238-42.

34. Wagner, J. G., Interpretation of percent dissolved-time plots derived from in vitro testing of conventional tablets and capsules. *J. Pharm. Sci.* **1969,** *58*, 1253-7.

35. Higuchi, T., Rate of release of medicaments from ointment bases containing drugs in suspension. *J. Pharm. Sci.* **1961,** *50*, 874-5.

36. Higuchi, T., Mechanism of sustained-action medication. Theoretical analysis of rate of release of solid drugs dispersed in solid matrices. *J. Pharm. Sci.* **1963,** *52*, 1145-9.

37. Korsmeyer, R. W.; Gurny, R.; Doelker, E.; Buri, P.; Peppas, N. A., Mechanisms of solute release from porous hydrophilic polymers. *Int. J. Pharm.* **1983,** *15*, 25-35.

38. Ritger, P. L.; Peppas, N. A., A simple equation for description of solute release. II. Fickian and anomalous release from swellable devices. *J. Controlled Release* **1987,** *5* (1), 37-42.

39. Ritger, P. L.; Peppas, N. A., A simple equation for description of solute release. I. Fickian and non-Fickian release from non-swellable devices in the form of slabs, spheres, cylinders or disks. *J. Controlled Release* **1987,** *5* (1), 23-36.

40. Peppas, N. A.; Sahlin, J. J., A simple equation for the description of solute release. III. Coupling of diffusion and relaxation. *Int. J. Pharm.* **1989,** *57* (2), 169-72.

41. Arrondo, J. L. R.; Muga, A.; Castresana, J.; Goni, F. M., Quantitative studies of the structure of proteins in solution by Fourier-transform infrared spectroscopy. *Prog. Biophys. Mol. Biol.* **1993,** *59*, 23-56.

42. Tamm, L. K.; Tatulian, S. A., Infrared spectroscopy of proteins and peptides in lipid bilayers. *Q. Rev. Biophys.* **1997,** *30*, 365-429.

43. Dong, A.; Huang, P.; Caughey, W. S., Protein secondary structures in water from second-derivative amide I infrared spectra. *Biochemistry* **1990,** *29*, 3303-8.

44. Kumosinski, T. F.; Unruh, J. J., Quantitation of the global secondary structure of globular proteins by FTIR spectroscopy: comparison with x-ray crystallographic structure. *Talanta* **1996,** *43*, 199-219.

45. Westad, F.; Schmidt, A.; Kermit, M., Incorporating chemical band-assignment in near infrared spectroscopy regression models. *J. Near Infrared Spectrosc.* **2008,** *16*, 265-273.

46. Westad, F.; Martens, H., Variable selection in near infrared spectroscopy based on significance testing in partial least squares regression. *J. Near Infrared Spectrosc.* **2000,** *8*, 117-124.

47. Bernstein, F. C.; Koetzle, T. F.; Williams, G. J. B.; Meyer, E. F., Jr.; Brice, M. D.; Rodgers, J. R.; Kennard, O.; Shimanouchi, T.; Tasumi, M., The Protein Data Bank: a computer-based archival file for macromolecular structures. *Arch. Biochem. Biophys.* **1978,** *185*, 584-91.

48. Kabsch, W.; Sander, C., Dictionary of protein secondary structure: pattern recognition of hydrogen-bonded and geometrical features. *Biopolymers* **1983,** *22*, 2577-637.

49. Rahmelow, K.; Huebner, W., Secondary structure determination of proteins in aqueous solution by infrared spectroscopy: a comparison of multivariate data analysis methods. *Anal. Biochem.* **1996,** *241* (1), 5-13.

50. Cai, S.; Singh, B. R., A distinct utility of the amide III infrared band for secondary structure estimation of aqueous protein solutions using partial least squares methods. *Biochemistry* **2004,** *43*, 2541-2549.

51. Wang, Y.; Boysen, R. I.; Wood, B. R.; Kansiz, M.; McNaughton, D.; Hearn, M. T. W., Determination of the secondary structure of proteins in different environments by FTIR-ATR spectroscopy and PLS regression. *Biopolymers* **2008,** *89* (11), 895-905.

52. Navea, S.; Tauler, R.; De Juan, A., Application of the local regression method interval partial least-squares to the elucidation of protein secondary structure. *Anal. Biochem.* **2005,** *336* (2), 231-242.

53. Vonhoff, S.; Condliffe, J.; Schiffter, H., Implementation of an FTIR calibration curve for fast and objective determination of changes in protein secondary structure during formulation development. *J. Pharm. Biomed. Anal.* **2010,** *51* (1), 39-45.

54. Geladi, P., Herman Wold, the father of PLS. *Chemom. Intell. Lab. Syst.* **1992,** *15* (1), vii-viii.

55. Abdi, H.; Williams Lynne, J., Partial least squares methods: partial least squares correlation and partial least square regression. *Methods Mol Biol* **2013,** *930*, 549-79.

56. Wold, S.; Sjostrom, M.; Eriksson, L., PLS-regression: a basic tool of chemometrics. *Chemom. Intell. Lab. Syst.* **2001,** *58*, 109-130.

57. Gowen, A. A.; Downey, G.; Esquerre, C.; O'Donnell, C. P., Preventing over-fitting in PLS calibration models of near-infrared (NIR) spectroscopy data using regression coefficients. *J. Chemom.* **2011,** *25* (7), 375-381.

58. Anker, L. S.; Jurs, P. C., Prediction of carbon-13 nuclear magnetic resonance chemical shifts by artificial neural networks. *Anal. Chem.* **1992,** *64* (10), 1157-64.

59. Mehmood, T.; Liland, K. H.; Snipen, L.; Saeboe, S., A review of variable selection methods in Partial Least Squares Regression. *Chemom. Intell. Lab. Syst.* **2012,** *118*, 62-69.

60. McShane, M. J.; Cote, G. L.; Spiegelman, C., Variable selection in multivariate calibration of a spectroscopic glucose sensor. *Appl. Spectrosc.* **1997,** *51* (10), 1559-1564.

61. Anderssen, E.; Dyrstad, K.; Westad, F.; Martens, H., Reducing over-optimism in variable selection by cross-model validation. *Chemom. Intell. Lab. Syst.* **2006,** *84* (1-2), 69-74.

62. Balabin, R. M.; Smirnov, S. V., Variable selection in near-infrared spectroscopy: Benchmarking of feature selection methods on biodiesel data. *Anal. Chim. Acta* **2011,** *692*, 63-72.

63. Li, R.; Wang, D., Preparation of regenerated wool keratin films from wool keratin-ionic liquid solutions. *J. Appl. Polym. Sci.* **2013,** *127*, 2648-2653.

64. Peplow, P. V.; Dias, S. N. G. P. J.; Roddick-Lanzilotta, A. D.; Kelly, R. J. Orthopedic materials derived from keratin. US Patent 7297342, Nov 20, 2007.

65. Fang, J.-Y.; Chen, J.-P.; Leu, Y.-L.; Wang, H.-Y., Characterization and evaluation of silk protein hydrogels for drug delivery. *Chem. Pharm. Bull.* **2006,** *54*, 156-162.

66. Byler, D. M.; Susi, H., Examination of the secondary structure of proteins by deconvolved FTIR spectra. *Biopolymers* **1986,** *25*, 469-87.

67. Pelton, J. T.; McLean, L. R., Spectroscopic Methods for Analysis of Protein Secondary Structure. *Anal. Biochem.* **2000,** *277* (2), 167-176.

68. Ye, S.; Li, H.; Yang, W.; Luo, Y., Accurate Determination of Interfacial Protein Secondary Structure by Combining Interfacial-Sensitive Amide I and Amide III Spectral Signals. *J. Am. Chem. Soc.* **2014,** *136* (4), 1206-1209.

69. Karaman, I.; Qannari, E. M.; Martens, H.; Hedemann, M. S.; Knudsen, K. E. B.; Kohler, A., Comparison of Sparse and Jack-knife partial least squares regression methods for variable selection. *Chemom. Intell. Lab. Syst.* **2013,** *122*, 65-77.

70. Lovejoy, K. S.; Lou, A. J.; Davis, L. E.; Sanchez, T. C.; Iyer, S.; Corley, C. A.; Wilkes, J. S.; Feller, R. K.; Fox, D. T.; Koppisch, A. T.; Del Sesto, R. E., Single-Pot Extraction-Analysis of Dyed Wool Fibers with Ionic Liquids. *Anal. Chem. (Washington, DC, U. S.)* **2012,** *84*, 9169-9175.

71. Aluigi, A.; Zoccola, M.; Vineis, C.; Tonin, C.; Ferrero, F.; Canetti, M., Study on the structure and properties of wool keratin regenerated from formic acid. *Int. J. Biol. Macromol.* **2007,** *41* (3), 266-273.

72. Cardamone, J. M., Investigating the microstructure of keratin extracted from wool: Peptide sequence (MALDI-TOF/TOF) and protein conformation (FTIR). *J. Mol. Struct.* **2010,** *969*, 97-105.

73. Idris, A.; Vijayaraghavan, R.; Patti, A. F.; MacFarlane, D. R., Distillable Protic Ionic Liquids for Keratin Dissolution and Recovery. *ACS Sustainable Chem. Eng.* **2014,** *2*, 1888-1894.

74. Sowa, M. G.; Wang, J.; Schultz, C. P.; Ahmed, M. K.; Mantsch, H. H., Infrared spectroscopic investigation of in vivo and ex vivo human nails. *Vib. Spectrosc.* **1995,** *10*, 49-56.

75. Burnes, D. A.; Ciurczak, E. W.; Editors, *Handbook of Near-Infrared Analysis. [In: Pract. Spectrosc., 1992; 13]*. 1992; p 681 pp.

76. Liu, Y., Vibrational spectroscopic investigation of Australian cotton cellulose fibers Part 1. A Fourier transform Raman study. *Analyst (Cambridge, U. K.)* **1998,** *123* (4), 633-636.

77. Yan, J.; Villarreal, N.; Xu, B., Characterization of Degradation of Cotton Cellulosic Fibers Through Near Infrared Spectroscopy. *J. Polym. Environ.* **2013,** *21* (4), 902-909.

78. Elliott, A., Infrared dichroism and chain orientation in crystalline ribonuclease. *Proc. R. Soc. London, Ser. A* **1952,** *211*, 490-9.

79. Fraser, R. D. B., Side-chain orientation in fibrous proteins. *Nature (London, U. K.)* **1955,** *176*, 358-9.

80. Krikorian, S. E.; Mahpour, M., Identification and origin of N-H overtone and combination bands in the near-infrared spectra of simple primary and secondary amides. *Spectrochim. Acta, Part A* **1973,** *29*, 1233-46.

81. Ellis, J. W.; Bath, J., Modifications in the near infrared absorption spectra of protein and of light and heavy water molecules when water is bound to gelatin. *J. Chem. Phys.* **1938,** *6*, 723-9.

82. Kaye, W., Near-infrared spectroscopy. I. Spectral identification and analytical applications. *Spectrochim. Acta* **1954,** *6*, 257-87.

83. Tonin, C.; Zoccola, M.; Aluigi, A.; Varesano, A.; Montarsolo, A.; Vineis, C.; Zimbardi, F., Study on the conversion of wool keratin by steam explosion. *Biomacromolecules* **2006,** *7*, 3499-504.

84. Miyazawa, M.; Sonoyama, M., Second derivative near infrared studies on the structural characterization of proteins. *J. Near Infrared Spectrosc.* **1998,** *6*, A253-A257.

85. Varum, K. M.; Egelandsdal, B.; Ellekjaer, M. R., Characterization of partially N-acetylated chitosans by near infrared spectroscopy. *Carbohydr. Polym.* **1996,** *28* (3), 187-93.

86. Pedram Rad, Z.; Tavanai, H.; Moradi, A. R., Production of feather keratin nanopowder through electrospraying. *J. Aerosol Sci.* **2012,** *51*, 49-56.

87. Iridag, Y.; Kazanci, M., Preparation and characterization of bombyx mori silk fibroin and wool keratin. *J. Appl. Polym. Sci.* **2006,** *100* (5), 4260-4264.

88. Sun, P.; Liu, Z.-T.; Liu, Z.-W., Particles from bird feather: A novel application of an ionic liquid and waste resource. *J. Hazard. Mater.* **2009,** *170* (2-3), 786-790.

89. Yoshimizu, H.; Ando, I., Conformational characterization of wool keratin and S-(carboxymethyl)kerateine in the solid state by carbon-13 CP/MAS NMR spectroscopy. *Macromolecules* **1990,** *23*, 2908-12.

90. Tanabe, T.; Okitsu, N.; Tachibana, A.; Yamauchi, K., Preparation and characterization of keratin-chitosan composite film. *Biomaterials* **2002,** *23*, 817-25.

91. Persson, A. M.; Sokolowski, A.; Pettersson, C., Correlation of in vitro dissolution rate and apparent solubility in buffered media using a miniaturized rotating disk equipment: Part I. Comparison with a traditional USP rotating disk apparatus. *Drug Discoveries Ther.* **2009,** *3*, 104-113.

92. Reichl, S.; Borrelli, M.; Geerling, G., Keratin films for ocular surface reconstruction. *Biomaterials* **2011,** *32* (13), 3375-3386.

93. Phaechamud, T.; Ritthidej, G. C., Formulation variables influencing drug release from layered matrix system comprising chitosan and xanthan gum. *AAPS PharmSciTech* **2008,** *9*, 870-877.

94. Qi, L.; Xu, Z.; Jiang, X.; Hu, C.; Zou, X., Preparation and antibacterial activity of chitosan nanoparticles. *Carbohydr. Res.* **2004,** *339* (16), 2693-2700.

95. Zhang, Z.; Chen, L.; Ji, J.; Huang, Y.; Chen, D., Antibacterial properties of cotton fabrics treated with chitosan. *Text. Res. J.* **2003,** *73*, 1103-1106.

96. Cadogan, E. I.; Lee, C.-H.; Popuri, S. R.; Lin, H.-Y., Effect of Solvent on Physico-Chemical Properties and Antibacterial Activity of Chitosan Membranes. *Int. J. Polym. Mater. Polym. Biomater.* **2014,** *63*, 708-715.

97. Jeon, S. J.; Oh, M.; Yeo, W.-S.; Galvao, K. N.; Jeong, K. C., Underlying mechanism of antimicrobial activity of chitosan microparticles and implications for the treatment of infectious diseases. *PLoS One* **2014,** *9*, e92723/1-e92723/10, 10 pp.

98. Levengood, S. K. L.; Zhang, M., Chitosan-based scaffolds for bone tissue engineering. *J. Mater. Chem. B* **2014,** *2* (21), 3161-3184.

99. Ivan, F. D.; Marian, A.; Tanase, C. E.; Butnaru, M.; Verestiuc, L., Biomimetic composites based on calcium phosphates and chitosan - hyaluronic acid with potential application in bone tissue engineering. *Key Eng. Mater.* **2014,** *587*, 191-196.

100. Magdalou, J.; Stoltz, J. F.; Netter, P.; Pinzano, A.; Brun, V.; Guillaume, C.; Mechiche Alami, S.; Josse, J.; Jing, J.; Draux, F.; Bouthors, S.; Laurent-Maquin, D.; Gangloff, S. C.; Kerdjoudj, H.; Velard, F., Chitosan/hydroxyapatite hybrid scaffold for bone tissue engineering. *Bio-Med. Mater. Eng.* **2014,** *24* (Suppl. 1), S63-S73.

101. Tan, M. L.; Shao, P.; Friedhuber, A. M.; van Moorst, M.; Elahy, M.; Indumathy, S.; Dunstan, D. E.; Wei, Y.; Dass, C. R., The potential role of free chitosan in bone trauma and bone cancer management. *Biomaterials* **2014,** *35* (27), 7828-7838.

CHAPTER 6

A FACILE METHOD FOR *IN SITU* SYNTHESIS OF GOLD NANOPARTICLES IN CELLULOSE-CHITOSAN-KERATIN COMPOSITE MATERIALS

6.1. Background

Metal nanoparticles, including gold (AuNPs) and silver nanoparticles (AgNPs), have been widely used in various biomedical applications due to their unique physical and chemical properties.[1-4] Interestingly, these properties are different from those of the corresponding bulk material. For example, whereas the color of bulk gold is yellow, the color of AuNPs varies from red to blue to green depending on their size, shape and dielectric constant of the surrounding medium. Therefore, by changing these parameters (*i.e.* size, shape, and dielectric constant), the properties of AuNPs can be tuned to suit specific applications. The color of the AuNPs originate from a phenomenon called localized surface plasmon resonance (LSPR).[5] In this phenomenon, a narrow range of frequencies of incident light induces the oscillation of conduction band electrons in the nanoparticles. For AuNPs and AgNPs, these frequencies lie in the visible and near infrared region. Spherical AuNPs exhibit a single "plasmon" band in the visible region.[6]

The extinction coefficient of AuNPs is higher than those of general organic chromophores.[7] This is due to the larger surface area to volume ratio, which enables more electrons to be exposed to the radiation thereby enhancing the absorption. Most importantly, the position of this band changes when the nanoparticle gets attached to some larger chemical. In addition, AuNPs can enhance surface Raman scattering.[8] These properties enable AuNPs to be used as chemical sensors. Recently, AuNPs were shown to exhibit antibacterial activity against three pathogenic bacteria; *Pseudomonas syringae,*

Eschericia coli, and *Shigella sonnei*.[3] Such results are intriguing and they provided an impetus for us to synthesize AuNPs to evaluate their antibacterial properties against other bacterial species. In addition, AgNPs have been shown to be active not only against bacteria but also against viruses.[9] The proposed mechanism for virucidal action was that Ag would bind with the polyvalent receptor sites on the viral envelope thereby preventing the virus from binding and infecting host cells. Most importantly, in one of the studies, both AuNPs and AgNPs coated with mercaptoethane sulfonate (MES) were found to be able to inhibit herpes simplex virus type 1 (HSV-1).[10,11] This also motivated us to synthesize AuNPs with the intention of evaluating them for their activity against viruses. However, despite all this potential, the synthesis of AuNPs remains a challenge.

On one hand, the small size of nanoparticles present many potential benefits in biomedical field. For example, the larger surface are enables them to be used in drug delivery. On the other hand, this larger surface area makes it more difficult to synthesize nanoparticles that remain separated in the solution. Nanoparticles tend to agglomerate, thereby adversely altering their desirable properties. To circumvent the likelihood of agglomeration, AuNPs have been capped with organic substrates such as the cationic surfactant, cetyltrimethylammonium bromide (CTAB). However, CTAB is toxic to cells at submicromolar dose.[7] Therefore, the use of CTAB is less attractive. To mitigate this challenge, polyethylene glycol (PEG) has been used as an outer coating for the CTAB-coated AuNPs or as a sole coating for the AuNPs. The resultant AuNPs were found to be non-toxic. However, PEG forms films with poor rheological properties. Thus, there is still need to synthesize AuNP-based composites with better rheological properties.

The information presented in the previous paragraphs motivated us to evaluate the possibility of synthesizing AuNPs encapsulated in biopolymer matrices. We chose natural, biocompatible polysaccharides (*i.e.* cellulose and chitosan) and proteins (*i.e.* keratin). In addition to being biocompatible, these biopolymers are relatively abundant. For example, cellulose (CEL) is the most abundant biopolymer on earth followed by chitin (from which chitosan is derived by partial deacetylation). Keratin (KER) is present in greater than 95% per weight of wool. Thus, their exploitation will almost guarantee an inexhaustible supply of resources. Furthermore, chitosan (CS) is antibacterial due to the amino groups that are present in its structure. Most importantly, these biopolymers can form films with better rheological properties than PEG films.

We, therefore, explore a method to encapsulate AuNPs in the biopolymer matrices. This was accomplished by using potentially green solvents, ionic liquids, to dissolve the biopolymers together with the Au salts. Thereafter, the casted gels were soaked in solutions of reducing agents; sodium borohydride and sodium citrate. This was done to form the nanoparticles *in situ*. The ionic liquids used for dissolving the biopolymers and gold salt were 1-butyl-3-methylimidazolium chloride ($BMIm^+Cl^-$) and 1-ethyl-3-methylimidazolium bis (trifluoromethylsulfonylimide) ($EMIm^+Tf_2N^-$) respectively. The resultant AuNP-based biopolymers were characterized by X-ray powder diffraction (XRPD), X-ray photoelectron spectroscopy (XPS) and scanning electron microscopy (SEM) techniques. The results of these characterizations are reported herein.

6.2. Experimental

6.2.1.Chemicals

Cellulose (microcrystalline, DP≈300), chitosan (84±2% degree of deacetylation), chloroauric acid ($HAuCl_4.3H_2O$), and tetrahydrofuran (THF) were purchased from Sigma-Aldrich (Milwaukee, WI). Sodium borohydride was obtained from Alfa Aesar. The ionic liquid, 1-butyl-3-methylimidazolium chloride was synthesized using the same method described earlier (*see Chapter 2 for details)*, using freshly distilled methylimidazole (Alfa Aesar) and *n*-butylchloride (Alfa Aesar).The other ionic liquid, $EMIm^+Tf_2N^-$ was synthesized as described in the next section. Water was purified (18.2 $M\Omega\ cm^{-1}$) using a Barnstead Nanopure unit (Dubuque, IA, USA). Sodium citrate was obtained from Matheson Coleman & Bell.

6.2.2. Synthesis of 1-butyl-3-methylimidazolium bis (trifluoromethylsulfonyl) imide

Freshly distilled 1-methylimidazole was added into a flask and bubbled with Ar to remove any oxygen. After 10 min of Ar bubbling, ethyl bromide was added drop wise each time ensuring that the temperature does not exceed 40 °C. The contents were then refluxed at 40 °C for 3 h. Crude $EMIm^+Br^-$ was then allowed to cool down to room temperature. During cooling, the IL solidified into a thick mass. Subsequently, the IL was washed with three portions of ethyl acetate. Residual ethyl acetate was removed by rotavaping the clean IL at 60 °C. Finally, the IL, $EMIm^+Br^-$, was dried at 70 °C under vacuum for at least 10 h. The purity of the IL was confirmed by ^1H NMR spectroscopy.

$EMIm^+Br^-$ (16.639 g, 87 mmol) was dissolved in 50 mL of double distilled water in a beaker before being transferred to a round bottomed flask. Subsequently, lithium bis (trifluoromethylsulfonyl) imide (25.000 g, 87 mmol) dissolved in 50 mL of double distilled water was added slowly to the aqueous solution of $EMIm^+Br^-$. The mixture was stirred at room temperature for 3-3.5 h. As the reaction progressed, two phases were formed. At the end of the reaction, the mixture with two phases was transferred to a separatory funnel. The top layer, which is the aqueous layer was decanted off. The bottom layer, the IL layer, was diluted with 40 mL dichloromethane (DCM). Then, this solution was washed several times with 50 mL portions of double distilled water to remove any remaining LiBr. The IL was considered clean when the aqueous washings tested negative to the AgBr test. Then, the purity was further confirmed by ^{1}H NMR spectroscopy. ^{1}H NMR (DMSO, 400 MHz) δ in ppm: 1.41 (t, 3H, C$\underline{H_3}$CH$_2$), 3.84 (s, 1H, NC$\underline{H_3}$), 4.20 (q, 2H, NC$\underline{H_2}$), 7.70 (d, 2H, 2 NC$\underline{H}$), 9.10 (s, 1H, NC$\underline{H}$N). It is noteworthy mentioning that even after drying for several hours, water was still detectable at δ 3.34 ppm.

6.2.3. Synthesis of CEL/CS/KER+Au composites

We synthesized [CEL+KER], [CS+KER] and [CEL+CS] containing various amounts of gold salt. In the case of KER-containing composites, the polysaccharides (either CEL or CS) and KER were dissolved separately in $BMIm^+Cl^-$ ionic liquid. For example, 50:50 CEL:KER was synthesized as follows. CEL (0.600 g) and KER (0.600 g) were dissolved separately each in 10.000 g $BMIm^+Cl^-$ for 5-6 h under the continuous flow of Ar gas. Whereas the polysaccharides were dissolved at 90-105 °C, KER was dissolved at 115-125 °C. After this dissolution, the less viscous KER solution was poured

into CEL solution. The mixture was kept at 90-105 °C for a further 1 h to ensure homogeneous mixing of KER and CEL. Approximately five minutes before the lapse of that one hour, 160 mg $HAuCl_4.3H_2O$ was dissolved in 1.000 g $EMIm^+Tf_2N^-$ in a separate flask. To speed the rate of dissolution, the flask was warmed up in oil bath at 90-105 °C. At the one hour mark of mixing CEL and KER solutions, this gold solution was added drop wise into the [CEL+KER] solution. The mixture was left stirring for a further one hour. Then, the mixture was casted into two moulds of dimensions of 45 mm (L) x 45 mm (W) and 3 mm (T). The mixture was left to gel for at least 12 h. However, later on, it was found that 24 h is needed for complete gelation.

6.2.4. Reduction of Au^{3+} to Au nanoparticles (AuNPs)

The Au (III) ions, which were encapsulated in the biopolymer matrices, were reduced by either sodium citrate or sodium borohydride. For reduction in sodium citrate, 5.800 g (≡20 mmol) of this reducing agent was dissolved in 200 mL of double distilled water. The gel film was removed from the mold and sandwiched between two PTFE meshes with the same L x W dimensions as the gel film. Three cylindrical plastic with both ends open were stacked on top of each other inside a 600 mL beaker. A stir bar was put inside the space created by these cylinders. These cylinders were used to prevent any damage of the films from the spinning magnetic stir bar. Then, the sandwiched film was laid flat on top of this crown stack. The mesh was desirable because it would allow free circulation of solution thereby exposing much film surface to the solution. Subsequently, sodium citrate solution was poured slowly into this beaker. The beaker was then covered with parafilm to reduce evaporation of water. The reaction was allowed to proceed under stirring at room temperature for 48 h. Subsequently, the film was washed for 24 h in 200

mL of 50:50 THF:H_2O to remove $EMIm^+Tf_2N^-$ ionic liquid from the film and then with film was washed with water until clean. This was confirmed by the disappearance of IL UV absorption bands in the washing solution. The water was replaced every 24 h to maximize the removal of $BMIm^+Cl^-$ and any inorganic salts remaining inside the sample. It took at least 5 d for the films to be completely clean. Reduction using sodium borohydride was carried out the same way as in sodium citrate. It should be pointed out that sodium borohydride was dissolved in methanol because it reacts faster with water.

6.2.5. Drying the films

The films were then dried in a home-made drier under a continuous flow of air, which was being drawn through the drier chamber by a fan. During the drying process, weights had to be laid flat on the films to ensure that the film would remain flat. If this is not done, the film would curl up and shrink. This is undesirable in later characterizations and applications which require the films to be flat to get reliable results.

6.2.6. Instruments

X-ray powder diffraction was performed on a Rigaku Miniflex II within the 2θ range 2 to 85° scanning at the rate of 5° 2θ per min. X-ray photoelectron spectra were taken on a HP 5950A ESCA spectrometer with Al monochromatic source and a flood gun was used for charge suppression.

6.3. Results and Discussion

In the synthesis of AuNPs, sodium borohydride and sodium citrate are widely used to reduce Au(III) to Au(0). However, in the absence of capping agents, the resultant

nanoparticles tend to aggregate, which is undesirable because these particles often times do not possess the attractive properties of AuNPs. Therefore, the use of polysaccharides and proteins was desirable because these can stabilize the AuNPs without the possibility of aggregation. The polysaccharides would impede or even stall the movement of AuNPs once formed by the reducing solutions. Interestingly, there were some observable differences in the colors of films in sodium borohydride compared to the ones in sodium citrate. Specifically, on one hand, as soon as the films were dipped in sodium borohydride solution, the films became darker. On the other hand, films dipped in sodium citrate took at least 24 h to change to a faint purple color. These observations are significant because they suggest that the AuNPs formed have sizes that are dependent on the identity and probably the reducing power of the reducing agents. Therefore, by switching between reducing agents of different reducing power, one can make AuNPs that are suited for particular applications. For example, smaller nanoparticles may be able to interact with the polyvalent sites of a matching size. During the first stages of reduction, surface adsorbed gold ions get desorbed into the solution. This was confirmed by the formation of a darker solution as soon as the films were dipped in sodium borohydride. In sodium citrate, the solution remains colorless probably because citrate is a much weaker reducing agent than sodium borohydride.

We used XRD spectroscopy to monitor structural changes that might have taken place during the reactions of either $NaBH_4$ or sodium citrate and the gold ions distributed throughout the biopolymer matrix. As illustrated in Figure 6-1, broad bands appeared at $2\theta = \sim 10.0^0$, and $\sim 20.0^0$. These bands are ascribable to the biopolymers. Interestingly, films that were treated in either of the reducing agents exhibited new sharp peaks at $2\theta =$

38.0°, 44.3°, 64.6°, 77.5°, and 81.4°. These bands can be attributed to the formation of AuNPs during reduction of Au ions. These results demonstrate the possibility of synthesizing AuNPs within the biopolymer matrices. This has the advantage of providing ease of handling during applications. In addition, biopolymers help to stabilize the nanoparticles.

However, the peaks observed after treating the films with $NaBH_4$ were much broader than those observed when sodium citrate was used. The broader the XRD band the smaller the nanoparticle. This, therefore suggests that AuNPs synthesized using $NaBH_4$ are smaller than the ones synthesized using sodium citrate. To estimate the sizes of these nanoparticles, we used the well-known Scherrer equation ($B = (K\lambda)/(\beta \cos\theta)$) where B is the crystallite size in nm, K is the dimensionless shape factor, λ is the X-ray wavelength, β is the line broadening at half maximum height of the particular peak after subtracting instrument line broadening.[12] We considered K to be equal to 0.94 by assuming that AuNPs formed in these experiments are spherical. It was determined that the size of AuNPs in 50:50 CEL:KER containing 160 mg Au is 33.7 nm when sodium citrate was used as compared to 8.4 nm when sodium borohydride was used. For 50:50 CS:KER containing 110 mg $HAuCl_4.3H_2O$, the size of nanoparticles synthesized by using sodium citrate (43.1 nm) was 10X larger than those synthesized using sodium borohydride (4.0 nm). These differences in the effects of these reducing agents can be rationalized by considering their relative reducing power. Sodium borohydride is much stronger reducing agent than sodium citrate. Gold ions are expected to be more mobile than their Au(0) counterparts. As a result, with a stronger reducing agent like sodium borohydride, these ions are reduced before they have a chance to move around and

adsorb onto AuNP nucleation sites. On the other hand, the weaker reducing agent like sodium citrate gives the ions ample time to adsorb onto the AuNP nucleation sites before they are reduced thereby forming bigger particles.

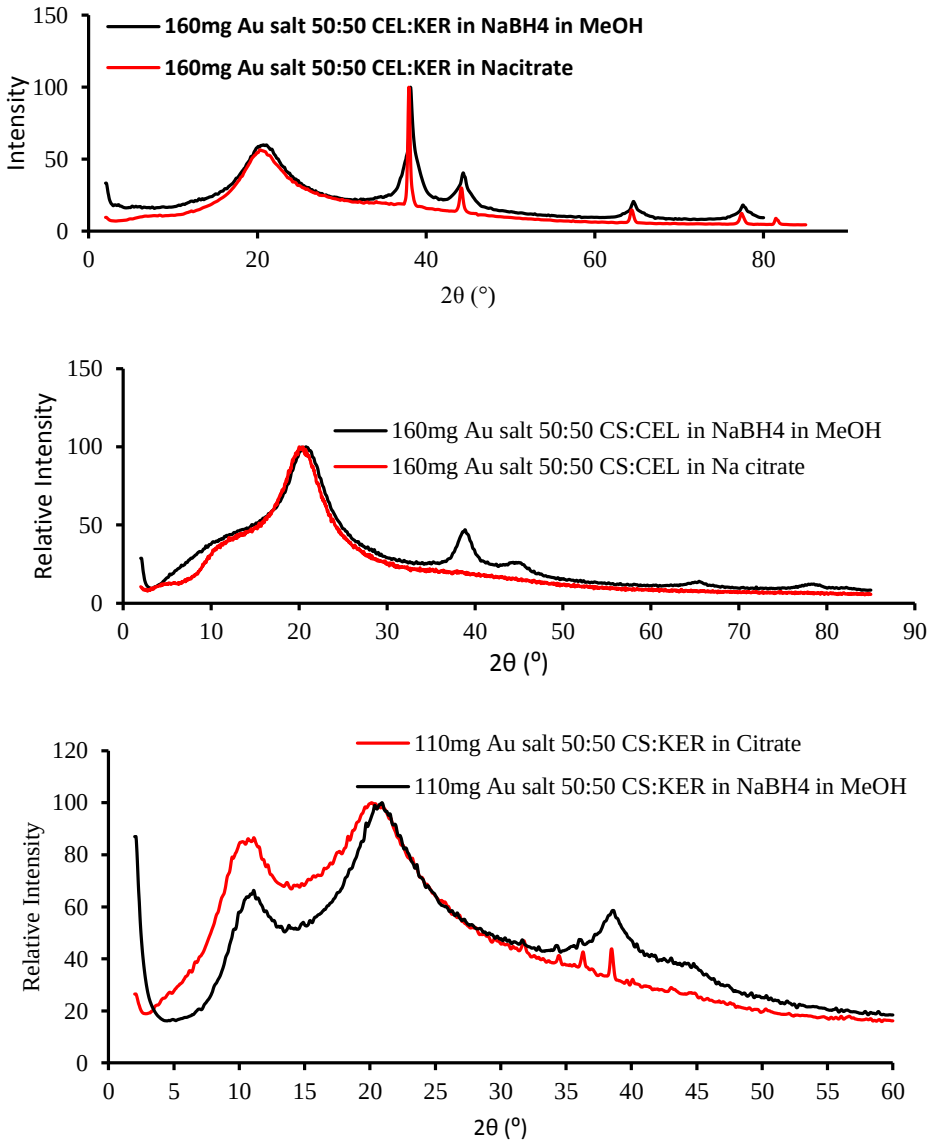

Figure 6-1 X-ray powder diffraction (XRPD) of AuNP-based composite films

We used XPS to confirm the oxidation state of the Au in the AuNPs. The results are presented in Figure 6-2 below. As can be seen from this figure, XPS of the CEL:KER composite displays a doublet at 87.1 eV and 83.5 eV which corresponds to $4f_{5/2}$ and $4f_{7/2}$ respectively. These results confirm that Au (III) was indeed reduced successfully to zero by the reducing agent. In addition, C1s and O1s bands at 284.8 eV and 532.0 eV respectively helped to further confirm the successful regeneration of the biopolymers CEL and KER. The absence of a peak in the XPS spectral trace in the Cl2p region confirmed that the ionic liquid was completely removed from the film.

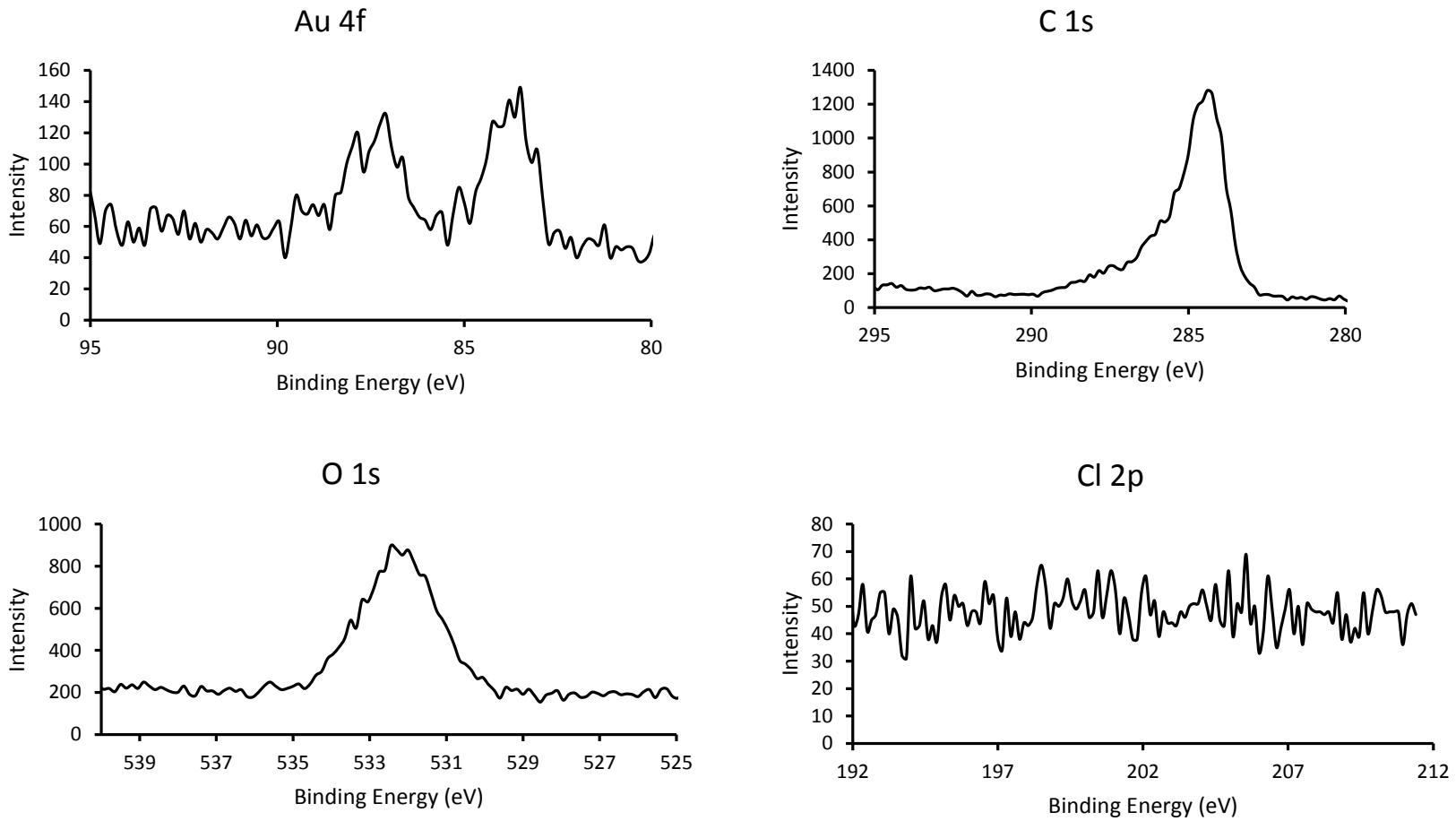

Figure 6-2 XPS spectral traces of Au 4f, C 1s, O 1s and Cl 2p

6.4. Conclusions

Results presented in this preliminary study are very encouraging because they show that it is indeed possible to synthesize AuNPs using biopolymers as capping agents. In addition, the approach followed here involves the use of green solvents thereby widening the potential applications of ionic liquids and AuNPs.

6.5. References

1. Huang, X.; Jain, P. K.; El-Sayed, I. H.; El-Sayed, M. A., Plasmonic photothermal therapy (PPTT) using gold nanoparticles. *Lasers Med Sci* **2008,** *23* (3), 217-28.

2. Jain, S.; Hirst, D. G.; O'Sullivan, J. M., Gold nanoparticles as novel agents for cancer therapy. *Br J Radiol* **2012,** *85* (1010), 101-13.

3. Mishra, A.; Kumari, M.; Pandey, S.; Chaudhry, V.; Gupta, K. C.; Nautiyal, C. S., Biocatalytic and antimicrobial activities of gold nanoparticles synthesized by Trichoderma sp. *Bioresour. Technol.* **2014,** *166*, 235-242.

4. Hainfeld, J. F.; Slatkin, D. N.; Focella, T. M.; Smilowitz, H. M., Gold nanoparticles: a new X-ray contrast agent. *Br. J. Radiol.* **2006,** *79*, 248-253.

5. Mayer, K. M.; Hafner, J. H., Localized surface plasmon resonance sensors. *Chem. Rev. (Washington, DC, U. S.)* **2011,** *111* (6), 3828-3857.

6. Dreaden, E. C.; Alkilany, A. M.; Huang, X.; Murphy, C. J.; El-Sayed, M. A., The golden age: gold nanoparticles for biomedicine. *Chem. Soc. Rev.* **2012,** *41*, 2740-2779.

7. Alkilany, A. M.; Nagaria, P. K.; Hexel, C. R.; Shaw, T. J.; Murphy, C. J.; Wyatt, M. D., Cellular uptake and cytotoxicity of gold nanorods: molecular origin of cytotoxicity and surface effects. *Small* **2009,** *5*, 701-708.

8. Murphy, C. J.; Sau, T. K.; Orendorff, C. J.; Gole, A. M. Surface enhanced Raman spectroscopy using shaped gold nanoparticles. WO2006065762A2, 2006.

9. Galdiero, S.; Falanga, A.; Vitiello, M.; Cantisani, M.; Marra, V.; Galdiero, M., Silver nanoparticles as potential antiviral agents. *Molecules* **2011,** *16*, 8894-8918.

10. Baram-Pinto, D.; Shukla, S.; Perkas, N.; Gedanken, A.; Sarid, R., Inhibition of Herpes Simplex Virus Type 1 Infection by Silver Nanoparticles Capped with Mercaptoethane Sulfonate. *Bioconjugate Chem.* **2009,** *20*, 1497-1502.

11. Baram-Pinto, D.; Shukla, S.; Gedanken, A.; Sarid, R., Inhibition of HSV-1 Attachment, Entry, and Cell-to-Cell Spread by Functionalized Multivalent Gold Nanoparticles. *Small* **2010,** *6*, 1044-1050.

12. Prathna, T. C.; Chandrasekaran, N.; Raichur, A. M.; Mukherjee, A., Biomimetic synthesis of silver nanoparticles by Citrus limon (lemon) aqueous extract and theoretical prediction of particle size. *Colloids Surf., B* **2011,** *82* (1), 152-159.

CHAPTER 7
CONCLUSIONS AND FUTURE DIRECTIONS

7.1. Conclusions

In summary, we have developed a simple, one-step method to synthesize novel composites containing polysaccharides and proteins. This was accomplished using ionic liquids, which are considered to be more 'green' than any other solvents that are currently being used to dissolve and fabricate biopolymer composites. The main attractive features of these ionic liquids include immeasurably low vapor pressure, higher thermal stability, tunable physical and chemical properties. Low vapor pressure and higher thermal stability enables these ionic liquids to be used at moderate temperatures like 90-130 °C without concerns for toxic vapor emissions and thermal degradation. Tunable properties enable ionic liquids to be used in a wide variety of applications. In our case, 1-butyl-3-methyl imidazolium chloride was the preferred ionic liquid because it could dissolve all the biopolymers we were using. The biopolymers used include cellulose, chitosan and keratin. These biopolymers offer so many advantages. They are relatively more abundant with cellulose being the most abundant biopolymer on Earth. There use would therefore guarantee an inexhaustible supply of inputs. Most of the materials in use today rely heavily on synthetic polymers. These are undesirable because they are derived from non-renewable sources. Their continued use will pose a threat because they will become extinct. Therefore, by using biopolymers, we help to reduce pressure on these non-renewable derived materials.

Another contribution by our study was that we extended the applications of these biopolymers to include purification of water. This was accomplished by doping these biopolymeric composites with selective macrocyclic compounds including crown ether and resorcinarene. By themselves, these macrocycles are difficult to handle in water purification. This is because after use, these macrocycles would have to be separated from the clean water. This would involve filtration. However, this separation technique has its own limitations, which preclude its wider adoption at commercial scale. Specifically, the membranes that are used for separation add an extra avoidable cost. In addition, membranes can become easily blocked by the macrocyclic particles. By encapsulating these macrocycles in biopolymeric composites such as CEL/CS, these selective adsorption properties can still be realized while at the same time deriving benefits such as easy handling. These biopolymers can form strong films, which when used in water purification, they can be removed without the need for filtration. Our experiments in this study have shown that such composites containing the polysaccharides and encapsulated macrocycles can selectively adsorb both organic and inorganic pollutants. Organic pollutants were mainly adsorbed by resorcinarene based composites. These organic pollutants represent one of the most deadly materials that are discharged ever day into the water ways. Using these composites would ensure that companies can be motivated to treat their water before discharging them into the water ways. Inorganic pollutants such as heavy metal ions have been implicated in some of the deadly accidents in the past notably Itai Itai disease caused by cadmium poisoning in Japan. Mining companies were discharging Cd-contaminated wastewater into the water ways, which eventually got into water that was being drunk by the communal people. By

developing these composites, we hope companies will be able to find a cheaper remedy to some of the avoidable accidents.

We also used these biopolymers as platforms for mineralizing calcium phosphate, which is the main component of teeth. This was done to alleviate the limitations faced by using hydroxyapatite as an implant material by itself. Hydroxyapatite tends to migrate from the implant site necessitating revision surgery which is painful and oftentimes costly. We exploited the film forming property of the biopolymers to synthesize compact materials which can potentially stay on the implant site throughout the whole bone tissue healing process. In addition, these biopolymers are both biocompatible and biodegradable. Their use would ensure that as the bone heals, the implant gets resorbed into the biological system without any need for surgical removal of the implant. By varying the ratios of cellulose and chitosan, the properties of the resultant composites could also be changed. One of the properties that was thoroughly studied in this project was tensile strength. Adding more cellulose to chitosan enhanced tensile strength of the resultant composite. This is quite interesting because it means the tensile properties of the implant can be tuned to match the mechanical requirements of the damaged bone. Most importantly, chitosan possesses innate antibacterial properties against a wide range of both gram positive and gram negative bacteria. This implies that using both cellulose and chitosan in the same bone implant would serve two purposes. Whereas cellulose would impart superior mechanical properties, chitosan would impart antibacterial properties; two of the most needed properties to ensure smooth healing of the implant wound site. Hydroxyapatite is required for osteoconductivity because it is similar in structure to the structure of the inorganic part of the bone material. The method developed in this project

is very simple and fast. The methods currently being used tend to either take unnecessarily too long or they are just too costly. By using these cheaper and readily available biopolymers would make bone implants more affordable to the low income earners.

We also evaluated these biopolymers for their suitability in controlling drug release. We used an antibiotic ciprofloxacin (CPX) as a model drug. In this project, we used keratin, in addition to the polysaccharides, cellulose and chitosan. It was found out that keratin considerably slowed down the release of CPX. Interestingly, adding either cellulose or chitosan helped to modulate the release of this drug. Although KER slows down the release of drug, by itself it is very brittle, which precludes its use at commercial scale. However, this could be ameliorated by adding either chitosan or cellulose to it. Again, these composites can be used in applications such as wound healing. The composites exhibited burst release during the initial stages, which is desirable in wound healing where large amounts of therapeautic drug should be delivered within a very short period of time. After this burst period, the composites were found to be able to prolong the release of the drug. Such composites are more attractive because, maintaining such levels of drug at the wound site would reduce chances of development of drug resistance. In addition, chitosan can also help in killing bacteria because it is naturally antibacterial.

Finally, some preliminary results about the synthesis of gold nanoparticles in CEL/CS/KER matrix were presented. In this project, AuNPs were synthesized in situ using the biopolymers as platforms to prevent the common problem of aggregation of the nanoparticles. Although there are so many capping agents that have been used in many studies, most of them involve the use of toxic agents such as CTAB. In our case, we have

used biocompatible agents, which allay the safety concerns associated with the current agents. In addition, these agents are naturally abundant, which ensures that cheaper sources are relatively available. More importantly, the sizes of the composites could be tuned by changing the reducing power of the reducing agents. AuNPs present many opportunities in a wide variety of applications including antiviral applications. This is because Au can bind more strongly with such ligands as the S-based ligands, which are mostly found on the surfaces of viruses. These are the points of contact when the virus attaches and infects a host cell. If our AuNPs attach strongly to those surfaces, that would prevent the binding of the virus with the host cell thereby preventing infection. Another advantage of the method we developed in this project is that it ensures that homogeneous composites are formed. This has implications on precise and accurate determination of the doses. The current methods of based on ex situ formation of AuNP composites are generally suffer from non-homogeneity problems.

7.2. Future Research

Although we obtained encouraging results from the projects undertaken in this thesis, there is still more that can be done to bring these materials closer to commercialization. For example, ionic liquids were recycled by distillation. However, this process consumes a lot of energy. Therefore, its adoption may be met by skepticism from the commercial community. Other methods need to be pursued such as phase separations. Such a method can be carried out at room temperature without any worries about the energy bill.

The projects on adsorption of heavy metal ions and organic pollutants can be extended to include more pollutants. In addition, we have to carry out competitive

adsorption experiments to ensure that the macrocycles are not going to be affected by some of the innocuous metal ions such as sodium and potassium ions. The results obtained in this study can help to extend the applications of these composites to include quantitative analysis of metal ions such as cadmium and zinc. This would have strong implications in designing potable sensors, which can be used on-site to do quantitative analysis. More studies have to be carried out to optimize these adsorbents. This could be done by studying the effects of some other factors such as temperature. Another experiment that can be tried is that of making composites containing both resorcinarene and crown ether. Such a composite is expected to adsorb both organic and inorganic pollutants due to the presence of resorcinarene and crown ether respectively.

Still a lot has to be done on the AuNP project. This includes making more samples with varying proportions of AuNPs, and the biopolymers. In addition, the reduction process itself can be optimized by studying such factors as time to reach completion of the reduction reaction. Currently, the samples are being reduced for 48 h. The samples can be reduced at different time intervals and then monitor the extent of reduction. To accomplish this though, we have to develop a precise method to quantify Au species that are in the film. XPS can offer a viable solution to this problem.